

Spectroscopic Investigation of the Interaction between Biomimetic Membranes and Protein Aggregates

By

Reem Ahmed Karaballi

A Thesis Submitted to
Saint Mary's University, Halifax, Nova Scotia
In Partial Fulfilment of the Requirements for the Degree of
Masters of Science in Applied Science.

December 2015, Halifax, Nova Scotia

Copyright Reem Ahmed Karaballi, 2015

Approved: Dr. Christa L. Brosseau
Associate professor
Supervisor

Approved: Prof. Mary Sheppard
Professor
Committee member

Approved: Dr. Roby Austin
Associate professor
Committee member

Date: December 3, 2015

ABSTRACT

Spectroscopic Investigation of the Interaction between Biomimetic Membranes and Protein Aggregates

By Reem Ahmed Karaballi

Human diseases characterized by the deposition of insoluble extracellular proteins are referred to as amyloidoses. Such amyloidoses include Alzheimer's disease, Parkinson's disease, Huntington disease, and prion disease. These amyloidoses are found to have common cellular and molecular mechanisms including protein aggregation. These aggregates usually consist of fibers containing misfolded protein with a β -sheet conformation, termed amyloid. The protein aggregates associated with Alzheimer's disease are amyloid- β peptides which have been linked to neuronal death through a poorly understood mechanism. In this work, the interaction between a model protein (insulin) which forms amyloid aggregates and a biomimetic membrane was studied. Specifically spectroscopy was used to detect molecular level changes occurring upon this protein-membrane interaction. It was found that oligomers and protofibrils had the most significant effect on membrane quality; significant membrane deterioration was noted in their presence.

December 3, 2015.

Dedication

I would like to dedicate this body of work to God, as none of it would be possible without the strength he has given me to persevere.

Also, I would like to dedicate this work to my parents: Ahmed Karaballi and Nafissa Faidalla, and my brothers: Mohammed, Omar, Khalid, and Tariq.

It would be unfathomable for me to even start this work without the many blessings like that of my family who has stood with me from day one, believing in me when no one else would. The love and support that my parents showered me with speaks volumes to the power of God and how he uses his earthly instruments to bring out the best me. I would like to thank my four brothers who at times made the journey feel tougher but in hindsight they were also pushing me to do better. Even though you guys gave me hard times but this journey would not have been the same without all of you.

Acknowledgments

I would like to thank my supervisor Dr. Christa L. Brosseau for giving me the opportunity to complete my master's degree in her research group. I have worked in Dr. Brosseau's research lab for the past six years as an undergrad and graduate student and words cannot describe how much this experience has changed my life. Dr. Brosseau has been very helpful with guiding me through this project, so that I have both achieved my goals and learnt many useful life lessons along the way. I thank you for all your help and support you provided me throughout these years. I look up to you not only as a supervisor but also as a role model, thank you for everything!

I would like to thank my committee members: Dr. Roby Austin, and Professor Mary Sheppard for taking the time to meet with me through the past two years. You have provided me with lots of guidance and support, and shared lots of comments and suggestions that guided me through my research. I would like to thank Dr. Heather Andreas for agreeing to be the external examiner and taking the time to read my thesis.

I would like to thank Dr. Brosseau group members, especially; Osai Clarke for being there for me through good and bad, I'm very glad you were always there when I needed you. Soraya Merchant for spending a lot of time training me on the LB, and Marwa Yasmin for being supportive through my mood swings and providing me with energy when needed. Also, I would like to thank Barbara Goodall for reading my thesis and giving me awesome feedback.

I would like to also thank my non-chemist best friends Zeina J. and Mohammed K. who were also very instrumental by lending a listening ear to my many complaints always reassuring me with their optimistic spirits. Just want to say I may not have shown a great deal of gratitude during the rigorous process but know I deeply appreciated having people who would listen to me explain my project on countless occasions and for that I say thank you. Thanks to all my friends that were very supportive of my educational goals, and their support has been much appreciated.

Also, I would like to thank Xiang Yang and Ping Li for helping me image my samples using SEM and TEM, respectively.

Additionally, thanks to all of the Department of Chemistry Faculty and Staff. Without having received the support and love every day I would not have completed my secondary education, and I would not be the chemist I am today. Finally, I would like to thank NSERC and FGSR for providing the financial support required to complete this research.

Table of Contents	page
Abstract	II
Dedication	III
Acknowledgments	IV
Table of Contents	VI
List of Figures	XI
List of Tables	XVII
List of Abbreviations	XVIII

Table of Contents	page
Chapter 1: Introduction	1
1.1 Protein aggregation disorders	1
1.1.1 Introduction	1
1.1.2 Theories	2
1.1.3 Present therapeutic remedies / drawbacks	3
1.2 Objective of thesis	5
1.3 Scope of thesis	6
Chapter 2: Literature Review	7
2.1 Introduction	7
2.1.1 Protein structure and function	7
2.1.2 Protein misfolding and aggregation	10
2.1.3 Aggregated protein and human disease	12
2.1.4 Amyloid pore hypothesis	17
2.2 Cell membrane	21
2.2.1 Cell membranes: structure and function	21
2.2.2 Electrical properties of cell membranes	27
2.2.3 Interaction between proteins and cell membranes	28
2.3 Biomimetic membranes	29
2.3.1 Current models of biomimetic membranes	29
2.3.1.1 Early models	30
2.3.1.2 Solid-supported models	32
2.3.1.3 Characterization of bilayer lipid membranes	36
2.3.2 Applications of model membranes	38

2.4 Langmuir monolayers and films	39
2.4.1 Langmuir monolayers	39
2.4.2 Langmuir-Blodgettry	40
2.4.3 Langmuir Blodgett / Langmuir Schaefer deposition	43
2.5 Characterization of biomimetic membrane-protein interactions	45
2.5.1 Spectroscopic methods	45
2.5.2 Electrochemical methods	48
2.5.3 Other methods	50
Chapter 3: Theory	52
3.1 Langmuir monolayers and Langmuir Blodgettry	52
3.2 Electrochemistry	58
3.3 Vibrational Spectroscopy	62
3.3.1 Raman spectroscopy	62
3.3.2 Surface-Enhanced Raman Spectroscopy (SERS)	68
3.3.3 Attenuated Total Reflectance-Fourier Transform Infrared Spectroscopy (ATR-FTIR)	73
3.4 Electron Microscopy	74
3.4.1 Transmission Electron Microscopy (TEM)	74
3.4.2 Scanning Electron Microscopy (SEM)	77
Chapter 4: Experimental	81
4.1 Reagents	81
4.2 Nanoparticle synthesis and characterization	81
4.3 Construction of silver nanoparticle electrodes	82
4.4 Preparation of alkanethiol, dAMP, lipid, and insulin solutions	83
4.5 Preparation of the alkanethiol self-assembled monolayer	84

4.6 Aggregation of insulin protein and capturing of protofibrils	84
4.7 Langmuir-Blodgett / Langmuir-Schaefer (LB / LS) deposition	85
4.7.1 Instrumentation	85
4.7.2 Formation of bilayer lipid membranes	86
4.8 Raman spectroscopy	88
4.9 Electrochemistry	88
4.9.1 Electrochemical surface-enhanced Raman spectroscopy	89
4.9.2 Cyclic voltammetry	91
4.10 Turbidity measurements	91
4.11 Transmission and scanning electron microscopy	92
4.12 Attenuated total reflectance-Fourier transform infrared spectroscopy (ATR-FTIR)	93
Chapter 5: Results and Discussion	95
5.1 Self-assembled monolayer studies	95
5.2 Normal Raman of DMPC and cholesterol	102
5.3 Supported bilayer lipid membrane (s-BLM) studies	105
5.4 s-BLM with dAMP studies	112
5.5 Spectroscopic characterization of native insulin protein	116
5.5.1 Raman spectroscopy	117
5.5.2 Attenuated total reflectance-Fourier transform infrared spectroscopy (ATR-FTIR)	121
5.5.3 Electrochemical surface-enhanced Raman spectroscopy (EC-SERS)	124
5.6 Characterization of aggregated insulin	126
5.6.1 Raman spectroscopy	126

5.6.2 ATR-FTIR	127
5.6.3 EC-SERS	129
5.6.4 Turbidity measurements	131
5.6.5 Transmission electron microscopy (TEM)	132
5.6.6 Scanning electron microscopy (SEM)	136
5.7 Characterization of s-BLM + native insulin	144
5.7.1 s-BLM with native insulin	144
5.7.2 s-BLM studies with dAMP in the presence of native insulin	146
5.8 Characterization of s-BLM + oligomeric insulin	148
5.8.1 s-BLM studies with oligomeric insulin	148
5.8.2 s-BLM studies with dAMP in the presence of oligomeric insulin	151
5.9 Characterization of s-BLM + protofibrillar insulin	152
5.9.1 s-BLM studies with protofibrillar insulin	152
5.9.2 s-BLM studies with dAMP in the presence of protofibrillar insulin	154
5.10 Characterization of s-BLM + fibrillar insulin	157
5.10.1 s-BLM studies with fibrillar insulin	157
5.10.2 s-BLM studies with dAMP in the presence of fibrillar insulin	158
Chapter 6: Conclusion and Future directions	166
Chapter 7: References	171
Appendix	187

List of Figures	Page
Figure 1: General structure of an amino acid.....	7
Figure 2: Representation of all twenty essential amino acids.....	8
Figure 3: Representations of primary, secondary, tertiary, and quaternary structures of proteins.....	9
Figure 4: (a) Schematic illustration of the characteristic cross- β spacing from X-ray fibre diffraction from amyloid fibrils, (b) shows the meridian reflection at 4.7 Å corresponding to hydrogen bonding distance between β -strands, and equatorial reflection at 10 Å corresponding to intersheet distance, cross- β structure of amyloid- β	14
Figure 5: Illustration of the fibrillization process of protein and the associated phases.....	17
Figure 6: Illustration of the correlation between pore activity and cell toxicity for various sizes of amyloid- β aggregates.....	21
Figure 7: Fluid-mosaic model of the biological cell membrane.....	23
Figure 8: The structure of a typical glycerophospholipid; phosphatidylcholine: a) chemical structure b) schematic representation.....	25
Figure 9: Schematic illustration of phase transition behaviour and molecular order of liquid crystals.....	26
Figure 10: Illustration of the different bilayer lipid membrane systems: a) supported bilayer lipid membrane (s-BLM), b) floating bilayer lipid membrane (f-BLM), c) hybrid bilayer lipid membrane (h-BLM), and d) tethered bilayer lipid membrane (t-BLM).....	35
Figure 11: Langmuir-Blodgett transfer of a monolayer onto a) hydrophilic substrate, b) hydrophobic substrate.....	41
Figure 12: a) Y-type, b) Z-type, and c) X-type Langmuir-Blodgett film deposition schemes.....	42
Figure 13: Langmuir-Schaefer transfer (horizontal touch technique) on a solid substrate.....	44
Figure 14: Cohesive and adhesive forces acting on molecules at the gas-liquid interface and molecules in the bulk liquid.....	53

Figure 15: Compression of a lipid monolayer on the Langmuir-Blodgett trough using a movable barrier.....	54
Figure 16: The Wilhelmy plate method to measure the surface tension.....	55
Figure 17: Compression isotherm of an amphiphilic molecule at the air-water interface.	57
Figure 18: Illustration of the electrical double layer according to Bockris / Devanathan / Mueller model.....	61
Figure 19: Diagram showing the energy-level diagram for: Infrared absorption, Rayleigh, Stokes, and anti-Stokes scattering.....	64
Figure 20: Polarization of a diatomic molecule in an electric field.....	65
Figure 21: Schematic illustration of localized surface plasmon resonance on metal nanospheres.....	69
Figure 22: Schematic diagram of a typical attenuated total reflectance (ATR) system.....	74
Figure 23: Schematic diagram of transmission electron microscopy (TEM) system.....	75
Figure 24: Schematic diagram of scanning electron microscopy (SEM) system.....	78
Figure 25: The Langmuir trough and its main components.....	86
Figure 26: The EC-SERS set-up.....	90
Figure 27: Comparison between a) normal citrate-reduced silver colloid, b) citrate-reduced silver colloid treated with 0.5 M KCl for 30 minutes. Spectra were measured at 2 mW for a time interval of 30 seconds using 532 nm excitation.....	96
Figure 28: The two surface orientations of 6-mercaptohexanoic acid on AgNP substrates: a) trans conformation, or b) gauche conformation.....	98
Figure 29: EC-SERS cathodic signal of 6-MHA SAM on a AgNP electrode in 0.1 M NaF solution. The spectra were measured at 4 mW for a time interval of 30 seconds using 532 nm excitation.....	100
Figure 30: EC-SERS anodic signal of 6-MHA SAM on a AgNP electrode in 0.1 M NaF solution. The spectra were measured at 4 mW for a time interval of 30 seconds using 532 nm excitation.....	101

Figure 31: Raman spectrum of solid 1,2-Dimyristoyl- <i>sn</i> -glycero-3-phosphocholine (DMPC) collected for 30 seconds at a laser power of 4 mW at 532 nm excitation.....	103
Figure 32: Raman spectrum of solid cholesterol collected for 30 seconds at a laser power of 4 mW at 532 nm excitation.....	104
Figure 33: Isotherm of DMPC / cholesterol (70:30) at a subphase temperature of 30 °C and 90% relative humidity using the Langmuir trough. Compression was completed at a rate of 5.0 mm / min.....	106
Figure 34: EC-SERS cathodic signal of DMPC / cholesterol (70:30) bilayer on a AgNP electrode modified with a 6-MHA SAM in 0.1 M NaF solution. The spectra were measured at 4 mW for a time interval of 30 seconds using 532 nm excitation.....	108
Figure 35: EC-SERS anodic signal of DMPC / cholesterol (70:30) bilayer on a AgNP electrode modified with a 6-MHA SAM in 0.1 M NaF solution. The spectra were measured at 4 mW for a time interval of 30 seconds using 532 nm excitation.....	109
Figure 36: Comparison at -1.0 V between a) 6-MHA + s-BLM and b) 6-MHA SAM on a AgNP electrode in 0.1 M NaF solution. The spectra were measured at 4 mW for a time interval of 30 seconds using 532 nm excitation.....	110
Figure 37: Comparison between bare AgNP electrode in 0.1 M NaF electrolyte (solid line), s-BLM on a 6-MHA modified AgNP electrode in 0.1 M NaF electrolyte (dashed line). The sweep rate: 50 mV / s.....	112
Figure 38: Raman spectra of (a) dAMP powder, (b) 1.0 mM dAMP solution at -1.0 V. The spectra were measured at 4 mW for a time interval of 30 seconds using 532 nm excitation.....	113
Figure 39: EC-SERS cathodic signal of DMPC / cholesterol (70:30) bilayer on a 6-MHA modified AgNP electrode in 1.0 mM dAMP / 0.1 M NaF solution. The spectra were measured at 4 mW for a time interval of 30 seconds using 532 nm excitation. Adenine peaks are indicated by arrows.....	115
Figure 40: Comparison between DMPC / cholesterol (70:30) bilayer on a 6-MHA modified AgNP electrode in 1.0 mM dAMP / 0.1 M NaF solution at a) OCP, and b) -1.0 V. The spectra were measured at 4 mW for a time interval of 30 seconds using 532 nm excitation. dAMP peak is shown by arrow.....	116

Figure 41: Raman spectrum of solid recombinant human insulin collected for 30 seconds at a laser power of 4 mW at 532 nm excitation.....	119
Figure 42: Raman spectrum of 2 mg / mL recombinant human insulin solution collected for 30 seconds at a laser power of 4 mW at 532 nm excitation.....	121
Figure 43: ATR-FTIR of human insulin powder collected on a diamond crystal for 190 scans.....	122
Figure 44: ATR-FTIR of 2 mg / mL human insulin solution prepared in 0.1 M NaCl and 12 M HCl solution at a pH of 1.6. The spectrum was collected using a diamond window for 190 scans.....	123
Figure 45: EC-SERS cathodic signal of native human insulin in 0.1 M NaF solution. The spectra were measured at 4 mW for a time interval of 30 seconds using 532 nm excitation.....	125
Figure 46: Raman spectrum of aggregated recombinant human insulin solution collected for 30 seconds at a laser power of 4 mW at 532 nm excitation.....	127
Figure 47: Comparison of ATR-FTIR spectra of (a) native human insulin, (b) oligomer, (c) protofibrillar, and (d) fibrillar insulin under conditions of pH 1.6 and temperature of 65 °C.	129
Figure 48: EC-SERS cathodic signal of aggregated human insulin in 0.1 M NaF solution. The spectra were measured at 4 mW for a time interval of 30 seconds using 532 nm excitation.....	130
Figure 49: A sigmodal curve showing the aggregation process of recombinant human insulin at a concentration of 2 mg/ mL. Circled points indicate times at which TEM was collected.	132
Figure 50: Transmission electron microscopy images of 2 mg / mL recombinant human insulin at a) 0, b) 45, c) 60, d) 70, e) 135, and f) 240 minutes. Human insulin solution prepared in NaCl and HCl at pH of 1.6 and heated to 65 °C.....	135
Figure 51: Scanning electron microscopy (SEM) images of NaCl salt crystals. SEM images were conducted using Tescan MIRA3 LMU Field Emission under high vacuum mode at 10 kV, and at a scanning speed of 32.00 μ s / pixel.....	136
Figure 52: SEM image of native human insulin. SEM images were conducted using Tescan MIRA3 LMU Field Emission under high vacuum mode at 10 kV, and at a scanning speed of 32.00 μ s / pixel	138

Figure 53: SEM image illustrating a 2 mg / mL native human insulin solution of pH 1.6 stored at room temperature for one month. SEM images were conducted using Tescan MIRA3 LMU Field Emission under high vacuum mode at 10 kV, and at a scanning speed of 32.00 μs / pixel	139
Figure 54: X-ray dispersive energy spectrum used for elemental analysis of human insulin.....	140
Figure 55: SEM images of human insulin aggregates at a) 0 b) 45 c) 75 d) 90 e) 135 and f) 225 minutes. SEM images were conducted using Tescan MIRA3 LMU Field Emission under high vacuum mode at 10 kV, and at a scanning speed of 32.00 μs / pixel.....	142
Figure 56: SEM image of 2 mg / mL protofibrillar human insulin gel stored at room temperature for weeks. SEM images were conducted using Tescan MIRA3 LMU Field Emission under high vacuum mode at 10 kV, and at a scanning speed of 32.00 μs / pixel.....	144
Figure 57: EC-SERS cathodic signal of a 6-MHA modified s-BLM + native human insulin in 0.1 M NaF solution. The spectra were measured at 4 mW for a time interval of 30 seconds using 532 nm excitation.....	146
Figure 58: EC-SERS cathodic signal of a 6-MHA modified s-BLM + native human insulin in 1.0 mM dAMP / 0.1 M NaF solution. The spectra were measured at 4 mW for a time interval of 30 seconds using 532 nm excitation.....	148
Figure 59: EC-SERS cathodic signal of a 6-MHA modified s-BLM + human insulin oligomer in 0.1 M NaF solution. The spectra were measured at 4 mW for a time interval of 30 seconds using 532 nm excitation.....	150
Figure 60: EC-SERS cathodic signal of a 6-MHA modified s-BLM + human insulin oligomer in 1.0 mM dAMP / 0.1 M NaF solution. The spectra were measured at 4 mW for a time interval of 30 seconds using 532 nm excitation. dAMP peaks are indicated by arrows.....	152
Figure 61: EC-SERS cathodic signal of a 6-MHA modified s-BLM + protofibrillar human insulin in 0.1 M NaF solution. The spectra were measured at 4 mW for a time interval of 30 seconds using 532 nm excitation.	154

- Figure 62:** EC-SERS cathodic signal of a 6-MHA modified s-BLM + protofibrillar human insulin in 1.0 mM dAMP / 0.1 M NaF solution. The spectra were measured at 4 mW for a time interval of 30 seconds using 532 nm excitation. dAMP peaks are indicated by arrows.....155
- Figure 63:** Comparison between s-BLM on AgNP electrode (solid line), s-BLM in the presence of protofibrils (dashed line). All comparisons are done in 1.0 mM dAMP / 0.1 M NaF solution. Scan rate: 50 mV / s.....157
- Figure 64:** EC-SERS cathodic signal of a 6-MHA modified s-BLM + fibrillar human insulin in 0.1 M NaF solution. The spectra were measured at 4 mW for a time interval of 30 seconds using 532 nm excitation.....158
- Figure 65:** EC-SERS cathodic signal of a 6-MHA modified s-BLM + fibrillar human insulin in 1.0 mM dAMP / 0.1 M NaF solution. The spectra were measured at 4 mW for a time interval of 30 seconds using 532 nm excitation. dAMP peaks are indicated by arrows.....160
- Figure 66:** CV of s-BLM (short dotted line), s-BLM in the presence of oligomers (solid line), s-BLM in the presence of protofibrils (dashed line), and s-BLM in the presence of fibrils (dotted line). All completed in 0.1 M NaF solution. Scan rate: 50 mV / s.....161
- Figure 67:** EC-SERS cathodic signal at OCP of a) s-BLM, b) s-BLM + native human insulin, c) s-BLM + oligomer human insulin, d) s-BLM + protofibril human insulin, e) s-BLM + fibril human insulin in 1.0 mM dAMP / 0.1 M NaF solution. The spectra were measured at 4 mW for a time interval of 30 seconds using 532 nm excitation. dAMP peak at 730 cm^{-1} is indicated by the arrow.....163
- Figure 68:** EC-SERS cathodic signal at -1.0 V of a) s-BLM, b) s-BLM + native human insulin, c) s-BLM + oligomer human insulin, d) s-BLM + protofibril human insulin, e) s-BLM + fibril human insulin in 1.0 mM dAMP / 0.1 M NaF solution. The spectra were measured at 4 mW for a time interval of 30 seconds using 532 nm excitation. dAMP peak at 730 cm^{-1} is indicated by the arrow.....165
- Figure A-1:** EC-SERS comparison at -1.0 V between a) s-BLM without dAMP, b) s-BLM with dAMP. dAMP peaks indicated by arrows.....190

Figure A-2: EC-SERS comparison at -1.0 V between s-BLM + native insulin a) without dAMP, b) with dAMP. dAMP peaks indicated by arrows. No dAMP peaks were observed.....190

Figure A-3: EC-SERS comparison at -1.0 V between s-BLM + oligomers insulin a) without dAMP, b) with dAMP. dAMP peaks indicated by arrows.....191

Figure A-4: EC-SERS comparison at -1.0 V between s-BLM + protofibrillar insulin a) without dAMP, b) with dAMP. dAMP peaks indicated by arrows.....191

Figure A-5: EC-SERS comparison at -1.0 V between s-BLM + fibrillar insulin a) without dAMP, b) with dAMP. dAMP peaks indicated by arrows.....192

List of Tables	Page
Table 1: Comparison of physical and electrical properties between biological cell membranes and bilayer lipid membrane models.....	30
Table A-1: Peak assignment for DMPC powder.....	187
Table A-2: Peak assignment for cholesterol powder.....	187
Table A-3: Peak assignment for recombinant human insulin powder.....	188
Table A-4: Peak assignment for native human insulin on AgNP surface.....	189

List of Abbreviations

AD	Alzheimer's disease
AFM	Atomic force microscopy
Ag/AgCl	Silver chloride electrode
AgNP	Silver nanoparticle
APP	Amyloid precursor protein
ATR-FTIR	Attenuated total reflectance-Fourier transform infrared spectroscopy
BLM	Bilayer lipid membrane
brain-BLMs	Brain total lipid extract-based supported lipid bilayer
CD	Circular dichroism
CE	Counter electrode
CFTR	Cystic fibrosis transmembrane conductance regulator
CTB	Cholera toxin B
CV	Cyclic voltammetry
CYP2D6	Human enzyme cytochrome P450
dAMP	2'-Deoxyadenosine 5'-monophosphate
DMPC	1-2-Dimyristoyl- <i>sn</i> -glycero-3-phosphocholine
DPPC	Dipalmitoylphosphatidylcholine
EC-SERS	Electrochemical surface-enhanced Raman spectroscopy
EC-STM	Electrochemical scanning tunnelling microscopy
EDS	Energy-dispersive X-ray spectroscopy

EM	Electron microscopy
f-BLM	Floating bilayer lipid membrane
FDA	Food and Drug Administration
FRAP	Fluorescence recovery after photobleaching
FTIR	Fourier transform infrared spectroscopy
GM1	Monosialotetrahexosylganglioside
h-BLM	Hybrid bilayer lipid membrane
HIAPP	Human islet amyloid polypeptide
IR	Infrared spectroscopy
LB/LS	Langmuir-Blodgett / Langmuir-Schaefer
LSPR	Localized surface plasmon resonance
MD	Molecular dynamics
MrG	Myrisoylated glycine
NMR	Nuclear magnetic resonance
NPs	Nanoparticles
NTU	Nephelometric turbidity units
OCP	Open circuit potential
PM-IRRAS	Polarization-modulation infrared reflection absorption spectroscopy
POPC	Palmitoyloleyphosphatidylcholine
pzc	Potential of zero charge
RE	Reference electrode

SAM	Self-assembled monolayers
s-BLM	Supported bilayer lipid membrane
SCE	Saturated calomel electrode
SEM	Scanning electron microscopy
SERS	Surface-enhanced Raman spectroscopy
SFG	Sum-frequency generation
SPE	Screen printed electrode
STM	Scanning tunnelling microscopy
t-BLM	Tethered bilayer lipid membrane
TCG	Trichogin-OMe
TEM	Transmission electron microscopy
T_m	Main phase transition temperature
WE	Working electrode
6-MHA	6-mercaptohexanoic acid
β	Beta
$A\beta$	Amyloid- β
α	Alpha
Å	Angstrom
nm	Nanometer
Ω	Ohm
mV	Millivolts

mN m^{-1}	Millinewton per meter
μF	Microfarad
mm	Millimeter
μm	Micrometer
μM	Micromolar
μL	Microlitre
mL	Millilitre
M	Molar
mM	Millimolar
γ	Surface tension
γ_0	Surface tension of water
Π	Surface pressure
F_p	Weight force
F_a	Archimedes buoyancy force
C	Capacitance
k	Relative permittivity of the material separating the plates
ϵ_0	Permittivity of free space
$\bar{\nu}$	Wavenumbers
λ	Wavelength
h	Planck's constant

ν	Frequency of light
Pa	Pascal
ν_s	Vibrational stretch
ν_{as}	Asymmetric vibrational stretch
δ_r	Rocking conformation
δ_d	Deformation conformation

Chapter 1: Introduction

1.1 Protein aggregation disorders

1.1.1 Introduction

Over the past several decades there has been increasing progress in our ability to understand and detect human disease. Many biosensors have been developed that demonstrate high sensitivity, selectivity, and specificity for disease diagnosis.¹ Biological molecules such as nucleic acids and proteins have been used as target biomarkers associated with various diseases.¹⁻³ However, many diseases are still undergoing extensive study in order to better understand the disease pathway to ensure more effective diagnosis and treatment. A disease class that is of major concern worldwide is caused by the presence of large amounts of accumulated proteinaceous aggregates. Collectively, these diseases are called amyloidoses, and include Alzheimer's disease, Parkinson's disease, spongiform encephalopathy, and Huntington's disease.⁴ Even though each of these neurodegenerative diseases is caused by different proteins, they are all characterized by the formation of structurally similar protein aggregates termed amyloids. At present there is no cure for these diseases due to the fact that the mechanism of protein aggregation and resultant cell death is poorly understood.

Much research has focused on Alzheimer's disease (AD) because it is the most common neurodegenerative disease. In Canada, more than 750,000 people are currently living with AD, at a cost of \$33 billion per year for direct and indirect costs combined.⁵ It is estimated that the number of AD patients will increase to 1.4 million by 2031, with the annual cost rising to \$293 billion by 2040.⁵ AD is characterized by the presence of

amyloid plaques which are extracellular deposits of amyloid- β peptide and found mostly in the cerebral cortex. Also, the presence of neurofibrillary tangles (intraneuronal filamentous aggregates) composed of abnormally phosphorylated tau protein has been noted to play a role in disease progression.

1.1.2 Amyloid hypothesis

There have been many plausible hypotheses proposed to understand the role of protein aggregates in human disease. Over the past two decades, numerous diseases have been linked to the progressive misfolding of specific proteins into aggregates which eventually result in cellular dysfunction.⁶ One important aspect toward curing amyloidoses is an improved understanding of the process by which native, soluble proteins misfold and aggregate. This prevailing theory behind amyloidoses, known as the "amyloid protein aggregation" theory, states that natively globular proteins upon misfolding exhibit a hallmark cross β -sheet structure under certain biochemical conditions and at high concentration levels.⁶ These β -sheet structures have characteristic features such as dye-binding properties, insolubility and a characteristic X-ray diffraction pattern.^{6,7} The initiation process of misfolding may be presented as a "seeded polymerization" where proteins present at a certain concentration start to misfold, leading to different sizes of aggregates.⁶ It was originally hypothesized that the fully aggregated proteins (fibrils) were the toxic species, however recent research has confirmed that proteins at an intermediate aggregation stage (protofibrils) are the toxic species.⁸

1.1.3 Present therapeutic remedies / drawbacks

The aggregation of protein results in metastable aggregate intermediate. These aggregates have been strongly correlated with high levels of cytotoxicity.⁹ This cytotoxic behaviour is believed to be a result of interactions which destabilize the cell membrane.⁹ Many therapeutic strategies for amyloidosis and more specifically Alzheimer's disease (AD) have been explored based on our current understanding of the structure of intermediate aggregates and their interaction with cellular membranes.¹⁰ Most of the treatments that are currently being explored are focused toward slowing the progression of the cognitive symptoms and controlling certain behaviors.¹¹ The brains of patients with AD have been found to have reduced cholinergic activity which is related to cognitive impairment.¹¹ This result led to the cholinergic hypothesis which suggests that a deficiency of acetylcholine containing neurons in the brain contributes substantially to decline in cognitive ability in patients diagnosed with AD.^{12,13} Cholinesterase inhibitors are a commonly used class of drugs to enhance acetylcholine levels in the brain in order to improve cognition.¹¹ Four cholinesterase inhibitors; tacrine, donepezil, galantamine, and rivastigmine have been approved by the U.S. Food and Drug Administration (FDA).¹⁴ Tacrine was the first drug used for treatment of AD which showed promise for slowing the progression of cognitive deterioration; however, its application was discontinued because of an increased risk of hepatotoxicity.¹⁴ The rest of the drugs are still in use to slow the worsening of cognitive functions, help patients perform various activities of daily living, and improve behaviour.¹⁴ However, these current treatments are unable to prevent, prohibit, or reverse the pathophysiology of AD. Therefore, different

strategies targeting amyloid- β plaques and neurofibrillary tangles should be targeted, and this starts with a better understanding of the disease mechanism of action.^{11,14}

Some strategies have been developed to inhibit protein aggregation. These strategies include the use of peptides or small molecules, interfering with post-translational modifications that simulate protein aggregation, upregulating molecular chaperones or enhancing aggregate-clearance mechanisms.¹⁵ Although these strategies initially showed promise, several drawbacks emerged. For example, molecular chaperones that were used to bind misfolded proteins and prevent them from further aggregation caused meningoencephalitis (brain inflammation).¹⁶ Increased levels of amyloid- β (A β) degrading enzymes such as neprilysin were able to reduce the level of A β monomers but had no effect on reducing plaque formation.¹⁴ Decreasing the amount of A β through regulation or modulation of certain secretases has been studied. For example, inhibiting γ -secretase showed lower level of A β monomers; however, it caused abnormalities in the gastrointestinal tract, thymus, and spleen in mice and humans.^{14,17} The goal of future AD treatments involves inhibiting the progression of the illness and ideally reversing its pathology, with the hope that cognitive function can be recovered.^{11,14} This can be done mainly by targeting the production, aggregation, and removal of existing amyloid- β aggregates.¹⁸ The difficulty in developing effective treatments that can target specific stages of the disease relies on the fact that the etiology of AD is not completely understood and it is within this area that the current thesis work resides.¹⁸

1.2 Objective of thesis

There is a growing body of evidence indicating that amyloid protofibrils play a role in membrane deterioration which would cause an alteration in the homeostasis of cellular membranes thereby causing cell death. However, the exact mechanism of protein aggregation and cell death is not clear as of yet. The aim of this research was focused toward understanding the interaction between protein aggregates and cellular membranes at the molecular level. This was achieved by studying the interaction between a model amyloid-forming protein and a model bilayer lipid membrane. This system will have the capability to provide information about the role of protein aggregates in cell death, and whether any defects or pores are formed due to the presence of these peptide aggregates.

In this research, human insulin, an amyloid-forming peptide will be used as a model of A β in Alzheimer's disease. The accelerated aggregation process will be monitored using a variety of spectroscopic measurements including Fourier transform infrared spectroscopy (FTIR), Raman and turbidity measurements. Also, microscopic techniques such as Transmission Electron Microscopy (TEM) and Scanning Electron Microscopy (SEM) will be used for imaging various stages during the aggregation process. The native and aggregated insulin will be introduced to a supported bilayer lipid membrane (s-BLM) that will be formed on a solid substrate using the Langmuir-Blodgett / Langmuir-Schaefer (LB / LS) technique. The interaction between the aggregated protein and the membrane will be followed using spectroscopy and electrochemistry. In particular, electrochemical surface-enhanced Raman spectroscopy (EC-SERS) is demonstrated as a useful tool for probing protein-biomembrane interactions.

1.3 Scope of thesis

This thesis consists of 7 chapters. Chapter 1 gives brief introduction to the research conducted in this thesis, and highlights the major goal of this work. Chapter 2 provides a detailed literature review of the important aspects of this project including protein structure and function, protein aggregation and misfolding, cell membranes, different models of cell membranes, and the techniques used to study protein-lipid interactions. Chapter 3 provides a detailed description of the theory which underlies the major experimental techniques used in this work including Raman spectroscopy, Langmuir-Blodgett / Langmuir-Schafer deposition, SEM, TEM, and ATR-FTIR. Chapter 4 summarizes the experimental procedure including description of the electrochemical methods, preparation of Langmuir-Blodgett / Langmuir-Schafer bilayer membrane on AgNP, and sample preparation for SEM, TEM, and ATR-FTIR.

The major experimental results are presented in Chapter 5 discusses the characterization of DMPC, cholesterol, dAMP, and insulin using Raman spectroscopy. The characterization of insulin using other techniques including ATR-FTIR, SEM, TEM, and EC-SERS were also discussed. This chapter also discusses the EC-SERS measurements of the interaction between aggregated insulin (oligomer, protofibrils, fibrils) and supported bilayer lipid membrane (s-BLM). The interaction between insulin and s-BLM were further investigated using a dAMP probe molecule. Chapter 6 summarizes the most important results obtained from this work, and future work for this project is proposed. Chapter 7 includes the references used in this thesis.

Chapter 2: Literature Review

2.1 Introduction

2.1.1 Protein structure and function

Proteins are biological molecules that control nearly every physiological process in living organisms.¹⁹ The building blocks of proteins are amino acids, which are small organic molecules that consist of an α -carbon atom linked to an amino group, a carboxyl group, a hydrogen atom, and a side chain (R), as depicted in Figure 1.¹⁹ Each protein consists of a large polymeric sequence of amino acids that are linked together by peptide bonds. Peptide bonds are covalent bonds that occur between the carbonyl carbon atom of one amino acid and the nitrogen atom of the other. Since there are 20 different naturally occurring amino acids (Figure 2), the total number of different proteins possible is enormous.^{19,20} The properties of a protein are dependent on the polarity and charge of the side chains of the amino acids.

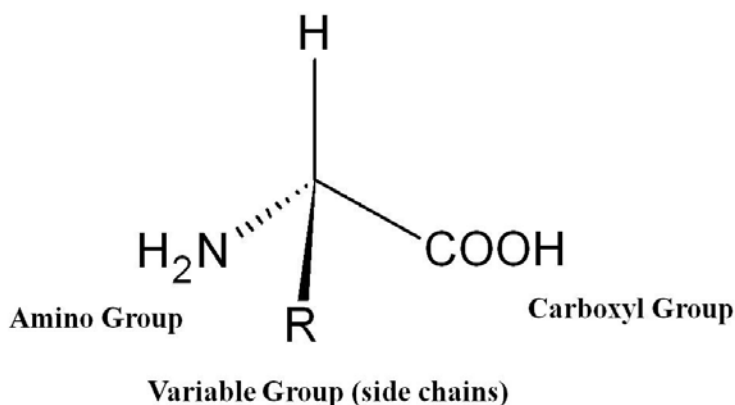
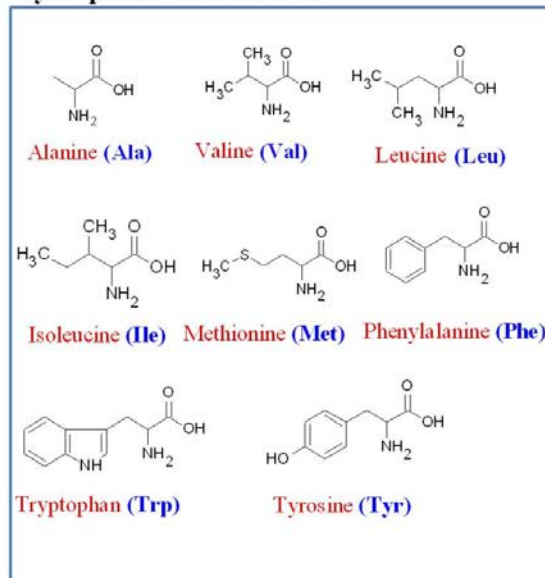
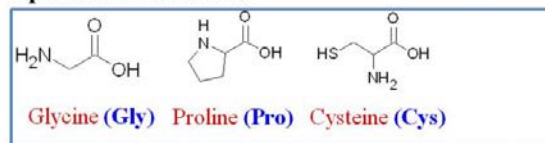


Figure 1: General structure of an amino acid.

Hydrophobic Amino Acids



Special Amino Acids



Hydrophilic Amino Acids

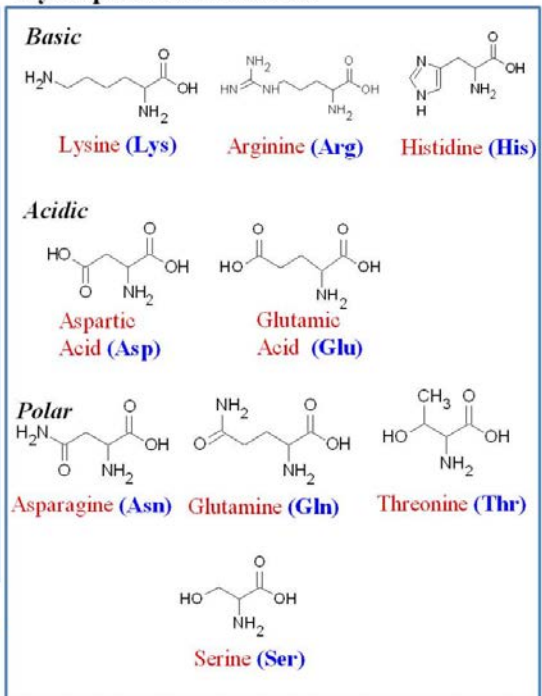


Figure 2: Representation of all twenty essential amino acids. Adapted from reference [20].

The linear sequence of amino acids is considered the primary structure of the protein, and it is the driving force for intramolecular bonding which stabilizes the protein structure.²⁰ Hydrogen bonding between amino groups and carboxyl groups can cause folding to occur which determines the protein's three dimensional shape, known as the protein secondary structure.²⁰ The two most stable secondary structure elements in proteins are α -helices and β -sheets. These helices and sheets assemble and fold to give the tertiary structure of proteins.^{20,21} Protein tertiary structure is the result of hydrogen bonding and three other possible types of interactions: disulphide bridges, ionic bonds, and hydrophobic interactions.²² Disulphide bridges are strong covalent bonds that occur

between sulphur atoms arising from sulphur in cysteine.²² Ionic bonds occur between carboxyl and amino groups that are not involved in the peptide bond, such formation as those in asparagine and aspartic acid; these ionic bonds are weaker than disulphide bonds and can be destabilized by changes in pH.²² Hydrophobic Van der Waals interactions occur between non-polar side chains (R) in amino acids which repel water such as those found in tyrosine and valine.²² The most prevalent examples of tertiary structures include β -barrels, β -sandwiches, and β -bundles.²³ The polypeptide can also fold and interact with other polypeptides and subunits giving rise to the quaternary structure of proteins.²⁰ Figure 3 shows the four different protein structural levels. Based on the protein sequence and the ability to fold into unique three dimensional shapes, proteins tend to have specific characteristics that translate into high selectivity and diversity in function.

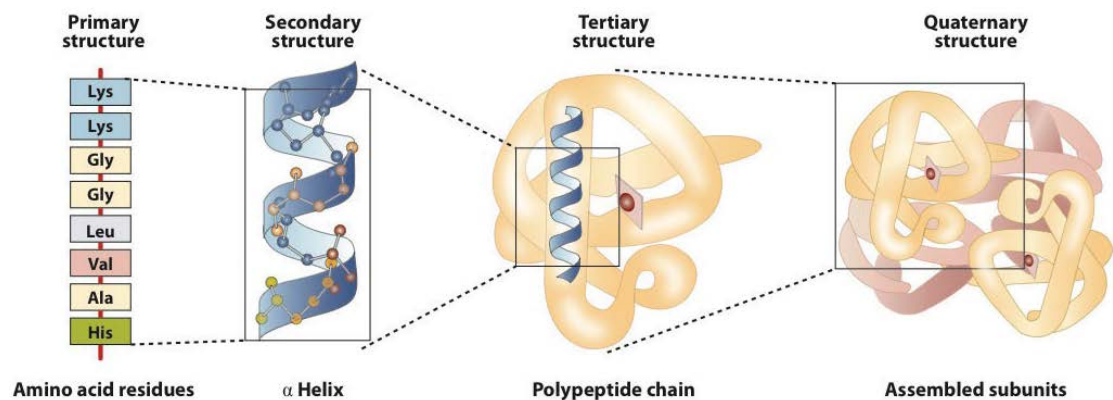


Figure 3: Representations of primary, secondary, tertiary, and quaternary structures of proteins. Reproduced with permission.²⁰

Proteins have many biochemical functions in living systems such as molecular recognition, catalysis, operating as molecular switches, and serving as structural components of cells and organisms.²⁴ Specific interaction between proteins and other

molecules such as other proteins, DNA, small molecules, etc. is governed by the shape and composition of the protein. For example, the protein myoglobin has specific sites for binding oxygen molecules as it is responsible for storing oxygen for use in muscle tissue.²⁴ Certain proteins act as transporters as well, for example hemoglobin carries oxygen and transports it from the lungs to various tissues.²⁴ In addition, many proteins function as biological catalysts, termed enzymes. An example of an enzyme is DNA polymerase which is responsible for catalyzing DNA replication by copying the genetic material and editing errors in the DNA copy.²⁴ Protein molecules also serve as structural elements of living systems, for example structural proteins are found in silk, hair, keratin, horns, and feathers.²⁴ These are just some examples of the variety of functions proteins have in living systems which are dependent on the ability of the protein to fold correctly into different structures. When proteins fail to fold correctly, disastrous consequences such as debilitating diseases can result.

2.1.2 Protein misfolding and aggregation

A powerful example of evolutionary biology is the ability of proteins to fold properly which is necessary for functioning.²⁵ The environment in the interior of a cell is very crowded, containing many proteins and other macromolecules. Therefore in order for proteins to fold properly there are several factors that assist in the folding process.²⁵ These factors include folding catalysts and molecular chaperones which are responsible for enabling the polypeptide chains to fold efficiently in the interior of the cell. Catalysts can be used to accelerate the folding process; for example, peptidylprolyl isomerases increase the rate of cis / trans isomerization of peptide bonds.²⁵ Chaperones such as

bacterial "chaperonin", GRoEL, can bind non-specifically to hydrophobic residues in chains to prevent aggregation, or it can assist in later stages of folding.²⁵

The correct folding of proteins is rapid, taking only milliseconds to seconds for a complete folded structure to be generated.²⁶ The process is highly dependent on the amino acid sequence, and as the polypeptide chain folds into the native state the polypeptide chain becomes more restricted and highly ordered.²⁶ Higher enthalpy is associated with stable native structures, and as the polypeptide chain becomes ordered, the entropy decreases.²⁵ The mechanism of protein folding can be described as a "nucleation-condensation" process, in which a folded nucleus of a small number of residues forms first, and the remainder of the structure is then condensed.²⁵⁻²⁷ There are many intermolecular forces that have a huge influence on the folding process such as hydrogen bonding, hydrophobic interactions, electrostatics, and conformational forces. If a balance is not achieved between these forces, protein misfolding and aggregation can occur.²⁶

Since the protein is present in a complex environment surrounded by different co-solutes such as salts, other proteins, carbohydrates, and lipids, the misfolding process can be highly influenced by the presence of these ions and molecules. Co-solutes have two classifications: kosmotropes and chaotropes.²⁸ Kosmotropes are smaller ions that are heavily hydrated and have the ability to organize water molecules around themselves.²⁸⁻³⁰ Kosmotropes tend to sequester water from protein molecules, which can cause salting-out of proteins from aqueous solution.²⁸⁻³⁰ Some examples of kosmotropes include: F^- , CH_3COO^- , Na^+ , and glutamate. Kosmotropes are also known as structure stabilizers,

since they have the ability to stabilize folded and unfolded proteins.³¹ Chaotropes are larger ions that are less hydrated and lack the ability to organize water molecules around themselves.²⁸⁻³⁰ As a result, chaotropes tend to lend water molecules to proteins which facilitates their hydration. Some examples of chaotropes include: Cl^- , K^+ , Mg^{2+} , and urea, and are known as structure destabilisers, where they have the ability to weaken the hydrophobic effect, and therefore cause misfolding.³¹ The process of protein misfolding can be defined as reaching a state that has significant amount of non-native interactions between residues. The failure to fold properly can result in malfunctioning of living systems which can lead to various disease states. There are many human diseases that are associated with the misfolding of proteins.

2.1.3 Aggregated protein and human diseases

Many human diseases result from proteins that are unable to fold properly, which directly affects their function.²⁵ For example, in cystic fibrosis a mutation in the gene that encodes the cystic fibrosis transmembrane conductance regulator (CFTR) protein occurs and causes CFTR to misfold.³² Other diseases (amyloidoses) are caused by the deposition of misfolded proteins within cells or the extracellular matrix.³³ These peptides and proteins change their conformation based on certain conditions and undergo a change from a native soluble form to insoluble aggregates that can accumulate in a variety of organs and tissues. There are over 20 different proteins that are known to be involved in the occurrence of different amyloidoses through their structurally similar amyloid aggregate state, even though they all have different sequences and native structures.³³

Some of the amyloidoses are associated with neurodegenerative disorders, including Alzheimer's disease, Huntington disease, Parkinson's disease, and spongiform encephalopathy. These diseases are caused by the presence of amyloid- β , polyglutamine, α -synuclein, and prion protein, respectively, in brain tissue.²⁷ There are also non-neuropathic amyloid diseases such as type II diabetes mellitus which is caused by the build-up of Islet amyloid polypeptide aggregates in the pancreas. Each disease outlined above is caused by a different peptide and the location of the deposition is generally different. The common characteristic feature of all of these diseases is the deposition of insoluble amyloid fibrils and plaques that are rich in β -sheet structure.²⁶ These amyloid fibrils are the hallmark feature of the amyloid aggregation pathology. The deposition of these amyloid fibrils was first observed in the spleen, liver, and kidneys of deceased patients in the eighteenth century.³⁴ Since then, researchers have been characterizing amyloid fibrils in order to provide possible therapeutic approaches to halting, reversing, or avoiding these debilitating diseases.³⁴

There have been many biophysical techniques used to characterize amyloid structures including nuclear magnetic resonance (NMR) spectroscopy, circular dichroism (CD) spectroscopy, X-ray diffraction, atomic force microscopy (AFM), electron microscopy (EM), and Fourier transform infrared spectroscopy (FTIR).^{26,32-35} Amyloid aggregates bind to the dye Congo Red and exhibit an apple green birefringence when examined using light microscopy, suggesting that amyloid proteins contain fibrillar structure.³⁵ Electron microscopy has shown that amyloid fibrils are straight, unbranched, with a 50-120 Å diameter, and several micrometres in length.^{36,37} The first structural

study was conducted using X-ray diffraction in the 1930s, which showed that amyloid fibrils contain a cross- β structure, as shown in Figure 4.³⁴ The X-ray diffraction studies reported that amyloid fibrils have two major reflection bands at 4.7 and 10 Å.³⁵⁻³⁸ The meridian reflection band at 4.7 Å is due to the hydrogen bonding distances between β -strands, and the equatorial reflection band at 10 Å is due to the side chain packing between the sheets.³⁵⁻³⁸ This pattern explains the cross- β structure of amyloid fibrils where the polypeptide chain is organized in β -sheets arranged parallel to the fibril axis and their constituent β -strands perpendicular to the fibril axis.³⁵⁻³⁸ Amyloid fibrils are composed of several protofilaments having diameters of 20-30 Å that are arranged around a hollow centre.³⁸ The structure and morphology of amyloid fibrils is very important toward understanding many of the amyloidoses such as Alzheimer's disease.

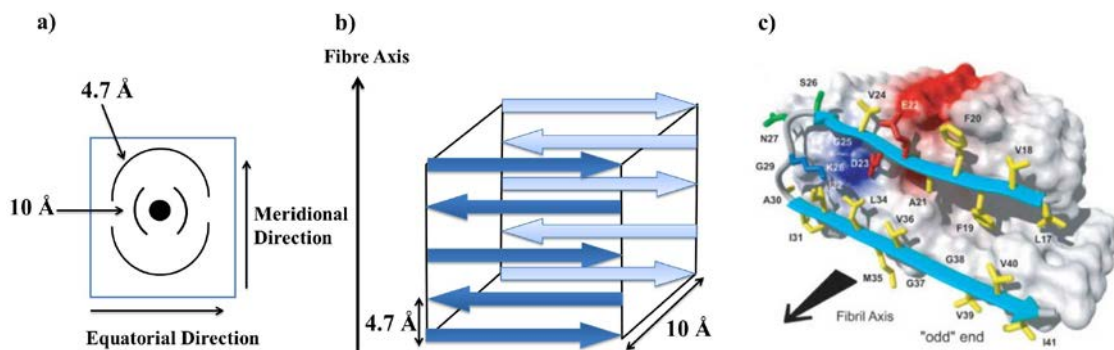


Figure 4: (a) Schematic illustration of the characteristic cross- β spacing from X-ray fibre diffraction from amyloid fibrils, (b) shows the meridian reflection at 4.7 Å corresponding to hydrogen bonding distance between β -strands, and equatorial reflection at 10 Å corresponding to intersheet distance, (c) cross- β structure of amyloid- β . Reproduced with permission “Copyright (2005) National Academy of Sciences, U.S.A.”³⁹

The most common type of amyloidosis is Alzheimer's disease (AD) which leads to dementia and eventually death. More than 35 million people worldwide have Alzheimer's disease, with death generally occurring within 3-9 years of diagnosis.⁴⁰ Some of the early symptoms of AD include memory loss, speech difficulty, struggle to perform certain motor tasks, and inability to recognize familiar people and objects.⁴⁰ Amyloid- β aggregates are found to be deposited in the brain and more specifically in the cerebral cortex and hippocampus upon post-mortem examination.²⁶ These aggregates are found in the extracellular space and are referred to as neuritic plaques which are derived from proteolytic processing of the amyloid precursor protein (APP).⁴¹ APP is a transmembrane protein that is expressed at high levels in the brain and plays a major role in a number of physiological functions such as synapse formation, neuronal survival, and neuritic outgrowth.⁴² APP can be cleaved in two ways but only one pathway produces the specific AD fragment.⁴³ The amyloidogenic pathway involves the sequential cleavage of APP, first by β -secretase in the extracellular matrix followed by interior membrane cleavage by γ -secretase.⁴³ Another kind of protein aggregate exists intracellularly and leads to neurofibrillary tangles, these are derived from microtubule-associated protein tau.⁴¹

The mechanism behind protein aggregation is not well understood. However, there has been much research focusing on understanding the mechanism of protein aggregation, and different techniques have been used to monitor the process.^{27,44,45} Many microscopic techniques have been used such as: transmission electron microscopy,⁴⁶ atomic force microscopy,⁴⁷ scanning electron microscopy,⁴⁸ and scanning tunnelling

microscopy.⁴⁹ Other analytical and biophysical techniques including fluorescence spectroscopy, dynamic light scattering, and infrared spectroscopy have also been employed.⁵⁰ Amyloidogenic proteins are prone to aggregation under various conditions including elevated temperatures, low pH, high ionic strength, and mechanical stress.⁵¹ The process occurs via the aggregation of partially folded intermediates through a nucleation mechanism.⁵² The kinetic process of protein aggregation is often characterized by a sigmoidal profile, as shown in Figure 5.⁵¹ This sigmoidal graph consists of three regions that are used to characterize the formation of amyloid aggregates. The first region is the lag phase which is assumed to be the time required for nuclei to form. The lag phase consists of the protein present in its native structure; different types of aggregates can be present in this region including monomers, dimers, trimers, and tetramers.⁵¹ The second region is the growth regime which is characterized by a region of exponential growth; this region includes the presence of small oligomers and protofibrillar aggregates.⁵¹ The third region is the plateau regime which consists of fully aggregated fibrils that are considered the final product of the aggregation process.⁵¹

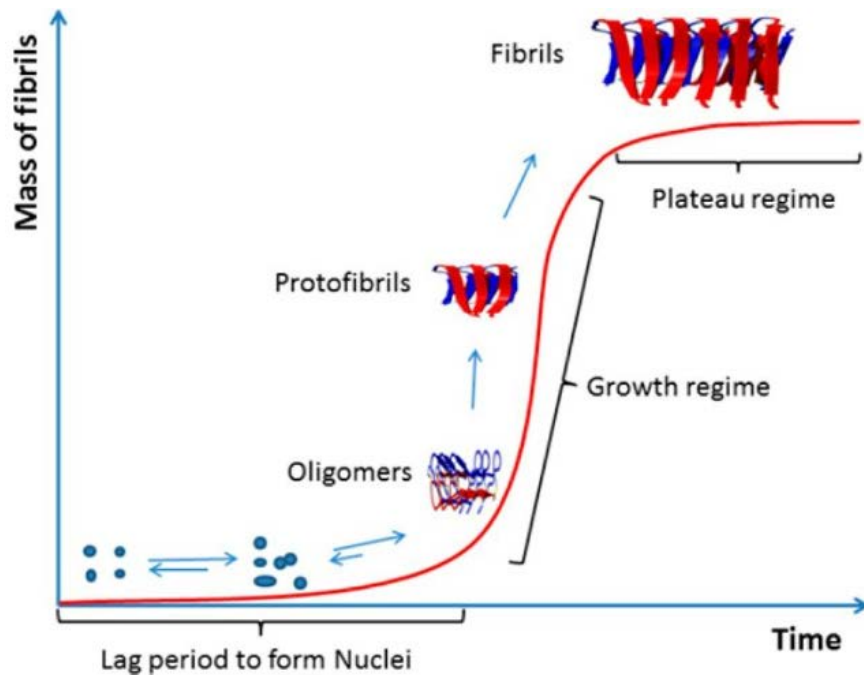


Figure 5: Illustration of the fibrillization process of protein and the associated phases. Reproduced with permission.⁵¹

2.1.4 Amyloid pore hypothesis

It is becoming increasingly clear that protein aggregation is a complex, non-linear process, involving several kinds of intermediates. In the past decade there has been a substantial amount of research focused on identifying, characterizing, and isolating the different intermediates of the aggregation process.^{45,52,53} Most recent evidence has suggested that amyloid fibrils may not be the toxic species, but smaller aggregates such as oligomers or protofibrils are likely to blame.^{52,53} Oligomers (dimers, trimers, and tetramers) are clusters of a small number of peptides that do not exhibit any fibrillary characteristics.²⁶ Protofibrils are protein aggregates of clustered spherical beads that have significant β -sheet structure.²⁶

Amyloid fibrils can be identified in the post-mortem brain sections of patients who had exhibited clinical signs of AD, and the hypothesis was originally that these fibrils were the toxic species. However, this hypothesis has failed to explain many pathological and clinical characteristics of Alzheimer's disease.⁵⁴ For example, there was no correlation between the amount of amyloid- β deposits and the severity of Alzheimer's disease. Inhibiting the formation of amyloid- β fibrils did not reduce toxicity towards cultured neurons.⁵⁴ Finally, transgenic animals that overproduce APP exhibit neuronal and behaviour abnormalities before the formation of amyloid plaques.⁵⁴ These inconsistencies led scientists to propose that soluble prefibrillar intermediates such as oligomers and protofibrils are the species actually responsible for altering neuronal function and causing cell death. The toxicity of protofibrils is not specific to Alzheimer's disease and the hypothesis proposed seems to support findings for other neurodegenerative diseases.⁵⁴ As a result, recent research efforts have focused on these intermediate species, especially the protofibrils.

Amyloid protofibrils share morphological and toxicological properties that suggest the toxicity is dependent on shared structural features rather than amino acid sequence. Antibodies used against protofibrillar amyloid- β were reported to recognize protofibrillar species from other amyloidogenic proteins such as α -synuclein, polyglutamine, Islet amyloid polypeptide, and human insulin.⁵⁴ Such a finding suggests that these structures may exert toxicity through a common mechanism. A common feature of these protofibrils is that they are capable of self-assembling into pore-like structures on artificial or biological membranes and all the amyloidogenic proteins

mentioned previously have been shown to have channel / pore activity.⁵⁴ Annular pore-like structures with variable diameters have been observed during the in vitro aggregation of synthetic amyloid- β protein.⁵⁵ For example, using AFM amyloid- β was found to form annular structures with outer diameters of 6-9 nm, and inner diameters of 1.5-2 nm.⁵⁶ Another study observed that the incorporation of amyloid- β into artificial lipid bilayers resulted in uniform pore-like structures with outer diameters of 8-12 nm and an inner diameter of 2 nm.^{57,58} Other researchers have also shown using AFM that α -synuclein forms pores with an inner diameter of 2-3 nm that are β -barrel structures composed of 20-24 α -synuclein monomers.⁵⁹ One disadvantage of these AFM investigations however is that it only offers a top view perspective; one cannot be sure how far the pore structures penetrate into the membrane.

In Alzheimer's disease, the production of peptides consisting of 39-42 amino acids (amyloid- β_{1-42}) is produced by endoproteolytic processing of APP.⁶⁰ These peptides are the prime constituent of amyloid deposits in the brain tissue of Alzheimer's patients. In-vitro experiments have demonstrated that the cytotoxicity of intermediate amyloid- β aggregates is related to their ability to form ion permeable channels. An initial experiment conducted in 1993 demonstrated the formation of ion permeable channels in planar lipid bilayer membranes in the presence of amyloid- β .⁶¹ The channels observed consisted of several different conductance sizes which is related to the fact that oligomers / aggregates of varying number and size can provide different channel structures.⁶¹ The channels obtained were cation selective; permeable to divalent cations such as calcium (Ca^{2+}). Also, it was observed that zinc (Zn^{2+}) and aluminium (Al^{3+}) can be used to block

these channels.⁶¹ The formation of these channels may be responsible for the cytotoxic properties of amyloid- β for neurons. These channels have the ability to depolarize neuronal membranes which leads to an increased level of Ca^{2+} influx through voltage-dependent Ca^{2+} channels, and subsequently to cytotoxicity.⁶¹

A correlation between pore formation and cytotoxicity on various sizes of amyloid- β aggregates has been recently investigated by Prangkio *et al.*, where the ability of these aggregates to form ion pores in planar lipid bilayers was examined.⁵² As indicated in Figure 6, pore formation and cytotoxicity showed nearly identical dependence on different size aggregates. The amyloid- β monomers and fibrils were found to exhibit a negative correlation between pore formation and cytotoxicity which suggests that monomers and fully formed fibrils are non-toxic, and may in fact play a protective role. However, the intermediate forms of amyloid- β aggregation, ranging from tetramers to 18-mers exhibited a positive correlation between pore formation and cytotoxicity suggesting that these species are indeed the toxic elements.⁵²

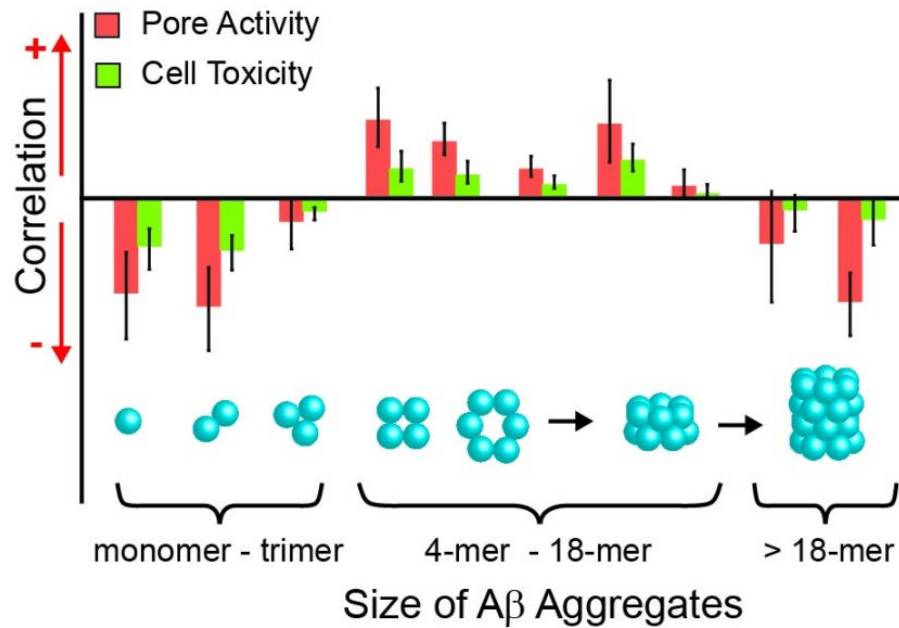


Figure 6: Illustration of the correlation between pore activity and cell toxicity for various sizes of amyloid- β aggregates. Reproduced with permission.⁵²

2.2 Cell membranes

2.2.1 Cell membranes: structure and function

One of the most important cellular structures is the plasma membrane, the complex envelope that separates the interior of the cell from extracellular components. The thickness of the membrane varies between 5-10 nm depending on the composition of different proteins, lipids, lipopolysaccharides and glycopolysaccharides.⁶² Due to the ultrathin nature of cell membranes, it has historically been very difficult to establish their existence and study their structure and properties. Research developments in physics had a huge impact towards characterizing the structure and understanding the properties of biomembranes.

The development of the light microscope allowed the first observation of the cell structure by Robert Hooke in 1662.^{20,62} Further studies on cell structure were made in 1831 when Robert Brown proved the existence of a nucleus in the interior of the cell.⁶² In 1855, the existence of a cellular membrane surrounding the cell was proposed by Negeli, where undamaged cells were observed to change volume upon changes in the osmotic pressure of the surrounding environment.⁶² Overton was then able to show that cell membranes are composed of amphiphilic molecules through the observation that non-polar molecules were able to penetrate more easily through the cell membrane than polar molecules.⁶²

Further studies to determine the structure of membranes were conducted by Gorter and Grendel where they proposed that the membrane is composed of two monomolecular lipid layers constituting a lipid bilayer. Direct evidence of these biomembranes was only possible after the discovery of electron microscopy in the 1950s, which reported that the cell is surrounded by a membrane approximately 5-10 nm in thickness.⁶² The electron micrographs showed that the cell membrane consists of two high electron density layers (2 nm) separated by a thick low electron density layer (3.5 nm).⁶² This finding was then used to propose that the two high electron density layers correspond to polar head groups of phospholipids covered with protein, and the low electron density layer corresponds to hydrophobic chains of phospholipids. Further development of electron microscopy allowed for the observation of additional details to be determined such as the presence of channels within cell membranes.⁶²

Based on all the results that were obtained it was finally suggested that biomembranes are present as a fluid-mosaic structure.^{63,64} The "fluid" part refers to the fact that the phospholipids in the cell membrane exhibit lateral and rotational mobility.^{63,64} The "mosaic" part comes from the heterogeneous composition of lipids and proteins.^{63,64} Biomembranes have an asymmetrical and inhomogeneous structure because different compositions of lipids, proteins, and hydrocarbons exist across the membrane, as shown in Figure 7.⁶³⁻⁶⁶ Also, biomembranes contain lipid rafts which are small (10-200 nm) highly dynamic assemblies of proteins, sphingolipids, and cholesterol in the outer exoplasmic leaflet that connect to phospholipids and cholesterol in the inner cytoplasmic leaflet.⁶⁶⁻⁶⁹ Lipid rafts are fluid but more ordered and tightly packed than other regions of the lipid bilayer due to the high cholesterol content. Interest in lipid rafts arose when it was recognized that many membrane-associated proteins interact with the biomembrane through lipid rafts.⁶⁷⁻⁶⁹ It has been found that many proteins that are associated with amyloidogenic diseases interact with cell membranes through lipid rafts. In Alzheimer's disease, both APP and β -secretase partition into lipid rafts in the cellular membrane.⁶⁹ In addition, amyloid- β was found to contain a cholesterol binding domain.⁷⁰

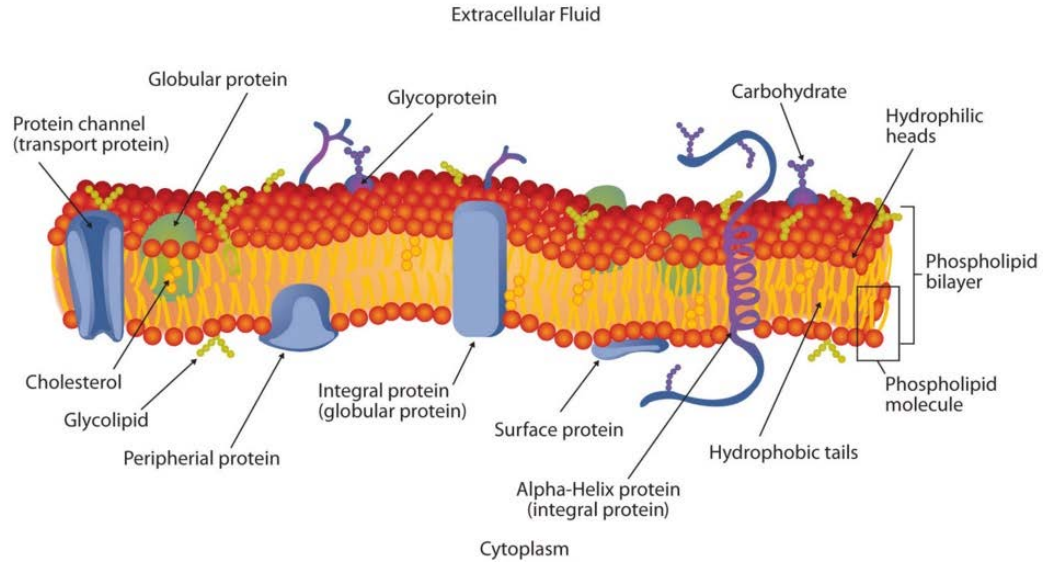


Figure 7: Fluid-mosaic model of the biological cell membrane. Reproduced with permission.⁷⁰

Biological membranes provide a unique barrier function that allows directional transport of species into the cell, and also allows for transport of waste and toxic compounds out of the cell. Membranes have low permeability for charged particles which provides a non-equilibrium ion distribution between the extracellular and intercellular regions.⁶⁵ Maintenance of this non-equilibrium state is key to cellular homeostasis. The biological membrane can fulfil a number of important functions including:^{65,71}

- 1) Structural support to the cell and its associated organelles.
- 2) Controlling movement of certain ions, low molecular weight compounds, and proteins in and out of the cell.
- 3) Cell-to-cell communication through receptor sites.

- 4) Signal reception using specific proteins which are incorporated in cell membranes. The signals from the environment may include light, mechanical deformation, specific molecular interaction.
- 5) Providing active and passive transport function to transport ions, glucose, amino acids, and other compounds across the membrane.

All cell membranes share these basic functions due to the similar features that different cell membranes share. The most common feature is that they are composed of lipid molecules that make up the two lipid bilayers. Lipid molecules can be divided into three main classes: phospholipids, glycolipids and sterols.⁷¹ Cell membranes are composed mainly of phospholipids, of which many examples exist in nature. Phospholipids have various polar head groups as well as various hydrophobic chains that differ in composition and saturation.^{71,72} An example of phospholipids are glycerophospholipids (i.e. phosphatidylcholine) which are amphiphilic molecules that contain a polar head group and two hydrophobic fatty acid chains connected via a glycerol backbone.⁷² A schematic representation of a typical glycerophospholipid is shown in Figure 8. Phospholipid bilayers provide a barrier to passive translocation of ions and other species through the membrane, a favourable environment for protein functioning, and a fluid and flexible environment allowing components to move within the membrane.^{71,72} Generally phospholipids are permeable to small molecules such as oxygen, water and carbon dioxide. Ions and large polar molecules such as sugar are not able to permeate across the phospholipid bilayer.^{71,72}

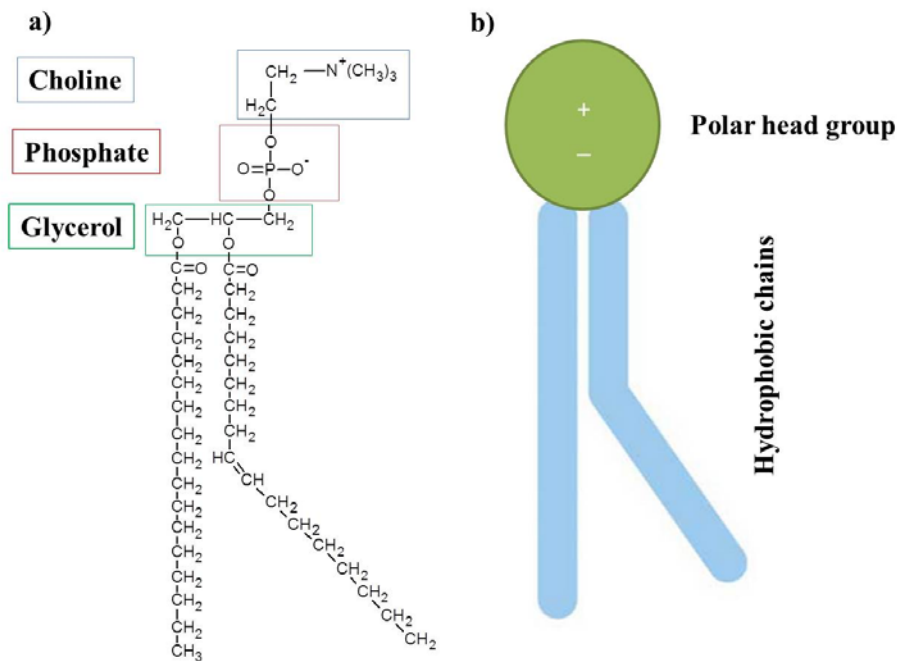


Figure 8: The structure of a typical glycerophospholipid; phosphatidylcholine: a) chemical structure b) schematic representation. Adapted from reference [62].

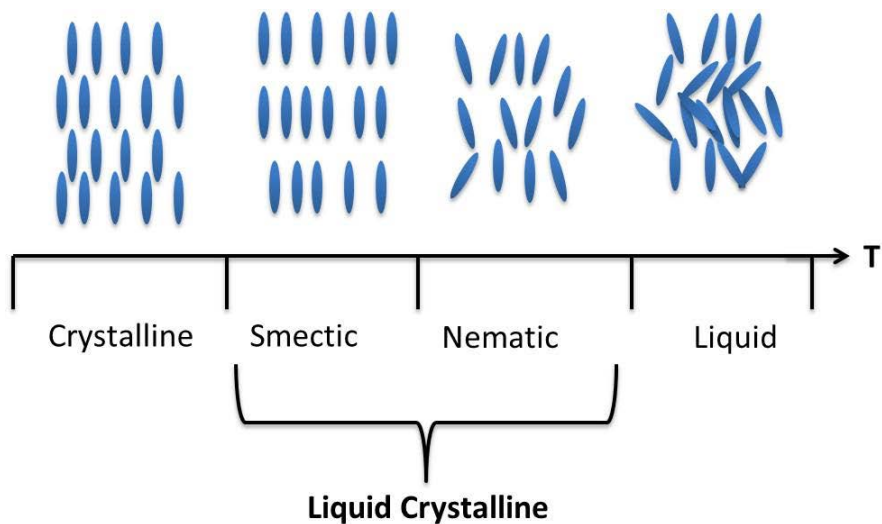


Figure 9: Schematic illustration of phase transition behaviour and molecular order of liquid crystals. Adapted from reference [71].

Under normal physiological conditions, the lipid bilayer is present in a smectic-type liquid crystalline state.⁷¹ As shown in Figure 9, increasing temperature can allow the lipid molecules to be present in an intermediate phase between crystalline and liquid. The ordering of lipid molecules within the cell membrane can vary depending on the temperature, which can result in changes in the fluidity of the membrane. At low temperatures the lipid molecules are present in a gel phase where they are tightly packed, rigid, and highly ordered.⁷³⁻⁷⁵ At higher temperatures the lipid molecules are present in a liquid crystalline state where they are not as tightly packed, and movement between the acyl chains is increased which results in a higher area occupied by each lipid molecule and therefore the thickness of the membrane decreases.⁷⁵ The temperature at which the lipid molecules transition from a gel phase to a liquid crystalline phase is called the main phase transition temperature, T_m .^{74,75} Variation of the T_m is dependent on the lipid chain length, lipid chain saturation, and type of lipid polar head. For example, the T_m of dipalmitoylphosphatidylcholine (DPPC) which is composed of two saturated fatty acid chains each with 16 carbon atoms is approximately 41 °C.⁷⁵ Palmitoyloleoylphosphatidylcholine (POPC) which differs from DPPC only by the presence of one double bond in one of the fatty acid chains has a T_m of -5 °C.⁷⁵ This shows that the presence of unsaturated fatty acids lowers the T_m drastically. Unsaturated fatty acids are commonly found in biological membranes in order to achieve a liquid-crystalline state at physiological temperatures.⁶² Determination of T_m can be very useful in identifying lipid bilayer composition and fluidity of cell membranes.

2.2.2 Electrical properties of cell membranes

The electrical properties of cell membranes are key to the proper function of cells, especially with regards to cellular communication. These electrical properties arise from the physical properties of the membrane, as well as the presence of ion channels within the membrane. The thickness of a cell membrane ranges from 50-100 Å, and the movement of ions and certain molecules across the membrane is restricted due to the nature of the hydrophobic region. The restriction of the flow of ions across the cell membrane allows it to act as a resistor.^{76,77} Typically, cell membranes have resistivity values in the range of 10^3 - $10^5 \Omega \text{ cm}$.³³ The potential difference between the intercellular and extracellular fluids is maintained around -60 to -90 mV due to the distribution of ions on either side of the cell membrane.⁷⁸ The separation of these ions across the cell membrane allows for the existence of an electric field. Due to the nanometer thicknesses of cell membranes, very large electric fields of a 10^7 V m^{-1} exist across the membrane.^{62,79} The electric field plays a large role in forcing directional movements of ions across the insulating barrier formed by the lipid bilayer. The insulating lipid bilayer acts as a capacitor, in that a charge tends to build up on the intercellular side that is opposite to the charge on the extracellular side of cell membrane.⁷⁷ The cell membrane capacitance typically ranges from 0.5 - $1 \mu\text{F cm}^{-2}$ for biological cells.⁷⁴

2.2.3 Interaction between proteins and cell membranes

Cell membranes contain a number of different proteins that have varied and important roles including as ion channels, receptors, enzymes, and transporters. Ion channels are porous proteins that allow certain ions to pass through depending on size and / or charge.^{71,72,80} Receptors are embedded proteins within the cell membrane that receive chemical signals from outside the cell, causing a coordinated response inside the cell. Protein enzymes allow reactions to occur more quickly.⁸⁰ Transporter proteins exist permanently across the membrane and function as transporters of specific substances into and out of the cell. All of these proteins are associated with the cell membrane and are thus referred to as membrane proteins. Membrane proteins are divided into three different categories: peripheral proteins, integral proteins, and structural proteins.⁸⁰ Peripheral proteins are localized at the membrane by electrostatic interactions or short hydrophobic chains that anchor the protein to the membrane. These proteins can be isolated from the membrane by changes in pH or ionic strength. Integral proteins are translocated across the lipid bilayer where the hydrophilic regions interact with aqueous domains, and the hydrophobic regions interact with the hydrophobic interior of the membrane.⁸⁰ Integral membrane proteins are more complex than peripheral proteins and can span the membrane either once or several times. Isolation of these proteins for characterization is difficult and requires the use of organic solvents or detergents.⁶² Structural proteins are responsible for forming part of the membrane cytoskeleton and are not strictly membrane proteins, but instead are present on the intracellular side of the cell and are connected to the cell membrane through integral proteins. Structural proteins

protect the cell against changes in shape or volume, and maintain the regular structure of the cell membrane.⁸⁰

Studying the interaction between proteins and cell membranes can be useful in understanding how such proteins function and their role in many diseases. However, one of the major difficulties in studying membrane proteins is that the isolation process from cell membranes causes denaturation of the protein, resulting in complete loss of function. Therefore, significant research has focused on mimicking cell membranes and introducing transmembrane proteins to such systems in order to study membrane proteins in their natural environment.

2.3 Biomimetic membranes

2.3.1 Current models of biomimetic membranes

Due to the complicated structure of biological membranes, including their inherent anisotropy and inhomogeneity, several models of biomembranes have been developed. These models are referred to as biomimetic models, which are designed to model biological systems as closely as possible. These models simplify the membrane system in order to study a single component in a membrane, such as a protein, and these models can range from simple micelles to supported lipid films. The different types of biomimetic models will be explained briefly in the next section.

2.3.1.1 Early models

Biomimetic membranes must resemble the molecular and electrical properties of biological cell membranes. Table 1 presents a comparison of such properties between biological cell membranes and biomimetic membranes.⁶²

Table 1: Comparison of physical and electrical properties between biological cell membranes and bilayer lipid membrane models. Adapted from reference [62].

Membrane Properties	Biological Cell Membranes	Bilayer Lipid Membrane Model
Thickness (Å)	60-130	60-90
Resistivity ($\Omega \cdot \text{cm}$)	10^2 - 10^5	10^6 - 10^8
Capacitance ($\mu\text{F}/\text{cm}^2$)	0.5-1.3	0.3-1.3
Resting Potential (mV)	10-90	0-140
Water permeability ($10^{-4}\text{cm}/\text{sec}$)	0.25-58	2.3-24
Surface tension, mN m^{-1}	0.03-3.0	0.2-6.0
Conductivity, $\Omega^{-1} \text{cm}^{-2}$	10^{-2} - 10^{-5}	10^{-6} - 10^{-10}
Breakdown voltage, mV	100	150-300

Over the past few decades many models were proposed in order to mimic biological cell membranes. Initial model membranes were prepared using two different methods: 1) black lipid membrane fabrication, and 2) liposome formation. Both of these methods are described below.

In 1962 the first stable bilayer lipid membranes were prepared by Mueller and coworkers. The bilayer was formed from a crude fraction of phospholipids in a Teflon cup with circular holes of a small diameter (0.8-2.5 mm) immersed in aqueous solution.⁸⁰ The addition of phospholipids to the hole resulted in the immediate formation of a thick film (>100 nm). Due to changes in hydrodynamic pressure, the solvent tends to escape from the central part of the film to the borders. This would result in thinning of the membrane, and as this process caused black spots to appear, these membranes were initially called "black lipid membranes".^{62,80} The advantage of using the black lipid membrane model system is that both lipid layers are in contact with aqueous solution which can be useful for incorporating transmembrane protein. Disadvantages of this technique include difficulty in incorporating large molecules (i.e. proteins) within the

lipid bilayer, presence of residual organic solvents, low stability, difficulty in manipulating the lipid bilayers, and characterization is limited to conductivity and microscopic techniques.⁸⁰

Another common model membrane is lipid vesicles, also called liposomes. Discovered by Bangham and coworkers in 1965, liposomes quickly became the most popular and widely used model system for studying physical properties of biomembranes.⁸¹ Liposomes are spherical lipid bilayers that are formed from water dispersions of lipids by various methods. Depending on the method used, different sizes of multilamellar or unilamellar liposomes can be obtained.⁸¹ Advantages of using liposome models include the ability to incorporate various components such as peripheral or integral proteins due to the presence of water on both sides of the membrane, and the method is cost effective as no specialized instrumentation is needed.⁸² Disadvantages of multilamellar liposomes include size inhomogeneity and fast sedimentation. Disadvantages of unilamellar liposomes include non-uniform diameter, small size vesicles, and low stability.^{82,83} One of the major issues with using black lipid membranes and vesicles include the limited number of tools available for characterization, hence a transition to surface supported membrane models was made.

2.3.1.2 Solid-supported models

To overcome the disadvantages of black lipid membrane and liposomes, different models have been used to mimic biological membranes. The formation of a lipid bilayer on a solid support makes it accessible for characterization using a broad range of biophysical methods. A major advantage of using supported membrane models is to

increase the robustness and stability of the phospholipid bilayer membrane.⁸⁰ Also, there is an enhanced ability to probe interactions that occur at the membrane surface with various surface analytical techniques such as atomic force microscopy, surface plasmon resonance, surface-enhanced Raman spectroscopy (SERS), polarization-modulation infrared reflection absorption spectroscopy (PM-IRRAS), and vibrational sum frequency generation spectroscopy (SFG).⁸⁰ Many different supported membrane models have been developed over the past several decades; some of these models are described below.

(a) Hybrid bilayer lipid membrane (h-BLM)

The use of self-assembled monolayers (SAM) is very important for forming lipid bilayers due to their ability to form tightly packed and well-ordered monolayers.⁸⁴ The most common and widely used SAMs are composed of alkanethiols which have the ability to form strong covalent bonds with the metal surface through the thiol group.⁸⁵⁻⁸⁷ This led to the development of hybrid bilayer lipid membranes (h-BLMs), as shown in Figure 10 (image a). In h-BLMs the upper leaflet consists of lipid components, and the lower leaflet consists of a self-assembled non-lipid thiolated monolayer.^{80,84} The physical properties of h-BLMs can be altered by using different alkanethiols as the lower leaflet. The advantages of using h-BLMs involve coupling of a phospholipid monolayer directly to a metallic surface, and the strong interaction between alkanethiol SAM and substrate offers a robust, rigid, and close-packed system.⁸⁰ However, there are some drawbacks of h-BLMs including the inability to incorporate transmembrane proteins because the alkanethiol SAM is rigid and present in a more crystalline structure.⁸⁰

(b) Supported bilayer lipid membrane (s-BLM)

Solid supported bilayer lipid membranes (s-BLM) are the most commonly used platforms for biomimetic membranes. In this model the lipid bilayers are non-covalently attached to a solid support, typically a metal surface. The advantages in using a solid support include long term stability which allows for surface analytical techniques to be employed; more specifically imaging and electrochemical measurements can be easily integrated using this model.⁸⁶ Disadvantages of this model include direct contact of the lipid bilayer with the solid support which creates issues for incorporating transmembrane proteins, and decreased fluidity due to the absence of a water reservoir between the solid substrate and the membrane.⁸⁶

Modification of traditional s-BLMs has been successfully demonstrated in order to separate the lipid bilayer from the solid substrate. The most common method uses an alkanethiol SAM to form a covalent bond with the metal surface, as shown in Figure 10 (image b). The main advantage of using a SAM spacer is to avoid direct contact of lipid molecules and embedded proteins with substrate which can cause denaturation.⁸⁸⁻⁸⁹ However, lipid bilayers that are deposited onto the SAM experience reduced fluidity which makes it difficult to transport biological molecules across the membrane.⁶⁸ There is still a lack of a water reservoir between the membrane and the metal surface making it difficult to incorporate proteins into the bilayer without causing protein denaturation.^{80,90}

(c) Floating bilayer lipid membrane (f-BLM)

To overcome the fluidity issue of the supported bilayer lipid membrane, floating bilayer lipid membranes (f-BLMs) have been developed as a model membrane, as shown in Figure 10 (image c). This model does not tether the bilayer to the surface of the solid substrate, and therefore allows the membrane to float just above the surface.⁹¹ The floating lipid bilayer is separated from the solid substrate that is covered with lipid molecules by a 1-2 nm water-rich layer, which allows transmembrane proteins to be easily incorporated into the membrane.⁹¹⁻⁹⁵ Also, the presence of a water reservoir allows the lipid molecules to be fully hydrated and free to fluctuate.⁹⁶ Some of the drawbacks of f-BLM include difficulty in fabrication, stability issues, and the large distance between the bilayer and substrate limit its analysis using SERS.⁸⁹

(d) Tethered bilayer lipid membrane (t-BLM)

Tethered bilayer lipid membranes (t-BLMs) have been developed to overcome some of the drawbacks observed with s-BLMs, most specifically the lack of a water reservoir on the substrate side of the membrane. These bilayers use hydrophilic spacer molecules, lipopeptides or a polymer layer to increase the hydrophilic region between the metal and the bilayer, as shown in Figure 10 (image d).^{79,86,90} Different lengths of these spacers, and also a mixture of different types of spacers have been used. The variety of different hydrophilic spacers that can be used will allow for transmembrane protein incorporation across the bilayer lipid membrane.⁹⁷ However, one of the main disadvantages of t-BLMs is that these spacer molecules tether the model membrane to the

solid substrate and therefore restrict the mobility of the bilayer components.^{89,93-95} Also, in most cases the hydrophilic spacer molecules are typically custom made, and there are many synthetic challenges in preparing a good quality tethered system, and hence preparation steps are costly and challenging.⁹⁷

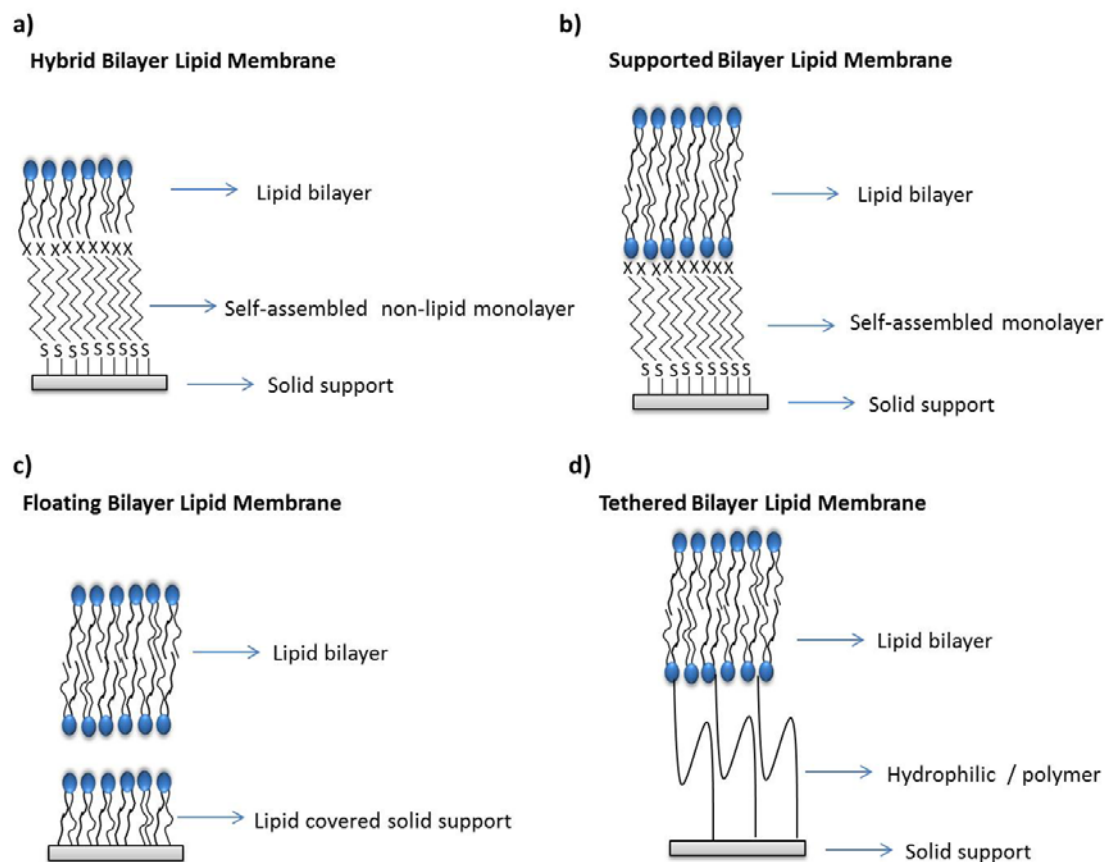


Figure 10: Illustration of the different bilayer lipid membrane systems: a) hybrid bilayer lipid membrane (h-BLM), b) supported bilayer lipid membrane (s-BLM), c) floating bilayer lipid membrane (f-BLM), and d) tethered bilayer lipid membrane (t-BLM).

2.3.1.3 Characterization of bilayer lipid membranes

The analytical technique used to characterize a biomimetic membrane system is dependent on the method used to create the bilayers. One of the typical measurements

done on BLM models is measuring lipid mobility by photobleaching a region of the BLM and monitoring fluorescence over time. This technique is referred to as fluorescence recovery after photobleaching (FRAP) where a fluorescent dye is added to a section of BLM and subjected to high intensity radiation, which causes photobleaching to occur.^{98,99} This results in a dark region within the bilayer, and as the lipid components diffuse and migrate across the surface the fluorescence will be recovered.⁹⁹

Spectroscopic techniques can be used to analyze model membranes and provide further information regarding the lipid bilayers. Surface infrared spectroscopy such as PM-IRRAS is considered a powerful surface specific technique for investigating biomimetic membranes.⁸⁶ PM-IRRAS can provide information on the molecular orientation and conformation of molecular components within a lipid bilayer deposited on a flat metallic substrate. This technique is considered simple, provides high sensitivity, and in situ measurements can be obtained.¹⁰⁰ Some drawbacks include interference from water absorption, limitation to atomically flat substrates and the relatively high cost.¹⁰⁰ Another spectroscopic technique is SFG which is a non-linear optical spectroscopic technique that can provide vibrational spectra of interfacial molecules with high surface selectivity and sensitivity. SFG can provide qualitative analysis on lipid chain conformation and orientation with high sensitivity. Some drawbacks of this technique include its relative complexity and costly experimental setups, and it can only probe non-centrosymmetric molecules.¹⁰⁰ An additional technique that can be used is surface-enhanced Raman spectroscopy (SERS) which is a vibrational spectroscopic technique based on Raman scattering. SERS has been used to investigate biological systems without

the need of labels and can provide molecular structure and chemical composition of the sample analyzed.¹⁰¹ SERS is advantageous in comparison with PM-IRRAS and SFG as it has extremely high sensitivity, no spectral interference from water, narrow spectral bands, and fast acquisition times.¹⁰¹ There are some drawbacks including an inability to provide orientational information easily, a requirement for roughened metal surfaces, sharp distance dependence of enhancement, and that the lipid components are usually weak Raman scatterers.¹⁰²

There are many other spectroscopic methods used for structural analysis of BLMs including X-ray and neutron diffraction techniques. These methods can provide information on the composition, location, and distance between components in BLMs by observing the scattered X-rays and neutrons as they interact with the sample.¹⁰³ In addition, microscopic techniques that provide high resolution images of the topography of lipid bilayer surfaces can be used to analyze BLMs. One of the most common microscopic methods used is atomic force microscopy (AFM). In this technique, the surface of the bilayer is scanned to provide images with micro and nanometer scale resolution.¹⁰⁴ The images obtained can be useful in confirming bilayer formation, and whether there are pores or defects on the membrane surface. The interaction between protein and lipid molecules can also be seen in these images which can prove the formation of pores upon this interaction.¹⁰⁵ AFM can also be very useful for measuring the thickness of BLMs on the surface. This measurement can be done using force-distance measurements which can provide information regarding lateral organization of lipids and the thickness of the bilayer.¹⁰⁶ Although AFM provides good resolution and provides a three dimensional surface profile of the lipid bilayer, AFM is expensive,

sensitive to vibration, requires skilled operators, and non-contact modes used for delicate biomaterials can be challenging.¹⁰⁵

2.3.2 Applications of model membranes

The main application of model membranes is for investigating various biological processes that occur within and across biological cell membranes. These can include the investigation of enzymatic reactions, protein structure and function, pore formation, and understanding the operation of specific channels. In addition, biomimetic membranes can be used as biosensor platforms for studying the interaction between lipid molecules and target molecules such as enzymes, antibodies, and nucleic acids.¹⁰⁶ There has been continuous progress in advancing both the fabrication and applications of biomimetic membranes in a variety of fields including material science, geochemistry, biophysics and catalysis.¹⁰⁷ One of the main applications of these biomimetic membranes is to study the interaction between proteins and lipid molecules. Specifically, the use of t-BLMs allows protein incorporation in non-denaturing conditions, which makes them very suitable model membranes for investigating membrane-protein interactions.⁸⁶ As such, t-BLMs can be used as models in a variety of medical applications in order to understand various neurodegenerative disorders that are caused due to interactions occurring between proteins and biological cell membranes. The progress achieved from using such biomimetic membranes will involve studying more complex compositions of lipids and proteins which can be used to study more biological processes such as membrane fusion and trafficking, cell-cell recognition, and signaling.¹⁰⁷

In order to be able to use these biomimetic bilayer lipid membranes for various applications, the formation of lipid molecules onto the substrate should be well controlled. The bilayer lipid membrane system should be stable, robust for long-term stability, easily prepared, provide reproducible results, and ensure no defects or pinholes are present.¹⁰⁸ The formation of a bilayer lipid membrane can be easily prepared using vesicle fusion, however the membrane formed is fragile and unstable making them unsuitable for many applications such as pharmaceutical screening.¹⁰⁸⁻¹⁰⁹ In addition, multilayers rather than single bilayers typically form. Other methods have been developed in order to increase the stability of lipid membranes on solid substrates. One such method that has arisen over the last decade is Langmuir Blodgett- Langmuir Schaefer (LB / LS) deposition. This method is used in the present work and is outlined below.

2.4 Langmuir monolayers and films

2.4.1 Langmuir monolayers

A Langmuir monolayer refers to a monomolecular thick insoluble film formed at the interface of two adjoining bulk phases.¹¹⁰⁻¹¹² In the 1900s, Irving Langmuir undertook a body of work studying the relationship between surface pressure and area per molecule on an aqueous surface.¹¹³ Langmuir's original experimental contributions focused on theoretical concepts and behaviour of insoluble monolayers at the air-water interface. Langmuir films are formed on the surface of an aqueous medium, usually pure water, which is referred to as the subphase.^{112,113} Molecules that are amphiphilic in nature such as lipids partition spontaneously at the air-water interface, allowing the monolayer to

remain as an insoluble film on the surface of the subphase.¹¹² When lipids are dissolved in a non-aqueous volatile solvent and introduced onto an aqueous surface, the solvent will evaporate leaving the lipid molecules oriented at the liquid-gas interface. The hydrophilic head group of an amphiphilic molecule is in contact with the subphase while the hydrophobic portion is pointed away from the subphase into the air. Although molecules spread spontaneously at the interface without applying any external pressure, a compact monolayer will only be formed if these molecules are compressed at a slow and steady speed. Once the compact monolayer is formed it can then be transferred onto a substrate of interest.^{112,113}

2.4.2 Langmuir-Blodgettry

A compressed monolayer at the air-water interface exhibits a particular surface pressure that is dependent on the amphiphilic molecule and the subphase. The compressed monolayer can be transferred onto a solid substrate at a constant pressure; this technique is referred to as Langmuir-Blodgettry. This was first demonstrated by Katherine Blodgett who worked with Langmuir to develop this technique for transferring monolayer films onto solid substrates.¹¹³ An important aspect to consider while transferring the compressed monolayers is the hydrophilic or hydrophobic nature of the solid substrate, as seen in Figure 11. This would cause the lipid molecules to orient differently on the surface of the substrate.

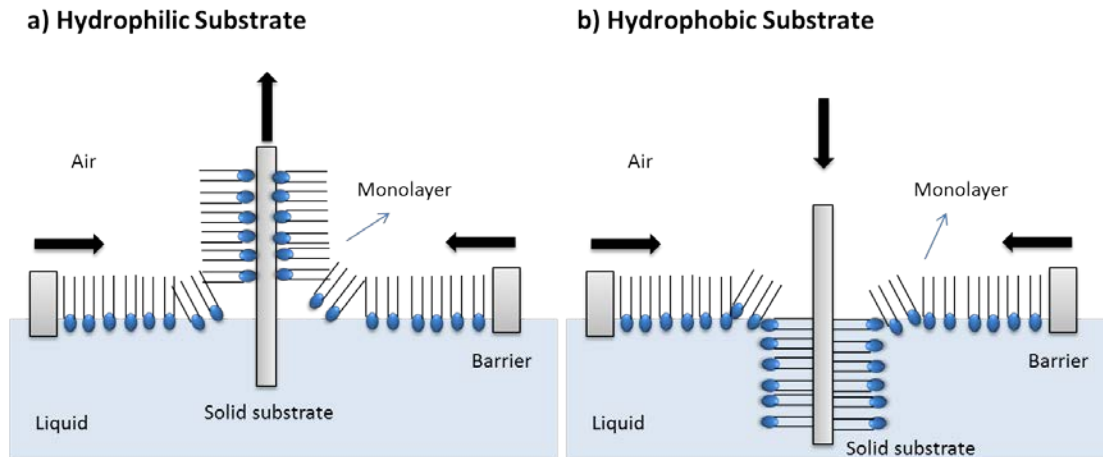


Figure 11: Langmuir-Blodgett transfer of a monolayer onto a) hydrophilic substrate, b) hydrophobic substrate. Adapted from reference [114].

There are different methods to transfer a monolayer onto a solid substrate. One method involves immersing a hydrophilic substrate in the subphase prior to monolayer formation. Once the monolayer is formed, the substrate is slowly drawn vertically through the compressed monolayer at the air-water interface. This allows the hydrophilic heads of the lipid molecules to adsorb onto the hydrophilic substrate, with the hydrophobic tails oriented perpendicular to the surface of the substrate. This process can be repeated multiple times to achieve bilayers or multilayers. There are different styles used in order to form multilayers which include a) Y-type, b) Z-type, and c) X-type, as shown in Figure 12.¹¹⁴ Y-type deposition involves the formation of a multilayer film by passing the solid substrate through the air-water interface in alternating up and down strokes. The Z-type deposition involves passing the solid substrate in an upward stroke only, hence hydrophilic substrates need to be used.¹¹⁴ The X-type deposition involves

passing the solid substrate in a downward stroke only, hence hydrophobic substrates need to be used.¹¹⁴

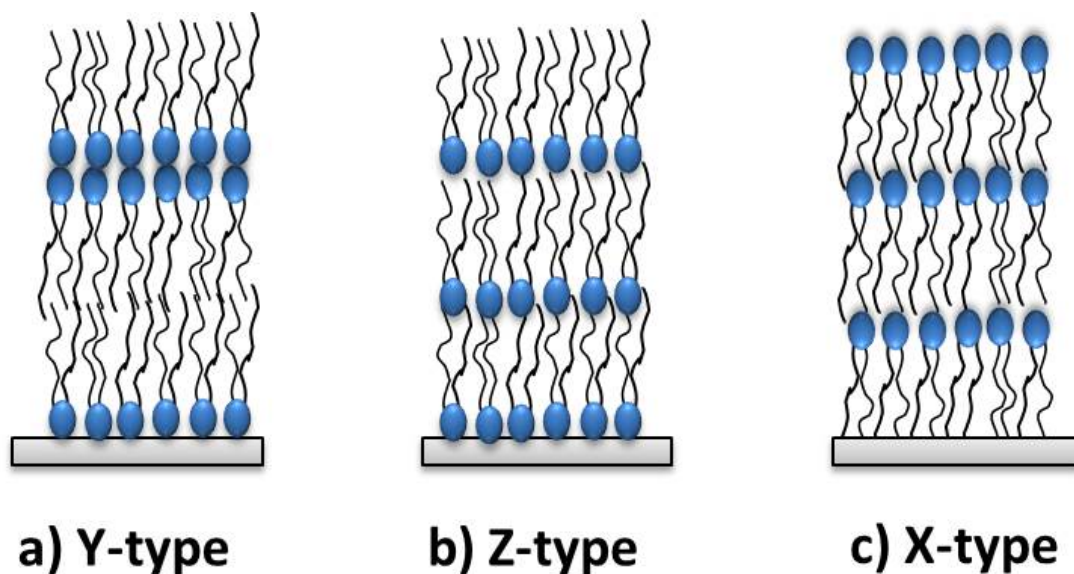


Figure 12: a) Y-type, b) Z-type, and c) X-type Langmuir-Blodgett film deposition schemes. Adapted from reference [114].

The Langmuir-Blodgett technique is a very sensitive method and considerable care should be taken while transferring these monolayers onto solid substrates. There are a number of factors that should be considered prior to performing any experiments in order to ensure successful monolayer transfer and afford reproducible results. Some of these factors include the nature and dimensions of the solid substrate, the nature of the amphiphilic molecule, the nature of the subphase such as composition, pH, ionic strength, temperature, surface pressure during deposition, the rate of speed of the substrate passing through the interface, and number of layers deposited.¹¹⁴ The transfer of a poor quality monolayer will have an effect on the compactness and stability of the monolayer.

2.4.3 Langmuir Blodgett / Langmuir Schaefer deposition

As shown in Figure 7, biological membranes consist of two monolayers having their hydrophobic tails sandwiched between the hydrophilic polar heads. In theory, this can be achieved using the Y-type deposition to obtain the lipid bilayer structure, however the solid substrate used must be hydrophilic to ensure the hydrophilic heads of the first monolayer are adsorbed onto the substrate. In this research, 1-2-Dimyristoyl-*sn*-glycero-3-phosphocholine (DMPC) bilayers will be deposited on modified SPEs. However, it has been shown experimentally that many lipids, including DMPC bilayers cannot be successfully produced using the Y-type deposition.¹¹⁵ The removal of the DMPC monolayer using an upward stroke to form the second leaflet is problematic because the force to pull the DMPC monolayer from the air-liquid interface is not sufficient. The polar head groups of DMPC interact strongly with the liquid subphase making it impossible to achieve a DMPC bilayer using the Y-type deposition.¹¹⁵

To overcome this drawback, a Langmuir-Schaefer method is used to transfer the second lipid leaflet, as shown in Figure 13.^{113,114} The deposition of the Langmuir film onto the monolayer-coated solid substrate is done by horizontally lowering the substrate towards the air-water interface until it just touches the floating monolayer at the subphase surface. The transfer of the monolayer onto the solid support is obtained via electrostatic interactions, Van der Waals forces, or covalent bonding depending on the nature of amphiphile and substrate.¹¹³ The film obtained is highly organized, and the molecules are well ordered.¹¹³

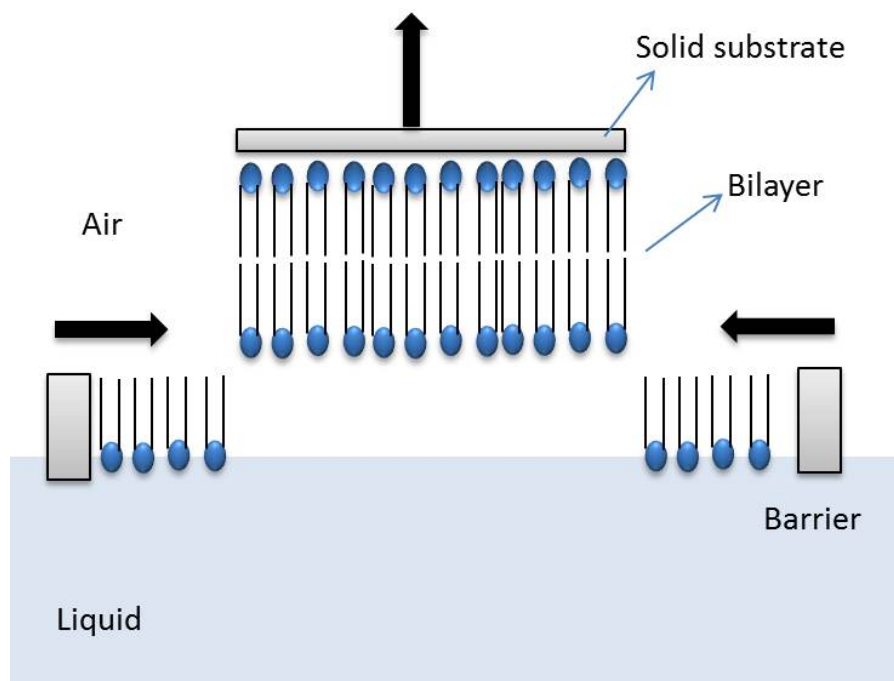


Figure 13: Langmuir-Schaefer transfer (horizontal touch technique) on a solid substrate. Adapted from reference [113].

The formation of a bilayer lipid membrane using the Langmuir-Blodgett / Langmuir Schaefer (LB / LS) method has been used in literature for a decade and offers several advantages over the more common vesicle fusion method.^{116,117} For example, monolayers can be transferred onto the substrate at a precisely known surface pressure, molecular area, and physical state of the film.⁷⁹ Also, LB / LS allows for a different lipid composition in the bottom and the top leaflet of the bilayer lipid membrane.⁷⁹ A PM-IRRAS experiment conducted by Garcia-Araez *et al.* showed that the LB / LS method allows for the formation of a stable and well-ordered bilayer lipid membrane that can be used for mimicking biological membranes.¹¹⁸ A layer-by-layer characterisation of a DMPC bilayer where one of the DMPC leaflets is all-hydrogenated (h-DMPC) and the

other DMPC leaflet is all-deuterated (d-DMPC) was completed.¹¹⁸ The DMPC bilayer membrane was produced having the h-DMPC as the lower leaflet (in contact with the metal substrate), and the d-DMPC as the upper leaflet (in contact with aqueous solution), and *vice versa*. The two studies were compared by observing the C-H stretching region (only present in h-DMPC) using PM-IRRAS.¹¹⁸ This study allowed for the determination of tilt angles of the chains in the two leaflets separately showing that the solid substrate does introduce a small amount of disorder to the leaflet in closest contact with the metal.

2.5 Characterization of biomimetic membrane-protein interactions

2.5.1 Spectroscopic methods

In literature, there has been a substantial increase toward optimizing techniques to characterize biomimetic membrane-protein interactions.^{108,117,119} One of the common spectroscopic methods used is PM-IRRAS because it has the ability to monitor both protein and peptide backbone vibrational modes and lipid vibrational modes simultaneously. Casel *et al.* have used PM-IRRAS to study the effect of the polysaccharide chitosan on the adsorption of proteins onto a phospholipid monolayer, and its role in removing the protein from the monolayer.¹²⁰ This research was conducted to test the action of chitosan in biological applications since it has been shown that chitosan has the ability to remove the protein β -lactoglobulin from whey. β -lactoglobulin was adsorbed onto a DMPA lipid monolayer that was prepared using the Langmuir technique.¹²⁰ The amide bands of β -lactoglobulin were monitored using PM-IRRAS; the disappearance of these bands from the spectrum would indicate that β -lactoglobulin was no longer adsorbed on the monolayer.¹²⁰ It was successfully shown that chitosan present

in the subphase is capable of removing β -lactoglobulin. These results demonstrate that protein-protein or protein-lipid interactions can be monitored using PM-IRRAS.

Leitch *et al.* has also shown the importance of PM-IRRAS in characterizing structural and orientational changes of cholera toxin B (CTB) as it interacts with monosialotetrahexosylganglioside (GM1) that is incorporated into a DMPC / cholesterol bilayer lipid membrane.¹²¹ A major finding in this study was that the opening and closing of the CTB pore occurs via the α -helical components in the center of the pore, and the pore opening was found to be voltage-dependent.¹²¹ The results shown in this study can be very useful in explaining the mechanism of CTB translocation across the membrane.

Another method used to investigate lipid-protein interactions is 2D infrared spectroscopy. This technique is well-developed to probe molecular structure and dynamics. It has been used in a variety of applications such as monitoring chemical exchange in small molecules, protein structure and dynamics, and solvent hydrogen bonding dynamics.¹²² However, the main application of 2D infrared spectroscopy involves characterizing aqueous proteins and peptides, and probing the structure of lipids and membrane proteins. Volkov *et al.*, have shown that this method can be used to successfully characterize the incorporation of myrisoylated glycine (MrG) dipeptide into a PLPC bilayer.¹²³ The results indicated that MrG is strongly associated with the phospholipids, and that the peptide backbone is oriented 60° with respect to the plane of the bilayer.¹²³ Despite the heavy use of PM-IRRAS for such protein-lipid interaction studies this method has several disadvantages, as mentioned earlier, such as complicated set-up, long acquisition times, and background interference. As a result, other spectroscopic tools are needed.

Another powerful spectroscopic technique that can be used to monitor lipid-protein interactions is surface-enhanced Raman spectroscopy (SERS). SERS is becoming a popular tool for analyzing biological molecules and studying their conformational changes on metal substrates.^{124,125} There are as of yet relatively few studies that have shown the potential of using SERS for analyzing biomembranes deposited on metal surfaces. One study has shown the ability of SERS to investigate the interaction between h-BLMs and human enzyme cytochrome P450 (CYP2D6).¹²⁶ CYP2D6 is a peripheral membrane protein that is responsible for drug metabolism, making it a relevant topic in pharmacology and toxicology.¹²⁶ This study was aimed toward understanding the interaction between CYP2D6 and h-BLMs using SERS. Based on the results obtained, peaks that are due to the heme group in the CYP2D6 were monitored using SERS.¹²⁶ However, there were major difficulties in enhancing the Raman signal of the protein due to the large distance between the protein and the SERS substrate.¹²⁶ This showed that because SERS is a distance-dependent technique, depending on the thickness of the bilayer lipid membrane and the size of the protein, it might be difficult to observe protein signal. However, in some cases this could be advantageous, for example in probing membrane transport events.

The combination of surface spectroscopic methods with electrochemistry can provide more information toward analyzing biological systems. One of the methods that can be readily coupled with electrochemistry is SERS (EC-SERS). In order to use EC-SERS it is very important to determine the stability of the bilayer lipid membrane as a function of applied potential. In most cases this should not be problematic since natural

biological membranes are frequently exposed to electric fields on the order of 10^7 - 10^8 V m^{-1} .^{79,106} Vezvaie *et al.* showed that EC-SERS can be used to determine the stability of bilayer lipid membrane as potential is being applied.¹²⁷ It was observed that the bilayer lipid membrane is most ordered at potentials between -0.7 and -0.9 V.¹²⁸ The change in intensity of the acyl peaks at 2935 cm^{-1} and 2880 cm^{-1} was used to determine the quality of the acyl chain packing on the silver substrate.¹²⁹ The results obtained from this work have demonstrated that EC-SERS can provide unique molecular level understanding of potential-dependent properties of s-BLMs.¹²⁹ This is an example showing that EC-SERS can monitor lipid-lipid interactions, however EC-SERS has not yet been used to monitor protein-lipid interactions.

This research work will focus on developing EC-SERS as a spectroscopic tool in order to monitor the interaction between proteins and biomimetic membranes. The results obtained will provide molecular level information and be useful in further exploring the amyloid pore hypothesis of Alzheimer's disease.

2.5.2 Electrochemical methods

One common electrochemical method used to study membrane integrity and membrane-protein interactions is cyclic voltammetry (CV). CV can be used to obtain information regarding membrane thickness, porosity, and extent of defects present in a monolayer.¹⁰⁸ This is achieved through cycling the potential of the working electrode between two limits and monitoring the resultant current.¹⁰⁸ Recently, CV was used to study the interaction between protein toxins and h-BLMs by the use of three different redox probes.¹²⁴ As these redox probes interact with the surface due to defects in the

h-BLMs caused by the toxins, distinctive redox peaks will be apparent in the cyclic voltammogram.¹²⁴ The results obtained have indicated that pores were indeed formed by the presence of these toxins.¹²⁴

A recent study completed by Juhaniewicz *et al.* has highlighted the importance of electrochemical methods in order to evaluate the mechanisms involved in melittin membranolytic activity.¹²⁹ Melittin is a membrane active peptide that consists of 26 amino acids and interacts with biological and artificial membranes. Melittin is considered a toxin due to its ability to cause hemolysis of cells and perturbation of lipid vesicles.¹²⁹ In this study CV was used in order to verify the permeability of a DMPC bilayer lipid membrane in the presence and absence of melittin. The permeation was monitored using the ferricyanide / ferrocyanide redox couple and the peak-to-peak separation of the cyclic voltammogram was measured.¹²⁹ It was observed that the peak-to-peak separation of the redox probe on a bare gold electrode is 60 mV, and in the presence of bilayer lipid membrane the peak-to-peak separation increases to 550 mV.¹²⁹ This indicates that the electron transfer process is slowed by the presence of the bilayer and surface access of the probe is hindered. Melittin was then introduced to the bilayer for 15 and 30 minutes and the peak-to-peak separation was measured to be 320 mV and 200 mV, respectively.¹²⁹ This confirmed the destabilizing effect of melittin on the DMPC bilayer membrane, which had caused the membrane to become less compact. Longer exposure of melittin caused the surface to become more accessible for ions diffusing from bulk of the solution and hence a decrease in the peak-to-peak separation occurred.¹²⁹

2.5.3 Other methods

Some methods have been used to visually study the interaction between lipid molecules and proteins such as atomic force microscopy (AFM) and scanning tunneling microscopy (STM). STM can be coupled with electrochemistry (EC-STM) in order to monitor the lipid-protein interaction. In this study the interaction between trichogin, an antimicrobial peptide, and DMPC monolayer was investigated using EC-STM.¹³⁰ More specifically, an analog of trichogin, trichogin-OMe (TCG) was used to study the nature of the aggregation and the structure of the aggregates formed on the DMPC monolayer.¹³⁰ Based on the results obtained by EC-STM, the authors showed direct visualization of channels formed by the TCG aggregates. The channels formed consisted of a bundle of six TCG molecules which provided the first direct visualization of a hexameric pore.¹³⁰ This shows that EC-STM can be very useful in imaging lipid-protein interactions. Other antimicrobial peptide aggregates that were also imaged using EC-STM include gramicidin¹³¹ and alamethicin.¹³² There are other microscopic techniques that have the ability to image the lipid-protein interaction. Lee *et al.*, have monitored the interaction between amyloid- β aggregates on brain total lipid extract-based supported lipid bilayer membranes (brain-BLMs) using dark-field microscopy.¹³³ Dark-field microscopy has an advantage over fluorescence-based imaging methods because it does not require the use of dyes such as Congo red and Thioflavin T. The amyloid- β aggregates were introduced to the brain-BLMs and bare glass surfaces as well in order to monitor the difference in interactions.¹³³ It was observed that amyloid- β aggregates were seen on the brain-BLMs and not on the glass surface which suggests that there were repulsive forces between the

glass surface and the aggregates.¹³³ This study showed that brain-BLMs promote fast and efficient formation of amyloid- β aggregates.

Another example showing the effect of proteins on lipid bilayers was examined using molecular dynamics (MD) simulations. In this work, the effect of human islet amyloid polypeptide (HIAPP) on a lipid bilayer was studied.¹³⁴ It was observed that the interaction between HIAPP is dependent on the level of cholesterol present in DPPS / DPPC bilayers. The HIAPP was found to form disordered pores inside the bilayer in the absence of cholesterol, and amorphous aggregates located at the bilayer-water interface in the presence of cholesterol. The incorporation of cholesterol was found to increase the thickness and improve the order of the lipid bilayers and prevent HIAPP aggregates from inserting into the lipid bilayer.¹³⁴

Chapter 3: Theory

3.1 Langmuir monolayers and Langmuir-Blodgett

In order to transfer a compact bilayer or multilayer structure onto a solid substrate using the LB / LS technique some basic monolayer thermodynamics principles should be studied. Molecules at an interface will tend to orient themselves to minimize their free energy. In thermodynamics, free energy is referred to as the energy required for the system to do work. Molecules at the interface will diffuse from the bulk of the liquid to its surface and *vice versa* in order to achieve equilibrium, and hence minimize the free energy of the system.¹¹⁴ At an interface, molecules are surrounded by fewer molecules than the molecules in the bulk liquid as shown in Figure 14. Molecules within the bulk liquid are subjected to equal forces of attraction in all directions, whereas molecules located at the interface are subjected to unbalanced forces resulting in a net inward force.¹³⁵ The intermolecular forces between two or more substances can be referred to as cohesive and adhesive forces. Cohesive forces are intermolecular forces acting between molecules of the same phase (between like molecules).¹³⁶ Cohesive forces tend to keep the phases separate by the tendency for a substance to hold itself together.¹³⁶ Adhesive forces are intermolecular forces acting between molecules of different phases (between unlike molecules). Adhesive forces tend to increase the affinity between two phases by the tendency for a substance to interact with the other.¹³⁶ As a result of this imbalance in force, a surface tension (γ) results. The surface tension can be determined by the energy or work required to increase the surface area of a liquid.

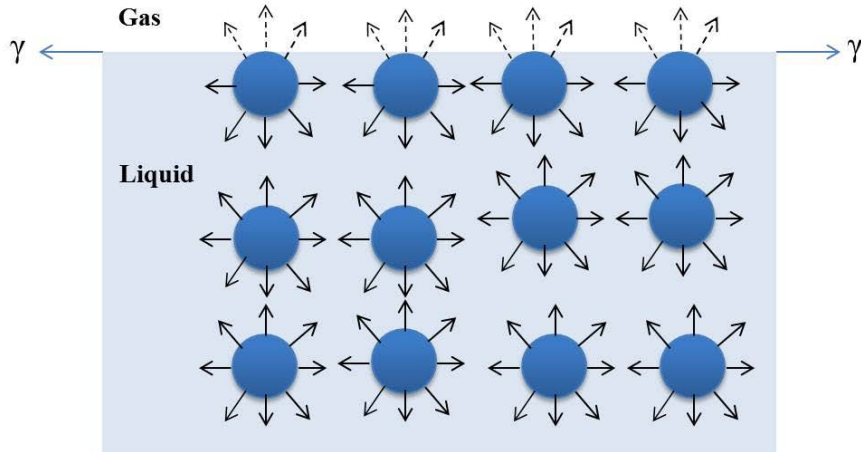


Figure 14: Cohesive (\longleftrightarrow) and adhesive ($---\rightarrow$) forces acting on molecules at the gas-liquid interface and molecules in the bulk liquid. Adapted from reference [135].

The force acting on molecules at the gas-liquid interface is the surface tension (γ) which is one of the basic physical values that characterizes liquid phases, including lipid monolayers.¹¹³ The surface tension is a result of short-range intermolecular forces including Van der Waals forces and hydrogen bonding.¹³⁵ A convenient way to explain surface tension is by comparing it to surface pressure, Π . This can be explained by the compression of a lipid monolayer using a barrier at the air-water interface on the LB trough.⁶² Surface pressure increases as molecules are compressed with a movable barrier. Figure 15 shows the compression of a lipid monolayer.

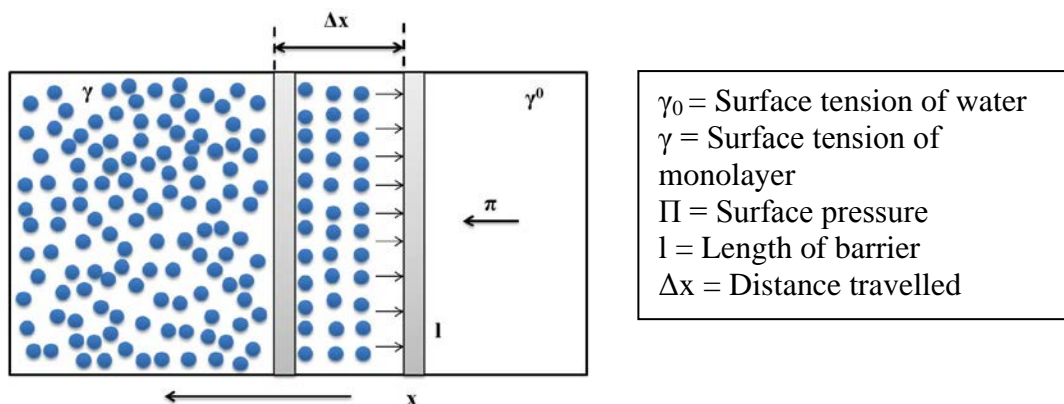


Figure 15: Compression of a lipid monolayer at the air-water interface using a movable barrier. Adapted from reference [62].

The work done by moving the barrier can be expressed as the product of the distance travelled by the barrier (Δx), its length (l), and the surface pressure (Π), as shown in equation 1:

$$w = \Delta x * l * \Pi \quad (1)$$

As the molecules are compressed at the interface, a change in the surface energy results. In monolayer experiments, it is very common to refer to a measurement of surface pressure instead of surface tension.^{113,114} The difference between the surface tension of water (γ_0) and the surface tension of the monolayer (γ) is equal to the surface pressure, as shown in equation 2:

$$\Pi = \gamma_0 - \gamma \quad (2)$$

The surface tension can also be expressed as the force per length acting on the surface. The SI unit of surface tension is mN m^{-1} ; for example, the surface tension of water at 20°C is 72.75 mN m^{-1} .^{113,114} There are different methods used to obtain the

surface tension as the monolayer is compressed, and the most commonly used method is known as the Wilhelmy plate method.^{113,114} This method involves dipping a flat plate through the surface of a liquid and measuring the force acting on it.¹¹⁴ The plate can be made of glass, mica, platinum or filter paper and is connected to an electromicrobalance. An illustration of a Wilhelmy plate is shown in Figure 16.

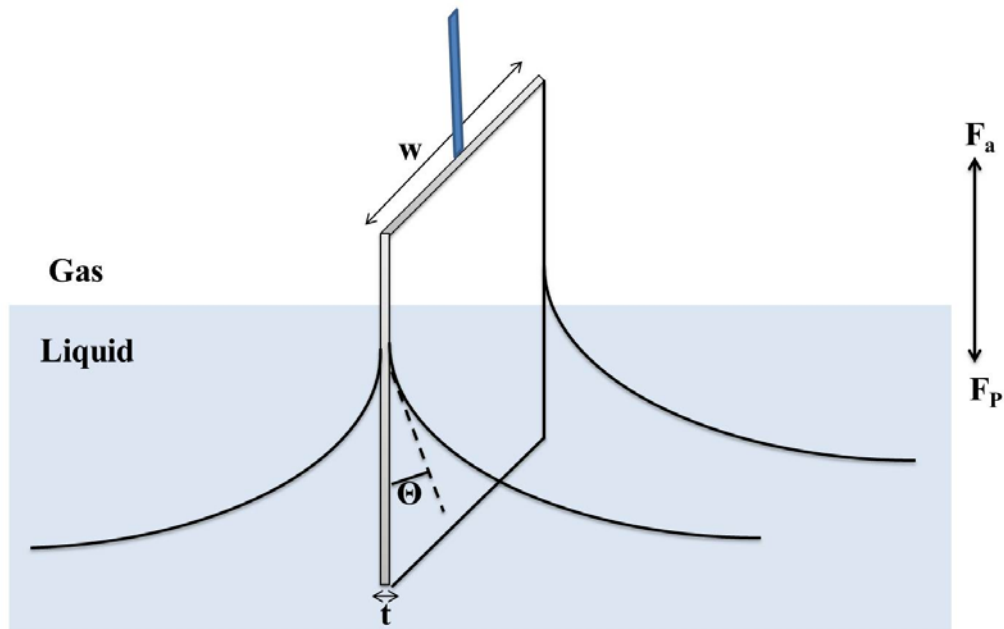


Figure 16: The Wilhelmy plate method to measure the surface tension. Adapted from reference [114].

There are two forces that act on the plate which include 1) weight force F_p acting downward, and 2) Archimedes' buoyancy force, F_a acting upward.¹¹⁰ The resulting net force acting on the Wilhelmy plate is shown in equation 3:

$$F = F_p + 2\gamma w - F_a \quad \left(\begin{array}{l} \gamma = \text{Surface tension of monolayer} \\ w = \text{width of the plate} \end{array} \right) \quad (3)$$

During the compression the plate is held constant which means F_p and F_a will be constant, and since the surface pressure is the change in surface tension, the surface pressure can be obtained as shown in equation 4:

$$\Pi = \frac{-\Delta F}{2w} \quad (4)$$

These equations show how surface tension and surface pressure are related, and the importance of knowing the parameters of the Wilhelmy plate in order to control the compression of the monolayers. In this research work, a thin filter paper was used as the Wilhelmy plate to measure the surface tension during the monolayer compression process.

During the compression process, the Langmuir film typically exists as four phases: gaseous phase, liquid-expanded (L-E) phase, liquid-condensed (L-C) phase, and a solid phase.^{62,112,113} Figure 17 illustrates the different monolayer phases observed during compression. The gaseous phase occurs immediately after the deposition of the amphiphilic molecules onto the subphase surface. These molecules tend to spread all over the surface with no net force exerted between the molecules.¹¹³ Once compression begins, the molecules are now present in a L-E phase, where they tend to get closer to each other and experience a small amount of attractive interactions. At this phase, the hydrophobic tails start to experience vertical alignment however the molecules are still randomly ordered.¹¹³ As the compression continues, the molecules reach the L-C phase where the area that each molecule occupies decreases and the neighbouring hydrophobic tails start to interact with each other.¹¹³ Further compression results in the solid phase

where the molecules are tightly packed and well-ordered at the subphase surface with their hydrophobic tails oriented into the air. This solid phase is characterized by a steep increase in surface pressure, describing the linear relationship between the surface pressure and the molecular area.¹¹³ The compression of a monolayer beyond the solid phase eventually leads to monolayer collapse where the molecules are forced from the surface of the liquid yielding the formation of undesirable multilayers and rapid decrease in Π .⁶⁸

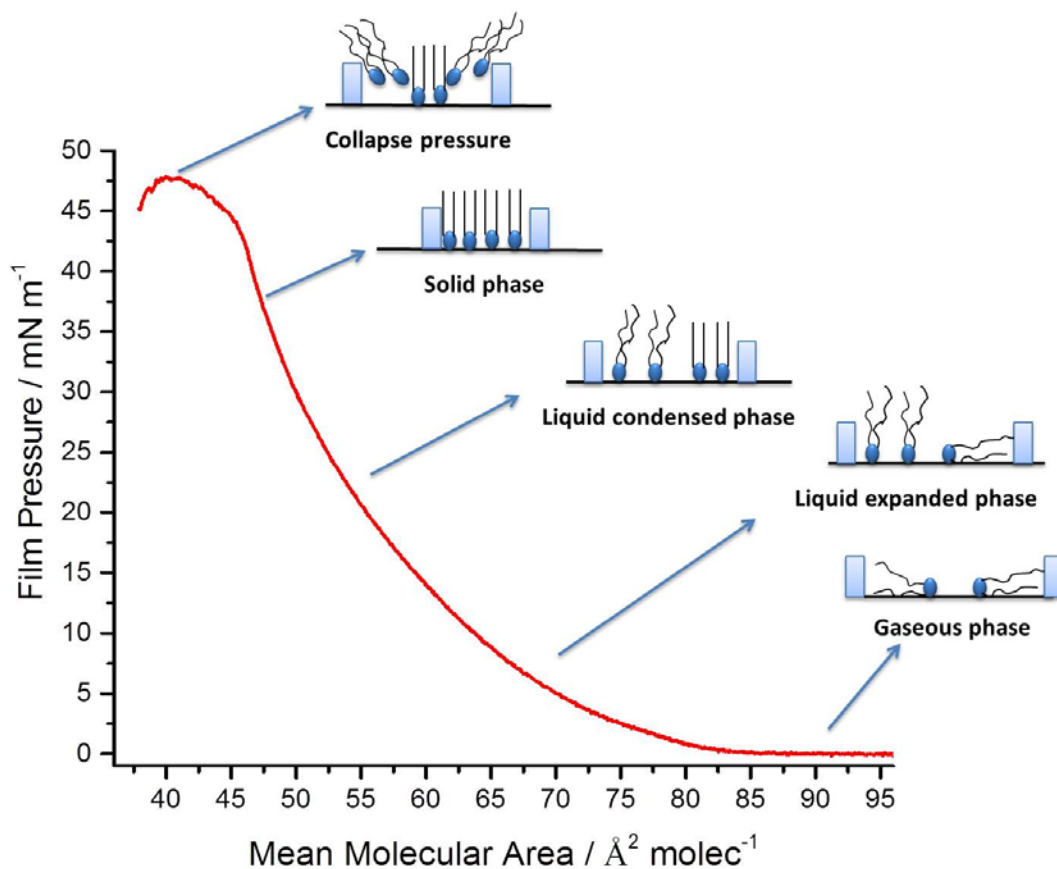


Figure 17: Compression isotherm of an amphiphilic molecule at the air-water interface.

3.2 Electrochemistry

Electrochemistry involves using electrical measurements to observe chemical effects. Electrical quantities such as current, potential, or charge can be monitored in order to understand chemical systems. In order to conduct an electrochemical measurement two main components are required: an electrolyte and electrodes. The electrolyte is an aqueous salt solution that has the ability to allow current to flow.¹³⁷ The ideal electrolyte solution is prepared using highly purified reagents, it should have a high concentration ionic strength (0.01-1.0 M), and it should not react with the analyte.¹³⁷ The presence of oxygen in the electrolyte solution can cause problems while performing electrochemistry. For example, a large background current is produced as oxygen is reduced which can interfere with the measurement of the analyte, and the products of the oxygen reduction may also affect the electrochemical process under investigation. The electrolyte is purged with an inert gas, such as argon or nitrogen, prior to use, to remove dissolved oxygen.¹³⁷

There are three different electrodes present in a typical electrochemical cell used for voltammetry, which include the reference electrode (RE), counter electrode (CE), and working electrode (WE).¹³⁸ The RE has a constant potential that is not affected by the applied potential. The most commonly used REs include the silver-silver chloride electrode (Ag / AgCl) and the saturated calomel electrode (SCE).^{137,138} The CE is made from an inert conductive material, such as a platinum or graphite, and its function is to complete the electrical circuit; by acting as an anode when the WE is acting as a cathode and *vice versa*.¹³⁹ The WE is where the redox reaction of interest takes place.

Electroanalysis is highly dependent on the material of the WE, and there are some characteristics that need to be considered such as: reproducibility, cost, availability, toxicity, potential window, and electrical conductivity.¹³⁷ One of the most widely used working electrodes in electroanalysis is carbon. Carbon electrodes are suitable for various sensing and detection applications because they have a demonstrated chemical inertness, a broad potential window, a low background current, and are inexpensive.¹³⁷

The two distinctive types of electroanalysis techniques are potentiometric and potentiostatic measurements. Both techniques measure the electrochemical process occurring at the electrode-solution interface. In this research, a potentiostat is used to study the charge transfer processes occurring at the interface by collecting a cyclic voltammetry (CV). CV consists of sweeping the potential of the working electrode between two limits, and measuring the resulting current.¹³⁷ As a result a cyclic voltammogram is obtained which plots the measured current versus the applied potential. While applying a voltage, charged molecules will move and orient themselves depending on their charge. For example, a negatively charged molecule will be attracted to the positively charged electrode, which can then allow for surface adsorption or electron transfer.¹⁴⁰

The electrical double layer model is used to describe the array of charged particles at the surface of an electrode.¹⁴⁰ A positively charged electrode will attract a layer of negative ions, and *vice versa*. This results in the formation of an electrical double layer. There have been many different models proposed to explain the electrical double layer at an electrified interface.¹⁴⁰ However, the model used by most researchers at present was

described by Bockris / Devanathan / Mueller in 1963.^{135,141} This model, referred to as the BDM model, describes the specific adsorption of ions and the role of solvent at the interface.¹⁴¹ This model takes into consideration the interaction between the electrode and dipolar solvents (i.e. water). The electrical double layer has a complex structure of several distinctive regions as shown in Figure 18. The first region to consider is the inner layer close to the electrode surface which is called the inner Helmholtz plane; this region contains solvent molecules and desolvated, adsorbed ions.¹⁴¹ The second region is the outer Helmholtz plane which is an imaginary plane that passes through the center of solvated ions that are non-specifically adsorbed.^{137,141} The third region which is beyond the compact layers is the diffuse layer which is a three-dimensional region of diffused solvated ions and solvent molecules.^{137,141} Depending on the ionic strength, the thickness of the double layer may extend more than 10 nm from the surface.^{137,141}

By changing parameters such as the electrode potential, the charge density and polarity of the surface, the charge can be changed. The potential at which the overall surface charge density is equal to zero is referred to as the potential of zero charge (pzc).¹⁴² If the electrode potential is more positive than the pzc, the surface will be positively charged, and hence negatively charged ions will interact preferentially with the surface.¹⁴² One of the simplest molecules to consider is water; when the surface is positively charged, water will orient itself such that the oxygen atom will interact with the surface. If the electrode potential is more negative than the pzc, the surface will have weaker affinity for anionic species and interaction with the oxygen atom of the water solvent will be weaker.¹⁴² In this case, a water molecule will orient itself such that the

hydrogen atoms will interact with the electrode surface, and cations will have a higher affinity as well.

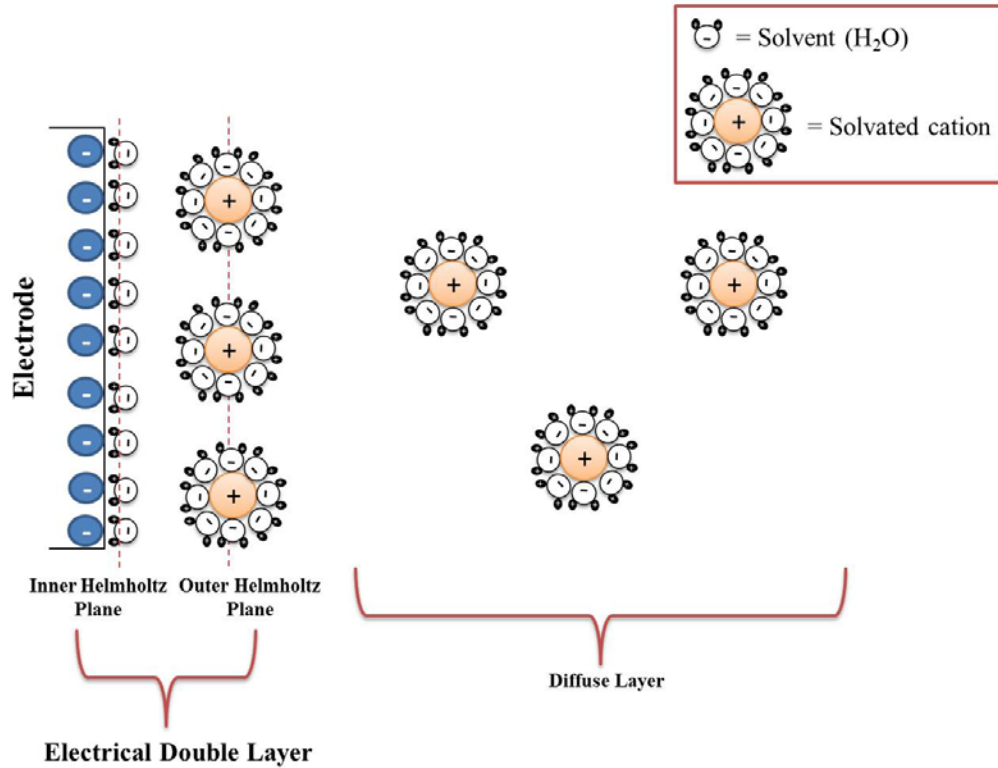


Figure 18: Illustration of the electrical double layer according to Bockris / Devanathan / Mueller model. Adapted from reference [141].

Due to the alternating charged layers, the electrical double layer resembles a parallel-plate capacitor.¹³⁷ The capacitance of a parallel-plate capacitor is described in equation 5:

$$C = \frac{k\epsilon_0 A}{d}$$

C = Capacitance
 k = Relative permittivity of the material separating the plates
 ϵ_0 = Permittivity of free space
 A = Area of plates
 d = Distance between plates

(5)

Capacitance is defined as the amount of stored charge a species can hold at an applied voltage. The charge is determined by the amount of current that flows at unit time.¹³⁷ Therefore, the capacitance of the electrical double layer describes the amount of current flow based on the applied voltage depending on unit time.¹³⁷ Equation 5 shows that capacitance is inversely proportional to the thickness between the plates.¹³⁷ This is a useful method to determine whether compact monolayers are formed at the surface of the electrode. Since capacitance is inversely proportional to the distance between the plates, one would expect that a compact layer on the surface will result in a measured decrease in the capacitance. There are certain factors that can affect the double layer capacitance such as the material and structure of electrodes, size and charge of ions, applied potential, and concentration of analyte ions in solution.¹⁴⁰ In this research, CV will be useful because it can provide information on the relative quality of the biomimetic membrane formed since the current vs. potential data can be used to obtain the differential capacitance as shown in equation 6.

$$C = \frac{dQ/dt}{dE/dt} = \frac{i}{\nu} \quad \boxed{\begin{array}{l} C = \text{Capacitance} \\ i = \text{current} \\ \nu = \text{scan rate} \end{array}} \quad (6)$$

3.3 Vibrational Spectroscopy

3.3.1 Raman spectroscopy

Raman spectroscopy is a form of vibrational spectroscopy based on the interaction between incident photons and a molecule. Specifically, Raman spectroscopy is based on the inelastic scattering, of incident monochromatic light. When source radiation is

focused onto a sample, the photons can be scattered either elastically or inelastically by the sample.¹⁴³ The source radiation has the ability to disturb the electron cloud which can be determined from the electron cloud polarizability.¹⁴⁴ The electron cloud in a chemical bond can oscillate due to electromagnetic radiation and cause light to be emitted, and this is what is called scattering in this thesis.¹⁴⁴ The energy of the incident light used to oscillate the electron cloud is completely given back in the emitted light.

As seen in Figure 19, there are three different types of scattering that can occur, which are referred to as Rayleigh, Stokes and anti-Stokes scattering. Rayleigh scattering, also known as elastic scattering, does not provide any vibrational information about the molecule because there is no net energy gain or loss.^{145,146} The molecule returns to the vibrational energy level from which it started and the emitted photons have the same energy and therefore the same wavelength as the initial photon. Stokes scattering is an inelastic scattering process which provides useful vibrational information about the analyte molecule.^{145,146} The molecule gains energy via the incident photons and is excited to a virtual energy state. A virtual energy state is not a stationary energy state, rather it is simply the distortion of the electron distribution of a covalent bond.¹⁴³ Once the molecule is excited it will relax back to a vibrational state higher than the ground state by emitting photons that have less energy, and therefore a longer wavelength, than the initial photon.¹⁴⁶ If the molecule is initially at an excited state it will reach a virtual energy state and fall back to the ground state whilst emitting photons that have a higher energy, and therefore a shorter wavelength, than the initial photon; this is referred to as anti-Stokes scattering.¹⁴⁶

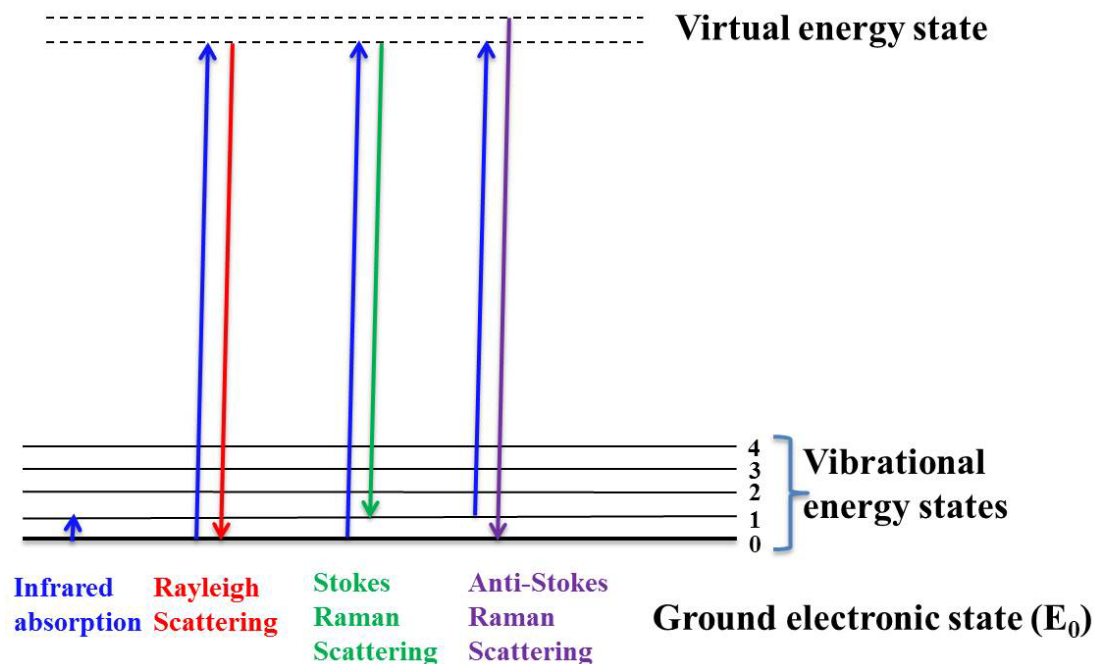


Figure 19: Diagram showing the energy-level diagram for: Infrared absorption, Rayleigh, Stokes, and anti-Stokes scattering. Adapted from reference [143].

Under typical experimental conditions molecules are mostly present in the ground state, and therefore Stokes Raman scattering is more probable and it is commonly what is measured in Raman spectroscopy. Since the intensity of the Raman scattering is not equivalent in all directions, a certain angle should be present between the incident source and the detector. Efficient Raman scattering can be obtained at 90° (right angle scattering) or 180° (back-scattering).¹⁴³ Each molecule will scatter light differently which provides a unique Raman signal for each sample component. The data obtained can be displayed as a plot of Raman scattering intensity versus wavelength. The x-axis in a Raman spectrum represents the difference between the excitation wavelength and the Raman wavelength expressed in wavenumbers ($\bar{\nu}$).¹⁴³ Wavenumbers are the reciprocal of

wavelength ($\bar{\nu} = 1/\lambda$) having units of cm^{-1} , which can also be expressed as a unit of energy, E as shown in equation 7:

$$E = h\nu = \frac{hc}{\lambda} = hc\bar{\nu}$$

<p>E = energy h = Planck's constant ν = Frequency of light c = Speed of light λ = Wavelength of light $\bar{\nu}$ = Wavenumber of light</p>	(7)
---	-----

The peaks observed in a Raman spectrum are a result of the photon interacting with the electron cloud and causing changes in the polarizability of the molecule, thus producing an induced dipole moment.¹⁴⁶ This is referred to as the Raman selection rule which determines whether certain vibrations are Raman active or inactive.¹⁴⁶ As shown in Figure 20, when an incident electric field (i.e. laser beam) is in contact with a molecule there is a distortion such that the nuclei and electrons are attracted to opposite poles.

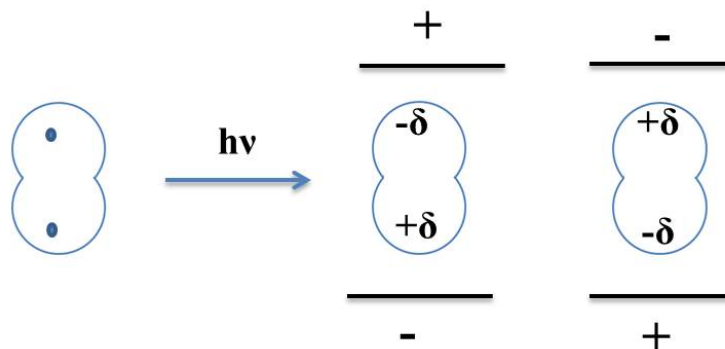


Figure 20: Polarization of a diatomic molecule in an electric field. Adapted from reference [146].

The induced dipole moment as a result of this charge separation can be represented by equation 8:

$$P = \alpha E \quad \boxed{\begin{array}{l} P = \text{Induced dipole moment} \\ \alpha = \text{polarizability} \\ E = \text{electric field} \end{array}} \quad (8)$$

This simple relationship does not hold for actual molecules because both P and E are vectors and consist of three components in x, y, and z directions, therefore equation 9 can be written in a matrix form as:

$$\begin{bmatrix} P_x \\ P_y \\ P_z \end{bmatrix} = \begin{bmatrix} \alpha_{xx} & \alpha_{xy} & \alpha_{xz} \\ \alpha_{yx} & \alpha_{yy} & \alpha_{yz} \\ \alpha_{zx} & \alpha_{zy} & \alpha_{zz} \end{bmatrix} \begin{bmatrix} E_x \\ E_y \\ E_z \end{bmatrix} \quad (9)$$

The right side of the matrix is referred to as the polarizability tensor, and any changes in this tensor during the vibration will be considered Raman-active.¹⁴⁶ The selection rule is not exclusive to Raman spectroscopy and can be applied to other spectroscopic techniques such as Infrared spectroscopy (IR).¹⁴⁶ IR is a vibrational technique that measures the absorption of infrared light by the sample. The selection rule of IR differs from Raman spectroscopy by the fact that vibrations are considered IR active if the dipole moment is changed during vibrations.¹⁴⁶ In some cases molecules would have some modes that are Raman active and IR inactive, and *vice versa*. This is dependent on the symmetry of the molecule; vibrations that are symmetric with respect to the centre of symmetry are Raman-active, and vibrations that are antisymmetric with respect to the centre of symmetry are IR-active.¹⁴⁶ This is referred to as the rule of mutual exclusion which states that in centrosymmetric molecules a vibrational mode may be either IR active

or Raman active.¹⁴⁶ Molecules can be characterized using these two techniques in order to observe different vibrational modes.

Raman spectroscopy offers many advantages compared to IR. One of the main advantages is that water molecules are weak scatterers which is very useful when analysing biological samples that are prepared in aqueous solutions since water will not interfere.¹⁴⁷ Also, carbon dioxide, glass, and alcohols are weak Raman scatters and therefore cause less interference with the analyte signal compared to IR. The use of a small diameter laser beam (1-2 mm) allows for small sample analysis, which is a great advantage over IR which has typical spot sizes of mm to cm.¹⁴⁷ Other advantages include the simplicity in obtaining a Raman spectrum, minimal sample preparation and modification required, it is non-destructive, and it offers rapid analysis time, and portable, hand-held instrumentation is widely available.^{144,147,148} Disadvantages of Raman spectroscopy include the use of a powerful laser source which can cause photodecomposition of the sample. However, reducing the laser power can often resolve this issue.¹⁴⁶ Also, some compounds fluoresce when irradiated by the energetic laser beam, resulting in a significant background.¹⁴³ The main disadvantage of Raman spectroscopy is that the Raman Stokes scattering is relatively weak, and only a small amount of the light is scattered inelastically.¹⁴⁹ Usually only one in a million photons undergo inelastic scattering.¹⁴⁹ As a consequence only strongly scattering molecules present as bulk solids, liquids, or gases exhibit useful normal Raman spectra. Some of these disadvantages can be overcome by using surface-enhanced Raman spectroscopy (SERS) which is a variation of normal Raman spectroscopy.

3.3.2 Surface-Enhanced Raman Spectroscopy (SERS)

In 1974 Fleischmann *et al.* showed that pyridine and other molecules exhibit an enhancement of their Raman signal when adsorbed onto electrochemically roughened silver.¹⁵⁰ After this observation, Van Duyne and Jeanmaire examined some factors that would affect the intensity of the Raman signal, such as surface roughness, effect of applied potential, solution analyte concentration, and electrolyte composition of the solution.¹⁵¹ This analysis showed that molecules present on the surface of a nanostructured coinage metal surface can exhibit an extraordinary enhancement of their Raman signal.¹⁵² This phenomenon is referred to as surface-enhanced Raman spectroscopy (SERS) which is a selective and sensitive technique which can increase the Raman signal of an analyte by 4 to 11 orders of magnitude.¹⁵³ The contribution of this enhancement is still under debate but it can at present be related to two mechanisms a) a chemical enhancement mechanism (minor contribution) and b) an electromagnetic enhancement mechanism (major contribution).^{153,154}

Chemical enhancement is due to charge transfer between the chemisorbed molecule and the metal surface and contributes up to 2 orders of magnitude to the observed enhancement signal.¹⁵³⁻¹⁵⁵ The electron coupling between the analyte and the metal has the ability to change the polarizability of the molecule and form a surface species that acts as a resonant intermediate in Raman scattering.^{155,156} This mechanism varies between substrates, adsorbed molecules, and substrate adsorption sites.¹⁵³ In order to achieve this enhancement the molecules should be directly adsorbed on the metal surface.

Electromagnetic enhancement is a wavelength-dependent effect that contributes up to 4-10 orders of magnitude in terms of signal enhancement.^{154,157} This primarily arises from the collective oscillation of conduction electrons when an electric field (i.e. incident electromagnetic radiation of a laser) interacts with nano-structured metallic surfaces. The collective oscillation of free electrons in the metal is termed the localized surface plasmon resonance (LSPR).^{154,158,159} The LSPR is dependent on the size, shape, nanometric roughness, and the material of the nanostructured surface.¹⁵⁵ As shown in Figure 21, LSPR occurs in nano-structures that are smaller in all dimensions than the wavelength of incident light which will cause the free electrons in the metal to collectively oscillate in resonance with the electric field whereas the positively charged metallic nuclei remain fixed.^{155,159}

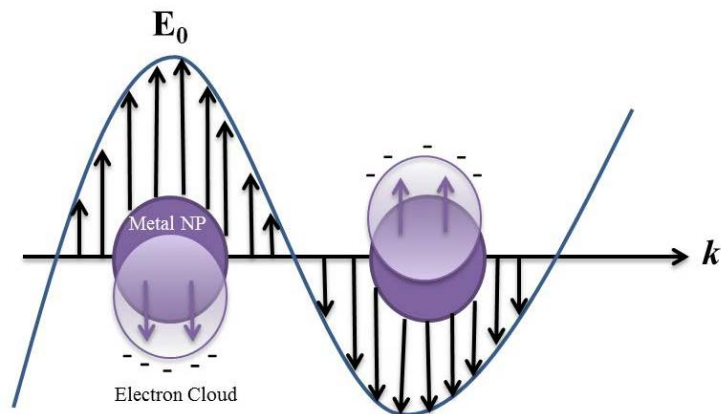


Figure 21: Schematic illustration of localized surface plasmon resonance on metal nanospheres. Adapted from reference [154].

The electromagnetic enhancement does not require the analyte to be in direct contact with the surface but it does have to be within a certain sensing range.¹⁵³ Studies have shown that the electromagnetic enhancement decreases as the distance between the analyte and metal surface increases; this is due to the localization of the LSPR on the metal surface.^{153,154} According to literature, the ideal distance for SERS detection is within 2-4 nm of the nanoscale roughness feature.¹⁵³ In many cases SERS studies are performed on molecules containing a thiol or amine group which can allow the molecule to chemisorb onto the metal surface in order to achieve maximum SERS intensity.¹⁵³ Also, the intensity can vary depending on the orientation of these molecules and the tensor symmetry with respect to the surface. Moskovits has developed the concept of surface selection rules that discusses the local field polarizations of the molecule and its connection with increasing the observed SERS intensity.¹⁶⁰ This concept suggests that the local field polarizations should be perpendicular to the metal substrate in order to achieve the maximum SERS intensity, whereas polarizability tensors that are parallel to the metal substrate will result in a weaker SERS intensity.¹⁶¹ In other words, the vibrational bands that have contribution from the Raman polarizability tensor component α_{zz} , where z is the surface normal, will be more intense than contributions from α_{xz} and α_{yz} . This is essentially because the electric field of the exciting light is enhanced in the direction of the surface normal.^{83,162}

One of the most important aspects regarding SERS enhancement is choosing the appropriate metal substrate with the right size and shape. Coinage metal nanoparticles have been increasingly used due to their unique chemical, physical, optical and electronic

properties, and ease of production.¹⁶² Nanoparticles (NPs) have been used in a variety of different fields such as chemistry, physics, biology, nanotechnology, material science, medicine, computer science, and engineering.¹⁶³ Different metals such as aluminium, gold, silver, copper, palladium, and platinum have been used for different applications depending on their plasmonic properties.¹⁶⁴ The most commonly used metals for SERS substrates are gold (Au) and silver (Ag) since they have good plasmonic properties in the visible region and are relatively inert. Although AuNPs are very stable, biocompatible, and different shapes can be readily achieved, they are relatively expensive to make and provide strong plasmon resonance only for wavelengths longer than 500 nm which can limit their application.¹⁶⁴ On the other hand, even though AgNPs have biocompatibility issues and can be prone to oxidation they have the highest plasmon resonance effect over the widest wavelength range (300-1200 nm).¹⁶⁴ There are other advantages that make Ag a good metal candidate such as having the highest electrical and thermal conductivity of plasmonic metals, it is relatively cheap, and exhibits a demonstrated ease of making different nanostructures with controllable size and shape.¹⁶⁴

There are many methods used to prepare different shapes of nanoparticles such as spheres, cubes, triangles, rods, and hollow structures.¹⁶⁵ Even though these methods provide interesting nano-structures, they might not be SERS-active. In this research, all the experiments conducted were done on spherical AgNPs. The first SERS experiment performed on spherical AgNPs was conducted by Creighton in 1979.¹⁶⁵ There are many syntheses used to prepare these spherical AgNPs, one of the simplest procedures for synthesis that does not require extensive laboratory reagents or equipment is the citrate

reduction method by Lee and Meisel.¹⁶⁶ This method was reported in 1982, and involves the use of citrate to reduce Ag^+ to metallic Ag colloids.^{166,167} One of the disadvantages of this synthesis is that it provides a variety of colloidal sizes ranging between 20-600 nm with relatively poor shape control, therefore other synthetic strategies such as seed-mediated growth can be used to produce more monodisperse samples.¹⁶⁴

Since all SERS substrates are metallic, they can also function as the working electrode in an electrochemical cell. Coupling SERS with electrochemistry is referred to as electrochemical SERS (EC-SERS). This technique is used to detect the signal of the analyte present on the metal surface at a chosen applied voltage. Electrochemical SERS can be useful in detecting the signal of the analyte in relevant biological environments, and to observe potential-dependent changes in the conformation or orientation of an analyte.¹²⁸ It can also be used to monitor the electrochemical stability of certain analytes at metal surfaces. Changing the voltage can have an effect on the chemical and electromagnetic enhancement by altering the Fermi level of the metal and dielectric constant of interfacial electrolyte.¹⁴¹

EC-SERS is considered one of the most complicated SERS systems due to the changes occurring on the electrode surface in the presence of applied potential. However, this technique can provide a lot of useful information about the orientation, conformation, and the behaviour of molecules at the metal / electrolyte interface. There have been some studies in literature showing the diverse application of EC-SERS in detecting and characterizing DNA aptamers,¹⁶⁸ alkanethiol SAMs,¹⁶⁹ bovine insulin,¹⁷⁰ and bilayer lipid

membranes.¹²⁸ The work presented here will focus on studying the interaction of proteins with a biomimetic membrane using EC-SERS, as well as other techniques.

3.3.3 Attenuated Total Reflectance-Fourier Transform Infrared Spectroscopy (ATR-FTIR)

ATR-FTIR is a variation of IR spectroscopy designed to reduce water absorption interference and has been used since the early 1970's to investigate biological systems, such as proteins.¹⁷⁴ Some of the advantages of using ATR-FTIR for protein analysis includes minimal sample requirement, little to no sample preparation is required, fast sampling time, no probe or dye molecule is needed, and analysis can be done in an aqueous environment.^{174,175} ATR-FTIR operates by measuring the changes that occur in a totally internally reflected IR beam, as shown in Figure 22. The IR beam is directed onto a crystal with a high refractive index such as zinc selenide, germanium, or diamond.¹⁷⁵ The internal reflectance creates an evanescent wave that extends beyond the crystal surface only a few microns (0.5-5 μm) and interacts with the sample present directly on the crystal surface.¹⁷⁴⁻¹⁷⁶ The sample is placed directly on the crystal, and as the sample absorbs energy, the evanescent wave will be attenuated (weakened) before passing to the detector.¹⁷⁴⁻¹⁷⁶

In order to achieve optimal results using ATR-FTIR two requirements must be met. First, the sample must be in direct contact with the ATR crystal because the evanescent wave will only extend a few microns through the sample. Second, the refractive index of the crystal must be significantly greater than that of the sample in

order for internal reflectance to occur.¹⁷⁴⁻¹⁷⁶ ATR-FTIR has been widely used to analyze a wide variety of materials such as fiber, glass, paint, and also biological components such as lipid, proteins, cells, and tissues.¹⁷⁴⁻¹⁷⁶

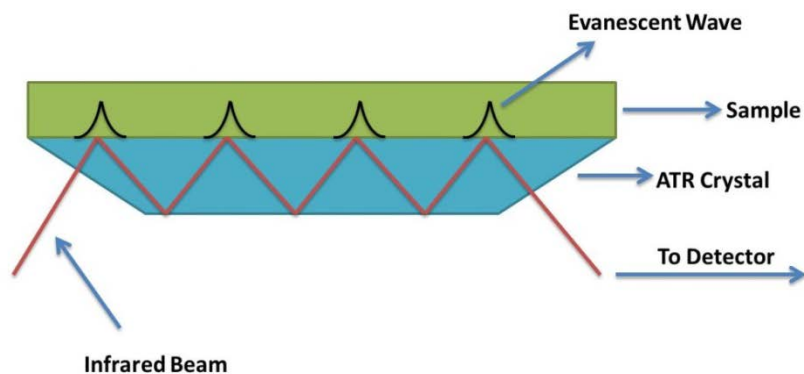


Figure 22: Schematic diagram of a typical attenuated total reflectance (ATR) system. Adapted from reference [176].

3.4 Electron Microscopy

3.4.1 Transmission Electron Microscopy (TEM)

Electron microscopes were developed to overcome the limited image resolution of light microscopes, which is imposed by the wavelength of visible light.¹⁷⁷ In 1925, the first theory stating that electrons had wave-like characteristics with a wavelength substantially less than visible light was developed by Louis de Broglie.¹⁷⁷ This allowed the development of the first electron microscope in 1932 by Knoll and Ruska.¹⁷⁷ Later on, transmission electron microscopy (TEM) were commercially developed and became widely available. Since the initial discovery of TEM, significant developments have led to major improvements such as using digital technology for high sensitivity images, use

of vibration isolation, high voltage stability, and electronic and mechanical stability.¹⁷⁷ The basic imaging arrangement of TEM involves the use of an electron gun to produce an electron beam that interacts with the sample. The electron beam is focused using a series of lenses prior to reaching the sample. A TEM image is then produced by magnifying lenses. TEM requires high vacuum in order for the electrons to interact with sample to obtain good quality images. Figure 23 shows a schematic illustration of the TEM components.

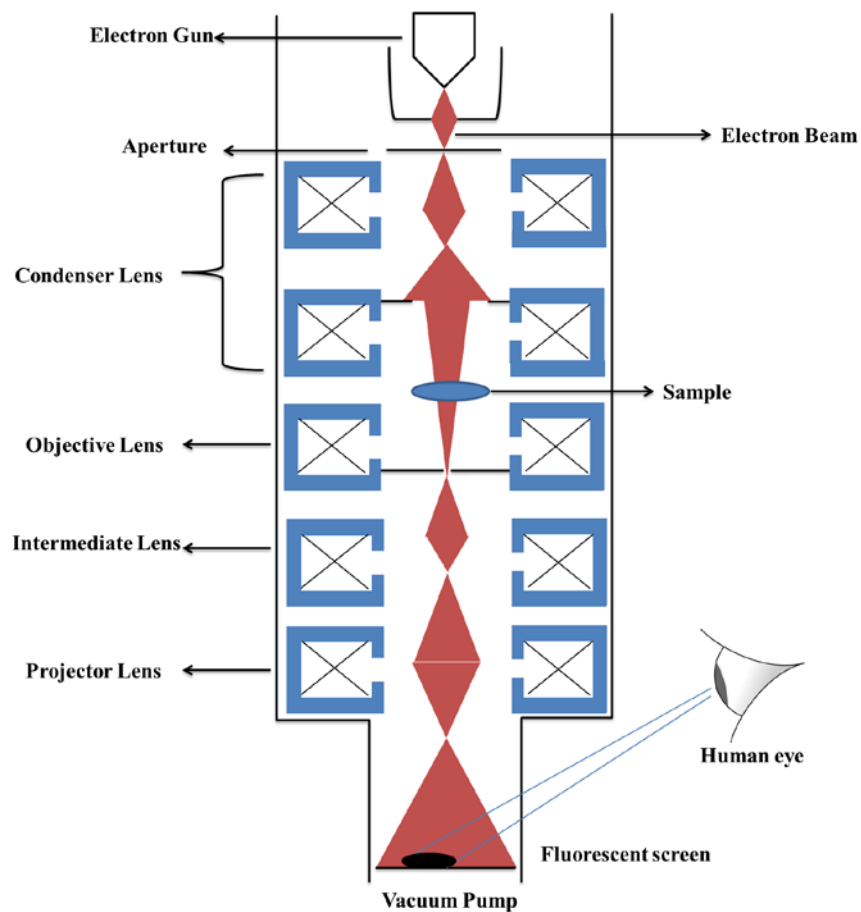


Figure 23: Schematic diagram of transmission electron microscopy (TEM) system. Adapted from reference [179].

The illumination system consists of the electron gun which is located in the upper portion of the electron column in the microscope. The purpose of the electron gun is to generate a fine, focused electron beam to probe the surface.¹⁷⁸⁻¹⁸⁰ There are three different electron guns that are widely used to produce the electron beam which includes thermionic emission, field-emission, and Schottky-emission.¹⁷⁸⁻¹⁸⁰ The diameter of the electron beam is focused by placing a series of different lenses below the electron gun. Condenser lenses are present along the column and their role is demagnification of the electron beam.¹⁷⁸⁻¹⁸⁰ The design and operation of condenser lenses determines the diameter of the electron beam at the sample and the intensity level in the final TEM image. The sample stage is where the sample can be held and inserted or withdrawn from the TEM. The mechanical stability of the sample stage plays a role in determining the spatial resolution of the TEM image.^{179,180} The imaging system contains three lenses that together produce a magnified image of the sample on either a fluorescent screen, on photographic film, or on the monitor screen of an electronic camera system.^{179,180} The three lenses present are the objective lens, intermediate lens, and projector lens. The objective lens is the most important lens in TEM because it is the closest to the sample which is used primarily to focus and magnify the image.^{179,180} The intermediate lens magnifies the image coming from the objective lens. The projector lens further magnifies the image and projects it onto the fluorescent screen to produce an image.¹⁸⁰ The design of all the imaging lenses determines the spatial resolution that can be obtained using TEM.¹⁸⁰ The electron image is then converted to a visible form using a fluorescent screen. A fluorescent molecule is chosen so that light is emitted in the yellow-green region which

is sensitive to the human eye. In order to save the image a charged-coupled diode (CCD) camera is used.¹⁸⁰

TEM has been widely used in different fields such as life sciences, nanotechnology, medical, biological and material research, and industry. TEM has been used to examine the ultrastructure of metals, plant and animal tissues, bacteria, and viruses.¹⁷⁸⁻¹⁸¹ Although TEM demonstrates exceptional resolution (i.e. 0.2 nm) one of the major limitations of TEM is that the sample has to be very thin in order for the electrons to be transmitted.¹⁸¹ If the sample is too thick the electrons are strongly scattered or absorbed and TEM images cannot be acquired.¹⁸¹ This constraint has provided the incentive to develop electron microscopes that have the ability to examine relatively thick samples. This was achieved by the development of scanning electron microscopy.

3.4.2 Scanning Electron Microscopy (SEM)

Scanning electron microscopy (SEM) is a method used to characterize organic and inorganic materials on the nanometer to micrometer scale. The first commercial SEM appeared in the early 1960s, and the design of the SEM has been constantly evolving and improving since then.¹⁸² One of the main advances made was the development of different types of electron sources such as high-brightness and field emission sources.¹⁸² SEM is one of the most versatile instruments due to its capability in obtaining three-dimensional images of the topography and morphology of a sample.¹⁸³ One of the main advantages of SEM includes fast data acquisition, ease of operation, high resolution, minimal sample preparation, small sample requirement, rapid acquisition time, and large

depth of field.¹⁸³ Figure 24 shows a schematic drawing of a typical SEM. The basic theory of SEM involves scanning a high energy focused beam of electrons over the sample in order to produce an image.¹⁸²⁻¹⁸⁴

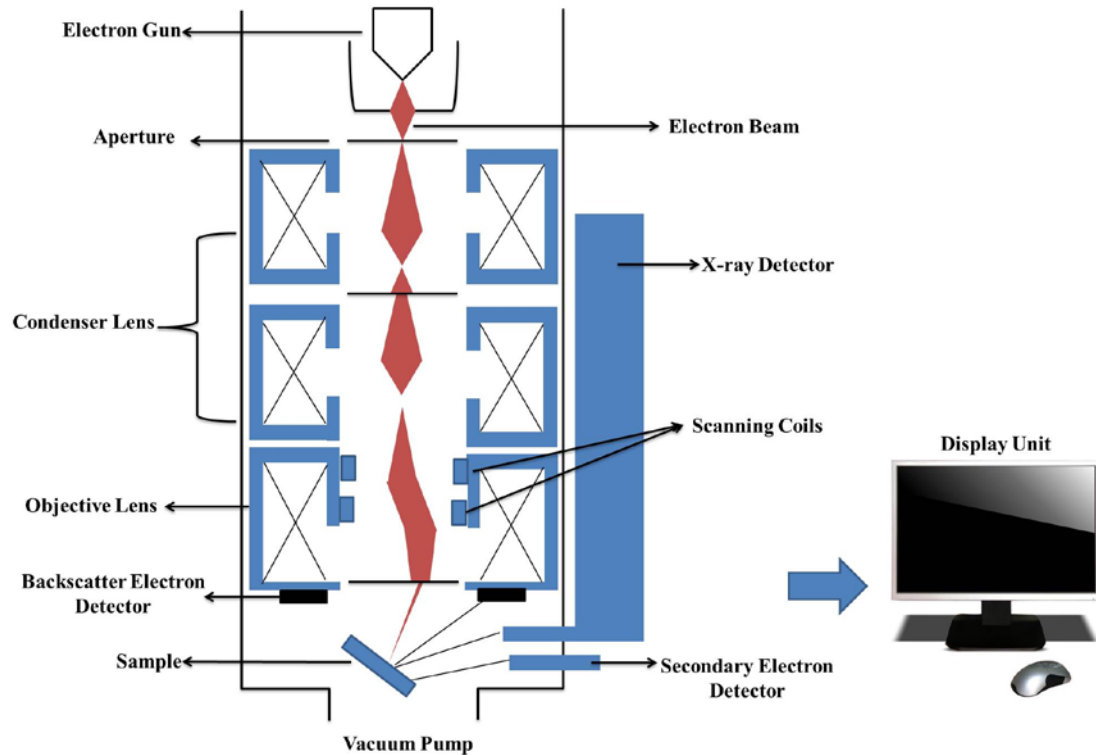


Figure 24: Schematic diagram of scanning electron microscopy (SEM) system. Adapted from reference [184].

The SEM column consists of the following main components: an electron gun, two condenser lenses, an objective lens, beam scanning coils, large sample chamber with a stage, and electron detection system, all operating in vacuum.¹⁸⁴ The chamber is kept at a high vacuum of about 10^{-3} to 10^{-4} Pa.¹⁸⁴ Most of the SEM components are very similar to the TEM components. SEM does not include a sample stage after the condenser

lenses. The condenser lenses produce a fine electron beam that can pass through the aperture.¹⁸¹⁻¹⁸⁶ There are several apertures present along the column which allow a part of the electron beam to reach the objective lens. The objective lens is very important in determining the final diameter of the electron beam and plays a major role in focusing the fine electron beam on the sample.¹⁸⁶ Slightly above the objective lens, a set of double-deflection coils are located to deflect the beam in opposite directions allowing the electron beam to scan across the sample.¹⁸⁶ The scan coils ensure that the beam is always passing through the optic axis of the objective lens.¹⁸⁴⁻¹⁸⁶ As the fine electron beam interacts with the sample, it can penetrate into the sample up to 1.0 μm . The sample analysed using SEM must be electrically conductive, or an ultrathin coating of metal can be applied onto non-conducting samples.¹⁸⁶ Upon interaction with the sample various types of scattered signal are generated and detected using electron detectors.¹⁸¹⁻¹⁸⁴ The two main detectors used in SEM are a secondary electron detector and a back scattered detector.¹⁸⁴⁻¹⁸⁶ The secondary electron detectors detects small energy beam which allows the observation of the topography of the sample surface. Also, SEM can be equipped with energy-dispersive X-ray spectroscopy (EDS) that detects the beam scattered as X-ray radiation.¹⁸⁴⁻¹⁸⁶ EDS is used to identify the elemental composition of the sample.¹⁸⁴⁻¹⁸⁶ The detected beam is then used to create images of the distribution of the sample using liquid-crystal screens.

SEM is a versatile tool and it has been used in different fields such as chemistry, biology, geology, forensic science, medical science, and material science. SEM has been used widely in chemistry to analyse the shape and size of nanoparticles and also to

determine their composition.^{168,187,188} Also, SEM has been used for different application such as examining metal fragments,¹⁸⁹ paint,¹⁹⁰ soils and rocks,¹⁹¹ and biological samples such as large and small insects,¹⁹² animal tissues,¹⁹³ proteins,¹⁹⁴ bacteria and viruses.¹⁹⁵

Chapter 4: Experimental

4.1 Reagents

Prior to use all glassware was immersed in an acid bath of sulfuric acid (Fisher Scientific, 95-98% ACS grade, NJ, U.S.A.) for several hours and rinsed thoroughly with ultra-pure water ($>18.2 \text{ M}\Omega \text{ cm}$) from a Milli-Q plus system (Millipore, California, U.S.A.). Millipore water was also used to prepare all solutions. Trisodium citrate ($>99\%$), 2'-Deoxyadenosine 5'-monophosphate (dAMP, 98-100%), sodium fluoride ($>99\%$), 6-mercaptohexanoic acid (6-MHA, 90%), and recombinant human insulin (98-100%) were all purchased from Sigma-Aldrich (St. Louis, MO, U.S.A.). Silver nitrate (99.9995%) was purchased from Alfa Aesar (Wardhill, MA, U.S.A.). Cholesterol (98%) and 1,2-Dimyristoyl-*sn*-glycero-3-phosphocholine (DMPC, 99%) were purchased from Avanti Polar Lipids (Alabaster, Alabama, U.S.A.). Chloroform was purchased from Caledon, HPLC grade (Georgetown, Ontario, Canada). Sodium chloride ($>99\%$) and potassium chloride ($>99\%$) were purchased from Chimiques ACP Chemicals (Saint-Léonard, QC, Canada). Ethyl alcohol (95%) was purchased from Commercial Alcohols (Brampton, Ontario, Canada).

4.2 Nanoparticle synthesis and characterization

A modified Lee and Meisel method was used to prepare citrate reduced silver colloids.¹⁶⁶ First, 0.09 g of silver nitrate was added to 500.0 mL of Millipore water and brought to a vigorous boil in a covered beaker with stirring. Next, 10.0 mL of a 1 % w/w trisodium citrate was added to reduce the silver, and the reaction mixture was left to

boil for exactly 30 minutes. The reaction mixture was then removed from heat and allowed to cool at room temperature. After cooling, a 1.0 mL aliquot of the colloidal nanoparticle sol was placed in Eppendorf tubes and centrifuged for 15 minutes at 3600 rpm (VWR Galaxy Analog Microcentrifuge, VWR International, Ontario, Canada) to concentrate and aggregate the colloids. After each round the supernatant was carefully removed, and a fresh aliquot of the colloidal sol was added. This procedure was repeated 10 times. After the tenth cycle, the supernatant was discarded and the resulting pellet, consisting of a nanoparticle paste, was applied to the working electrode surface of a carbon screen printed electrode (SPE) (Pine Research Instrumentation, CA, U.S.A.). The produced silver colloids have a peak absorption wavelength of ~420 nm and a full width at half maximum of ~100 nm. This reaction is photosensitive therefore the nanoparticle synthesis is conducted in the dark.

4.3 Construction of silver nanoparticle electrodes

Carbon screen printed electrodes (SPEs) (15 x 61 x 0.36 mm) were purchased from Pine Research Instrumentation (Durham, NC, U.S.A.). These SPEs consist of a silver/silver chloride (Ag / AgCl) reference electrode, a carbon counter electrode, and carbon working electrode. The SPEs were functionalized by depositing three 5.0 μ L layers of the concentrated silver nanoparticle (AgNP) paste onto the carbon working electrode (5 x 4 mm) using a micropipette as described above. The electrodes were left to dry completely in air between deposition of the AgNP layers, and the final layer was allowed to dry completely before the electrode was used.

4.4 Preparation of alkanethiol, dAMP, lipid, and insulin solution

The 6-MHA was used as a self-assembled monolayer to avoid direct contact between the lipid molecules and substrate. The 6-MHA was stored in the freezer at -20 °C; prior to any experiments the 6-MHA was taken out of the freezer and left to thaw for several minutes. After the solution had thawed, 14.0 µL was added to a 100.0 mL volumetric flask and made up to the mark with ethanol (Commercial Alcohols, 95%, Brampton, Ontario, Canada) to make a 1.0 mM solution of 6-MHA. The solution was then stored at room temperature in the fumehood prior to use.

A DNA nucleotide, 2'-deoxyadenosine 5'-monophosphate (dAMP) was used as the probe molecule throughout these experiments. 1.0 mM dAMP prepared in 0.1 M NaF was used as the supporting electrolyte for the majority of the EC-SERS studies. The solution was stored at room temperature and was purged with argon gas for 10 minutes prior to use.

The membrane components chosen for this research were 1,2-Dimyristoyl-*sn*-glycero-3-phosphocholine (DMPC) and cholesterol. A concentration of 2.0 mg / mL of 70:30 molar ratio of DMPC: cholesterol was prepared in chloroform.^{106,196} The solution was stored in the freezer at -20 °C and allowed to come to room temperature prior to use.

Recombinant human insulin powder was stored in the freezer at -20 °C. Insulin was prepared as an aqueous solution containing both 0.58 g of 0.1 M NaCl and 205.0 µL of 12 M HCl. The solution was prepared in water, and the pH was adjusted to 1.6 using 10 mM NaOH.¹⁹⁷⁻¹⁹⁹ The solution was always prepared fresh and stored in the fridge.

Insulin solution was prepared with the above aqueous solution to make up a concentration of 2.0 mg / mL.

4.5 Preparation of the alkanethiol self-assembled monolayer

In order to form a compact self-assembled monolayer on the electrode surface, the AgNP SPEs were immersed in a 1.0 mM ethanolic solution of 6-mercaptohexanoic acid for 2 hours. The electrodes were then rinsed gently with ethanol to remove any excess of 6-MHA that was not adsorbed on the surface. The electrodes were then left to air dry for several minutes prior to conducting experiments.

4.6 Aggregation of insulin protein and capturing protofibrils for BLM studies

The human insulin solution was aggregated under accelerated conditions at a pH of 1.6 and an elevated temperature of 65 °C using a water bath. The insulin solution was added to a vial and immersed in a water bath for 5 hours. As the insulin aggregated, the solution changed from a clear transparent solution to very cloudy (turbid) solution. At different stages of the aggregation (oligomers and protofibrils) the solution was taken out of the water bath and placed briefly in the freezer to cool and then it was used for membrane incubation studies. The SPE containing the deposited lipid bilayer was immersed in the insulin solution for 1 hour with slow stirring. The SPE was then taken out of the insulin solution and left to air dry prior to performing EC-SERS measurements.

4.7 Langmuir-Blodgett / Langmuir-Schaefer (LB / LS) deposition

4.7.1 Instrumentation

The formation of lipid monolayers at the air-water interface was accomplished using a KSV NIMA Langmuir-Blodgett Trough and its accompanying software (Biolin Scientific, Finland). This instrument is positioned on top of a 6.50 cm thick marble slab in order to reduce vibrations and to improve the quality of measurements. Surface pressure measurements were obtained by hanging a 10 mm wide (20.6 mm perimeter) Whatman #1 filter paper functioning as the Wilhelmy plate from the microbalance, and subphase temperatures were controlled by a Lauda K-2/R circulating water bath (Brinkmann Instruments, NJ, U.S.A.) attached to the trough. The subphase temperature was measured using a temperature probe that was immersed in the water during the experiment. In order to have precise control over immersion of the solid substrate, a dipping arm is used that can be automatically controlled. Figure 25 shows a representation of the Langmuir Blodgett system and its main components.

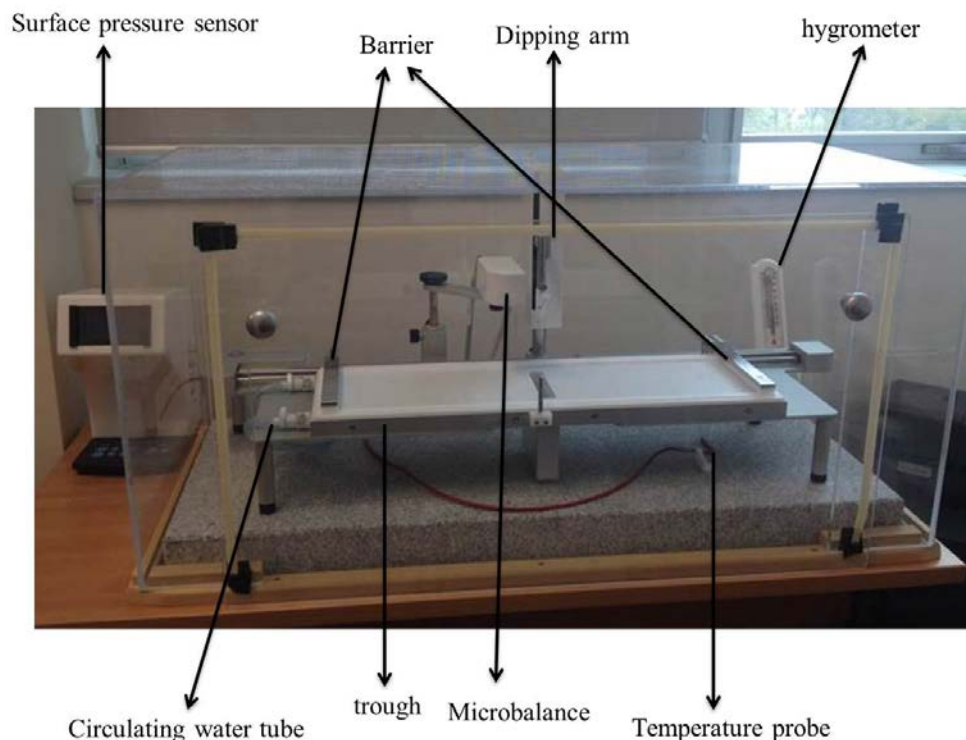


Figure 25: The Langmuir trough and its main components.

4.7.2 Formation of bilayer lipid membranes

The Teflon® trough and Delrin® hydrophilic barriers were cleaned with ethanol and rinsed thoroughly with Millipore water. The trough was then filled with Millipore water (~750 mL), the Wilhelmy plate was hung, and the temperature probe was immersed in the water while avoiding contact with the trough. After the trough was filled with the subphase, the surface was cleaned by gentle vacuum suction. 40 μL of lipid solution was carefully deposited dropwise via a Hamilton syringe over the water surface. After 30 minutes (allotted time for chloroform evaporation) the lipid components were compressed at the air-water interface at a rate of 5 mm / min until a surface pressure of 40 mN / m was attained.^{106,196} This surface pressure value was selected as the pressure to ensure a

condensed phase as was derived from the predetermined collapse pressure (50 mN / m) of the DMPC / cholesterol 70:30 mixture from a compression isotherm (Figure 17). The transfer of lipid molecules onto a AgNP modified SPE was done at a subphase temperature of 30 °C. The temperature was controlled through use of a circulating water bath. Also, all transfers were conducted at relatively high humidity (90% RH); this was done by placing a 250 mL beaker containing boiled Millipore water inside the Langmuir enclosure after depositing the lipid monolayers.¹⁹⁶ The humidity was measured using a hygrometer (Bios Weather, Markham, Canada). The first monolayer leaflet was added to the AgNP modified SPE using the LB technique, where the SPE was immersed in the water prior to adding any lipid molecules. The compressed lipid molecules were transferred onto the AgNP substrate by the Langmuir Blodgett technique. The second monolayer leaflet was then transferred by the LS horizontal touch method to the AgNP modified SPE containing the LB lipid monolayer leaflet. The SPE was then left to dry overnight in a closed glass chamber containing 50 mL of boiled water. This humid environment allowed for a slow drying of the monolayer in order to reduce defects.¹⁸⁴

The deposition of the lipid bilayer on the AgNP modified SPE was completed in two consecutive days. This was done to ensure slow and complete drying of each layer. Analysis of EC-SERS and CV measurements for the lipid bilayer was completed the day after the formation of the second monolayer leaflet. In the case of the addition of human insulin to the lipid bilayers, the day after the formation of the second leaflet the SPEs were incubated in insulin solution and EC-SERS and CV measurements were conducted on the same day.

4.8 Raman Spectroscopy

All Raman experiments in this research were conducted using a DXR Smart Raman Spectrometer (Thermo Fisher Scientific, Mississauga, ON, Canada). This spectrometer is equipped with two different laser excitation wavelengths (532 nm and 780 nm). This spectrometer can be fitted with two different gratings, a full range, low resolution (5 cm^{-1}) grating, and a shorter range, high resolution (3 cm^{-1}) grating. The spectrometer has a $10\text{ }\mu\text{m}$ diameter laser spot size, and is equipped with a ($25\text{-}50\text{ }\mu\text{m}$) aperture slit and an air-cooled CCD detector. In this research, 532 nm was used for all the experiments and in order to reduce the possible degradation of biological components, the laser power was kept below 5 mW. The collection exposure time was adjusted to 30 seconds, where a final spectrum represented the average of 30 spectra. For spectral processing and data analysis, the software program Origin 8.1 (OriginLab Corporation, Northampton, MA, U.S.A.) was used on a standard PC. All data measured were corrected for acquisition time and laser power, and also smoothed using the adjacent-averaging smoothing method of 10 points.

4.9 Electrochemistry

A Pine Research Instrumentation portable USB Wavenow potentiostat / galvanostat (Durham, NC, U.S.A.) was used for conducting electrochemical measurements. The electrochemical software was Aftermath Data Organizer (version 1.2.4843) produced by Pine Research Instrumentation.

4.9.1 Electrochemical surface-enhanced Raman spectroscopy

For spectroelectrochemistry (EC-SERS), the applied potential ranged from 0.0 V to -1.0 V in increments of 0.1 V for a time interval of 60 seconds. Positive voltages were avoided in order to prevent oxidation of the silver surface. The voltage was stepped first in the cathodic direction (0.0 V to -1.0 V) in 100 mV increments, and then returned in the anodic direction (-1.0 V to 0.0 V).¹⁶⁸ At each potential step the SERS spectrum was recorded. The voltammetry cell, also from Pine Research Instrumentation, was used as the spectroelectrochemical cell. The cell design consists of a modified glass vial (2 x 4.5 x 0.6 cm) and a special mini USB adapter that is made to fit the SPEs. A photograph of the electrochemical set-up is shown in Figure 26. All potentials are reported versus the Ag / AgCl reference electrode, unless otherwise indicated.

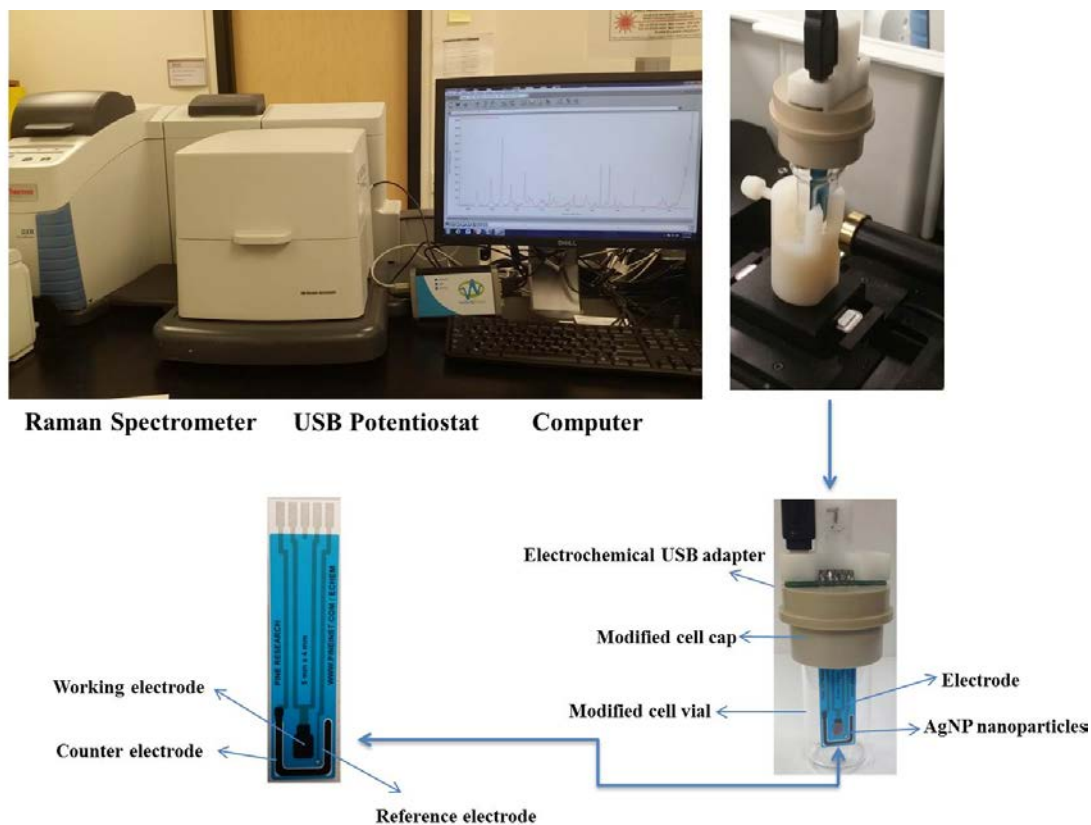


Figure 26: The EC-SERS set-up.

For most of the experiments, the analyte of interest was immobilized on the AgNP electrode, and 0.1 M NaF solution was used as the electrolyte. For EC-SERS, these electrodes were placed in the special adapter for the cell vial that connects to the USB potentiostat. The electrodes were then analysed in air using the Raman spectrometer to ensure that they were at the focal point of the laser before the electrolyte was added. Once focused, the Raman spectral analysis and the potentials were applied concurrently, acquiring the spectrum for one minute at each applied potential.

4.9.2 Cyclic voltammetry

Cyclic Voltammetry (CV) was conducted at the end of each experiment to assess film quality and probe redox behaviour. The CV parameters used were the same for all experiments; the initial and upper potential was set to 0.0 V, the sweep rate was set to 50 mV / s, a lower potential limit of -1.0 V was used, and the number of segments was set to 10.

4.10 Turbidity measurements

A turbidity sensor from Vernier (Vernier Software & Technology, Beaverton, Oregon, U.S.A.) was used to monitor insulin aggregation. This sensor has the capability to measure turbidity from 0 to 200 nephelometric turbidity units (NTU) with a resolution of 0.25 NTU. The accuracy for readings that are less than 25 NTU is 2 NTU, and above 25 NTU is 5 NTU. It is equipped with a LED wavelength of 890 nm, and the standard solution used for calibration is stableCal formazin standard 100 NTU. This solution contains (1.0-10.0%) of hexamethylenetetramine, (90.0-100.0%) demineralized water, and (<0.1%) formazin polymer. The turbidity sensor is connected to a HP laptop by a Go Link interface, and Logger ProTM software was used to collect data.

Recombinant human insulin solution (pH 1.6) was added to a clean vial with a small stir bar, and added to the water bath (65 °C). Every 15 minutes the vial was taken out of the water bath, wiped well with Kimwipes[®] and placed in the turbidity sensor with stirring. Once the value of the turbidity was stable, the data was collected using Logger ProTM.

4.11 Transmission and scanning electron microscopy

Transmission electron microscopy (TEM) images were acquired using a FEI TechaniTM 12 electron microscope (Hillsboro, Oregon, U.S.A.). The TEM images were conducted using 80 kV and magnification up to 60 kX. It is equipped with a Gatan 832 SC1000 11M pixels (4008 x 2672) CCD camera.

TEM images were obtained at different stages during the aggregation process of recombinant human insulin protein. The times chosen were 0, 45, 60, 75, 135, and 240 minutes. At the allotted time, a small amount (~ 50 μ L) of the sample was removed from the reaction vial and deposited onto a 200 mesh copper grid coated with a carbon film (Electron Microscopy Sciences, Hatfield, PA, U.S.A.). The copper grids containing the deposited samples were left to air dry for one day at room temperature. A negative staining process was performed using 2% uranyl acetate which is commonly used for staining proteins.¹⁹⁸ A drop of 2% uranyl acetate was deposited on a wax sheet, and then the copper grids were placed face down for 5 minutes on top of the drop. The copper grids were immersed in a 250 mL beaker containing ultra-pure water and rinsed 15 times. Using a wicking procedure, the grids were taken out of the beaker and dried using a Kimwipe[®] without touching the surface of the grid. The samples were left to dry completely at room temperature and images were obtained the next day.

Scanning electron microscopy (SEM) images were acquired using Tescan MIRA3 LMU Field Emission SEM (Warrendale, PA, U.S.A.). The SEM is equipped with a high brightness Schottky emitter electron gun, and a secondary electron detector. Images were acquired using resolution mode (1.2-2.5 nm), a high vacuum mode at 10 kV, and at a

scanning speed of 32.00 μs / pixel. This SEM is coupled to an INCA X-max 80 mm 2 EDS system to detect elements present in a selected SEM area, providing qualitative and semi-quantitative information. The EDS system uses a silicon drift detector (SDD).

SEM analysis was completed at different stages during the aggregation process of recombinant human insulin. The times chosen were 0, 45, 60, 75, 90, 135, and 225 minutes. At the allotted time, one drop of insulin solution was deposited on a 5 x 5 mm silicon wafer, (Ted Pella, Inc., Redding, CA, U.S.A.). The samples were left to dry at room temperature and images were obtained.

4.12 Attenuated total reflectance-Fourier transform infrared spectroscopy (ATR-FTIR)

A bench top ATR-FTIR spectrometer (22w x 31d x 14h) was used (Bruker Optik GmbH). It is designed to have sealed and desiccated optics housing. The ATR-FTIR contains a diamond crystal (2 x 2 mm) which provides a spectral range between 50-50000 cm^{-1} , and analysis can be done on samples with pH 1-14. The ATR-FTIR is equipped with an air cooled, low voltage (12 V, 20 W) IR source, a high resolution deuterated triglycine sulphate (DTGS) detector, and a class I diode laser (850 nm). The spectral resolution obtained using ATR-FTIR is between 0.8-2.0 cm^{-1} .

ATR-FTIR was completed on both powder and solution recombinant human insulin. For the powder human insulin experiment, a small amount of the powder was placed on the diamond window and a standard tip anvil was pressed against the powder sample in order to have a compact powder layer covering the crystal. Using OPUS 7.0,

the parameters were set for scanning the background for 64 scans and the sample for 64 scans. For the human insulin solution experiment, a small drop of the human insulin solution was placed on the diamond window without any further modification, and the same parameters were used to collect the spectra. The data was then plotted using Origin 8.1 (Northampton, MA, U.S.A.).

Chapter 5: Results and Discussion

5.1 Self-assembled monolayer studies

The AgNPs were prepared using a modified Lee and Meisel method which is a citrate reduction reaction that leaves residual citrate and its oxidation products on the surface of the metal.¹⁶⁶ In the synthesis, citrate reduces Ag^+ to Ag^0 and in the process is oxidized into an intermediate molecule, acetonedicarboxylate, which decomposes further into acetoacetate.¹⁶⁴ As a result of this reaction carbon dioxide and / or formate are released as byproducts.¹⁶⁴ Citrate is Raman active and has strong peaks around 935 and 1404 cm^{-1} which are assigned to $\nu(\text{C-COO})$ and $\nu_s(\text{COO})$, respectively.²⁰⁰ Also, peaks at 810 cm^{-1} and 840 cm^{-1} are due to $\nu_s(\text{CCCC-O})$, and a peak at 1033 cm^{-1} corresponds to $\nu_s(\text{C-O})$.²⁰⁰ As a result, citrate can be a major interference for both the adsorption and detection of analytes via SERS. In order to reduce the citrate signal, a displacement reaction is performed using potassium chloride (KCl). Studies have shown that Cl^- has a strong specific adsorption on Ag and is able to displace adsorbed citrate.¹⁹⁶ The citrate removal is done by immersing the AgNP electrode in 0.5 M KCl for 30 minutes followed by careful rinsing. Figure 27 shows the EC-SERS signal of the AgNP substrate in air with and without KCl treatment. After 30 minutes the citrate molecules were displaced by Cl^- and the interfering signal was mostly gone. There is only one strong peak present at 240 cm^{-1} which is due to the $\nu(\text{Ag-Cl})$ vibration.²⁰¹ Citrate removal was completed for all experiments conducted in this research work prior to performing any further studies. Not only did this reduce the interfering background but it also reduced electrostatic repulsion during monolayer deposition.

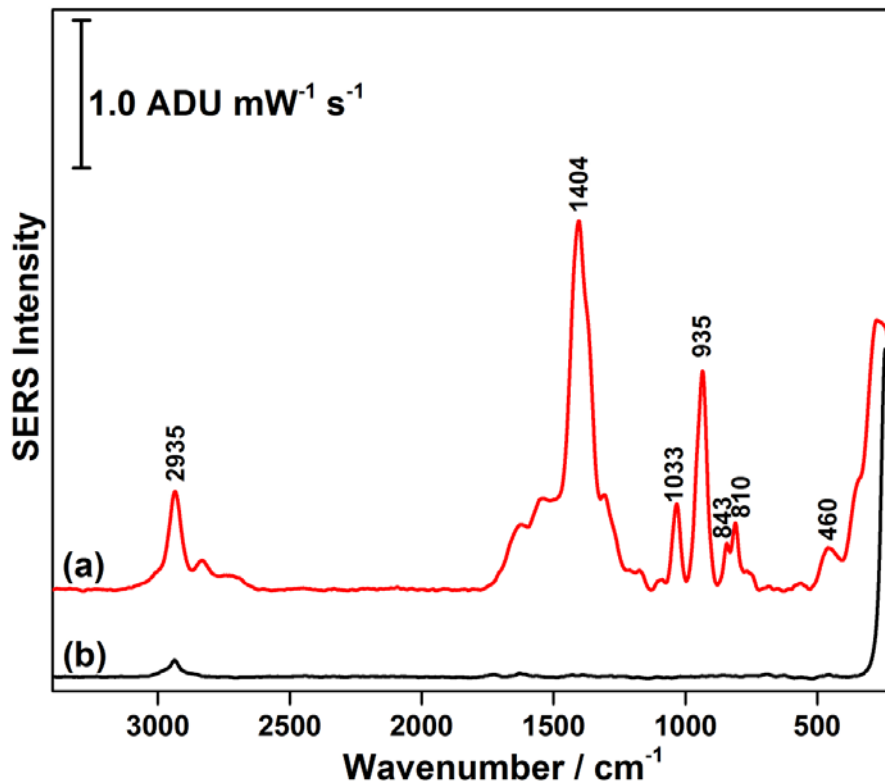


Figure 27: Comparison between a) normal citrate-reduced silver colloid, b) citrate-reduced silver colloid treated with 0.5 M KCl for 30 minutes. Spectra were measured at 2 mW for a time interval of 30 seconds using 532 nm excitation.

Prior to conducting any supported bilayer lipid membrane (s-BLM) studies it was important to choose the right self-assembled monolayer (SAM) molecule that would be able to provide a compact monolayer between the BLM and the electrode surface. This was necessary in order to increase the distance between the electrode surface and the biomembrane such that any species beyond the membrane would not be within the 2-4 nm enhancement region. Alkanethiols are the most commonly used SAMs and consist of an alkyl chain that has a thiol group at one end and various functional groups at the other end; $\text{SH}(\text{CH}_2)_n\text{X}$.²⁰²⁻²⁰⁵ Significant previous research has been conducted in our

laboratory in order to choose the optimal alkanethiol for this purpose.¹⁹⁶ For example 12-mercaptohexanoic acid and 1-octadecanethiol were investigated.¹⁹⁶ Both thiols were able to form a compact monolayer on the AgNP surface; however, the lengths of these thiols were too long to observe either the probe molecule or the first leaflet.¹⁹⁶ This is due to the sharp decay of the SERS enhancement from the metal surface noted previously. 6-mercaptohexanoic acid (6-MHA) was found to be the optimal thiol, and therefore was used throughout all the s-BLM studies reported in this thesis work. This SAM molecule consists of a six carbon chain, with a carboxylic acid on one end, and a thiol (-SH) on the other end. The -SH allows for formation of a strong metal-sulfur bond, while the -COOH group provides electrostatic interaction with the choline lipid head group. In literature, it has been shown that alkanethiols adsorb spontaneously onto noble metal surfaces.¹⁹⁶ Alkanethiols are usually dissolved in ethanol, and the concentration can vary from μM to mM .²⁰⁶ Researchers have shown that thiols can adsorb on Au and Ag substrates within minutes; however to obtain a compact and uniform monolayer it is recommended to incubate the metal substrates in the thiol solution for several hours.²⁰²⁻²⁰⁶ Figure 28 shows a representation of 6-MHA adsorption on the silver nanoparticle substrate. Ideally a compact 6-MHA monolayer would have an upright conformation; however in some cases the 6-MHA might be bent which introduces disorder to the monolayer (Figure 28).

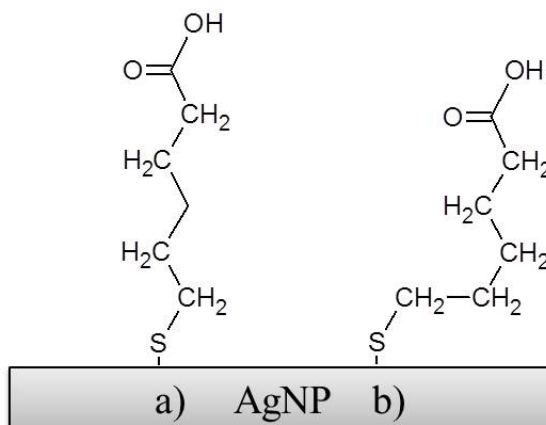


Figure 28: The two surface orientations of 6-mercaptohexanoic acid on AgNP substrates: a) trans conformation, or b) gauche conformation

The surface orientation of 6-MHA can be determined by looking at the peaks that are due to the vibrational modes of the C-C-S moiety. When the C-C-S moiety is present perpendicular to the metal substrate the 6-MHA is said to be present in a trans ($\nu(\text{C-S})_{trans}$) conformation, and can be observed by a peak around 690 cm^{-1} . When the $\nu(\text{C-S})$ moiety is bent and parallel to the metal substrate, the 6-MHA is said to be present in a gauche ($\nu(\text{C-S})_{gauche}$) conformation, and can be observed by a peak around 630 cm^{-1} .^{63,206-208} Figure 29 shows the EC-SERS cathodic scan of a AgNP substrate that has been incubated in 1.0 mM 6-MHA for two hours. Open circuit potential (OCP) is the resting potential for the metal and is measured without application of a voltage.²⁰⁹ At OCP, both the $\nu(\text{C-S})_{trans}$ and $\nu(\text{C-S})_{gauche}$ peaks were present, suggesting that the 6-MHA has a mixed orientation on the AgNP surface. As an increasingly negative potential was applied the peaks increased in intensity and the gauche conformation became more predominant, suggesting that increasing disorder is being introduced into the monolayer. There are other peaks that are also present which are due to the 6-MHA. For example, a

peak around 2921 cm^{-1} is due to $\nu_{\text{as}}(\text{CH}_2)$ stretching of 6-MHA which indicate that a disordered monolayer is formed.²⁰⁸ Other characteristic SAM peaks include C-H deformation (1434 cm^{-1}), CH_2 wagging (1297 cm^{-1}), and C-C stretching (1058 cm^{-1} , 1157 cm^{-1}).²¹⁰ The disorder of the monolayer can be explained by the SERS surface selection rules which dictates that polarizability tensors that are parallel to the AgNP surface will have a weakened SERS signal. On the other hand, vibrational modes that are perpendicular to the AgNP surface will exhibit higher SERS intensities.^{157-159,211} The application of potential can cause molecules to change orientation which causes different vibrational modes to be observed. The conformation of the 6-MHA molecules on the AgNP surface can be determined by the orientation of the $\nu(\text{C-S})$ peak observed. The SERS surface selection rule is also used to explain $\nu(\text{CH}_2)$ vibrations of the 6-MHA. As a negative potential was applied the $\nu(\text{CH}_2)$ peak intensity increased which suggests that the $\nu(\text{C-H})$ mode is present perpendicular to the surface. This behaviour occurs due to disorder introduced in the 6-MHA chain as potential is applied.

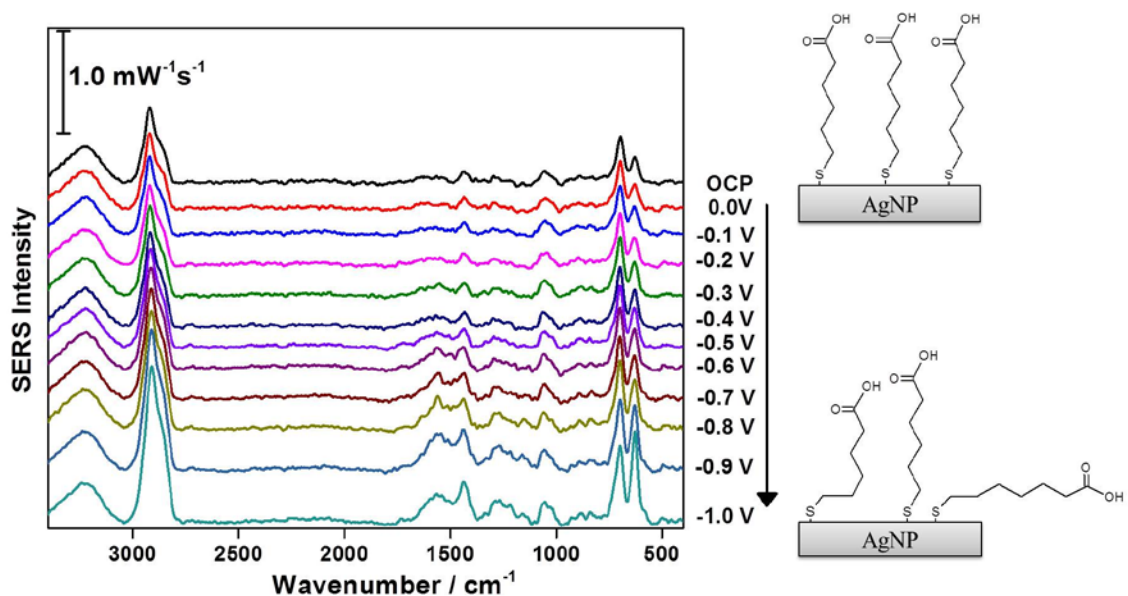


Figure 29: EC-SERS cathodic signal of 6-MHA SAM on a AgNP electrode in 0.1 M NaF solution. The spectra were measured at 4 mW for a time interval of 30 seconds using 532 nm excitation.

After applying a negative voltage up to -1.0 V, the voltage was then stepped in the anodic direction to 0.0 V to determine whether or not this monolayer would be stable. It would also show if there would be any change of conformation of the 6-MHA by applying a more positive voltage. As the potential was made less negative, the 6-MHA signal was stable and only a minor change in signal was observed, as is shown in Figure 30. This observation indicates that as the potential is stepped positively the 6-MHA SAM is still strongly adsorbed on the AgNP surface. However, as more positive potential is applied it is clear that the 6-MHA is becoming more ordered as the 630 cm⁻¹ and 2920 cm⁻¹ peaks are decreasing in intensity.²⁰⁸ Other peaks that appeared at positive potential include $\nu(\text{C-C})$ skeletal stretch (1062 cm⁻¹), CH₂ wagging (1270 cm⁻¹), CH₂ twisting (1336 cm⁻¹), CH₂ scissoring (1435 cm⁻¹).^{144,210}

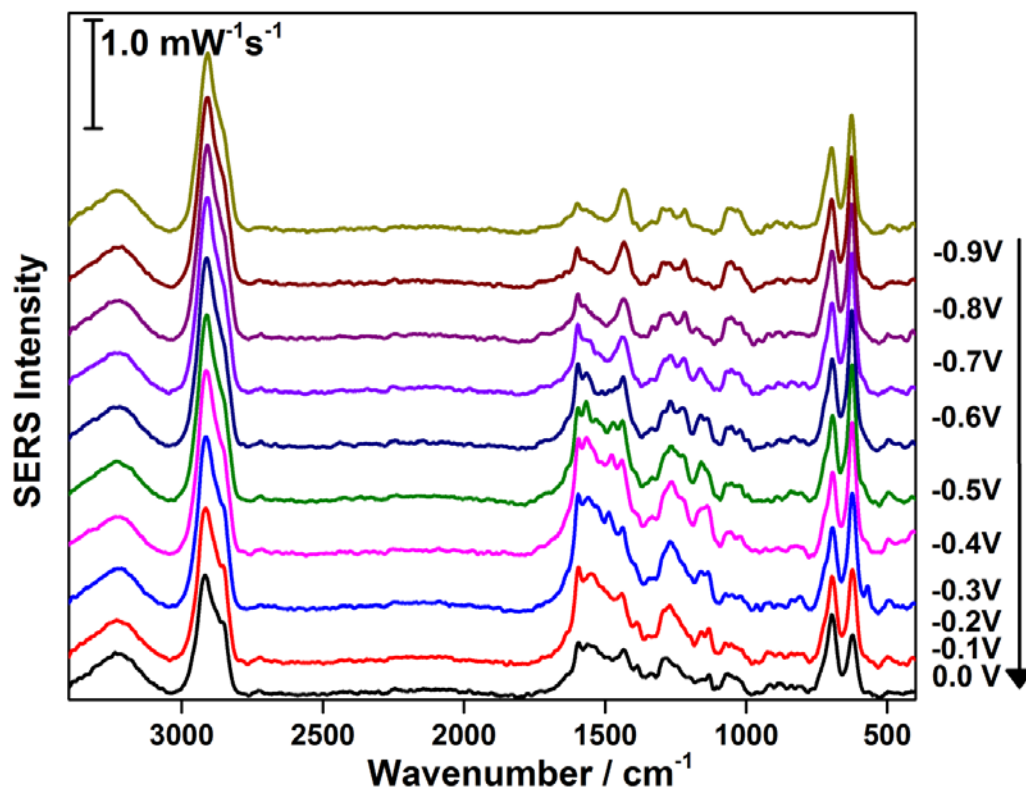


Figure 30: EC-SERS anodic signal of 6-MHA SAM on a AgNP electrode in 0.1 M NaF solution. The spectra were measured at 4 mW for a time interval of 30 seconds using 532 nm excitation.

Based on the results shown it was concluded that 6-MHA is mostly stable within the applied voltage range. Some disorder occurs as a negative potential is applied. This behaviour has been observed by other researchers where the tilt angles of the SAM molecules can be measured using methods such as neutron reflectivity and PM-IRAAS which can determine the extent of the disorder as potential is applied.^{117,212} Even though there is some disorder observed for the 6-MHA SAM, it is clear that that the SAM is still strongly adsorbed on the AgNP surface, and little to no reductive desorption has taken place. Therefore, 6-MHA was used for the lipid bilayer studies.

5.2 Normal Raman of DMPC and cholesterol

In order to begin studies using a DMPC / cholesterol mixture for forming a biomimetic membrane, initial studies investigated the normal Raman signal for the pure powder of each substance. This was completed by placing a small amount of the powder in a capillary tube and placing it into the Raman spectrometer. As shown in Figure 31, a Raman spectrum for DMPC was successfully obtained and different vibrational modes were observed. The strongest peaks present were due to the alkyl chain stretching modes which are located at 2930 cm^{-1} , 2880 cm^{-1} , and 2848 cm^{-1} .^{213,214} Other peaks present were mostly due to the polar head group of DMPC. Some of these peaks appeared at 719 cm^{-1} , 1062 cm^{-1} , 1090 cm^{-1} , 1438 cm^{-1} and 3035 cm^{-1} which were due to $\nu_s(\text{C-N}^+(\text{CH}_3))$, $\nu(\text{C-CO-PO}_2^-)$, $\nu_s(\text{PO}_2^-)$, $\delta(\text{CH}_2)$ and $\nu_{as}(\text{CH}_3)_3\text{N}^+$, respectively.^{213,214} Please refer to the appendix section, Table A-1, for a full peak assignment for DMPC.

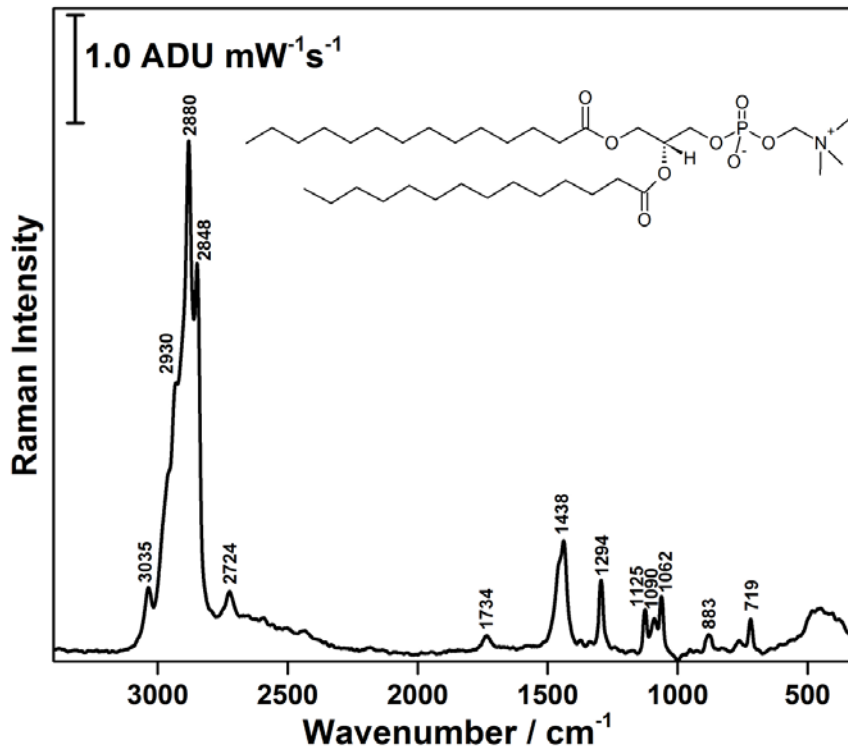


Figure 31: Raman spectrum of solid 1,2-Dimyristoyl-*sn*-glycero-3-phosphocholine (DMPC) collected for 30 seconds at a laser power of 4 mW at 532 nm excitation.

DMPC is a synthetic lipid that has been widely reported in literature to form biomimetic membranes on solid supports. In order to increase the fluidity of the DMPC bilayer lipid membrane, cholesterol was introduced. Cholesterol is a member of the sterol family and is present in biological cell membranes at various concentrations.²¹⁵ Cholesterol consists of a small hydrophilic region (OH group), and a large, extended hydrophobic region (sterol moiety and alkyl chain unit).²¹⁶ In general, cholesterol functions as a modulator of membrane fluidity, as the planar steroid ring structure increases the fluidity of the gel-state and reduces the fluidity of the liquid crystalline state.^{94,216} Since cholesterol is mostly hydrophobic it tends to orient itself at the interfacial region of the membrane.²¹⁷⁻²¹⁹ The normal Raman spectrum of cholesterol

powder was collected as shown in Figure 32. The strongest peaks present in the cholesterol spectrum were also due to alkyl chain stretching which occur at 2932 cm^{-1} , and 2867 cm^{-1} . Other peaks around 426 cm^{-1} , 699 cm^{-1} , 1439 cm^{-1} , 1672 cm^{-1} were also present which are due to cholesterol, $\delta_r(\text{CH}_2)$, $\delta_d(\text{CH}_2)$, and $\nu(\text{C}=\text{C})$ vibrational modes.^{144,218} Please refer to the appendix section, Table A-2, for a full peak assignment for cholesterol.

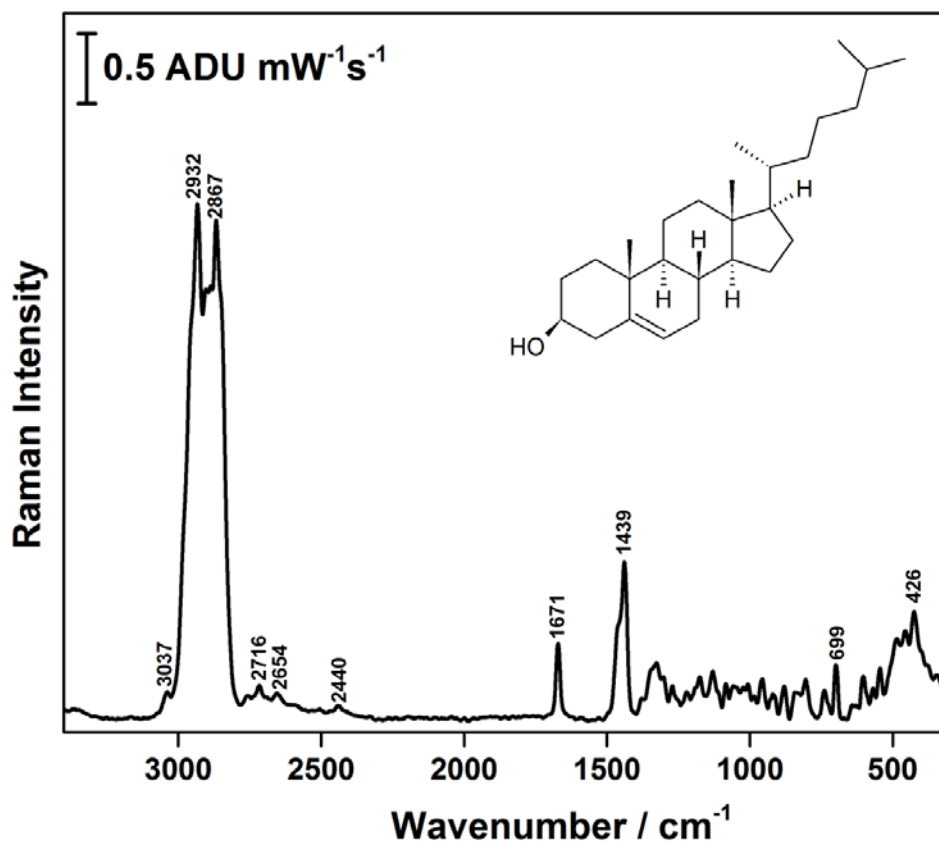


Figure 32: Raman spectrum of solid cholesterol collected for 30 seconds at a laser power of 4 mW at 532 nm excitation.

5.3 Supported bilayer lipid membrane (s-BLM) studies

An isotherm of DMPC / cholesterol (70:30) was performed to identify the collapse pressure, suitable transfer pressure, and the mean molecular area. As seen in Figure 33,

the collapse pressure was around 48 mN / m which suggested that the transfer onto the AgNP substrate must be completed below this pressure. The compact monolayer was transferred onto the AgNP substrate at a selected transfer pressure of 40 mN / m. The area per molecule for the DMPC / cholesterol (70:30) monolayer at the collapse pressure was found to be $37.0 \text{ \AA}^2 / \text{molecule}$, which is consistent with literature values.⁷⁶ The efficiency of the film transfer can be measured by the transfer ratio. The transfer ratio is defined as the decrease in the area occupied by the monolayer on the water surface, divided by the coated area of the solid substrate.²²⁰ An ideal transfer ratio of 1.0 represents a successful monolayer transfer onto the substrate. Transfer ratios less than 0.9 represent an insufficient monolayer transfer while greater than 1.1 suggest multilayer deposition.¹¹⁴ An acceptable transfer ratio can be obtained by choosing an appropriate transfer speed at which the substrate is brought through the monolayer. It is recommended that the substrate is allowed to completely dry before depositing the second leaflet in order to improve the deposition process. In order to deposit the second leaflet using the LS method and ensure complete transfer, a dip in the surface pressure is observed after the electrode is withdrawn from the water surface which indicates that fewer molecules are present at the air-water interface.

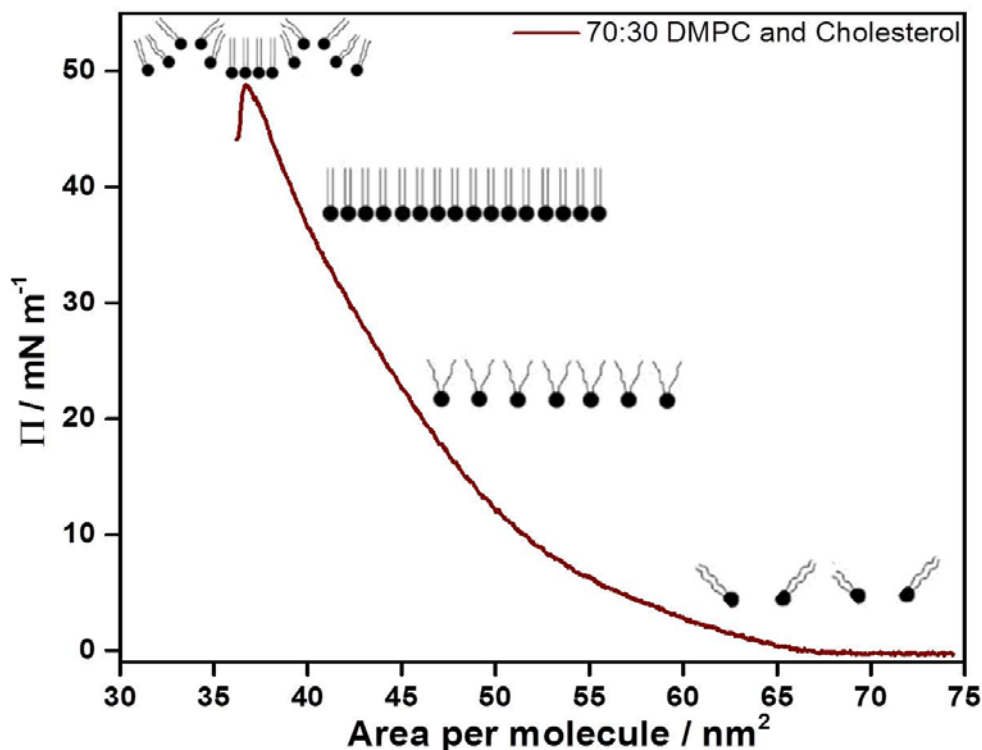


Figure 33: Isotherm of DMPC / cholesterol (70:30) at a subphase temperature of 30 °C and 90% relative humidity using the Langmuir trough. Compression was completed at a rate of 5.0 mm / min.

Previously in our research laboratory significant work was conducted toward obtaining optimal conditions for forming a good quality biomimetic membrane using the Langmuir trough.¹⁹⁶ This was an important preliminary step to ensure that there were no defects already present prior to the introduction of a probe molecule and application of a voltage. In this research, these experiments were repeated in order to show reproducibility of the results between different researchers. Figure 34 shows the cathodic scan of the s-BLM consisting of DMPC / cholesterol (70:30) deposited on 6-MHA SAM using the LB / LS technique. It is clear that the signal is very similar to the signal obtained from the 6-MHA SAM (refer to Figure 29); this is due to the fact that both lipid

molecules and 6-MHA consist mostly of alkyl groups. However, there are some signature peaks specific to DMPC that are distinguishable from 6-MHA. As the potential was stepped negative, the intensity of several peaks increased and also new peaks appeared which were indicative of DMPC, such as 953 cm^{-1} and 893 cm^{-1} , which are due to $\nu_{\text{as}}(\text{CH}_3)_3\text{N}^+$, and $\delta_{\text{r}}(\text{CH}_2)$, respectively.²¹³⁻²¹⁸ Other peaks due to C-C symmetric stretch / CH_2 wagging (1058 cm^{-1}), and CH_2 bend (1439 cm^{-1}) were present.¹⁴⁴ At -1.0 V the intensity at 2921 cm^{-1} is much stronger than the spectrum obtained for the 6-MHA SAM, which indicates that more CH_2 moieties are present on the surface due to the DMPC and cholesterol molecules.

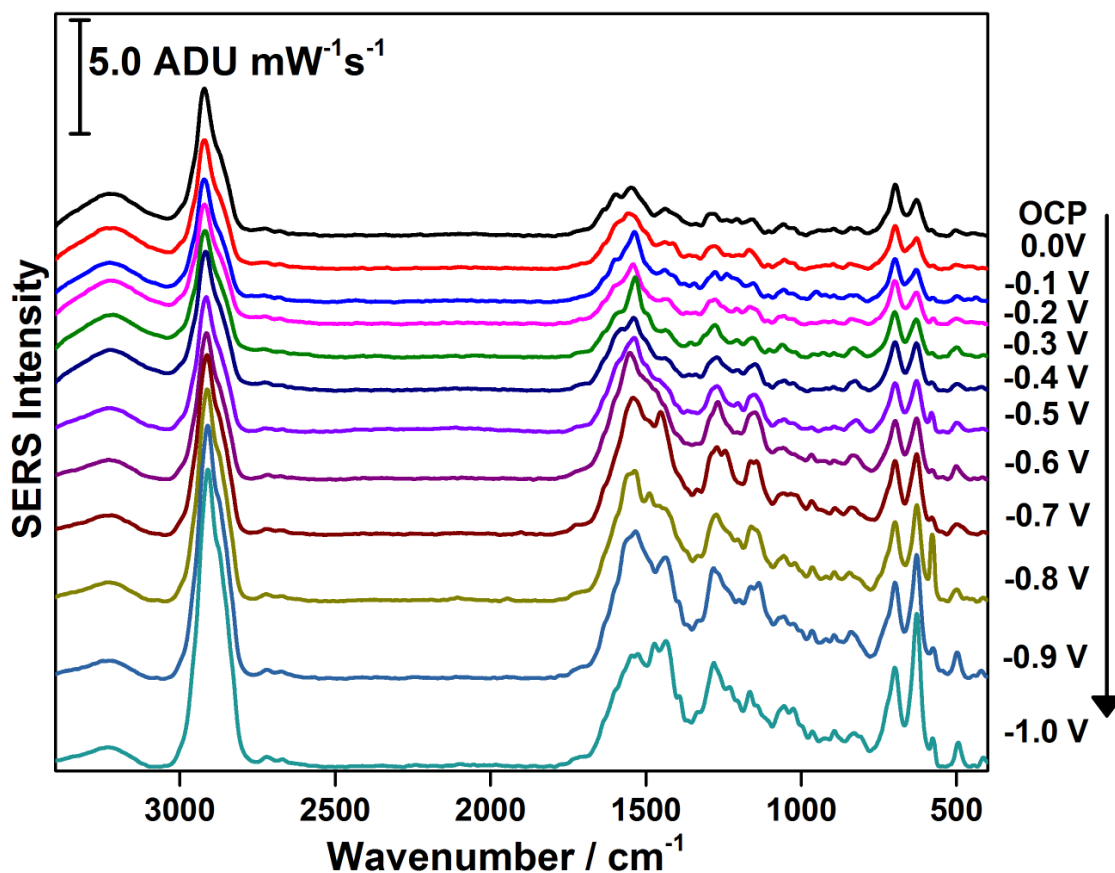


Figure 34: EC-SERS cathodic signal of DMPC / cholesterol (70:30) bilayer on a AgNP electrode modified with a 6-MHA SAM in 0.1 M NaF solution. The spectra were measured at 4 mW for a time interval of 30 seconds using 532 nm excitation.

As the potential was stepped anodically it is clear that the peak intensity decreased, shown in Figure 35, an indication that the system is mostly reversible. The signal observed indicates that the bilayer lipid membrane is not desorbed from the electrode surface after applying positive voltage. This is consistent with previous work done in our laboratory where the s-BLMs are still intact after application of a voltage. As a result of these observations, only the cathodic data will be focused on in this research work.

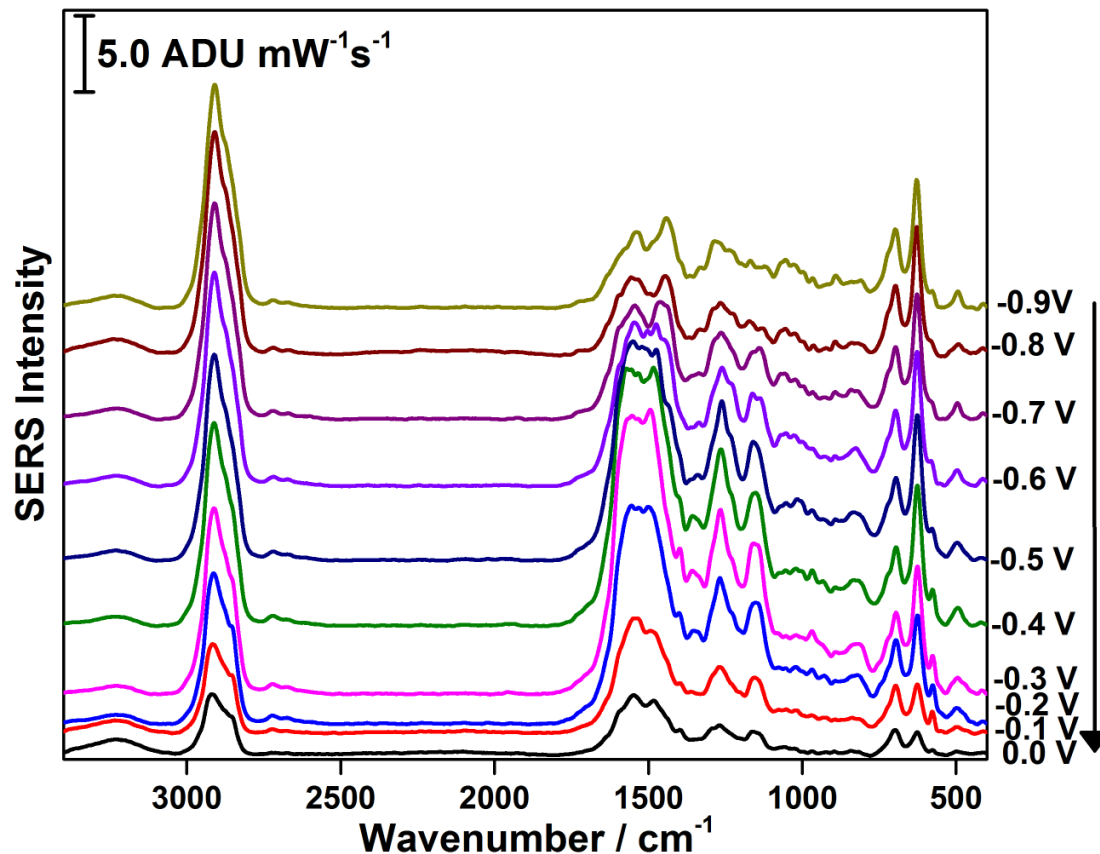


Figure 35: EC-SERS anodic signal of DMPC / cholesterol (70:30) bilayer on a AgNP electrode modified with a 6-MHA SAM in 0.1 M NaF solution. The spectra were measured at 4 mW for a time interval of 30 seconds using 532 nm excitation.

A comparison between the 6-MHA monolayer and s-BLM on a modified 6-MHA electrode was necessary to observe any spectral changes due to the presence of the bilayer. Figure 36 represents a comparison of 6-MHA SAM and s-BLM on a modified 6-MHA electrode at -1.0 V cathodic. It can be seen that the signal is similar, yet there are some differences to note. For example, it is very clear that the alkyl chain CH_2 region at 2920 cm^{-1} is stronger in the presence of lipid molecules, suggesting that the lipid molecules are indeed present on the AgNP surface. The region between $400\text{-}500 \text{ cm}^{-1}$ shows two peaks at 415 cm^{-1} and 495 cm^{-1} which are characteristic of the $\nu(\text{C-C})$ stretch in

cholesterol, and COO rocking of glycerol group of DMPC.²²¹⁻²²³ Other peaks that are present only when the s-BLM are 578 cm^{-1} and 959 cm^{-1} which are due to the phosphatidyl group, and CH_2 rocking vibration in cholesterol, respectively.^{224,225} Other peaks in the region between $1100\text{--}1500\text{ cm}^{-1}$ are 1167 cm^{-1} and 1470 cm^{-1} which are due to $\nu(\text{C}=\text{C})$ and $\delta(\text{OH})$ in lipid, and CH_2 scissoring vibrations, respectively.^{199,226} Based on this comparison it is clear that the DMPC / cholesterol bilayer lipid membrane is formed on AgNP substrates using the LB / LS technique.

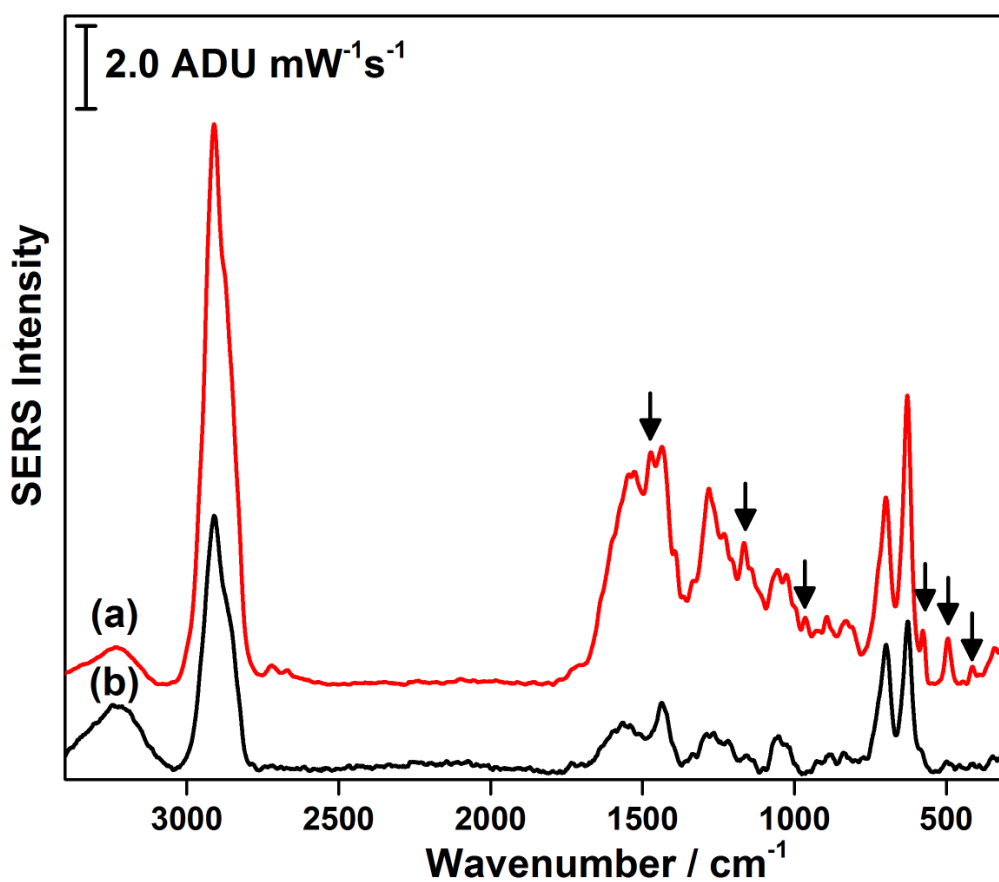


Figure 36: Comparison at -1.0 V between a) 6-MHA + s-BLM and b) 6-MHA SAM on a AgNP electrode in 0.1 M NaF solution. The spectra were measured at 4 mW for a time interval of 30 seconds using 532 nm excitation.

After each experiment, cyclic voltammetry (CV) was performed in order to determine if the electrode was working properly and whether there was a compact layer formed on the AgNP surface. As seen in Figure 37, a comparison between a bare AgNP electrode and another 6-MHA modified AgNP electrode with a supported lipid bilayer were measured in 0.1 M NaF electrolyte. As mentioned earlier, CV is used as a qualitative method to determine whether a compact monolayer is formed on an electrode surface.¹³⁷ This can be shown by the different resultant current measured for each experiment. It was clear that the electrode with the adsorbed lipid bilayer showed a large decrease in the current, reflective of a decrease in the capacitance (equation 6) as the thickness of bilayer increases. This result indicates that the lipid bilayer is forming a compact layer on the surface of the AgNP.

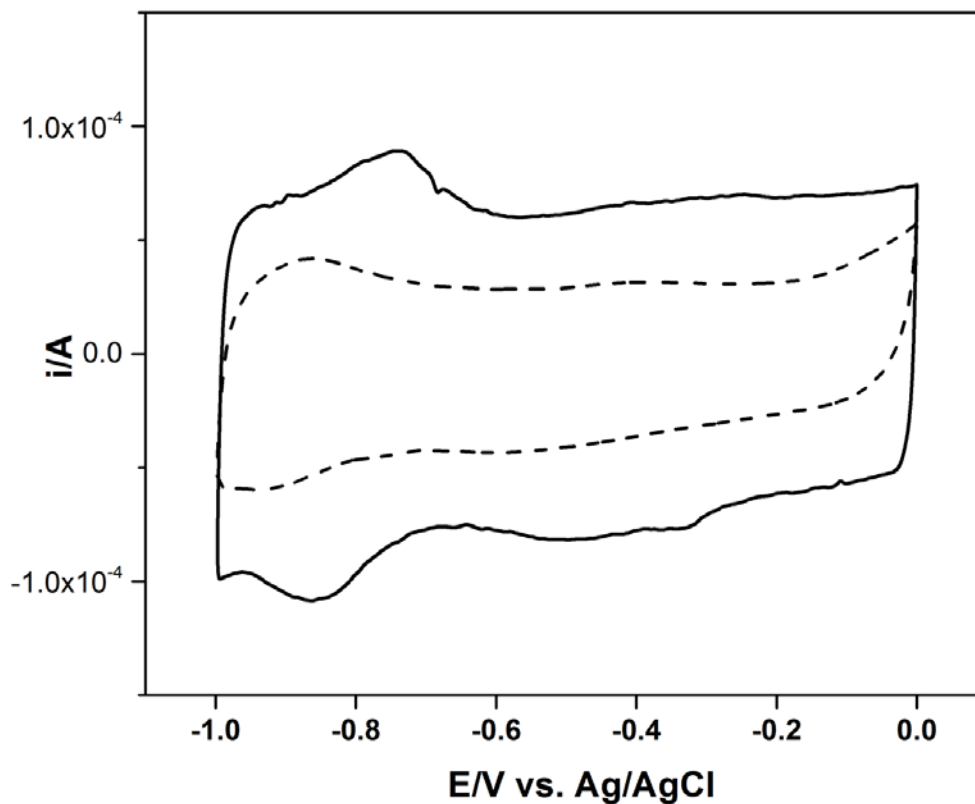


Figure 37: Comparison between bare AgNP electrode in 0.1 M NaF electrolyte (solid line), s-BLM on a 6-MHA modified AgNP electrode in 0.1 M NaF electrolyte (dashed line). The sweep rate: 50 mV / s.

5.4 s-BLM with dAMP studies

In order to study the quality of the s-BLM, a probe molecule was introduced. In these experiments a DNA nucleotide, dAMP which consists of a sugar base, a phosphate group, and adenine base was used.²²¹ dAMP was chosen as a probe for these studies because it is a model of the neurotransmitter adenosine and has an excellent Raman signal.¹⁷⁶ The normal Raman spectrum of dAMP powder is shown in Figure 38 (spectrum a). Many peaks observed such as 813 cm^{-1} , 1037 cm^{-1} , 1506 cm^{-1} , 1406 cm^{-1} , which are due to $\nu_s(\text{O-P-O})$, $\nu_s(\text{N-sugar})$, $\nu_s(\text{C=N})$, and $\delta_d(\text{N-H})$, respectively.¹²⁷ The two characteristic SERS peaks that are specifically due to dAMP are at 730 cm^{-1} and

1328 cm^{-1} which are indicative of the ring breathing vibrational modes of adenine.¹²⁷ By comparing the dAMP powder spectrum to the EC-SERS of 1.0 mM dAMP solution at -1.0 V (spectrum b) it is clearly shown that the most intense peaks are those at 730 cm^{-1} and 1333 cm^{-1} . Therefore for further studies these two peaks will be used as marker bands for dAMP.

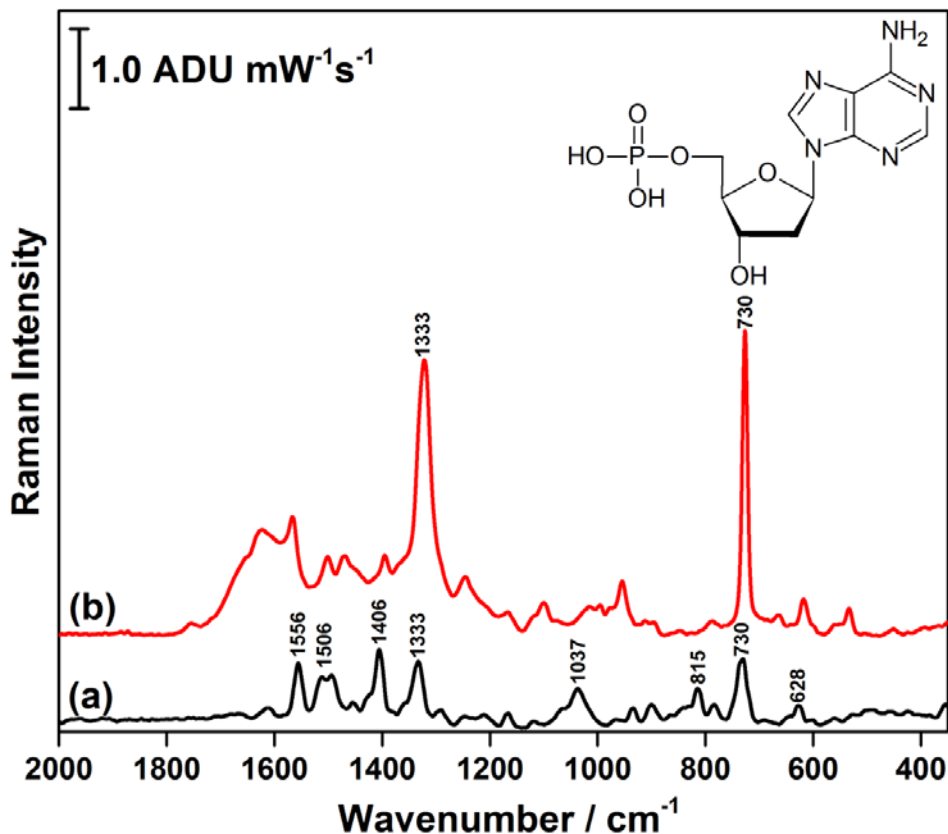


Figure 38: Raman spectra of (a) dAMP powder, (b) 1.0 mM dAMP solution at -1.0 V. The spectra were measured at 4 mW for a time interval of 30 seconds using 532 nm excitation.

The presence of dAMP peaks (730 cm^{-1} , 1328 cm^{-1}) in the EC-SERS spectra would suggest permeation of the dAMP molecule through the lipid bilayer. This would indicate whether a good quality bilayer lipid membrane is being formed. If peaks due to

adenine are observed then dAMP is accessing the surface via membrane defects. In addition, it would indicate if there are any defects being formed in the presence of protein aggregates. Since SERS is highly distance-dependent, an increase in the dAMP intensity would suggest the molecule is moving closer to the AgNP surface.

The dAMP was prepared as a 1.0 mM solution in 0.1 M NaF supporting electrolyte and introduced to the s-BLM system to conduct EC-SERS. As seen in Figure 39, the signal at OCP is relatively weak and mostly consists of the 6-MHA / DMPC / cholesterol peaks and no peaks of dAMP were present. As potential was stepped negatively, more specifically at -0.1 V, dAMP peaks started to appear. The appearance of dAMP peaks at 730 cm^{-1} and 1328 cm^{-1} at negative potentials can be explained by electroporation. Electroporation occurs in biological cells in the presence of high electric fields.⁷⁰ Since potential is being applied across the s-BLM system it is highly expected that electroporation would occur, resulting in membrane defects and allowing molecules to permeate across the membrane and to the electrode surface. As the potential is stepped negatively, the dAMP peaks increased in intensity which suggests that the molecule is moving closer to the AgNP surface and the surface concentration of dAMP is increasing. Also, peak broadening, an increase in the alkyl chain peak intensity, and the strong intensity of the $(\text{C-S})_{\text{gauche}}$ peak suggest deformation of the lipid bilayer / monolayer has occurred. The strongest signal at -1.0 V consisted of peaks indicative of 6-MHA (630 cm^{-1} , 690 cm^{-1}), dAMP (730 cm^{-1} , 1328 cm^{-1}), and DMPC (572 cm^{-1} , 1073 cm^{-1} , 1430 cm^{-1}).^{127,214} A comparison of the EC-SERS signal at OCP and -1.0 V is provided in Figure 40. Based on these results it was concluded that the s-BLM on the modified

AgNP electrode is defect free, and by applying a negative potential, defects and pores are formed which allows permeation of probe molecules. Thus, the 6-MHA / DMPC / cholesterol / dAMP system should function as an excellent model for evaluating amyloid pore formation at the molecular level. A comparison of s-BLM in the absence and presence of dAMP is shown in Figure A-1 in the appendix section.

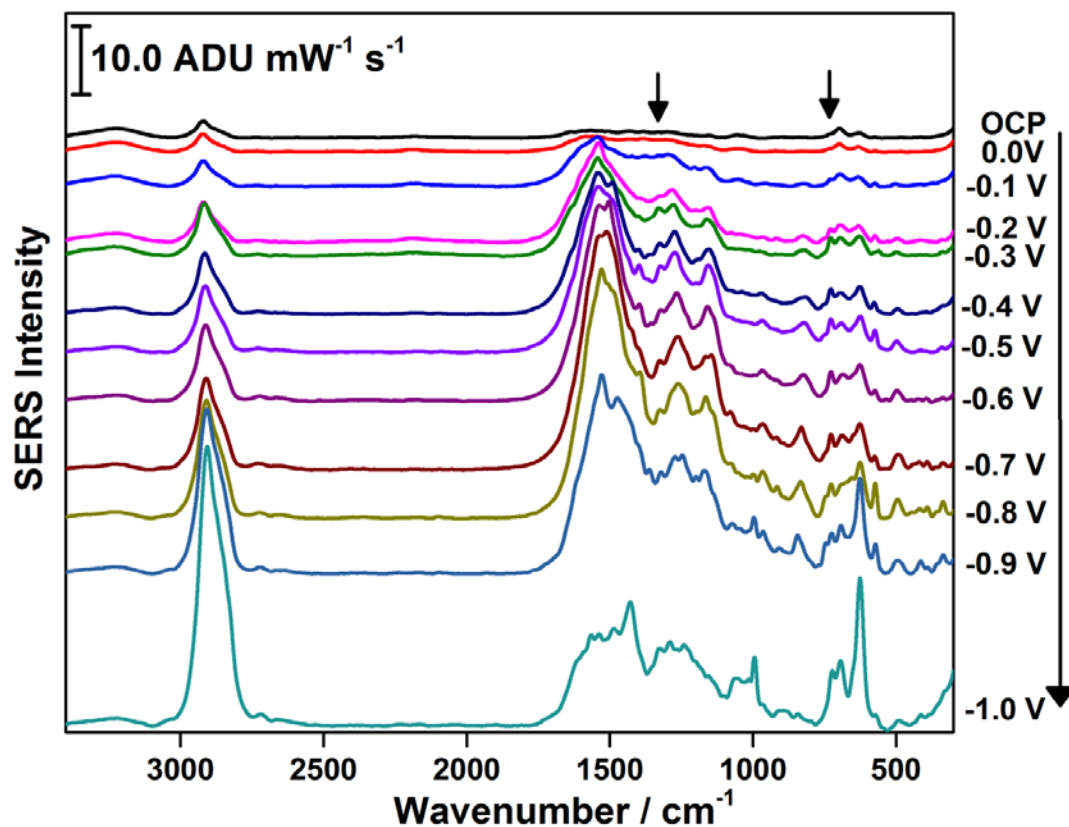


Figure 39: EC-SERS cathodic signal of DMPC / cholesterol (70:30) bilayer on a 6-MHA modified AgNP electrode in 1.0 mM dAMP / 0.1 M NaF solution. The spectra were measured at 4 mW for a time interval of 30 seconds using 532 nm excitation. dAMP peaks are indicated by arrows.

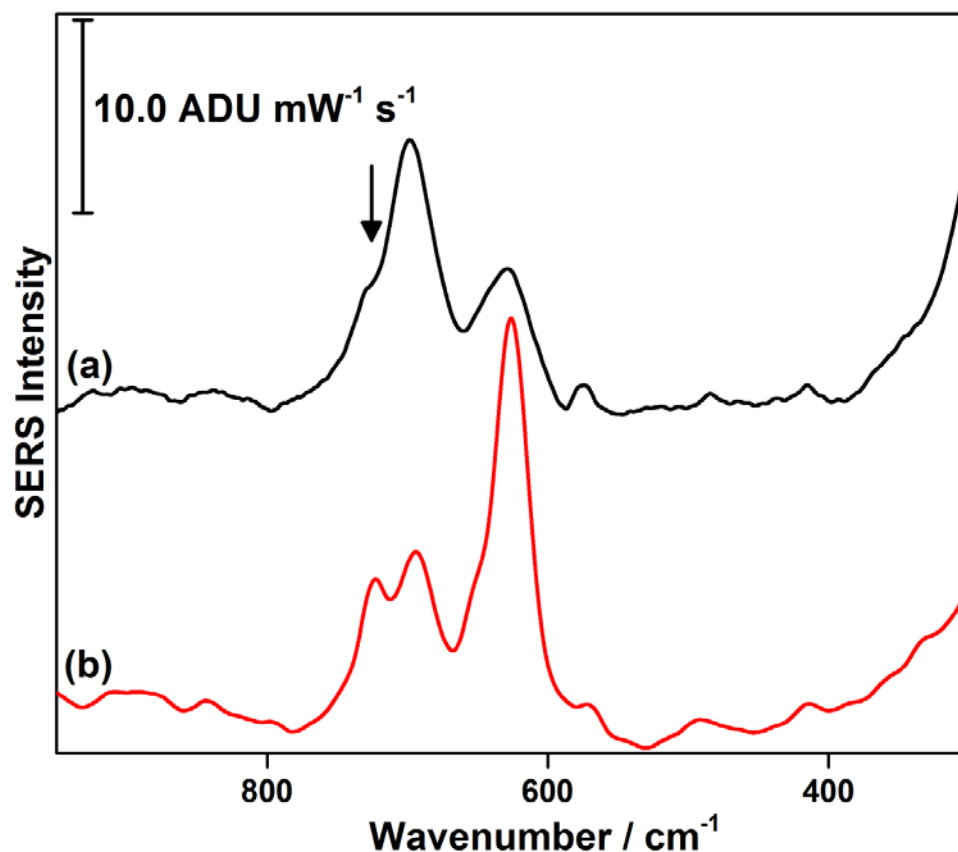


Figure 40: Comparison between DMPC / cholesterol (70:30) bilayer on a 6-MHA modified AgNP electrode in 1.0 mM dAMP / 0.1 M NaF solution at a) OCP, and b) -1.0 V. The spectra were measured at 4 mW for a time interval of 30 seconds using 532 nm excitation. dAMP peak is shown by arrow.

5.5 Spectroscopic characterization of native insulin protein

This research work was focused toward characterising the interaction between the s-BLM and aggregated protein to better understand the mechanism of protein aggregation disorders such as Alzheimer's disease. Recombinant human insulin was chosen as a model of amyloid- β for this purpose. Insulin is a polypeptide hormone composed of 51 amino acids; a 21-residue A-chain and a 30-residue B-chain that are linked together through two disulfide bonds.²²⁵⁻²²⁷ In literature, insulin is used as a model protein for

various amyloid diseases because it forms amyloid fibrillar structures under certain conditions.²²⁵⁻²²⁷ Insulin has the ability to aggregate both in vivo and in vitro conditions which makes it an effective model for protein aggregation studies.²²⁸ Therefore, the studies presented in this thesis will focus on aggregating insulin protein and introducing it to a s-BLM. Prior to studying this interaction, characterization of the aggregation process for recombinant human insulin was done using various techniques as outlined below.

5.5.1 Raman Spectroscopy

Raman spectroscopy is a useful tool in analyzing biological molecules, such as protein. The most important peaks to consider when analyzing proteins are the amide peaks which are at 1220-1250 cm^{-1} , 1530-1550 cm^{-1} , and 1630-1650 cm^{-1} and correspond to the amide III, amide II, and amide I respectively.²¹⁹⁻²²¹ The amide III band is due to the N-H bending and C-N stretching, and shifts in amide III vibrational modes can indicate changes in the secondary structure of protein.²²⁸ If the protein is exhibiting predominantly β -sheet structure this band will be shifted toward 1225-1240 cm^{-1} .²²⁸ The amide II band is due to predominantly N-H bending vibrations; this band is typically weak in Raman and therefore is mostly monitored by IR.²²⁸ The amide I band is due predominantly to the C=O stretching and is considered the most important vibrational mode for monitoring protein secondary structure.²²⁹ Shifts in the amide I band are useful in identifying secondary structures of protein; in particular, the amide I mode is very useful for following protein aggregation and amyloid formation. As the protein structure changes from primarily α -helix to primarily β -sheet, the amide I peak shifts from 1649-1658 cm^{-1} to 1620-1635 cm^{-1} , respectively.²³⁰ As seen in Figure 41, the observed normal

Raman spectrum of pure human insulin powder showed a rich spectrum which indicates that human insulin is Raman active. In the Raman signal it is evident that amide III (1267 cm^{-1}), and amide I (1656 cm^{-1}) are present and amide II is not Raman active. The position of amide I suggests that native human insulin is present in an α -helix conformation. Other peaks that are present are due to side chains of certain amino acids. Not all the amino acids are considered Raman active; the three amino acids that commonly contribute to the Raman signal of proteins are phenylalanine, tryptophan, and tyrosine (refer to Figure 2). These amino acids are Raman active due to the conjugated ring moiety containing delocalized electrons which have the ability to scatter light well. Other amino acids that provide some Raman signal are valine, glycine, and proline. Peak assignments for the Raman spectrum of human insulin powder is provided in Appendix section (Table A-3).

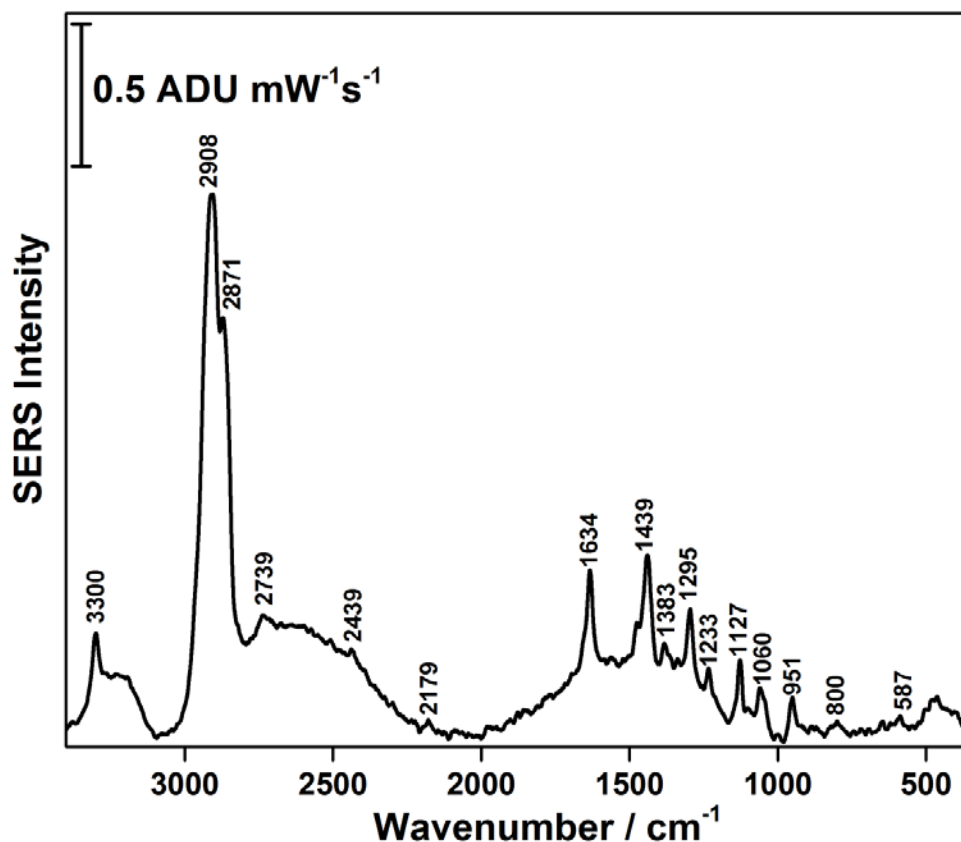


Figure 41: Raman spectrum of solid recombinant human insulin collected for 30 seconds at a laser power of 4 mW at 532 nm excitation.

In most cases it is difficult to obtain a Raman spectrum of a protein solution because it is more dilute and less concentrated than the solid sample. Based on Figure 42, a Raman spectrum of 2 mg / mL human insulin solution was successfully obtained. Many of the peaks that were seen in the Raman spectrum of human insulin powder sample were also observed in the solution spectrum. This showed that human insulin can be characterized in the form of a powder or concentrated solution using Raman spectroscopy. There were some slight changes in the spectrum obtained for the aqueous sample, for example a peak around 3306 cm⁻¹ was present in the solution which is due to

the $\nu_s(\text{O-H})$ of water. There were other peaks that were not observed in the solution spectrum including phenylalanine bands (1002 cm^{-1} , 1029 cm^{-1} , 1609 cm^{-1}), CH_2 wagging of proline (1206 cm^{-1}), and (C-C) twisting and stretching (642 cm^{-1} , 892 cm^{-1}). Also, some shifts in peaks occurred; the amide I band has shifted to lower wavenumbers (1645 cm^{-1}) which still suggest the presence of α -helical conformation, and also the CH_2 stretching vibrations were shifted to 2910 cm^{-1} .²³⁰ There were some peaks that were observed in the human insulin solution only such as 766 cm^{-1} (ring deformation of tryptophan), 1068 cm^{-1} (proline), 1307 cm^{-1} ($\delta(\text{CH}_2)$ twisting), 2150 cm^{-1} ($\nu(\text{CH}_3\text{-CH})$), 2743 cm^{-1} ($\nu(\text{CH})$), 2881 cm^{-1} ($\nu_{\text{as}}(\text{CH}_2)$), and 3247 cm^{-1} (O-H and N-H stretching).²³⁰

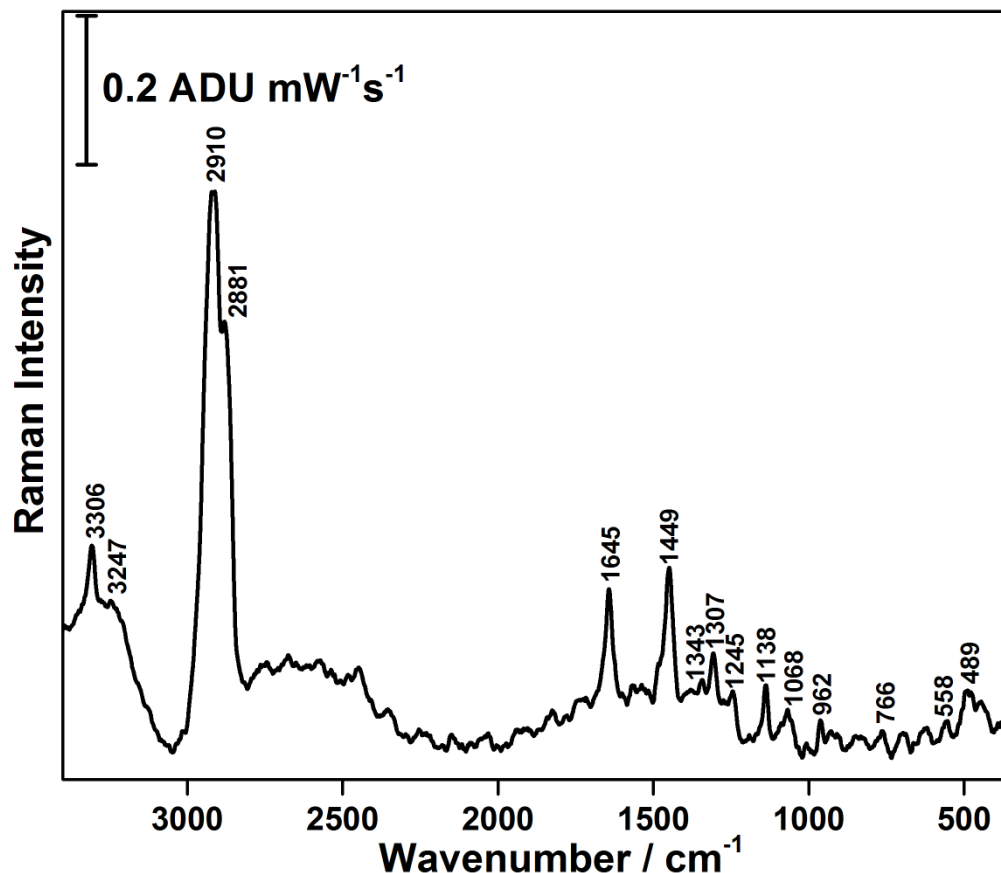


Figure 42: Raman spectrum of 2 mg / mL recombinant human insulin solution collected for 30 seconds at a laser power of 4 mW at 532 nm excitation.

5.5.2 Attenuated Total Reflectance-Fourier Transform Infrared Spectroscopy (ATR-FTIR)

Attenuated Total Reflectance-Fourier Transform Infrared (ATR-FTIR) is another vibrational spectroscopy technique used to characterize human insulin. As seen in Figure 43, the ATR-FTIR spectrum of human insulin powder was characterized and all three amide peaks were detected. Amide I (1648 cm^{-1}), amide II (1530 cm^{-1}), and amide III (1238 cm^{-1}) were all strongly observed. Other peaks observed include O-H, N-H stretching vibrations (3300 cm^{-1}), CH_3 asymmetric stretch (2956 cm^{-1}), CH_2 bending

(1446 cm^{-1}), CH_2 deformation (1396 cm^{-1}), C-H bending of tyrosine (1175 cm^{-1}), and $\nu_s(\text{C-C}, \text{C-N})$ (1124 cm^{-1}).¹²⁷ The ATR-FTIR spectrum obtained clearly suggests that protein bands can be easily monitored through ATR-FTIR. This indicates that ATR-FTIR can be useful in monitoring the aggregation pathway of proteins by looking at peak shifts of the amide peaks which can indicate changes in the secondary structure of protein.

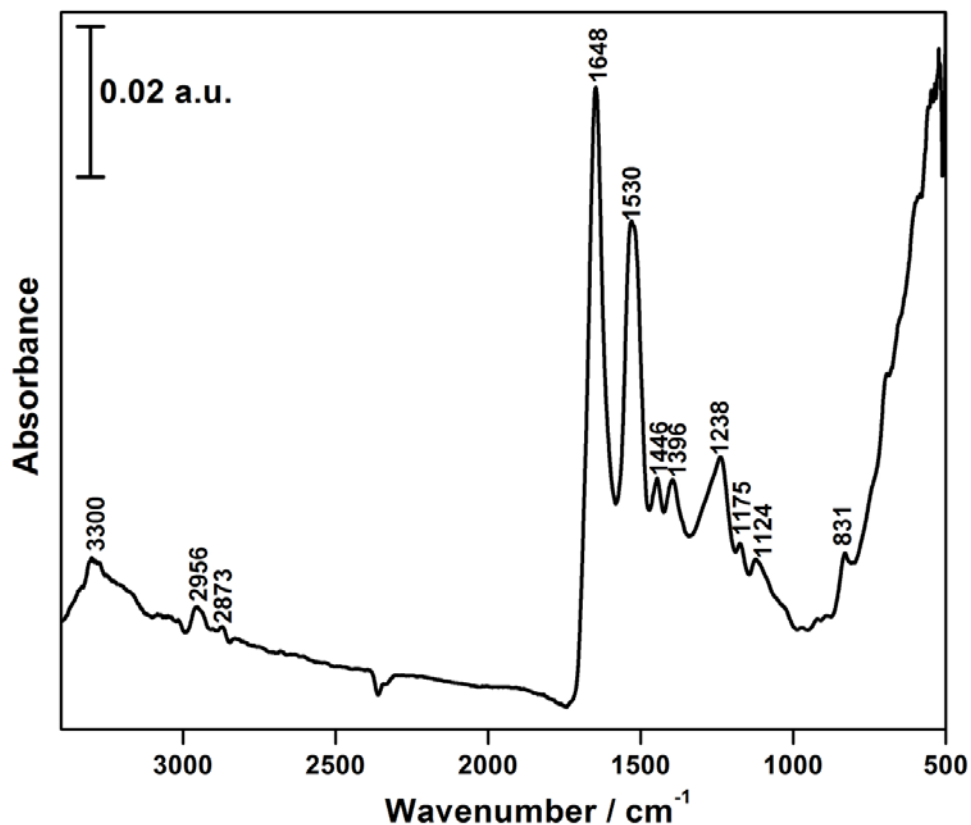


Figure 43: ATR-FTIR of human insulin powder collected on diamond crystal for 190 scans.

One of the important aspects to consider when using ATR-FTIR is the pH of the sample. The ATR crystal can be damaged if the pH of the sample is not within the working range (zinc selenide has a range of pH within 5-9).²³¹ The ATR-FTIR used in this research consisted of a diamond crystal which has the capability to analyze samples

with pH ranging from 1-10. This was very important since the aggregation process of insulin was done under very acidic conditions (pH 1.6). As seen in Figure 44, the human insulin solution was successfully analyzed using the ATR-FTIR as well. The results obtained are very similar to the human insulin powder which indicates that ATR-FTIR can analyze protein samples at lower concentration. The three amide peaks were all present, as well as other peaks that are due to the side chains of the amino acids.

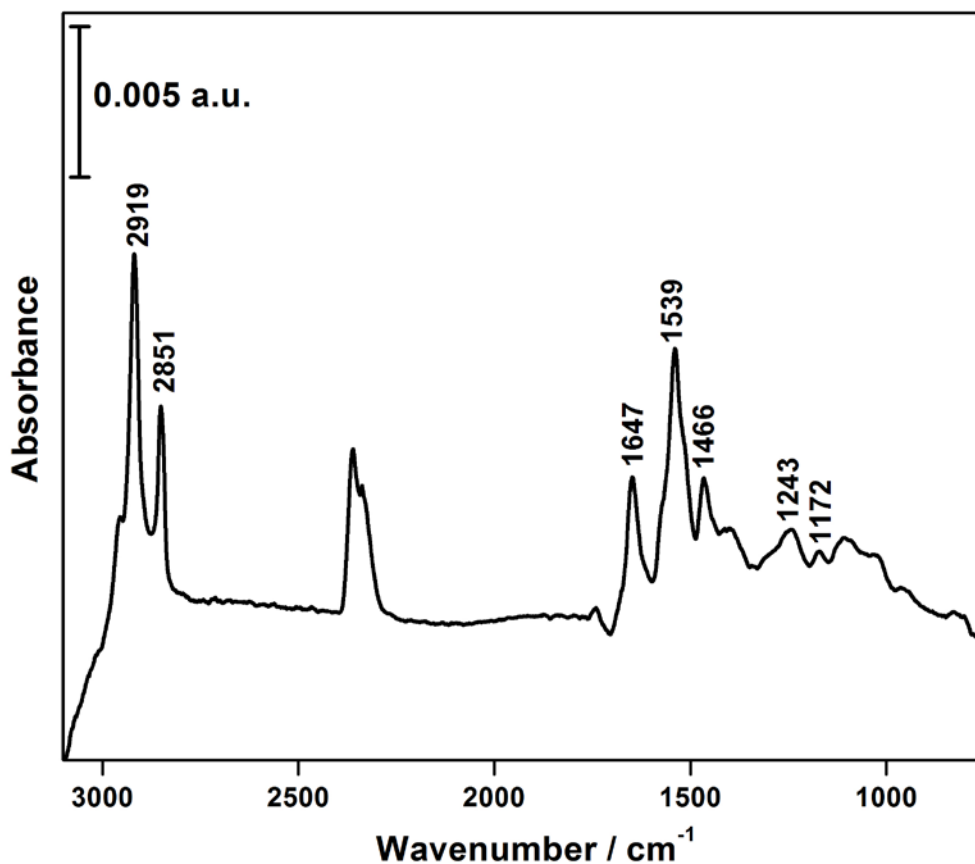


Figure 44: ATR-FTIR of 2 mg / mL human insulin solution prepared in 0.1 M NaCl and 12M HCl solution at a pH of 1.6. The spectrum was collected using a diamond window for 190 scans.

5.5.3 Electrochemical Surface-Enhanced Raman Spectroscopy (EC-SERS)

Native human insulin was characterized using EC-SERS to observe any structural changes occurring as potential was varied. A bare AgNP electrode was incubated in human insulin solution for 24 hours, rinsed and transferred to 0.1 M NaF and the EC-SERS data was recorded, as seen in Figure 45. At OCP there were several protein peaks present in the range 400-500 cm^{-1} such as 423 cm^{-1} and 493 cm^{-1} which are due to (S-S) stretch and ring deformation of phenylalanine, respectively.²³² Peaks were also present in the range of 1000-1300 cm^{-1} such as 1023 cm^{-1} , 1083 cm^{-1} , 1192 cm^{-1} which are due to phenylalanine $\delta(\text{CH})$, (C-N) stretch, and $\nu(\text{CCN})$ of phenylalanine / tyrosine, respectively.^{232,233} In the range of 1300-1650 cm^{-1} peaks at 1302 cm^{-1} , 1365 cm^{-1} , 1444 cm^{-1} , 1593 cm^{-1} , and 1616 cm^{-1} were present which are due to CH_2 bending, tryptophan CH_2 bending, phenylalanine / hydroxyproline, and (C=C) stretch of tyrosine / tryptophan.²³³ Based on the OCP spectrum it is clear that human insulin was able to adsorb onto the AgNP surface.

As the potential was stepped negatively the signal increased drastically and more peaks appeared. The maximum SERS signal of human insulin was obtained at -0.9 V. Some of the peaks that were present include peaks for cysteine, methionine, phenylalanine, and glutamic acid at 542 cm^{-1} , 633 cm^{-1} , 1100 cm^{-1} , and 1590 cm^{-1} , respectively. Other peaks include C-N asymmetric stretching (1303 cm^{-1}), CH_2 bending and stretching (1454 cm^{-1} and 2933 cm^{-1} , respectively), phenylalanine ring breathing (1080 cm^{-1}), and CH_2 wagging vibration from proline side chain (1202 cm^{-1}).^{127,234} Other peak assignments are shown in the appendix section in Table A-4. The EC-SERS signal

obtained was very useful in providing a spectral profile of native human insulin on the AgNP electrode. In the majority of cases SERS analysis of proteins is typically difficult due to their large molecular area, weak scattering of the majority of the amino acids and their weak physisorption on metallic surfaces.²³⁵ However, applying a potential can help in analyzing protein by changing the surface charge which can influence surface adsorption for proteins depending on their charge. These results show for the first time that EC-SERS can be used for analyzing non-heme protein adsorption at electrified interfaces.

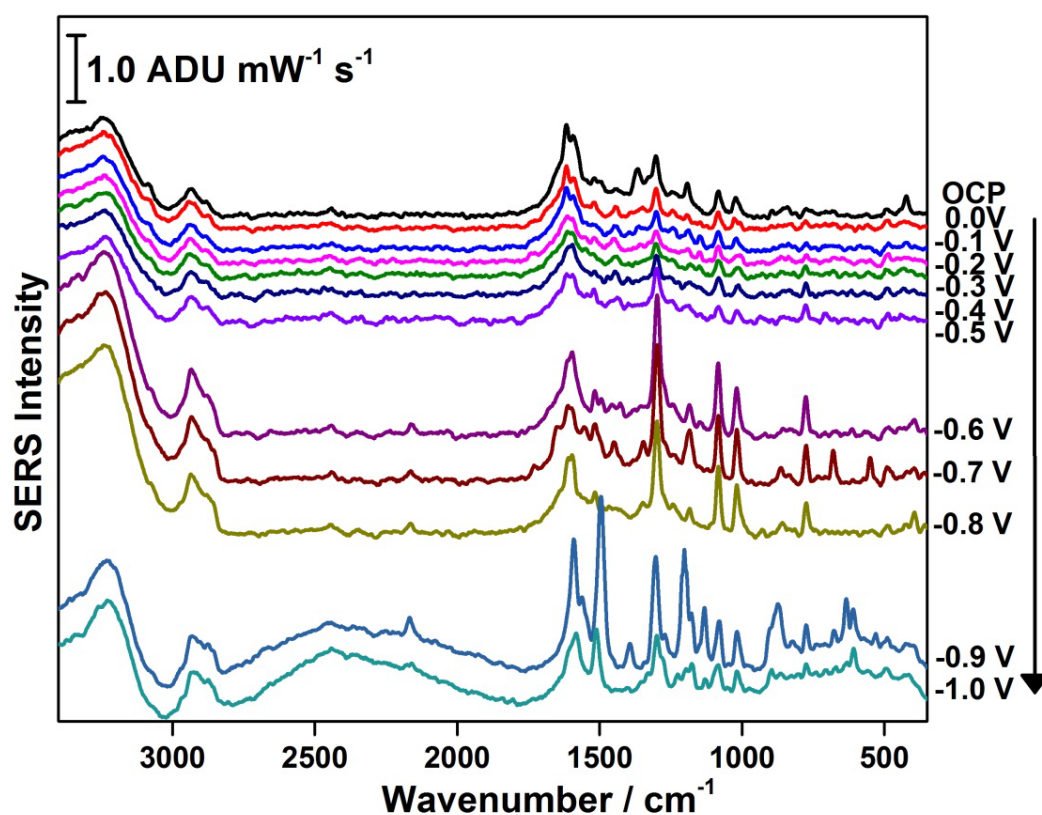


Figure 45: EC-SERS cathodic signal of native human insulin in 0.1 M NaF solution. The spectra were measured at 4 mW for a time interval of 30 seconds using 532 nm excitation.

5.6 Characterization of aggregated insulin

Aggregation of human insulin is a crucial step in this research work. Conditions were chosen for the aggregation pathway based on reports in the literature. The conditions that have been reported to cause accelerated protein aggregation are low pH, high temperature, mechanical stress, and agitation.²³⁶⁻²³⁹ The conditions used in this research involved preparing human insulin in an acidic 12 M HCl / 0.1 M NaCl solution at pH 1.6, and heating the resulting solution at 65 °C for several hours until the aggregation process was fully complete. These parameters have been used in literature by many researchers to aggregate different types of amyloid-forming proteins.²³⁷⁻²³⁹ Once insulin was aggregated under these conditions, it was further characterized using various techniques in order to confirm that the aggregation process was successful.

5.6.1 Raman spectroscopy

Once human insulin was fully aggregated, the Raman spectrum of the solution was obtained. As seen in Figure 46, it is clear that the signal obtained was very similar to the Raman signal of native human insulin solution (refer to Figure 42). Most of the peaks that were observed in the aggregated human insulin spectrum are found in either the powder or solution spectra of native human insulin (Figure 41 and 42). Some of the peaks that were present in the aggregated human insulin solution spectrum are 1303 cm^{-1} (CH_3 and CH_2 twisting), and 1374 cm^{-1} (tryptophan).²³³ The amide I band was observed at lower wavenumber (1636 cm^{-1}) which indicates that human insulin is present in a β -sheet conformation.²³³ This result showed that Raman spectroscopy is able to

characterize a concentrated solution of aggregated human insulin. Also, it has the ability to monitor structural conformation based on shifts in the amide I band.

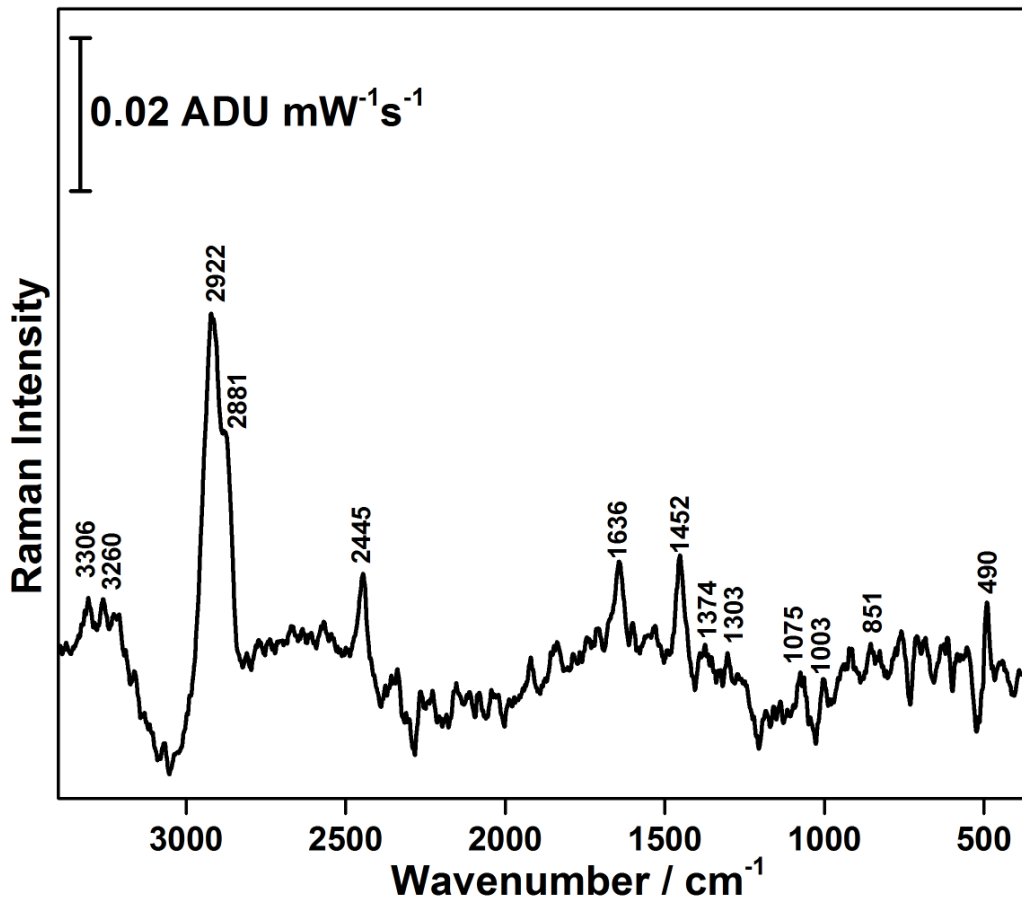


Figure 46: Raman spectrum of aggregated recombinant human insulin solution collected for 30 seconds at a laser power of 4 mW at 532 nm excitation.

5.6.2 ATR-FTIR

ATR-FTIR was able to monitor changes during the aggregation pathway, and all the amide peaks were observed for the native and aggregated insulin. Amide III and Amide II were observed at 1220 cm⁻¹ and 1540 cm⁻¹, respectively and they did not shift position upon aggregation. As seen in Figure 47, the amide I clearly showed a shift in

wavenumber as insulin was aggregated. In the native state (spectrum a) the amide I was observed at 1652 cm^{-1} which suggests that insulin is present as primarily α -helical structure, consistent with literature. In the oligomer state (spectrum b) the amide I is still in the same position suggesting that insulin has not undergone structural changes yet. In the protofibrillar state (spectrum c) the amide I peak has shifted to lower wavenumber (1639 cm^{-1}) indicating that insulin is present in a β -sheet conformation. As insulin further aggregates and reaches the fibrillar state (spectrum d) it is evident that the amide I has shifted further to lower wavenumbers (1631 cm^{-1}) which is indicative that insulin has fully aggregated and exhibits a β -sheet conformation. This indicates that the aggregation process of human insulin was successfully conducted under the conditions chosen. ATR-FTIR was able to confirm the aggregation process through monitoring the shifts in the amide I band.

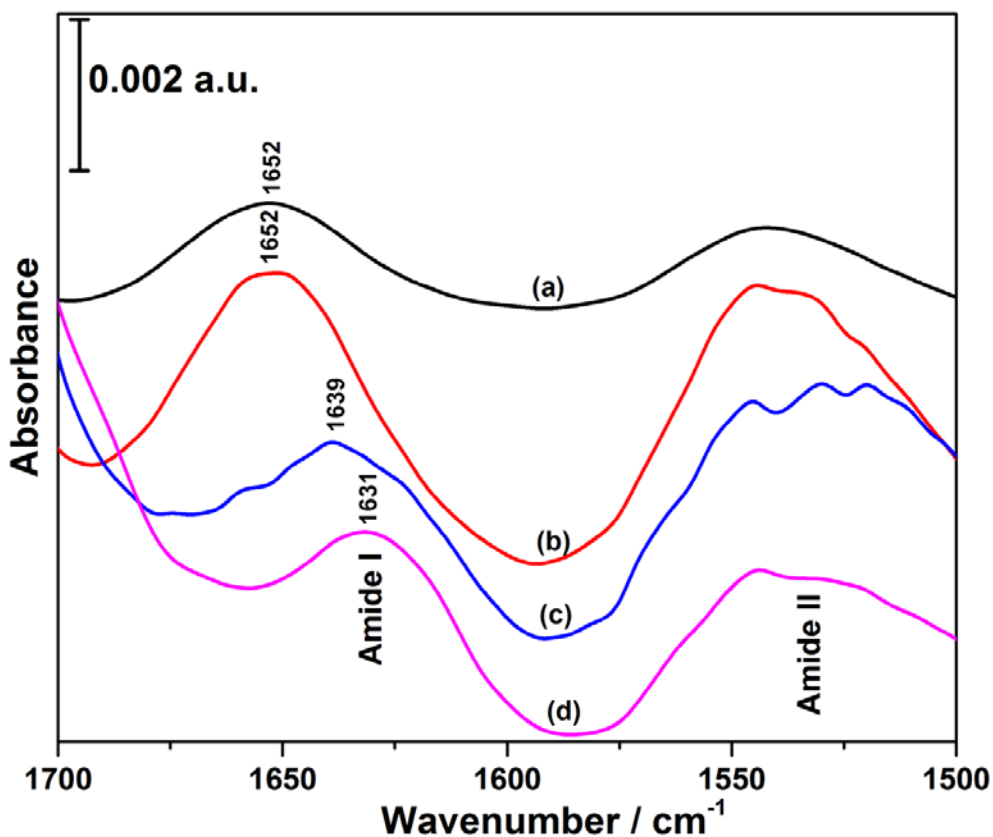


Figure 47: Comparison of ATR-FTIR spectra of (a) native human insulin, (b) oligomer, (c) protofibrillar, and (d) fibrillar insulin under conditions of pH 1.6 and temperature of 65 °C.

5.6.3 EC-SERS

The EC-SERS of the aggregated human insulin was obtained as seen in Figure 48. At OCP there were only a few peaks that arise due to the presence of protein. For example, peaks at 1176 cm⁻¹, 1284 cm⁻¹, 1459 cm⁻¹, 1597 cm⁻¹, and 1641 cm⁻¹ are due to $\nu_{as}(\text{CCN})$ stretch of tyrosine, histidine ring breathing, tyrosine ring stretching, C=O stretching of glutamic acid, and amide I, respectively.^{234,240} As the potential was stepped negatively more peaks appeared and the signal was maximal at -0.5 V. This observation was similar to the EC-SERS obtained for the native insulin where the signal started to

increase at -0.5 V. This showed that the aggregated protein has a stronger affinity for the AgNP surface when the surface charge is slightly positive which is around the potential of zero charge (pzc) of silver (-0.95 V vs. Ag / AgCl). Some of the protein peaks observed included tyrosine ring deformation (622 cm^{-1}), cysteine (C-S) stretch (676 cm^{-1}), symmetric vibration of tryptophan (743 cm^{-1}), (C-C) / (C-N) stretch of protein (1153 cm^{-1}), amide III (1233 cm^{-1} , 1273 cm^{-1}), tyrosine ring stretch (1338 cm^{-1}), and (N=H) bending (1506 cm^{-1}), respectively.^{234,240,241}

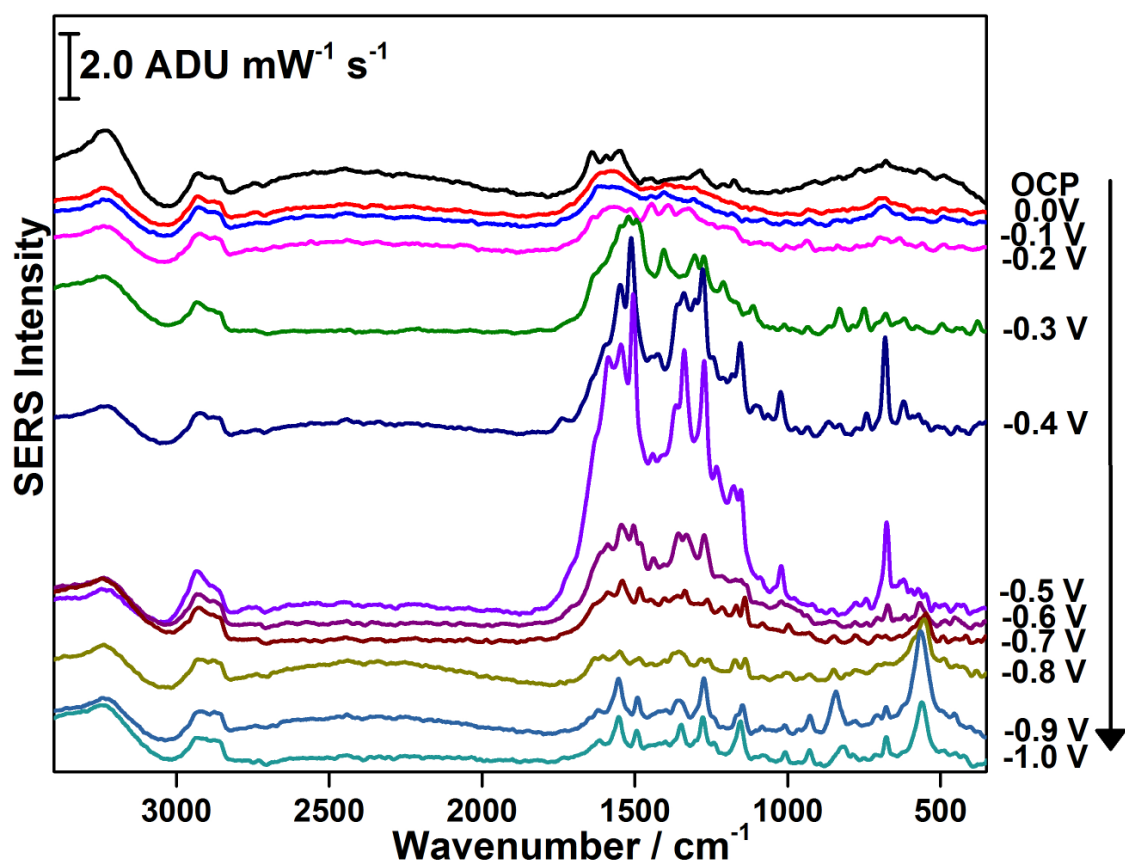


Figure 48: EC-SERS cathodic signal of aggregated human insulin in 0.1 M NaF solution. The spectra were measured at 4 mW for a time interval of 30 seconds using 532 nm excitation.

5.6.4 Turbidity measurements

One of the common methods used to monitor protein aggregation is using turbidity measurements. As protein aggregates, the solution becomes turbid and more light will be scattered indicating the presence of particles in the solution.^{242,243} Some of the advantages of using turbidity include ease of operation, no sample modification, minimal sample preparation, fast results, and non-destructive nature. As shown earlier in Figure 5, a sigmoidal behaviour can be observed through these measurements. Based on the results obtained in this experiment (Figure 49) it was very clear that the aggregation pathway followed the same pattern as reported in literature.^{52,244,245} It was observed that the lag phase lasted almost 50 minutes before the growth regime began. After 50 minutes, human insulin was present in the oligomeric state where it further aggregated to reach the protofibril state.²³⁷ The time at which the rate of formation of protofibrils is maximal can be obtained by taking the first derivative of this sigmoidal function. By doing this, it was concluded that the maximum rate of formation of protofibrils occurs at approximately 87 minutes. Further aggregation resulted in the formation of fully formed fibrils where the sigmoidal graph reaches a plateau region.²³⁷ This experiment was a preliminary step to determine the length of time required to form the various aggregates.

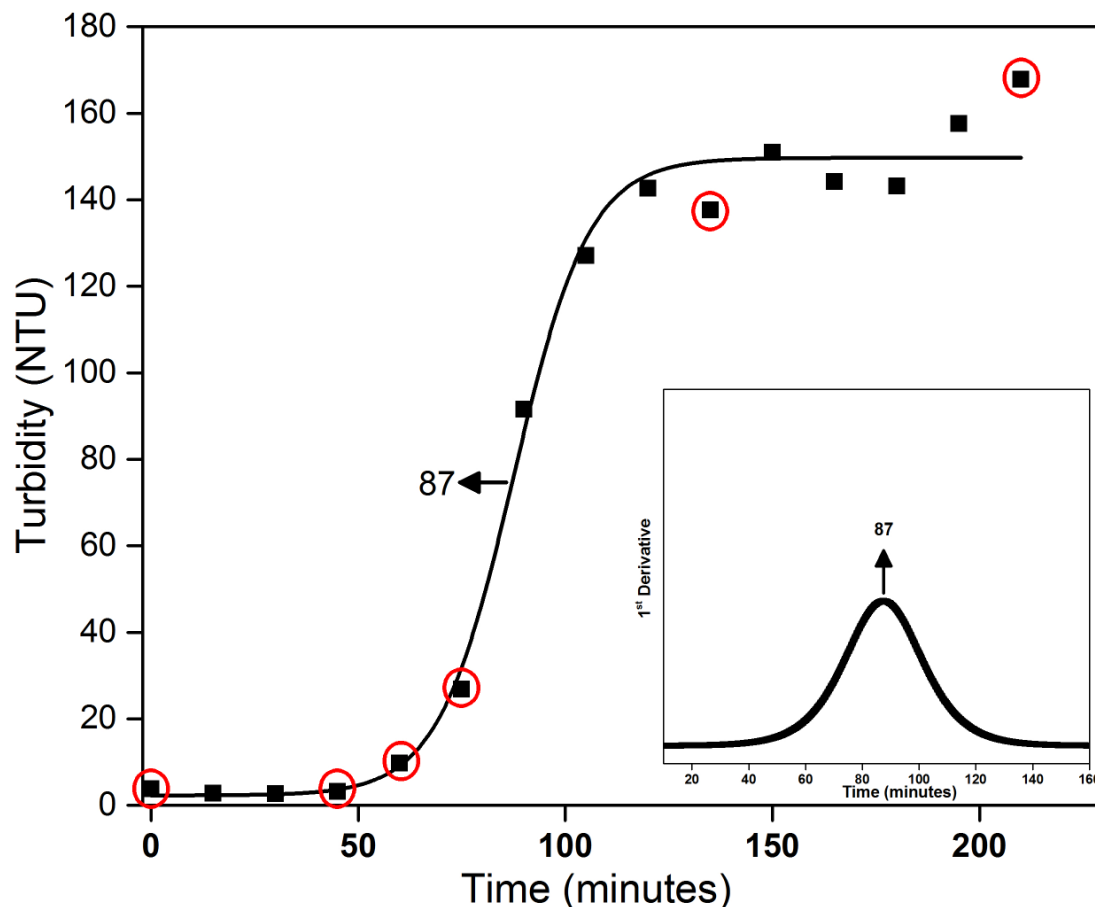


Figure 49: A sigmodal graph showing the aggregation process of recombinant human insulin at a concentration of 2 mg / mL. Circled points indicate times at which TEM was collected.

5.6.5 Transmission electron microscopy (TEM)

One of the common techniques used to provide evidence of the aggregate structure of amyloidogenic proteins is TEM.^{36-38,246,247} TEM has the capability of rendering images of the distinctive fibrillary nature of these proteins. TEM is used for visualization of proteins because it provides high resolution images and sample preparation is fairly simple.²⁴⁷ In literature, it has been shown that TEM has the ability to image objects on the order of a few Angstroms ($1 \text{ \AA} = 10^{-10} \text{ m}$) by using an electron beam that is transmitted through the specimen of interest.^{246,247} In this research TEM was used

to monitor the aggregation process and provide detailed information about the structure of these aggregate species. Native and aggregated insulin was placed on a copper grid and negatively stained using 2% uranyl acetate.²⁴⁷ Uranyl acetate is widely used in literature to stain protein, lipids, and DNA in order to enhance the contrast in electron microscopy.^{248,249}

The times chosen were at 0, 45, 60, 70, 135, 240 minutes as denoted in Figure 45. As seen in Figure 50, the TEM images obtained showed that at different times the protein exhibited a fibrillar nature however there were variations in the structures. At zero minutes (image a) the protein should be present in its native state, by looking at the TEM small and thin fibrils were observed. At 45 minutes the protein had started to aggregate but had not yet reached the growth phase. This explains the small amount of fibrils observed in the TEM image (image b). In addition, the fibrils were short in length and thin in diameter. At 60 minutes, there were more fibrils formed and they were longer in length and thicker in diameter (image c). At 70 minutes, the fibrils started to accumulate together and form longer and thicker fibrils (image d). At 135 minutes, the fibrils were accumulated together such that it became hard to see the diameter of these fibrils but they get larger in size as the protein is fully aggregated (image e). At 240 minutes, the surface of the grid was covered with fibrils with varying sizes and lengths (image f). Clumps of fibrils were formed and connected to each other by small branches. It is evident that the length and thickness of these fibrils increased drastically as the protein was aggregated. The native protein (image a) had a length and thickness that were measured to be 280 ± 102 nm and 11 ± 1 nm, respectively. The aggregated protein (image f) had a

length and thickness that were measured to be 5043 ± 736 nm and 311 ± 101 nm, respectively. These images proved that human insulin aggregates form fibrillary amyloid structures under the conditions used in this study which is consistent with studies found in literature.²⁴⁷

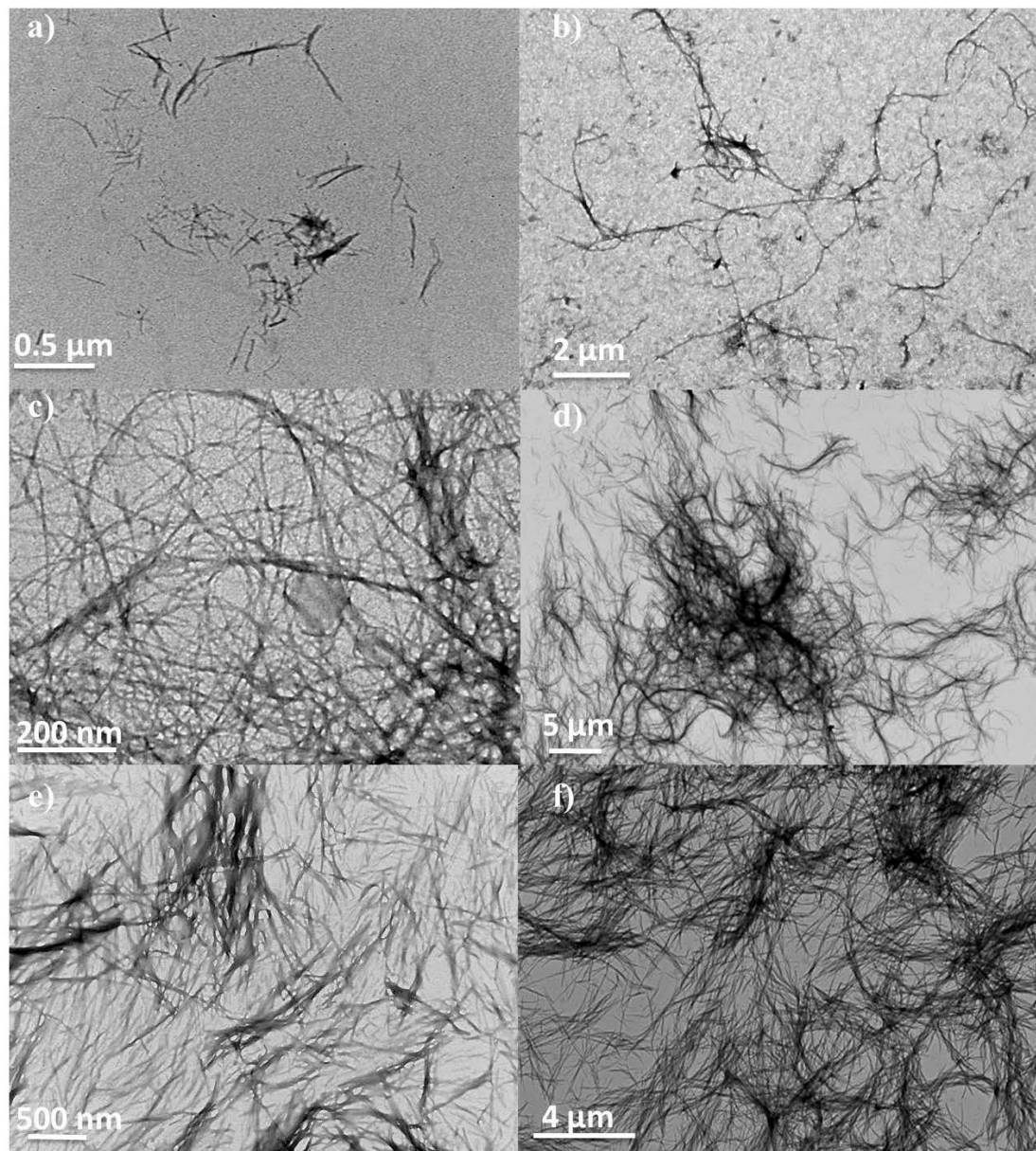


Figure 50: Transmission electron microscopy of 2 mg / mL recombinant human insulin at a) 0, b) 45, c) 60, d) 70, e) 135, and f) 240 minutes. Human insulin solution prepared in NaCl and HCl at pH of 1.6 and heated to 65 °C.

5.6.6 Scanning electron microscopy (SEM)

SEM is another microscopic technique that was also used to provide images of the human insulin aggregates. SEM does not provide as high resolution images as TEM does; however, it can provide more information such as morphology, topography, crystalline structure and orientation of minerals in samples.²⁵⁰ In addition, when paired with EDS, chemical composition can be ascertained.²⁵⁰ In this research, SEM images were obtained at different times during the aggregation process in order to observe the morphology of these aggregates. One of the major issues faced while imaging the samples was the presence of large amounts of salt, mostly NaCl. As seen in Figure 51, the images shown represent salt crystals forming on top of the SEM substrate which made it difficult to image the protein. To overcome this problem, human insulin was prepared in a solution containing only HCl without the presence of NaCl. However, when the turbidity measurements were done on this solution, a sigmodal graph was not obtained which indicated that the salt is necessary for the aggregation process.

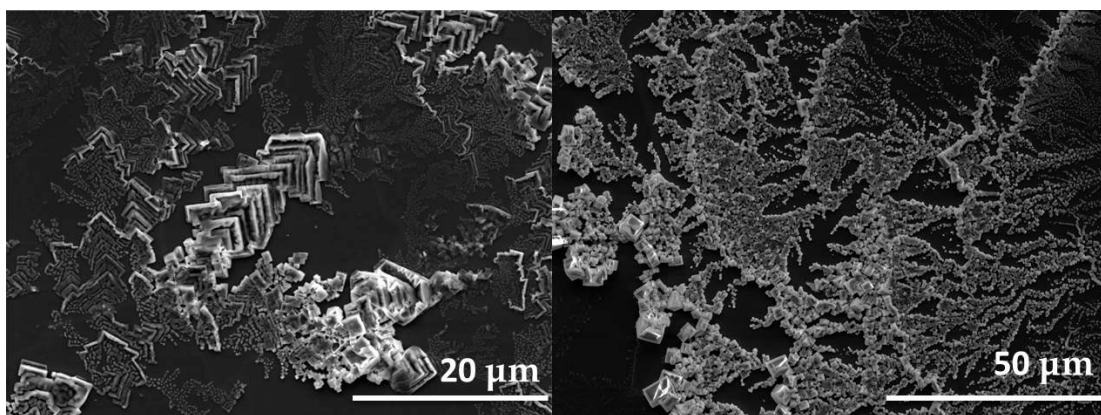


Figure 51: Scanning electron microscopy (SEM) of NaCl salt crystals. SEM images were conducted using Tescan MIRA3 LMU Field Emission under high vacuum mode at 10 kV, and at a scanning speed of 32.00 µs / pixel.

Significant work has been completed on rinsing the SEM substrates after the deposition of protein to remove the presence of salt. Even though this method showed success in removing salt, it was found that images of protein can be obtained without this rinsing procedure. In order to obtain good quality SEM images of the insulin aggregates, it was essential to image locations that did not have any salt interference. Initial studies involved looking at native human insulin, as seen in Figure 52. In this case the native insulin had a spherical shape with diameters ranging between 2 and 5 μm . It was interesting to observe that the human insulin spheres are joined together through a salt layer appearing as bright spots in SEM. This indicated that salt may play an important role in the nucleation step of amyloid aggregation. Also, this may explain why the aggregation process did not work in the absence of NaCl. These results show for the first time that SEM is capable of imaging spherical native insulin.

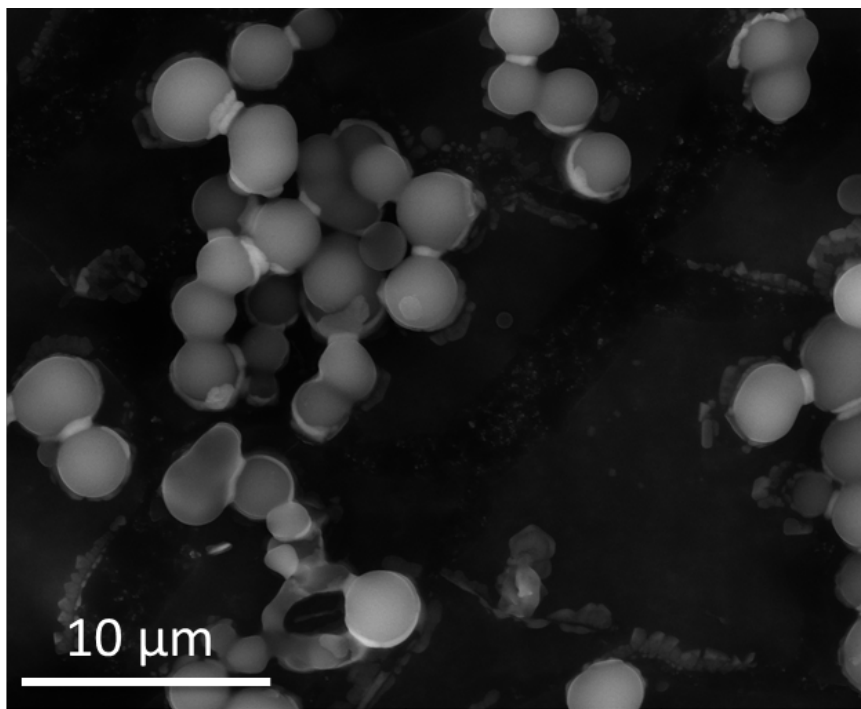


Figure 52: SEM image of native human insulin. SEM images were conducted using Tescan MIRA3 LMU Field Emission under high vacuum mode at 10 kV, and at a scanning speed of 32.00 μs / pixel.

Prior to performing any SEM imaging on aggregated human insulin it was interesting to image human insulin in its native state over time. The human insulin solution was prepared using the usual protocol (0.1 M NaCl / 12 M HCl solution, pH 1.6) and stored at room temperature for several weeks without any heating. By looking at the SEM image obtained in Figure 53, it was clearly evident that native human insulin does aggregate slowly at room temperature. The spheres were starting to aggregate together and eventually form a more fibrillar structure. This showed that human insulin does aggregate without the use of elevated temperatures; however, it would take months to years to reach fully aggregated structures under these conditions.

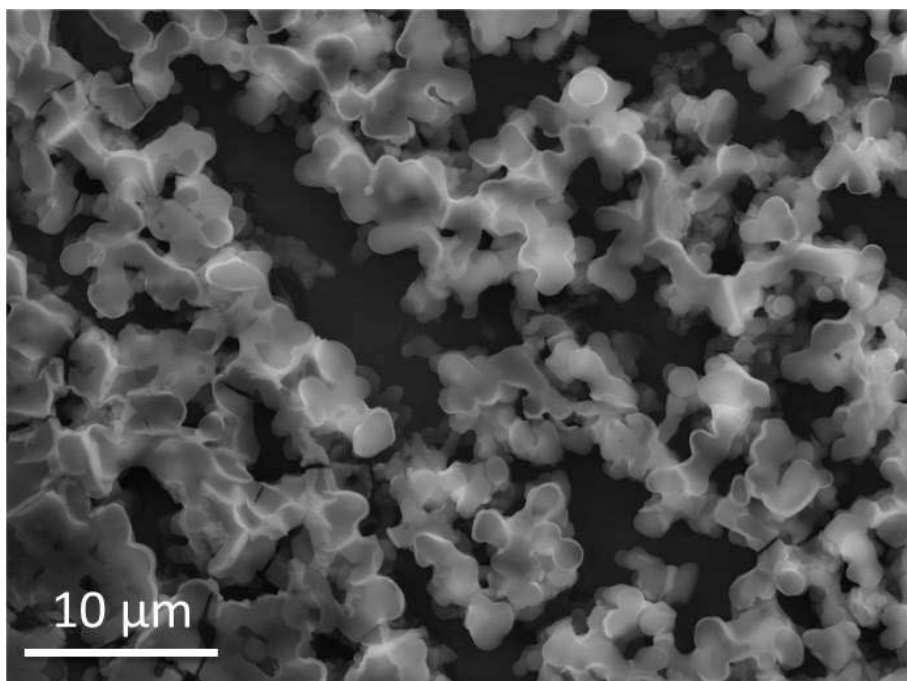


Figure 53: SEM image illustrating a 2 mg / mL native human insulin solution of pH 1.6 stored at room temperature for one month. SEM images were conducted using Tescan MIRA3 LMU Field Emission under high vacuum mode at 10 kV, and at a scanning speed of 32.00 μs / pixel.

In order to determine that the structures in these SEM images are in fact due to insulin aggregation, energy dispersive X-ray spectroscopy (EDS) was used. SEM can be coupled with EDS which is beneficial for elemental analysis and semi-quantitative analysis.²⁵⁰ An example of the X-ray spectra obtained is presented in Figure 54. The EDS spectra for the insulin aggregates showed carbon, nitrogen, oxygen, and sulfur which are common elements in proteins. Also, chlorine peaks were always present due to the presence of salt.

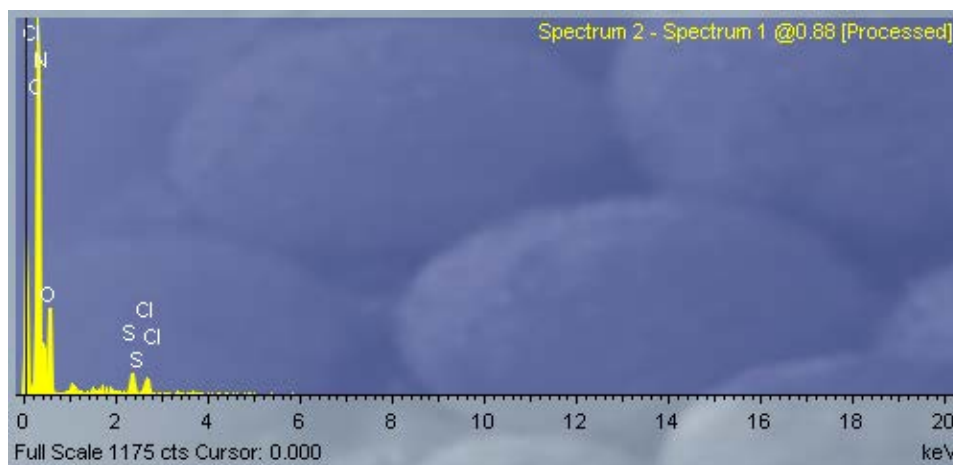


Figure 54: X-ray dispersive energy spectrum used for elemental analysis of human insulin.

Since the SEM was able to provide information on the native human insulin by avoiding spots that contained a lot of salt, the next step was to proceed with the aggregated form of insulin. The aggregation process of human insulin was imaged using the SEM, as shown in Figure 55. Image (a) shows that native insulin exhibits a hollow spherical shape which is commonly referred to in literature as a spheroidal,²⁵¹ or toroidal shape.²⁵² The size of these spheroids varies between 2.0 and 5.0 μm . After aggregating insulin for 45 minutes (image b) it was observed that many more spheres are formed all over the surface. This indicates that human insulin has started to aggregate and the spheres are close to each other with sizes varying between 0.5 to 1.0 μm . At 75 minutes (image c) further aggregation has resulted in major structural differences where the aggregates have increased in size dramatically. It was clear that the small spherical structures have accumulated together to form larger clumps that do not have a distinct structure and vary in size between 15.0 and 20.0 μm . At 90 minutes (image d) it was evident that the aggregates continued to grow in size and also branches between the

aggregates started to appear. These branches were more dominant at 120 minutes (image e). Protein branches seem to extend from the middle of aggregates and move away to connect with other aggregate clumps. It was observed that the size of the protein aggregates does not increase significantly but the presence of the branches allows it to cover more surface area. Once the protein was completely aggregated at 225 minutes (image f) more protein clumps and branches were present, and the size of the aggregate clumps varied between 50 and 100 μm .

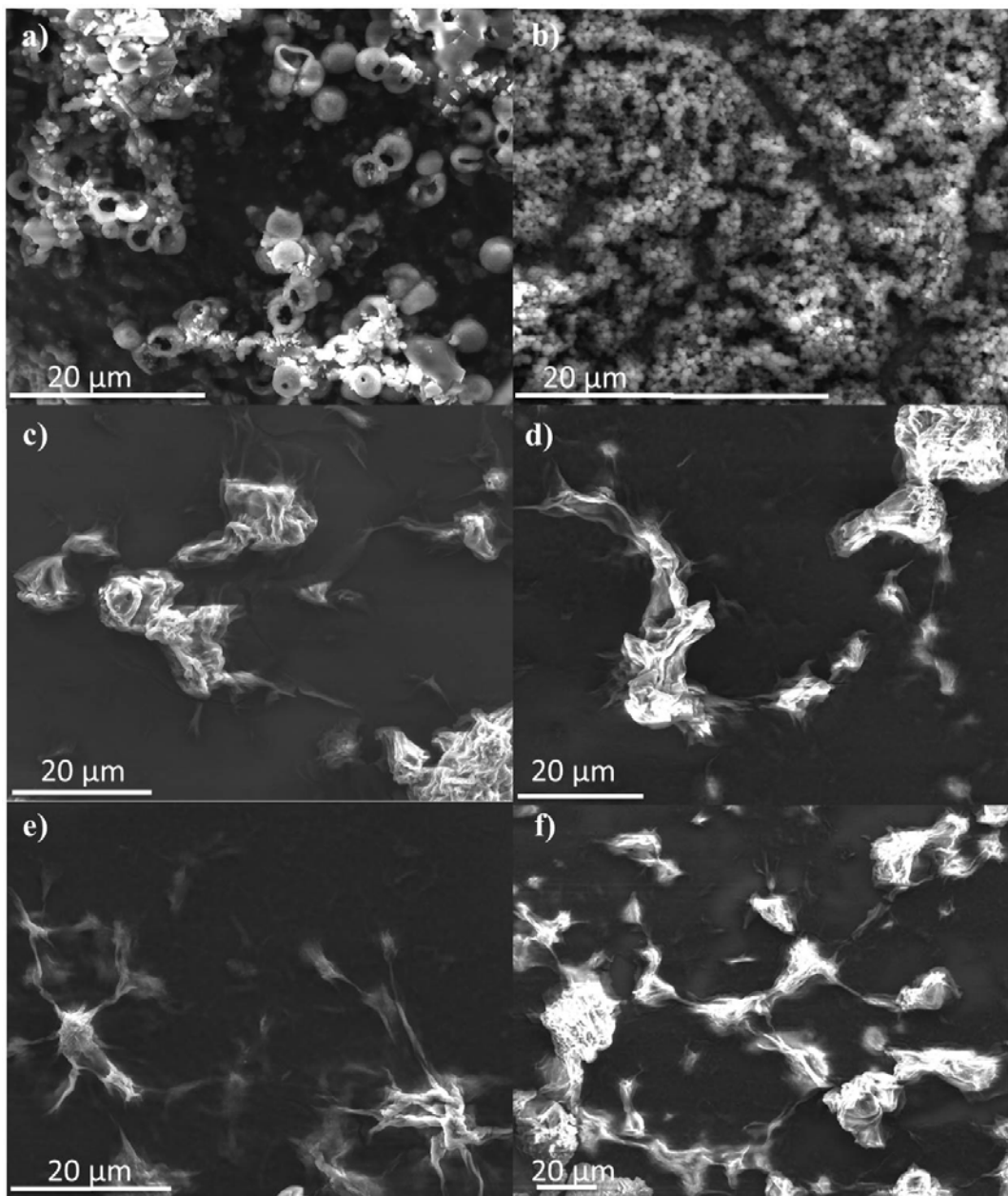


Figure 55: SEM images of human insulin aggregates at a) 0 b) 45 c) 75 d) 90 e) 135 and f) 225 minutes. SEM images were conducted using Tescan MIRA3 LMU Field Emission under high vacuum mode at 10 kV, and at a scanning speed of 32.00 $\mu\text{s} / \text{pixel}$.

The formation of protofibrils occurs rapidly during the aggregation process. One of the important aspects of this project was the ability to capture protofibrils and introduce them to the s-BLM. Once the protofibrils were formed the solution was kept at room temperature for several weeks in order to observe if the solution was stable over time. It was observed that the solution changed to a gel-like consistency after being stored at room temperature for a period of six weeks. An SEM image was obtained for this protofibril gel, as seen in Figure 56. The gel exhibited fibrillar morphology, with these fibrils having various lengths and thickness, all of which are connected to each other. This SEM image of the protofibril gel was similar to the fibrillar structure observed in the TEM images. Analysis on the diameter and length of these fibrils was difficult since the protein fibrils form a web-like system. It is important to note that once the protofibrils are prepared they are stable for one month when stored at low temperature (4 °C).

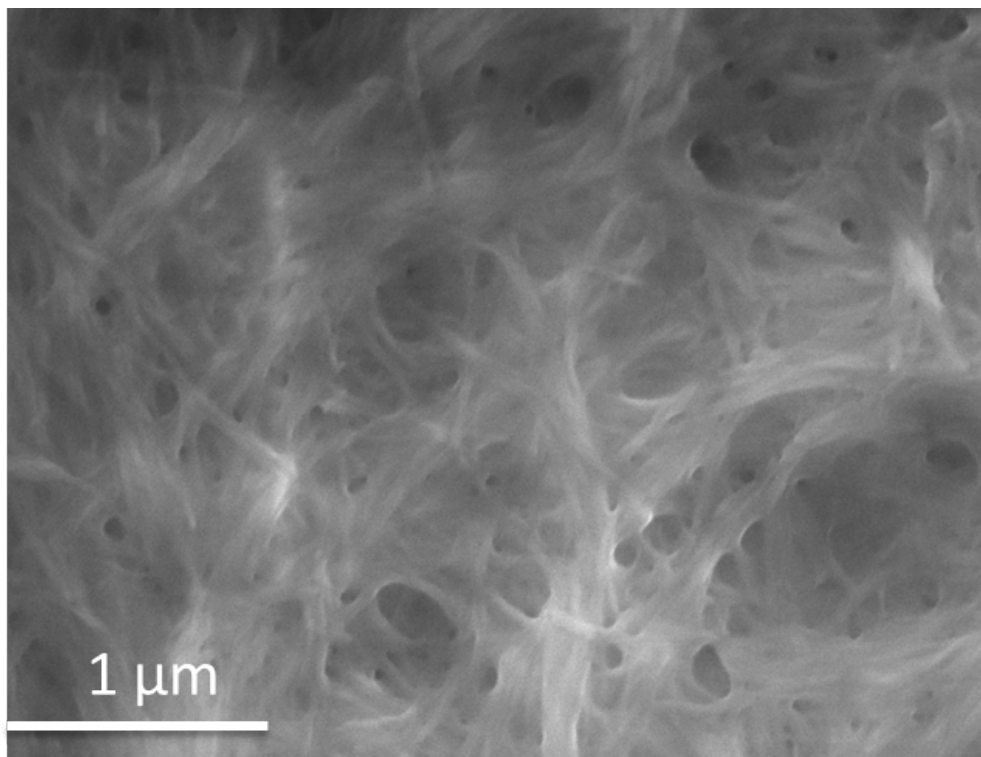


Figure 56: SEM image of 2 mg / mL protofibrillar human insulin gel stored at room temperature for weeks. SEM images were conducted using Tescan MIRA3 LMU Field Emission under high vacuum mode at 10 kV, and at a scanning speed of 32.00 μs / pixel.

5.7 Characterization of s-BLM + native insulin

5.7.1 s-BLM with native insulin

The amyloid pore hypothesis states that amyloid aggregates assemble themselves on cellular membranes and form defects and/or pores. Prior to studying the interaction between aggregated human insulin and a s-BLM, it was first necessary to complete a control study using human insulin in its native state to evaluate whether or not native insulin has any specific interaction with lipid bilayers. Figure 57 shows the EC-SERS signal obtained after a 6-MHA modified AgNP electrode containing a s-BLM was incubated in native human insulin for one hour. The OCP signal was similar to the s-

BLM in the absence of insulin (refer to Figure 34), which indicates that there is not much interaction between the membrane and the native protein. As the potential was stepped negatively some peaks appeared included C-C stretching and CH₂ wagging of DMPC (811 cm⁻¹, 1290 cm⁻¹), $\nu_{\text{as}}(\text{C-O-C})$ of glycerol ester group in DMPC (1184 cm⁻¹), $\nu_{\text{as}}(\text{P=O})$ of DMPC (1260 cm⁻¹), asymmetric bending modes of methyl group in DMPC (C-N⁺(CH₃) (1480 cm⁻¹), and CH₂ bending (1446 cm⁻¹).^{127,207} There was no significant change in the signal in the spectrum indicating the interaction between native insulin and the s-BLM. Therefore it can be concluded that native insulin does not cause any structural changes in the s-BLM. However, to fully prove this conclusion dAMP was introduced as a probe molecule.

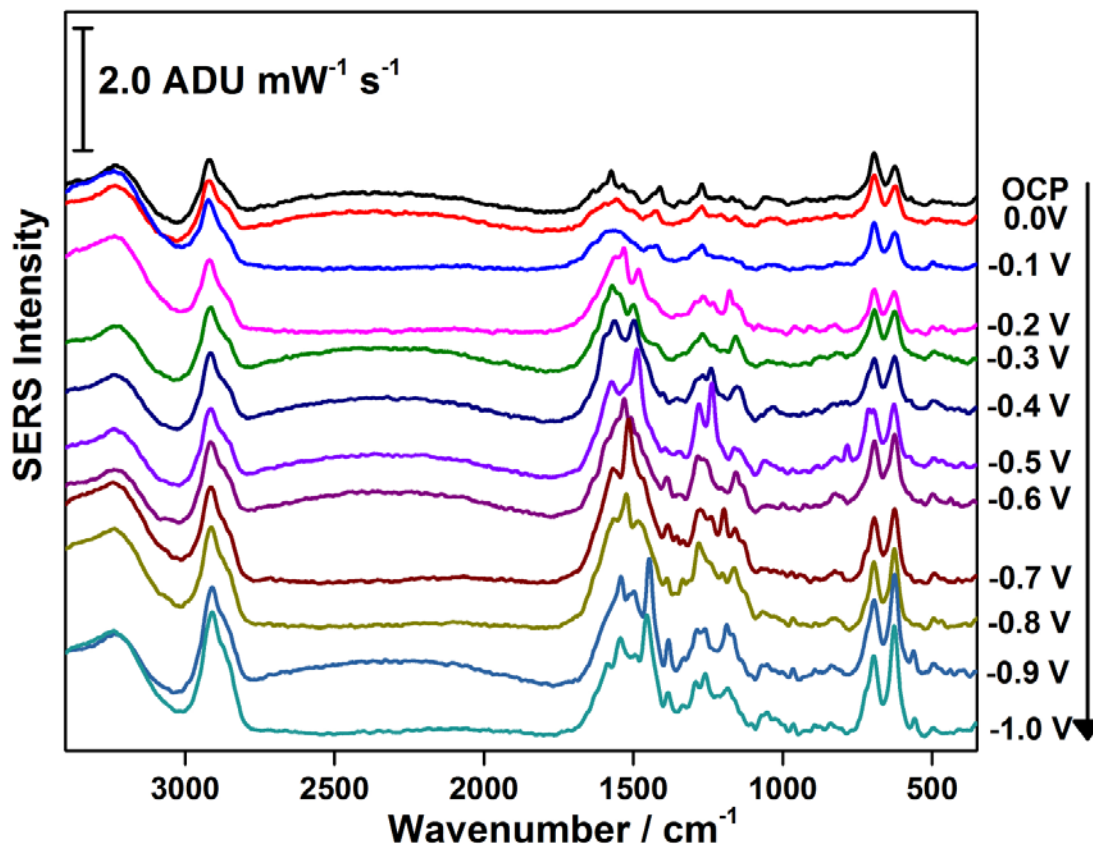


Figure 57: EC-SERS cathodic signal of 6-MHA modified s-BLM + native human insulin in 0.1 M NaF solution. The spectra were measured at 4 mW for a time interval of 30 seconds using 532 nm excitation.

5.7.2 s-BLM studies with dAMP in the presence of native insulin

The dAMP probe molecule is used to signal defects or pores in the membrane caused by native insulin. If there are any defects present, dAMP will make its way to the surface and peaks at 730 cm⁻¹ and 1328 cm⁻¹ will appear. Based on the signal obtained in Figure 58, at OCP there were no peaks indicative of dAMP. As the voltage was stepped negatively, more peaks appeared and the intensity of existing peaks were increasing as well. However, there were still no peaks indicative of dAMP, even at -1.0 V. This suggests that even under high electric field conditions, the dAMP was not able to

permeate through the lipid bilayer. This observation showed that in the presence of native insulin, electroporation is suppressed which suggests that insulin in its native state may play a protective role. In literature, it has been reported that some peptides can interact with the surface of a membrane without forming pores. This mechanism is referred to as the “carpet model” where the protein is spread on top of the membrane, and the positively charged amino acids are in contact with the polar head of the lipid molecules.²⁵³⁻²⁵⁴ After reaching a certain concentration of peptide, disruption of the membrane can occur. This model could explain why dAMP was not able to penetrate through the s-BLM, even under high electric field conditions. It is important to note that the 3223 cm^{-1} peak that is due to water O-H stretching is significantly higher than the alkyl chain peak which could indicate membrane permeation of water molecules.²⁰⁷ Some other peaks that were present at -1.0 V included DMPC (508 cm^{-1} , 571 cm^{-1} , 967 cm^{-1} , 1431 cm^{-1} , 2850 cm^{-1}), C-C stretching (822 cm^{-1}), CH_2 twisting (1282 cm^{-1}), and CH_2 rocking (1171 cm^{-1}).^{127,207} A comparison of s-BLM + native insulin in the presence and absence of dAMP is shown in Figure A-2 in the appendix section.

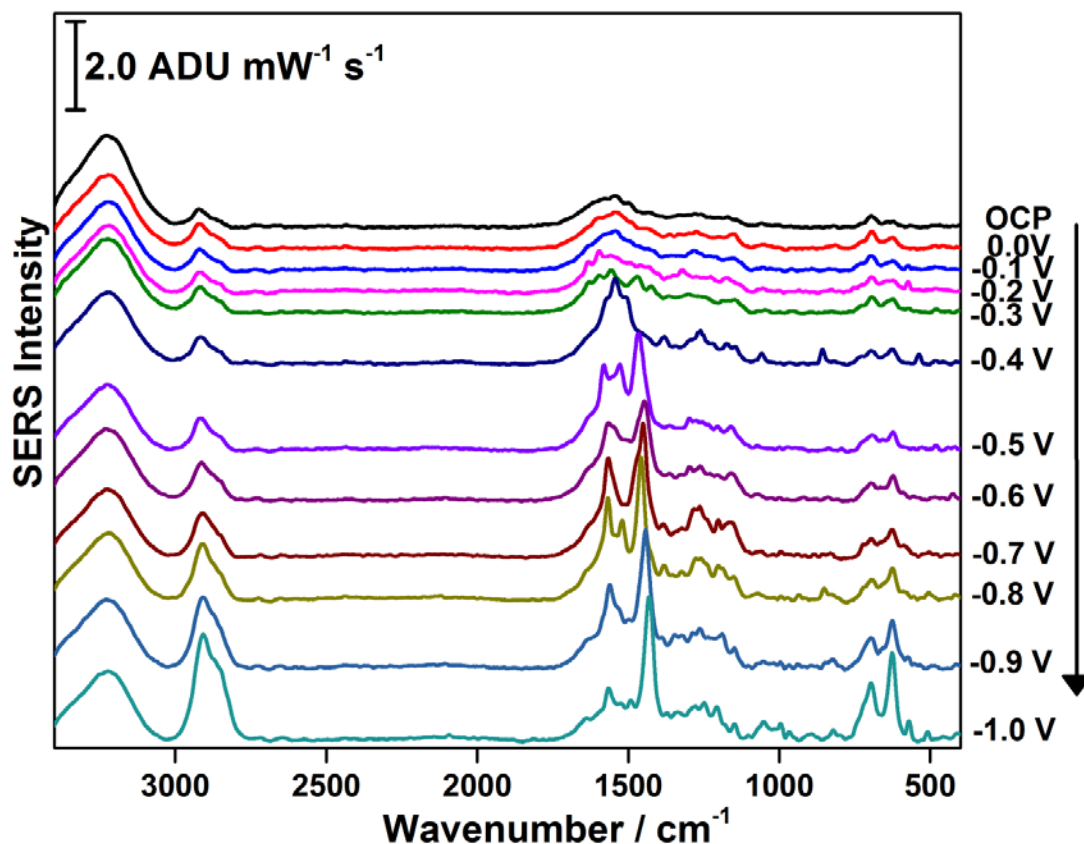


Figure 58: EC-SERS cathodic signal of 6-MHA modified s-BLM + native human insulin in 1.0 mM dAMP / 0.1 M NaF solution. The spectra were measured at 4 mW for a time interval of 30 seconds using 532 nm excitation.

5.8 Characterization of s-BLM + oligomeric insulin

5.8.1 s-BLM studies with oligomeric insulin

As mentioned earlier in section 4.6, at different times during the aggregation process human insulin was taken out of the reaction vial and introduced to the s-BLM. Oligomeric species are found prior to onset of the growth regime (refer to the sigmoidal curve in Figure 49). In literature, studies have shown that these oligomeric species can have toxic properties and their formation is considered an initiation step for the aggregation process.^{40,255,256} Based on the sigmoidal graph obtained it was clear that the

oligomers would form slightly below 50 minutes. For this case, a time of 45 minutes was chosen to capture the oligomers. Figure 59 shows the EC-SERS of a 6-MHA modified s-BLM in the presence of the human insulin oligomers. At OCP the EC-SERS was similar to the previous results, however some peaks such as 1100 cm^{-1} , and 1470 cm^{-1} which are due to CH deformation and C-C stretching of lipids, respectively, are more pronounced.^{127,257} As the potential was stepped negatively more peaks appeared. Further potential stepping resulted in a decrease in signal intensity which can be explained by degradation of the s-BLM. It is useful to study each region of the EC-SERS spectrum in order to gain full understanding of the interaction between the protein oligomers and lipid molecules.

The first region to consider is between 3500 cm^{-1} and 2500 cm^{-1} which consists mostly of the alkyl chains. The peak around 3226 cm^{-1} which is due to O-H and N-H stretching vibration is much larger in intensity than the 2913 cm^{-1} peak which is due to the CH stretch of lipid / proteins.^{127,207} The peak around 3226 cm^{-1} could be indicative of the presence of water molecules which may indicate that the membrane was being disrupted.¹²⁷ The second region to consider is between 2000 cm^{-1} and 1000 cm^{-1} . The polar head groups of the lipid molecules, and also the amino acid side chains from the protein are present within this region. Some of the peaks that were strongly present in this region are due to aromatic amino acids such as tyrosine (832 cm^{-1} , 861 cm^{-1} , 1212 cm^{-1}), proline (915 cm^{-1}), phenylalanine (1002 cm^{-1} , 1034 cm^{-1} , 1107 cm^{-1}), and tryptophan (1626 cm^{-1}). The presence of these peaks suggests that these amino acids are interacting with the substrate through electrostatic interactions. The amide III (1257 cm^{-1}) peak is

also observed, which suggests that the protein is present in a random conformation.²⁵⁸ The last region is between 1000 cm^{-1} and 500 cm^{-1} which is mostly due to the C-S stretching as shown earlier, however there are some peaks that were present such as 442 cm^{-1} , 483 cm^{-1} , and 566 cm^{-1} which are due to $\delta(\text{CCO})$ of 6-MHA, $\nu(\text{C-C-C})$ of 6-MHA and tryptophan, respectively.^{205,259} The EC-SERS of the s-BLM in the presence of oligomers provided different spectral features than the EC-SERS of the s-BLM in the presence of native insulin which suggests that oligomers might be interacting with the lipid molecules and causing disruption of the membrane.

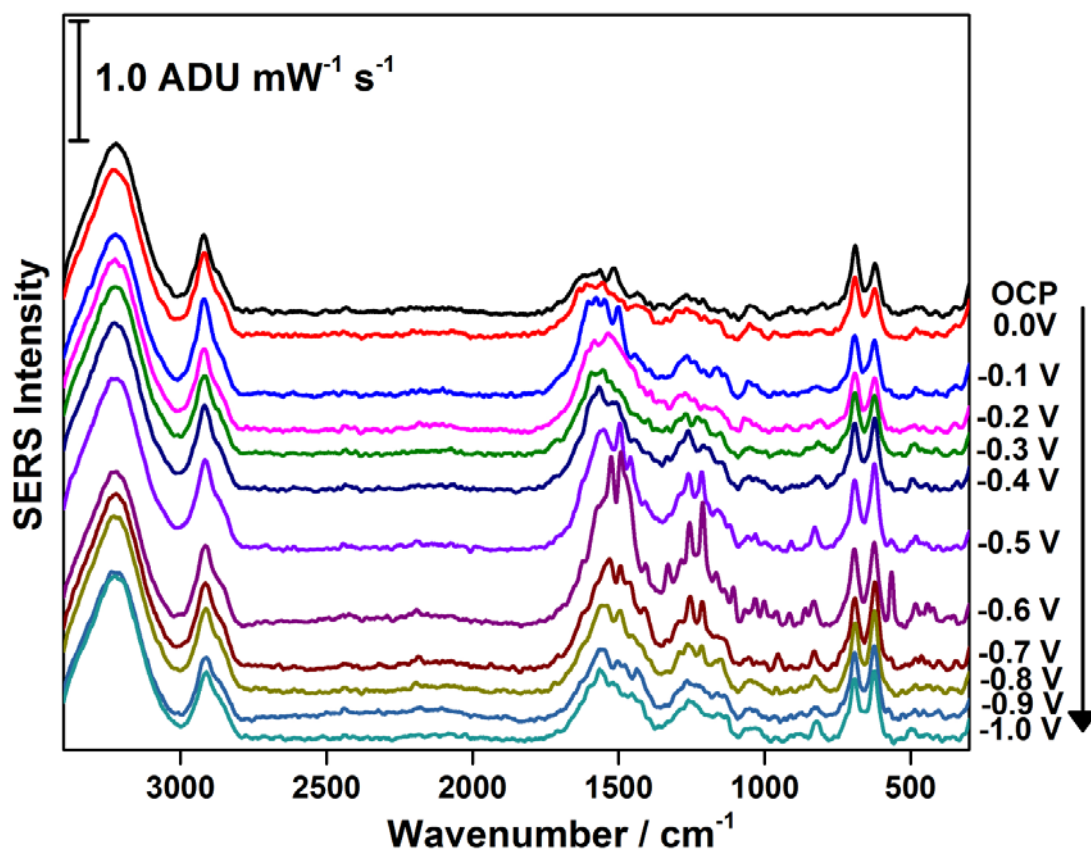


Figure 59: EC-SERS cathodic signal of 6-MHA modified s-BLM + human insulin oligomer in 0.1 M NaF solution. The spectra were measured at 4 mW for a time interval of 30 seconds using 532 nm excitation.

5.8.2 s-BLM studies with dAMP in the presence of oligomeric insulin

In order to further investigate whether oligomers cause defects in the s-BLM, dAMP was introduced. As seen in Figure 60, at OCP the dAMP peak at 730 cm^{-1} was strongly present which shows that dAMP was able to permeate through the s-BLM without an applied voltage. As the potential was stepped negatively, the dAMP peak was increasing in intensity as well as other peaks. The region between 2000 cm^{-1} and 1000 cm^{-1} showed some protein peaks such as phenylalanine (1105 cm^{-1} , 1219 cm^{-1}), and $\nu(\text{C-N})$ stretching (1051 cm^{-1} , 1153 cm^{-1} , 1254 cm^{-1}).^{127,207} The region between 1000 cm^{-1} and 500 cm^{-1} showed the same peaks as shown in Figure 55 except for the presence of the dAMP peaks and the appearance of a peak around 573 cm^{-1} which is due to tryptophan / tyrosine.¹²⁷ These studies indicate that oligomeric human insulin has the ability to form defects in the lipid bilayers without applying a voltage which allowed for permeation of molecules, in this case dAMP. A comparison of s-BLM + insulin oligomer in the presence and absence of dAMP is shown in Figure A-3 in the appendix section.

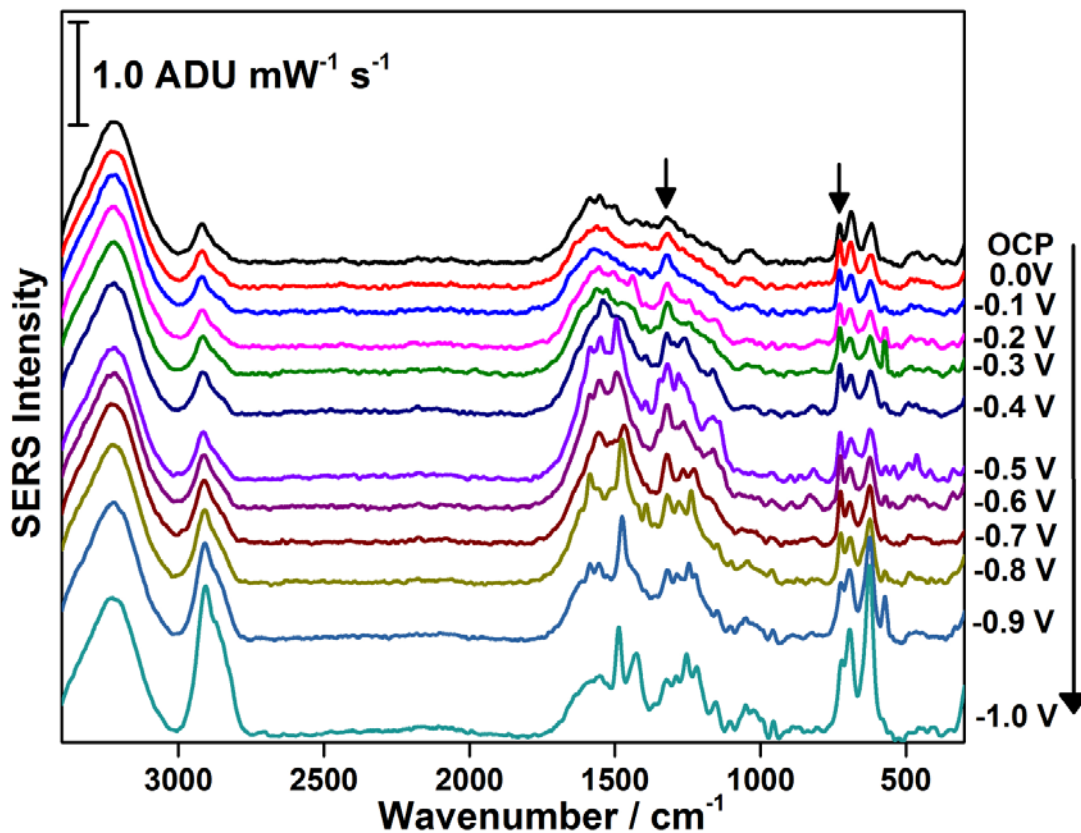


Figure 60: EC-SERS cathodic signal of 6-MHA modified s-BLM + human insulin oligomer in 1.0 mM dAMP / 0.1 M NaF solution. The spectra were measured at 4 mW for a time interval of 30 seconds using 532 nm excitation. dAMP peaks are indicated by arrows.

5.9 Characterization of s-BLM + protofibrillar insulin

5.9.1 s-BLM studies with protofibrillar insulin

Protofibrils have been known as the toxic species resulting from the aggregation process of amyloid proteins.^{53,54} The growth region on the sigmoidal curve consists of mostly protofibril species; the time chosen to capture protofibrils for this study was 75 minutes. The EC-SERS data showing the interaction between insulin protofibrils and the s-BLM is shown in Figure 61. At OCP there were some peaks present that were due to 6-MHA, DMPC and amino acids. As the potential was stepped in the cathodic

direction more peaks appeared and significant variation in signal at the different potentials occurred which suggests that the protofibrils are interacting with the lipid molecules. The strongest signal obtained was at -0.5 V which provides information about the lipid molecules and also the protofibrils. Many spectral features appeared between 2000 cm^{-1} and 350 cm^{-1} . For example, DMPC (592 cm^{-1} , 965 cm^{-1} , 1124 cm^{-1} , 1377 cm^{-1}), tryptophan (759 cm^{-1}), tyrosine (858 cm^{-1} , 1206 cm^{-1}), proline (942 cm^{-1}), cysteine (547 cm^{-1}), and amide III (1234 cm^{-1}).^{127,207} The position of the amide III indicates that insulin is present in its β -sheet conformation.²⁶⁰ This showed that the protofibrils do indeed interact with the lipid molecules and different spectral features appeared as a result. The protein peaks were present at stronger intensity which could indicate that the protein in this case is getting closer to the electrode surface. This suggests that it may be forming a pore, and that some of the hydrophobic amino acids are interacting with the hydrophobic region of the lipid molecules.

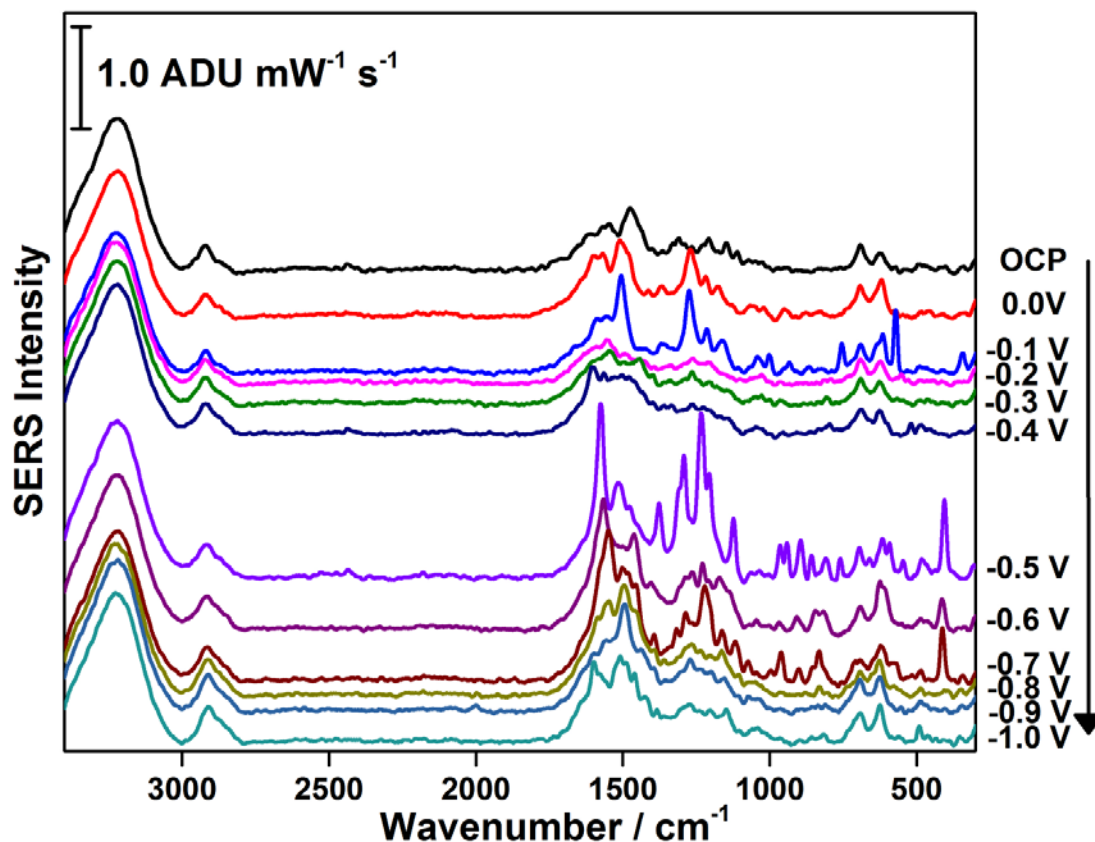


Figure 61: EC-SERS cathodic signal of a modified 6-MHA s-BLM + protofibrillar human insulin in 0.1 M NaF solution. The spectra were measured at 4 mW for a time interval of 30 seconds using 532 nm excitation.

5.9.2 s-BLM studies with dAMP in the presence of protofibrillar insulin

dAMP was used to signal the interaction between the protofibrils and the lipid molecules. In the OCP spectrum in Figure 62, the 730 cm^{-1} peak is strongly present which is similar to what was observed in the spectrum for the oligomers. As the potential was stepped negatively, the intensity of the peaks increased but there was not a lot of variation in signal. The strongest signal was obtained at -0.7 V where several peaks were observed, including peaks due to cysteine (531 cm^{-1}), phenylalanine (1006 cm^{-1}), tryptophan (1546 cm^{-1} , 1618 cm^{-1}), CH_2 deformation (1438 cm^{-1}), and amide III

(1256 cm^{-1}).^{127,207} This study has also shown that the presence of protofibrils causes defects to occur within the lipid bilayer which allows dAMP molecules to permeate and reach the surface. This finding is consistent with the suggestion that amyloid protofibrils perturb cellular membrane structures. A comparison of s-BLM + protofibrillar insulin in the presence and absence of dAMP is shown in Figure A-4 in the appendix section.

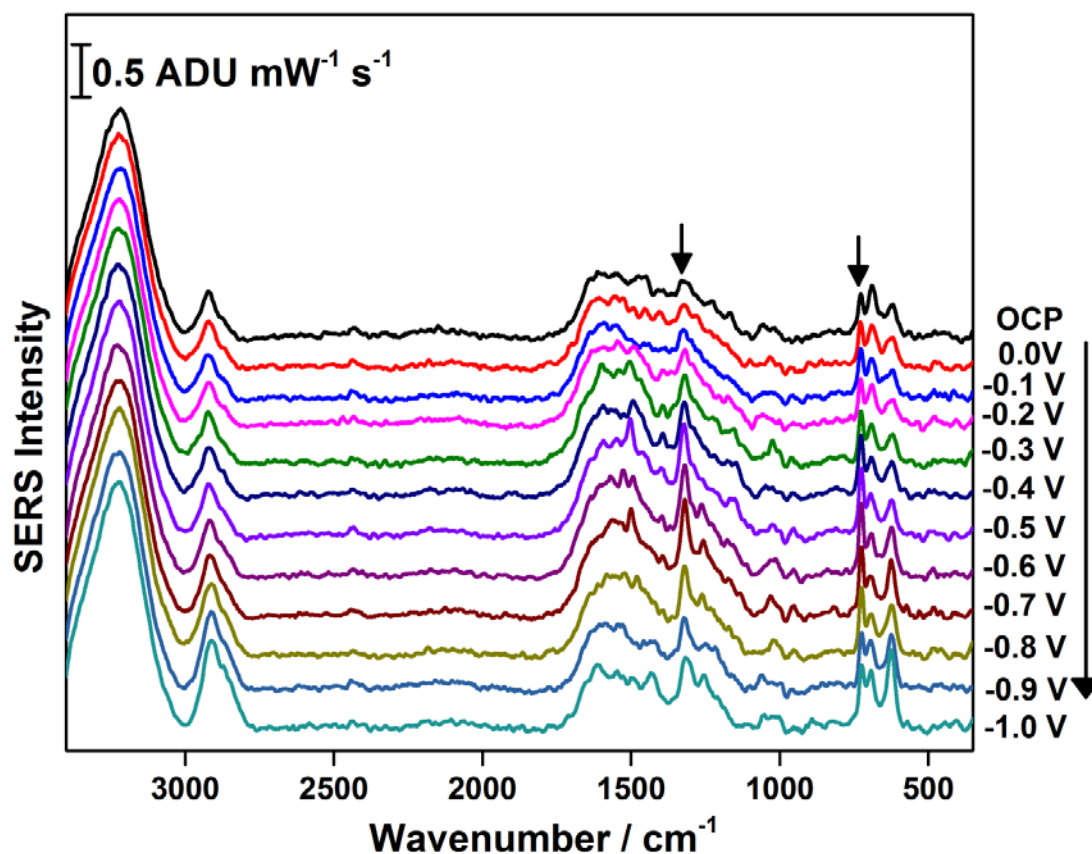


Figure 62: EC-SERS cathodic signal of a 6-MHA modified s-BLM + protofibrillar human insulin in 1.0 mM dAMP / 0.1 M NaF solution. The spectra were measured at 4 mW for a time interval of 30 seconds using 532 nm excitation. dAMP peaks are indicated by arrows.

In order to further understand the interaction between protofibrils and a lipid bilayer, cyclic voltammetry was conducted after the experiment. CV was always measured after EC-SERS analysis so as to not perturb the bilayer lipid membrane through electrochemical cycling. Figure 63 compares the cyclic voltammogram obtained for s-BLM in the presence and absence of protofibrils. The cyclic voltammogram of the 6-MHA modified s-BLM in the absence of protofibrils showed a low current which is indicative of the formation of a compact layer on the electrode surface. In the presence of protofibrils the current flow increases drastically, suggesting that the thickness of the s-BLM has decreased or defects have now formed. Also, redox peaks between -0.6 and -0.8 E / V of dAMP were observed.¹⁹⁶ This result could indicate that the protofibrils interact with the lipid bilayer causing defects to occur which can allow electrolyte ions and dAMP to penetrate through the s-BLM, and hence an increase in the current flow is measured. The redox features are consistent with dAMP.

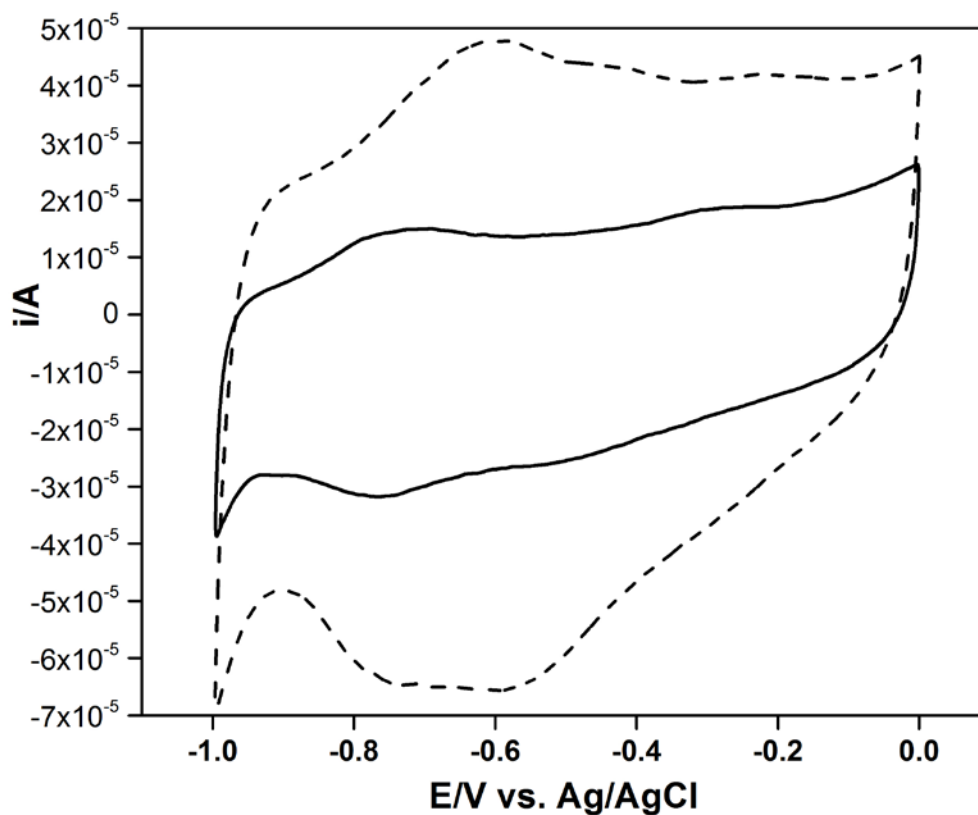


Figure 63: Comparison between s-BLM on AgNP electrode (solid line), s-BLM in the presence of protofibrils (dashed line). All comparisons are done in 1.0 mM dAMP / 0.1 M NaF solution. Scan rate: 50 mW / s.

5.10 Characterization of s-BLM + fibrillar insulin

5.10.1 s-BLM studies with fibrillar insulin

The literature indicates that fibrils do not play a toxic role in amyloidogenic diseases. Amyloid fibrils are found to have a negative correlation between pore formation and cytotoxicity and may therefore act as inert sinks that scavenge toxic oligomers and protofibrils.^{53,54} Figure 64 illustrates that as the potential was stepped negatively the peaks increased in intensity, without any variation in signal. This suggested that the fibrils do not interact with the lipid molecules to the same extent as the oligomers and protofibrils. Also, the EC-SERS spectrum collected for the s-BLM in the

presence of fibrils look very similar to the EC-SERS spectrum obtained for the s-BLM in the absence of native insulin. Most of the peaks present are similar to previous studies; this includes peaks due to tyrosine (833 cm^{-1}), proline (919 cm^{-1}), C-C / C-N stretching (1154 cm^{-1}), and amide III (1260 cm^{-1}).¹²⁷

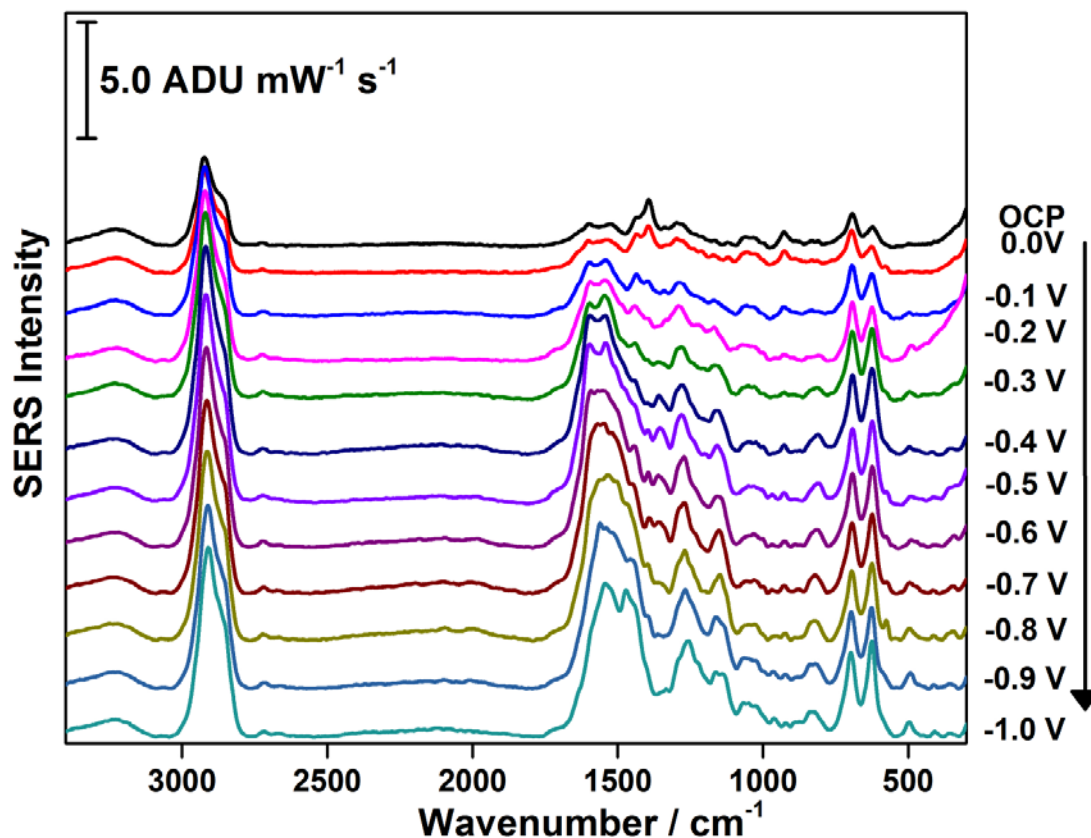


Figure 64: EC-SERS cathodic signal of a 6-MHA modified s-BLM + fibrillar human insulin in 0.1 M NaF solution. The spectra were measured at 4 mW for a time interval of 30 seconds using 532 nm excitation.

5.10.2 s-BLM studies with dAMP in the presence of fibrillar insulin

It is important to investigate whether the fibrils would have the same effect as the oligomers or protofibrils on the s-BLM. In Figure 65, the dAMP signal at OCP is not as strong as it was in the spectra for the oligomers and protofibrils (refer to Figure 60 and

Figure 62). As the potential was stepped negatively the peaks started to appear, and the 730 cm^{-1} peak was present. This suggested that dAMP was able to permeate through the lipid molecules but the peak intensity was not as strong as the oligomer or protofibrils. This could be due to the fact that fibrils do not cause as large of defects in the s-BLM as do the oligomers and protofibrils or that the dAMP molecules were not able to permeate fully through the s-BLM. The EC-SERS spectrum for insulin fibrils provided a different spectral profile than for the oligomers and protofibrils which indicates that each species interacts with the lipid molecules differently depending on their secondary structures. The peaks between 2000 cm^{-1} and 1000 cm^{-1} are due to tyrosine (834 cm^{-1} , 1163 cm^{-1}), tryptophan (1558 cm^{-1}), CH_2 bending of proteins (1447 cm^{-1}), amide III (1230 cm^{-1}), and CH_2 symmetric stretch of lipids / asymmetric stretch of proteins (2853 cm^{-1}).^{127,207} Also, the 2921 cm^{-1} peak is stronger in intensity than the 3226 cm^{-1} as the potential was stepped negative; this was completely reversed in the case of the previous studies involving the oligomer and protofibril. A comparison of s-BLM + fibrillar insulin in the presence and absence of dAMP is shown in Figure A-5 in the appendix section.

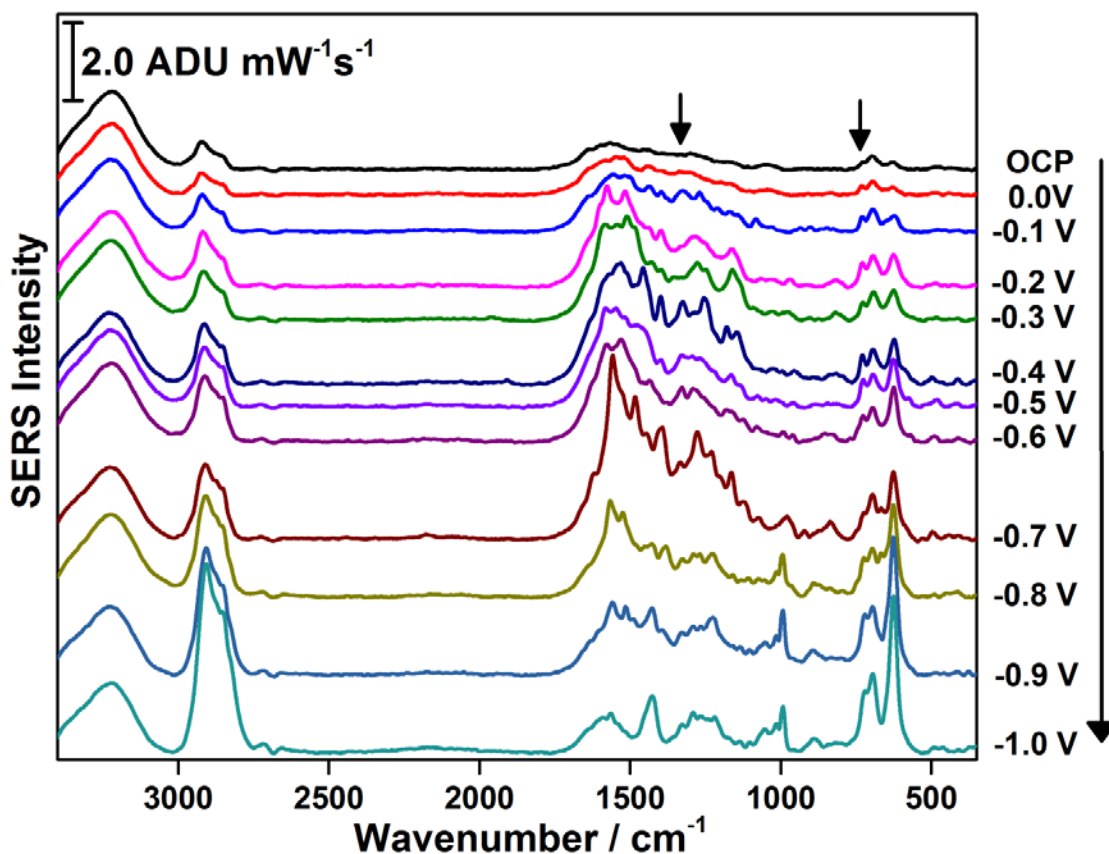


Figure 65: EC-SERS cathodic signal of a modified 6-MHA s-BLM + fibrillar human insulin in 1.0 mM dAMP / 0.1 M NaF solution. The spectra were measured at 4 mW for a time interval of 30 seconds using 532 nm excitation. dAMP peaks are indicated by arrows.

A CV comparison between the s-BLM in the absence of protein and the different protein aggregates (oligomers, protofibrils, and fibrils) in the presence of the s-BLM is shown in Figure 66. The s-BLM (short dotted line) shows desorption peaks between -1.0 and -0.8 V which suggest that the lipid bilayer is desorbing and adsorbing on the surface. The oligomers (solid line) exhibited the largest current which could indicate that the oligomers caused the most disruption of the lipid bilayer. The protofibrils (dashed line) showed very similar behaviour to the oligomers; the current was nearly the same. The

fibrils (dotted line) showed a very small current which indicates the persistence of a compact layer on the surface. This indicates that fibrillar insulin does not cause significant defects in the lipid bilayer, which was also observed in the EC-SERS data. It is important to note that in the presence of oligomers and protofibrils there was peak shifts to more positive potential.

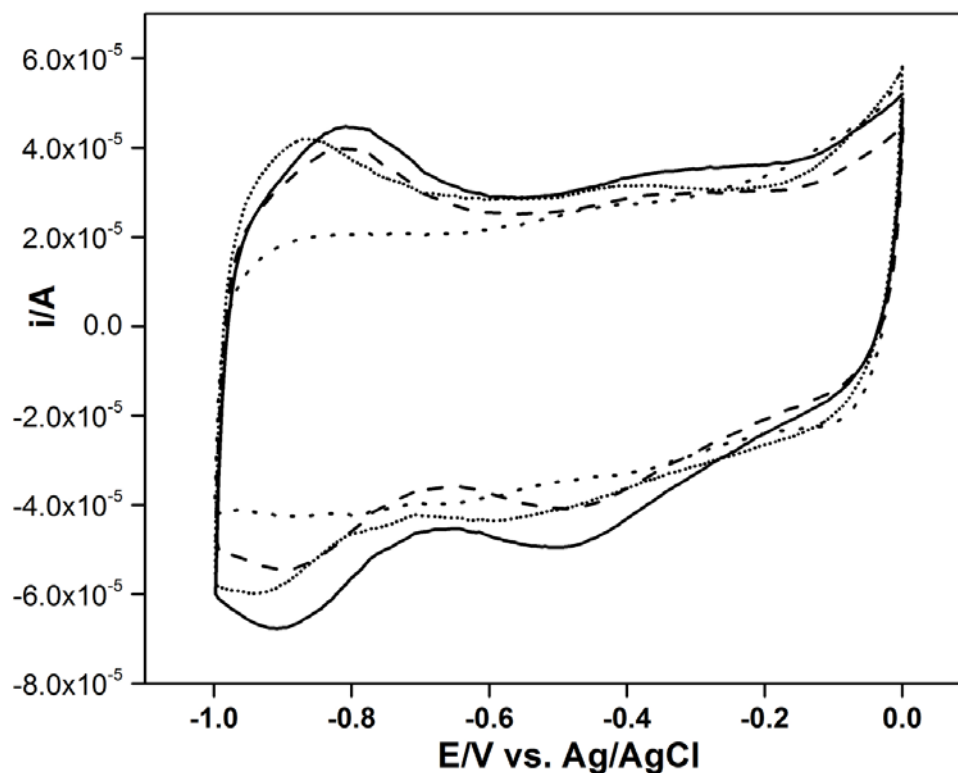


Figure 66: CV of s-BLM (short dotted line), s-BLM in the presence of oligomers (solid line), s-BLM in the presence of protofibrils (dashed line), and s-BLM in the presence of fibrils (dotted line). All completed in 0.1 M NaF solution. Scan rate: 50 mV / s.

Based on these results it was noted that different insulin structures along the aggregation pathway provided different spectral features. The addition of dAMP was helpful in studying the interaction between insulin and lipid molecules and whether large pores or defects were forming. An EC-SERS comparison at OCP between all the data

obtained in the presence of dAMP is shown in Figure 67. The dAMP peak at 730 cm^{-1} was observed at OCP in the presence of oligomers, protofibrils, and fibrils. This indicates that dAMP was able to permeate the s-BLM due to the presence of oligomers and protofibrils and not due to the application of voltage. The dAMP peak intensity was strongest in the presence of oligomers, and weakest in the presence of fibrils. This result showed that oligomers and protofibrils caused the most membrane perturbation. The dAMP peak was not observed in the presence of native insulin which indicates that dAMP was not able to permeate through the s-BLM suggesting that a good quality biomimetic membrane was developed.

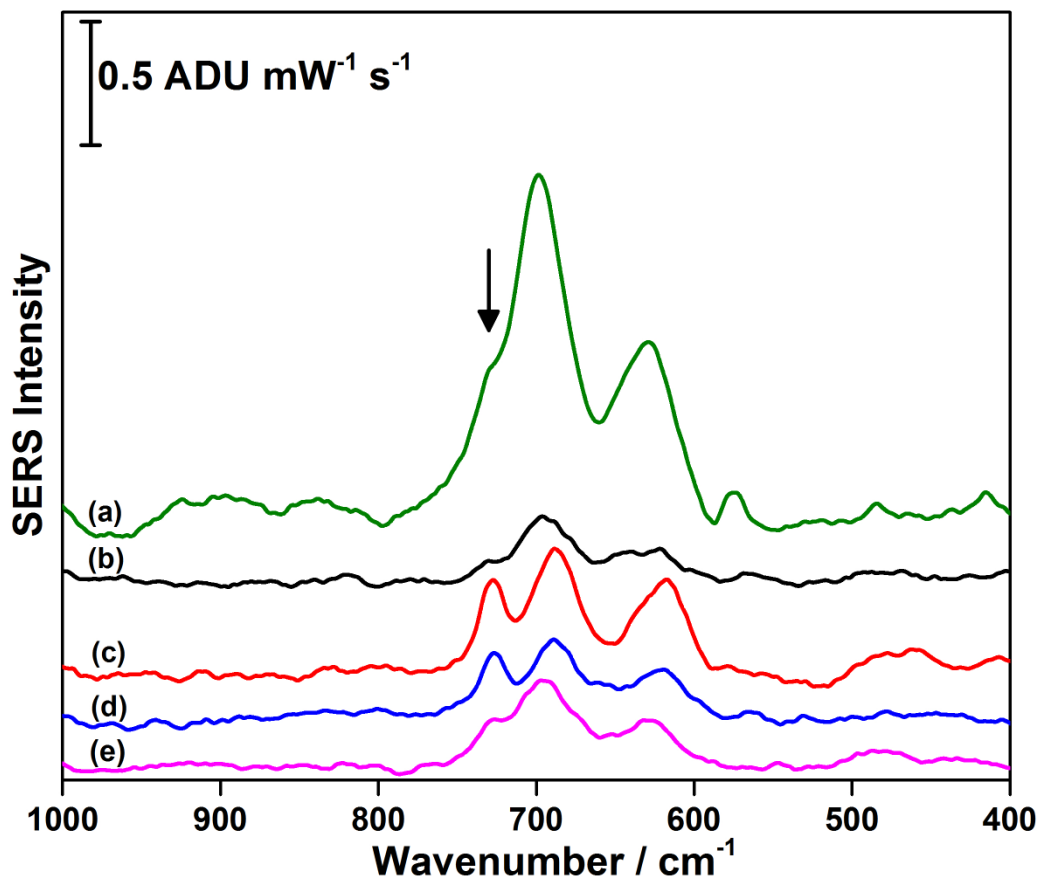


Figure 67: EC-SERS cathodic signal at OCP of a) s-BLM, b) s-BLM + native human insulin, c) s-BLM + oligomer human insulin, d) s-BLM + protofibril human insulin, e) s-BLM + fibril human insulin in 1.0 mM dAMP / 0.1 M NaF solution. The spectra were measured at 4 mW for a time interval of 30 seconds using 532 nm excitation. dAMP peak at 730 cm^{-1} is indicated by the arrow.

An EC-SERS comparison at -1.0 V between all the data obtained in the presence of dAMP is shown in Figure 68. The oligomer and protofibril are the membrane-perturbing species since they had a major effect on the EC-SERS signal of the s-BLM. As seen in spectra c and d the dAMP peaks at 730 cm^{-1} and 1328 cm^{-1} were present, confirming the presence of defects in the bilayer membrane. Native insulin did not show

any major spectral changes and dAMP was unable to permeate through the s-BLM in its presence. As seen in spectrum b, even after application of a high electric field, dAMP peaks were not present. In the case of the fibrils, the results were not significantly different than the EC-SERS of s-BLM in the absence of protein. By comparing spectra a and e it can be seen that the spectra are somewhat similar which indicates not a lot of membrane damage has occurred due to the presence of fibrils. Even though dAMP was observed in the presence of fibrils, the dAMP peak was not as intense as the peak observed in the presence of oligomers and protofibrils.

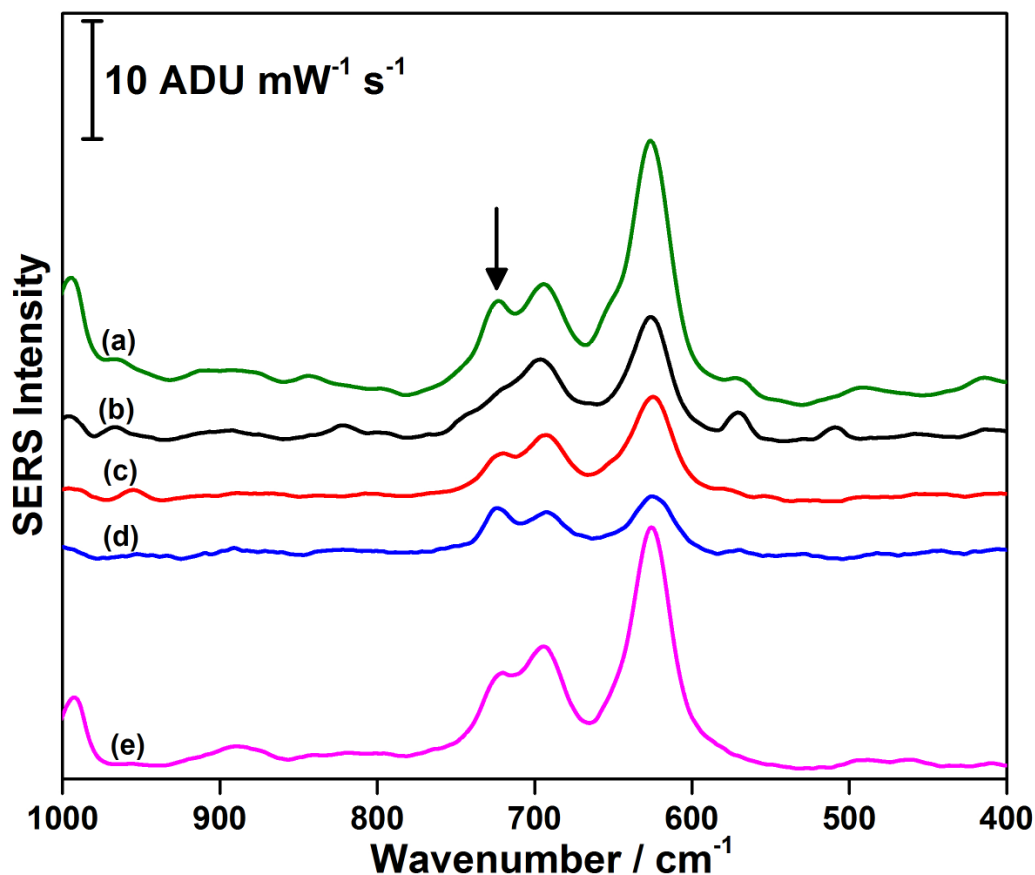


Figure 68: EC-SERS cathodic signal at -1.0 V of a) s-BLM, b) s-BLM + native human insulin, c) s-BLM + oligomer human insulin, d) s-BLM + protofibril human insulin, e) s-BLM + fibril human insulin in 1.0 mM dAMP / 0.1 M NaF solution. The spectra were measured at 4 mW for a time interval of 30 seconds using 532 nm excitation. dAMP peak at 730 cm^{-1} is indicated by the arrow.

In summary, the interaction between human insulin and s-BLM was investigated using EC-SERS. The most membrane-perturbing aggregates were the oligomers and protofibrils whereas the fibrillar insulin did not have significant impact on the s-BLM. The native insulin did not cause any perturbation which suggests that native insulin plays a protective role. These results showed for the first time that EC-SERS can be used as a useful spectroscopic tool in order to investigate the protein-lipid interactions.

Chapter 6: Conclusions and Future Work

The interaction between lipid molecules of a cell membrane and protein at various stages of aggregation can be useful in understanding amyloidogenic disorders. These amyloidogenic diseases are due to the accumulation of protein within various tissues which leads to cell death. This research was aimed towards using recombinant human insulin as a model amyloid to help better understand the “amyloid pore hypothesis” of Alzheimer's disease, however, this hypothesis can also be used for other amyloidogenic disorders such as Parkinson's and Huntington disease. A supported bilayer lipid membrane (s-BLM) was formed using the Langmuir-Blodgett / Langmuir Schaefer method in order to mimic biological cell membranes. Various spectroscopic and electrochemical methods were employed to understand this interaction at the molecular level. In particular, electrochemical SERS (EC-SERS) was used for the first time to investigate membrane-protein interactions.

This research involved aggregating recombinant human insulin under various conditions and allowing these aggregates to interact with the s-BLM. Prior to aggregating insulin, techniques were used to characterize it while present in its native state such as Raman spectroscopy and attenuated total reflectance-Fourier transform infrared spectroscopy (ATR-FTIR). Human insulin powder and concentrated solution were successfully characterized using both Raman and ATR-FTIR, and the amide bands were monitored. The next step of this project was to accelerate the aggregation process for human insulin using elevated temperature and low pH. Aggregated human insulin was achieved by preparing the solution in a pH of 1.6 (12 M HCl / 0.1 M NaCl) and heating it

for several hours at 65 °C. The aggregated insulin was successfully characterized using ATR-FTIR and the aggregation process was monitored using turbidity measurements. The aggregation process followed a sigmoidal behaviour that was consistent with literature. At selected times along the sigmoidal curve, transmission electron microscopy (TEM) and scanning electron microscopy (SEM) were used to image the aggregates. In both techniques changes in the morphology and assembly of insulin was noted during the aggregation process.

Once the aggregation process was successfully characterized, insulin aggregate structures were introduced to a s-BLM supported on a modified SPE and changes in signal were observed using EC-SERS. The insulin structures investigated were native insulin, oligomer, protofibril, and fibril. It was observed in the EC-SERS spectra that oligomer and protofibrillar insulin in the presence of the s-BLM caused significant structural changes. The native insulin did not show a significant variation in signal compared to the signal obtained from the s-BLM in the absence of insulin. The fibrillar insulin caused some minor changes but they were not as significant as the changes observed for the oligomers and protofibrils.

In order to test whether insulin forms defects in the s-BLM, a probe molecule was introduced. The probe molecule chosen was dAMP which has characteristic EC-SERS peaks at 730 cm^{-1} and 1328 cm^{-1} ; the presence of these peaks indicated the formation of defects. Due to the sharp distance dependence of SERS, dAMP peaks were observed only when dAMP accessed the surface, for example through defects. Based on the EC-SERS obtained for the s-BLM in the absence of insulin, dAMP penetrated through the

lipid bilayer at potentials more negative than -0.1 V, which indicates that electroporation was occurring due to the high electric field applied. In the presence of native insulin, dAMP did not penetrate through the lipid bilayer even at -1.0 V, which showed that electroporation did not play a role in this case. The native insulin is thought to have a protective role, preventing the dAMP molecules from penetrating through the lipid bilayer through formation of a “carpet-like” layer on the membrane surface. The oligomers and protofibrils have previously been identified as toxic species, and the EC-SERS measurements indicated that the dAMP permeated through the s-BLM in the presence of these species, even without the application of voltage. The fibrils also allowed the dAMP to permeate through the s-BLM; however, the dAMP peak intensity in the EC-SERS spectrum was not significantly strong. This could indicate that fibrillar insulin does not cause as many defects as the prefibrillar toxic species. The results obtained were consistent with cell toxicity and pore activity measurements obtained for amyloid- β mentioned earlier.

This research work has highlighted the ability to characterize recombinant human insulin in its native and aggregated state using various techniques. For the first time SEM showed the ability to monitor protein aggregation with high resolution images. One of the major aspects of this project was to monitor the formation of pores and defects caused by the presence of protein on s-BLM. This was achieved by using dAMP as a probe molecule to observe pores and / or defects introduced by different insulin aggregates. The EC-SERS data obtained for the different insulin aggregates have helped in understanding the extent of interaction between the protein aggregates, the bilayer and

lipids. This thesis has demonstrated the first use of electrochemical SERS towards obtaining a truly molecular level view of the nature of protein-membrane interactions.

The use of dAMP as a probe molecule confirmed the presence of defects. However, the pore hypothesis of Alzheimer's disease should be further investigated using Ca^{2+} . Calcium ion influx is found to increase through the cell membrane due to the defects formed. Therefore, the detection of Ca^{2+} ions is important in order to further validate the pore hypothesis. A major challenge going forward will be to develop ways to monitor Ca^{2+} using EC-SERS.

This system has used a supported bilayer lipid membrane (s-BLM) which consisted of an alkanethiol self-assembled monolayer. This self-assembled monolayer is considered a hydrophobic support which would not allow for a transmembrane protein to be properly incorporated into the lipid bilayer. In order to overcome this problem a tethered bilayer lipid membrane (t-BLM) can be utilized. In a t-BLM the self-assembled monolayer can provide a hydrophilic region where a transmembrane protein could be easily translocated. This would be a more realistic model for biological cell membranes than having the bottom leaflet interacting with a hydrophobic alkanethiol.

In this research recombinant human insulin was used as a model for amyloid- β because it aggregates in the same way as amyloid- β and is much more affordable than amyloid- β . A future goal of this research would be to study the interaction between amyloid- β and the lipid bilayer in order to fully understand the mechanism of Alzheimer's disease.

Chapter 7: References

- 1) Kimmel, D. W., LeBlac, G., Meschievitz, M. E., Cliffel, D. E. *Anal. Chem.* **2012**, *84*, 685-707.
- 2) Hering, K., Cialla, D., Ackermann, K., Dörfer, T., Möller, R., Schneidewind, H., Mattheis, R., Fritzsche, W., Rösch, P., Popp, J. *Anal. Bioanal. Chem.* **2008**, *390*, 113-124.
- 3) Duijvesz, D., Luider, T., Bangma, C. H., Jenster, G. *Eur. Urol.* **2011**, *59*, 823-831.
- 4) Chiti, F., Dobson, C. M. *Annu. Rev. Biochem.* **2006**, *75*, 333-366.
- 5) Alzheimer Society Canada. <http://www.alzheimer.ca/en/About-dementia/What-is-dementia/Dementia-numbers>, (accessed on August 4, 2015). Selkoe, D. J. *Nature*, **2003**, *426*, 900-904.
- 6) Porat, Y., Abramowitz, A., Gazit, E. *Chem. Biol. Drug Des.*, **2006**, *67*, 27-37.
- 7) Ross, C. A., Poirier, M. A. *Nature*, **2004**, *10*, S10-S17.
- 8) Kheterpal, I., Lashuel, H. A., Hartley, D. M., Wlaz, T., Lansbury Jr., P. T., Wetzel, R. *Biochemistry*, **2003**, *42*, 14092-14098.
- 9) Prangko, P., Yusko, E. C., Sept, D., Yang, J., Mayer, M. *PLOS ONE*, **2012**, *7*, 1-10.
- 10) Lanctôt, K. L., Rajaram, R. D., Herrmann, N. *Ther. Adv. Neurol. Disord.*, **2009**, *2(3)*, 163-180.
- 11) Terry, A. V., Jr., Buccafusco, J. J. *J. Pharmacol. Exp. Ther.*, **2003**, *306*, 821-827.
- 12) Davis, P. *JAMA*, **1999**, *281*, 1433-1434.
- 13) Husain, M. M., Trevino, K., Siddique, H., McClintock, S. M. *Neuropsychiatr. Dis. Treat.*, **2008**, *4(4)*, 765-777.
- 14) Rochet, J-C. *Expert Rev. Mol. Med.*, **2007**, *9*, 1-34.
- 15) Nicolli, J. A. R., Wilkinson, D., Holmes, C., Steart, P., Markham, H., Weller, R.O., *Nature*, **2003**, *9*, 448-452.
- 16) Panza, F., Frisardi, V., Solfrizzi, V., Imbimbo, B. P., Logroscino, G., Santamato, A., Greco, A., Seripa, D., Pilotto, A. *Curr. Med. Chem.*, **2011**, *35*, 5439-5447.
- 17) Jarvis, L. M., *Alzheimer's next chapter*, CEN. ACS. ORG., **2015**, 11-15.

- 18) O'Connor, C. M., Adams, J. U. *Essentials of Cell Biology*. Cambridge, MA: NPG Education, **2010**.
- 19) Karp, G. *Cell and Molecular Biology: Concepts and Experiments*, 6th edition. USA, John Wiley & Sons, Inc., **2010**.
- 20) Ball, D. W., Hill, J. W., Scott, R. J. *Introduction to Chemistry: General, Organic, and Biological*, PDF file. Chapter 18 (accessed on December 10, 2015).
- 21) The why biochemistry. <https://thewhyinbiochemistry.wordpress.com/page/2/> (accessed August 29, 2015).
- 22) Toole, G., Toole, S., *Essential AS Biology for OCR*. Cheltenham, United Kingdom: Nelson Thomes Ltd., **2004**, pg 38-39.
- 23) Petsko, G. A., Ringe, D., *Protein Structure and Function*. London, United Kingdom: New Science Press, Ltd., **2004**, pg 2-5.
- 24) Zhang, C., Kim, S.H., *Proteins*, **2000**, 40, 409-419.
- 25) Dobson, C. M. *Protein Misfolding, aggregation, and Conformational Diseases*. California, USA: Springer Science & Business Media, Inc., **2006**.
- 26) Murphy, R., Tsai, A. *Misbehaving Proteins: Proteins (Mis)Folding, Aggregation, and Stability*. Maryland, USA: Springer Science & Business Media, Inc., **2007**.
- 27) Chiti, F., Dobson, C. M. *Annu. Rev. Biochem.* **2006**, 75, 333-366.
- 28) Baldwin, R. L. *Biophys. J.* **1996**, 71, 2056-2063.
- 29) Paterová, J., Rembert, K. B., Heyda, J., Kurra, Y., Okur, H. I., Liu, W. R., Hilty, C., Cremer, P. S., Jungwirth, P. *J. Phys. Chem. B*, **2013**, 117, 8150-8158.
- 30) Arosio, P., Jaquet, B., Wu, H., Morbidelli, M. *Biophys. Chem.* **2012**, 168-169, 19-27.
- 31) Marcus, Y. *Ions in Solution and their solvation*. New Jersey, USA: John Wiley & Sons, 2015.
- 32) Cheung, J. C., Deber, C. M. *Biochemistry*, **2008**, 47, 1465-1473.
- 33) Atassi M. Z., *Protein Reviews: Protein Misfolding, Aggregation, and Conformational Diseases*. Singapore, Springer Science & Business Media, Inc. **2006**.
- 34) Toyama, B. H., Weissman, J. S. *Annu. Rev. Biochem.*, **2011**, 80, 1-31.
- 35) Rambaran, R. N., Serpell, L. C. *Prion*, **2008**, 2, 112-117.

- 36) Sunde, M., Serpell, L. C., Barlam, M., Fraser, P. E., Pepys, M. B., Blake, C. C. F. *J. Mol. Biol.*, **1997**, *273*, 729-739.
- 37) Serpell, L. C., Smith, J. M. *J. Mol. Biol.*, **2000**, *299*, 225-231.
- 38) Serpell, L. C. *Biochimica et Biophysica Acta.*, **2000**, *1502*, 16-30.
- 39) Lührs, T., Ritter, C., Adrian, M., Riek-Loher, D., Bohrmann, B., Döbeli, H., Schubert, D., Riek, R. *PNAS*, **2005**, *102*, 17342-17347.
- 40) Querfurth, H. W., LaFerla, F. M. *N. Engl. J. Med.* **2010**, *362*, 329-344.
- 41) Ross, C. A., Poirier, M. A. *Nature*, **2004**, *10*, 10-17.
- 42) Tyan, S. H., Shih, A. Y. J., Walsh, J. J., Maruyama, H., Sarsoza, F., Ku, L., Eggert, S., Hof, P. R., Koo, E. H., Dickstein, D. L. *Mol. Cell Neurosci.*, **2012**, *51*, 43-52.
- 43) O'Brien, R. J., Wong, P. C. *Annu. Rev. Neurosci.*, **2011**, *34*, 184-204.
- 44) Morris, A. M., Watzky, M. A., Finke, R. G. *Biochimica et Biophysica Acta.*, **2009**, *1794*, 375-397.
- 45) Selkoe, D. J. *Nature*, **2003**, *426*, 900-904.
- 46) Nielsen, L., Frokjaer, S., Carpenter, J. F., Brange, J. *J. Pharm. Sci.* **2001**, *90*, 29-37.
- 47) Wang, Z., Zhou, C., Wang, C., Wan, L., Fang, X., Bai, C. *Ultramicroscopy*, **2003**, *97*, 73-79.
- 48) Takai, E., Ohashi, G., Ueki, R., Yamada, Y., Fujita, J.I., Shiraki, K. *Am. J. Biochem. Biotech.* **2014**, *10*, 31-39.
- 49) Harris, J. Robin. *Protein Aggregation and Fibrillogenesis in Cerebral and Systemic Amyloid Disease*. New York, USA: Springer Science & Business Media, **2012**.
- 50) Dathe, M., Gast, K., Zirwer, D., Welfle, H., Mehlis, B. *Int. J. Peptide Protein Res.* **1990**, *36*, 344-349.
- 51) Li, S., Leblanc, R. M., *J. Phys. Chem. B*, **2014**, *118*, 1181-1188.
- 52) Prangko, P., Yusko, E. C., Sept, D., Yang, J., Mayer, M., *PLOS ONE*, **2012**, *7*, 1-10.

- 53) Celej, M. S., Sarroukh, R., Goormaghtigh, E. Fidelio, G. D., Ruyschaert, J.-M., Raussens, V. *Biochem. J.* **2012**, *443*, 719-726.
- 54) Lashuel, H. A., Lansbury Jr. P. T. *Q. Rev. Biophys.* **2006**, *39*, 167-201.
- 55) Benseny-Cases, N., Klementieva, O., Cladera, J. *Subcell Biochem.*, **2012**, *74*, 63-65.
- 56) Arce, F. T., Jang, H., Ramachandran, S., Landon, P. B., Nussinov, R., Lal, R. *Soft Matter*, **2011**, *7*, 5267-5273.
- 57) Lin, H., Bhatia, R., Lai, R. *FASEB Journal*, **2001**, *15*, 2433-2444.
- 58) Quist, A., Doudevski, I., Lin, H., Azimova, R., Ng, D., Frangionf, B., Kagan, B., Ghiso, J., Lai, R. *Proceedings of the National Academy of Sciences USA*, **2005**, *102*, 10427-10432.
- 59) Lashuel, H. A., Petre, B. M., Wall, J., Simon, M., Nowak, R. J., Walz, T., Lansbury Jr. P. T., *J. Mol. Biol.* **2002**, *322*, 1089-1102.
- 60) Kegan, B. L. *Protein Misfolding, aggregation, and Conformational Diseases*. California, USA: Springer Science & Business Media, Inc., **2006**. Pg 1-15.
- 61) Hianik Tibor, *Biological Membranes and Membrane Mimics*. USA: John Wiley & Sons, Ltd., **2008**.
- 62) Young, B., Lowe, J. S., Stevens, A., Heath, J. W. *Wheater's Functional Histology*. Philadelphia, USA: Elsevier Limited, **2008**, pg 2-5.
- 63) Starr, S. E. *Biology Concepts and Applications*. Belmont, USA: Brooks / Cole Cengage Learning, **2011**, pg 55-57.
- 64) Allen, J. P. *Biophysical Chemistry*. Hoboken, USA: Blackwell Publishing, 2008, pg 75-77.
- 65) Nelson, D. L., Lehninger, A. L., Cox, M. M., *Lehninger Principles of Biochemistry*. USA: W. H. Freeman and Company, **2008**. Pg 270-273.
- 66) Pike, L. J. *J. Lipid Res.*, **2009**, *50*, 323-328.
- 67) Simons, K., Eehalt, R. *J. Clin. Invest.* **2002**, *110*, 597-603.
- 68) Wegrzyn, R. D., Rudolph, A. S. *Alzheimer's Disease: Targets for New Clinical Diagnostic and Therapeutic Strategies*. Boca Raton, USA: Taylor & Francis Group, LLC, **2012**, pg 25-27.

- 69) Fosbery, R., Gregory, J. Stevens, I. *Revise as Biology*. USA: Heinemann, **2005**, 24-26.
- 70) Ball, D. W., Hill, J. W., Scott, R. J. *Introduction to Chemistry: General, Organic, and Biological*, PDF file. Chapter 17 (accessed on December 10, 2015).
- 71) Alberts, B. *Molecular Biology of the Cell, volume 1*. New York, USA: Courier Corporation, **1989**, pg 276-281.
- 72) Ramkaran, M. Badia, A. *J. Phys. Chem. B*. **2014**, *118*, 9708-9721.
- 73) Garrett, R. H., Grisham, C. M., *Biochemistry, 5th Edition*”, Brooks/Cole Cengage Learning, California, USA, **2013**.
- 74) Garcia-Manyes, S., Oncins, G., Sanz, F., *Biophys. J.*, **2005**, *89*, 4261.
- 75) Knoll, W. *Handbook of Biofunctional Surfaces*. Boca Raton, FL: CRC Press, **2013**.
- 76) Howard, H. *Neuromimetic Semantics: Coordination, Quantification, and Collective Predicates*. Amsterdam, Netherlands: Elsevier B. V. **2004**.
- 77) Nanda, B. K. *Electrotherapy Simplified*, New Delhi, India: Jaypee Brothers Publishers, **2008**.
- 78) Lipkowski, J. *Phys. Chem. Chem. Phys.* **2010**, *12*, 13874-13887.
- 79) Castellana, E. T., Cremer, P. S., *Surf. Sci.*, **2006**, *61*, 429.
- 80) Torchilin, V. P., Weissig, V. *Liposomes*. New York, USA: Oxford University Press, **2003**.
- 81) Akbarzadeh, A., Rezaei-Sadabady, R., Davaran, S., Woo Joo, S., Zarghami, N., Hanifehpour, Y., Samiei, M., Kouhi, M. Nejati-Koshki, K. *Nanoscale Res. Lett.* **2013**, *8*, 8:102, 1-9.
- 82) Akbarzadeh, A., Rezaei-Sadabady, R., Davaran S., Joo, S. W., Zarghami, N., Hanifehpour, Y., Samiei, M., Kouhi, M., Nejati-Koshki, K. *Nanoscale Res. Lett.* **2013**, *8*, 1-9.
- 83) Guidelli, R., Becucci, L. *Bioelectrochemistry, Fundamentals, Applications and Recent Developments: Model Lipid Bilayers at Electrode Surfaces*. Wenham, Germany: Wiley-VCH, **2011**.
- 84) Meuse, C. W., Niaura, G., Lewis, M. L., Plant, A. L. *Langmuir*, **1998**, *14*, 1604-1611.

- 85) Nuzzo, R. G.; Fusco, F. A.; Allara D. L. *J. Am. Chem. Soc.* **1987**, *109*, 2358.
- 86) Porter, M. D.; Bright, T.B.; Allara, D.L.; Chidsey, C.E.D. *J. Am. Chem. Soc.* **1987**, *109*, 3559.
- 87) Finklea, H.O. in A.J. Bard, I. Rubinstein (Eds.), *Electroanalytical Chemistry*. Marcel Dekker: New York, **1996**.
- 88) Atanasov, V., Knorr, N., Duran, R. S., Ingebrandt, S., Offenhäusser, A., Knoll, W., Köper, I. *J. Biophys.*, **2005**, *89*, 1780-1788.
- 89) Martin, D. *Fundamental Biomedical Technologies: Nanobiotechnology of Biomimetic Membranes*. Springer Sciences: Sydney, **2007**, pg 134-137.
- 90) Böcking, T., Gooding, J. J. *Nanobiotechnology of Biomimetic Membranes*, Sydney, Australia, Springer Science & Business Media, LLC, **2007**.
- 91) Tatur, S., Maccarini, M., Barker, R., Nelson, A., Fragneto, G., *Langmuir*, **2013**, *29*, 6606-6614.
- 92) Kycia, A. H., Wang, J., Merrill, A. R., Lipkowski, J. *Langmuir*, **2011**, *27*, 10867-10877.
- 93) Hughes, A. V., Howse, J. R., Dabkowska, A., Jones, R. A. L., Lawrence, M. J., Roser, S. J. *Langmuir*, **2008**, *24*, 1989-1999.
- 94) Su, Z., Jiang, Y., Velázquez-Manzanares, M., Leitch, J. J., Kycia, A., Lipkowski, J. *J. Electroanal. Chem.*, **2013**, *688*, 76-85.
- 95) Abdulreda, M. H., Moy, V. T. *J. Biophys.*, **2007**, *92*, 4369-4378.
- 96) Fragneto, G., Charitat, T., Graner, F., Mecke, K., Perino-Gallice, L., Bellet-Amalric, E. *Europhys. Lett.*, **2001**, *53*, 100-106.
- 97) Knoll, W., Frank, C. W., Heibel, C., Naumann, R., Offenhäusser, A., Rühle, J., Schmidt, E. K., Shen, W. W., Sinner, A. *Rev. Mol. Biotechnol.* **2000**, *74*, 137-158.
- 98) Wu, E.-S., Jacobson, K., Papahadjopoulos, D., *Biochemistry*, **1977**, *16*, 3936-3941.
- 99) Chen, Y., Lagerholm, B. C., Yang, B., Jacobson, K., *Methods*, **2006**, *39*, 147-153.
- 100) Volpati, D., Aoki, P. H.B., Pavinatoo, F. J., Miranda, P. B., Constantino, C. J.L., Oliveira Jr. O. N. *Adv. Colloid Interface Sci.* **2014**, *207*, 199-215.
- 101) Kühler, P., Weber, M., Lohmüller, T. *Appl. Mater. Interfaces*, **2014**, *6*, 8947-8952.

- 102) Kneipp, K., Kneipp, H., Itzkan, I., Dasari, R. R., Feld, M. S. *J. Phys. Condens. Matter*, **2002**, *14*, 597-624.
- 103) Lyubartsev, A. P., Rabinovich, A. L., *Soft Matter*, **2011**, *7*, 25-39.
- 104) Kaupp, G., *Atomic Force Microscopy, Scanning Near Field, Optical Microscopy and Nanoscratching, Application to Rough and Natural Surfaces*, Springer, Berlin, **2006**.
- 105) El Kirat, K., Morandat, S., Dufrène Y. F. *Biochimica et Biophysica Acta*. **2010**, *1798*, 750-765.
- 106) Chen, M., Li, M., Brosseau, C. L., Lipkowski, J., *Langmuir*, **2009**, *25*, 1028-1037.
- 107) Eeman, M., Deleu, M. *Biotechnol. Agron. Soc. Environ.* **2010**, *14(4)*, 719-736.
- 108) Guidelli, R., Aloisi, G., Becucci, L., Dolfi, A., Moncelli, M. R., Buoninsegni, F. T. *J. Electroanal. Chem.* **2001**, *504*, 1-28.
- 109) Iglic, A. *Advances in Planar Lipid Bilayers and Liposomes, Volume 11*. California, USA: Academic Press, **2010**, pg 88-90.
- 110) Chan, Y.H. M., Boxer, S. G. *Curr. Opin. Chem. Biol.* **2007**, *11*, 1-7.
- 111) Ghosh, P. *Colloid and Interface Science*. New Delhi, India: PHI Learning Private Limited, **2009**.
- 112) Ulman, A. *An Introduction to Ultrathin Organic Films from Langmuir-Blodgett to Self-Assembly*. London, United Kingdom: Academic Press Limited, Inc. **1991**.
- 113) Barnes, G. T., Gentle, I. R., *Interfacial science: an introduction*, New York, USA: Oxford University Press, **2011**.
- 114) Petty, M. C., *Langmuir Blodgett films, an introduction*, Britain, United Kingdom: Cambridge University Press, **1996**.
- 115) KSV NIMA, *Software Manual, Langmuir and Langmuir-Blodgett devices*, KSV NIMA Biolin Scientific, Finland, **2010**.
- 116) Zawisza, I., Bin, X., Lipkowski, J. *Langmuir*, **2007**, *23*, 5180-5194.
- 117) Matyszewska, D., Leitch, J., Bilewicz, R., Lipkowski, J., *Langmuir*, **2008**, *24*, 7408-7412.

- 118) Garcia-Araez, N., Brosseau, C. L., Rodriguez, P., Lipkowski, J. *Langmuir*, **2006**, *22*, 10365-10371.
- 119) Leverette, C. L., Dluhy, R. A. *Colloid Surfaces A*. **2004**, *243*, 157-167.
- 120) Martin, D., *Nanobiotechnology of Biomimetic Membranes, Volume 1*. New York, USA: Springer Science & Business Media Inc., **2006**.
- 121) Leitch, J. J., Brosseau, C. L., Roscoe, S. G., Bessonov, K., Dutcher, J. R., Lipkowski, J. *Langmuir*, **2013**, *29*, 965-976.
- 122) Casal, E., Montilla, A., Moreno, F.J., Olano, A., Corzo, N. J. *Dairy Sci*. **2006**, *89*, 1384-1390.
- 123) Smith, A. W. *Biochimica et Biophysica Acta*. **2012**, *1818*, 172-177.
- 124) Volkov, V. V., Chelli, R., Muniz-Miranda, F., Righini, R., *J. Phys. Chem.* **2011**, *115*, 5294-5303.
- 125) Wilkop, T., Xu, Danke, Cheng, Q. *Langmuir*, **2008**, *24*, 5615-5621.
- 126) Kundu, J., Levin, C. S., Halas, N. J. *Nanoscale*, **2009**, *1*, 114-117.
- 127) Millo, D., Bonifacio, A., Moncelli, M. R., Sergo, V., Gooijer, C., Zwan, G. V. D. *Colloids Surfaces A*. **2010**, *81*, 212-216.
- 128) Niaura, G., Nas, R. J., *J. Electroanal. Chem.*, **2001**, *510*, 50-58.
- 129) Vezvaie, M., Brosseau, C. L., Lipkowski, J. *Electrochimica Acta*. **2013**, *110*, 120-132.
- 130) Juhaniwicz, J., Sek, S. *Electrochimica Acta*. **2015**, *162*, 53-61.
- 131) Smetanin, M., Sek, S., Maran, F., Lipkowski, J. *Biochimica et Biophysica Acta*. **2014**, *1838*, 3130-3136.
- 128) Sek, S., Laredo, T., Dutcher, J. R., Lipkowski, J. *J. Am. Chem. Soc.* **2009**, *131*, 6439-6444.
- 132) Pieta, P., Mizra, J., Lipkowski, J. *Proc. Natl. Acad. Sci.* **2012**, *109*, 21223-21227.
- 133) Lee, H., Kim, Y., Park, A., Nam, J.M. *Small*, **2014**, *10*, 1779-1789.
- 134) Xu, W., Wei, G., Su, H., Nordenskiöld, L., Mu, Y. *Phys. Rev. E. Stat. Nonlin. Soft Matter Phys.* **2011**, *84*, 1-8.

- 135) Shaw, D. J. *Introduction to Colloid and Surface Chemistry*, Reed Educational and Professional Publishing Ltd., **1992**, pg. 64-96.
- 136) Furbish, D. J. *An Introduction to Fluid Motions on Earth's Surface and Within its Crust*. New York, USA: Oxford University Press, Inc., **1997**, pg 60-62.
- 137) Wang, J. *Analytical Electrochemistry*, 2nd ed.; New York, USA: Wiley-VCH:, **2000**.
- 138) Bard, A. J.; Faulkner, L. R. *Electrochemical methods: Fundamentals and applications, second edition*; John Wiley & Sons, Inc.: New York, 2001; p 26.
- 139) Derek, P. *First Course in Electrode Processes*, 2nd ed.; Royal Society of Chemistry: Cambridge, 2009, p139.
- 140) Wang, H., Pilon, L. *Electrochimica Acta*. **2012**, *64*, 130-139.
- 141) Zoski, C. G. *Handbook of Electrochemistry*, 1st ed.; Amsterdam, Netherlands: Elsevier, **2007**, pp 22-24.
- 142) Ren, B., Cui, Y., Wu, D.Y., Tian, Z. Q. *Electrochemical SERS and its Application in Analytical, Biophysical and Life Science*, Weinheim, Germany: Wiley-VCH Verlag & Co. **2011**, pp 191-193.
- 143) Pelletier, M. J. *Analytical Applications of Raman Spectroscopy*, Michigan, USA: Blackwell Science Ltd., **1999**.
- 144) Movasaghi Z.; Rehman S.; Rehman I. U. *Appl. Spectrosc. Rev.* **2007**, *42*, 493-541.
- 145) Harris, D.C.; Bertolucci, M. D. *Symmetry and Spectroscopy: An Introduction to Vibrational and Electronic Spectroscopy*; Dove Publication: New York, **1989**, pp 93-97, 151-159.
- 146) Ferraro, J. R., Nakamoto, K. *Introductory Raman Spectroscopy*, San Diego, USA: Academic Press Limited, Inc., **1994**.
- 147) Robinson, A. M., Harroun, S. G., Bergman, J., Brosseau C. L. *Anal. Chem.* **2012**, *84*, 1760-1764.
- 148) Doering, W. E., Piotti, M. E., Natan, M. J., Freeman, R. G. *Adv. Mater.* **2007**, *19*, 3100-3108.
- 149) Lyandres, O., Shah, N. C., Yonzon, C. R., Jr. Walsh, J. T., Glucksberg, M. R., Van Duyne, R. P. *Anal.Chem.* **2005**, *77*, 6134-6139.
- 150) Fleischmann, M., Hendra, P. J., McQuillan, A. *J. Chem. Phys. Lett.* **1974**, *26*, 163-166.
- 151) Jeanmaire, D. L., Van Duyne, R. P. *J. Electroanal. Chem.* **1977**, *84*, 1.

- 152) Das, G., Patra, N., Gopalakrishnan, A., Zaccaria, R. P., Toma, A., Thorat, S., Fabrizio, E. D., Diaspro, A., Salerno, M. *Analyst*, **2012**, *137*, 1785-1792.
- 153) Bantz, K. C., Meyer A.F., Wittenberg A.J., Im H., Kutulus Ö., Lee S.H., Lindquist N.C., Oh S.H., Haynes C.L. *Phys. Chem. Chem. Phys.* **2011**, *13*, 11551-11567.
- 154) Stiles, P. L., Dieringer, J. A., Shah, N. C., Van Duyne, R. P. *Annu. Rev. Anal. Chem.* **2008**, *1*, 601-626.
- 155) Haynes, C. L., McFarland, A. D., Van Duyne, R. P. *Anal. Chem.* **2005**, *77*, 338A-345A.
- 156) Kho, K. W., Fu, C. Y., Dinish, U. S., Olivo, M. *J. Biophotonics*, **2011**, *4*, 667-684.
- 157) Porter, M. D., Lipert, R. J., Siperko, L. M., Wang, G., Narayanan, R. *Chem. Soc. Rev.* **2008**, *37*, 1001-1011.
- 158) Moskovits, M. *J. Raman Spectrosc.* **2005**, *36*, 485-496.
- 159) Willets, K. A., Van Duyne, R. P. *Annu. Rev. Phys. Chem.* **2007**, *58*, 267-297.
- 160) Moskovits, M. *J. Chem. Phys.* **1982**, *77*, 4408-4416.
- 161) Le Ru, E. C., Meyer, S. A., Artur, C., Etchegoin, P. G., Grand, J., Lang, P., Maurel, F. *Chem. Commun.* **2011**, *47*, 3903-3905.
- 162) Eftekhari, A. *In Nanostructured Materials in Electrochemistry*, Weinheim, Germany: Wiley-VCH, **2008**; p 1.
- 163) Zhang, J. Z. *Optical Properties and Spectroscopy of Nanomaterials*. Singapore: World Scientific Publishing Co. Pte. Ltd., **2009**; p 1.
- 164) Rycenga, M., Cobley, C. M., Zeng, J., Li, W., Moran, C. H., Zhang, Q., Qin, D., Xia, Y. *Chem. Rev.* **2011**, *111*, 3669-3712.
- 165) Wang, Y., Wang, E. Nanoparticle SERS substrates, Weinheim, Germany: Wiley-VCH Verlag & Co. **2011**, pp 39-43.
- 166) Lee, P. C.; Meisel, D. *J. Phys. Chem.* **1982**, *86*, 3391-3395.
- 167) Aroca, R. *Surface-Enhanced Vibrational Spectroscopy*, Chichester, England: John Wiley & Sons Ltd., **2006**, pp 144-145.
- 168) Karaballi, R., Nel, A., Krishnan, S., Blackburn, J., Brosseau, C. L. *Phys. Chem. Chem. Phys.* **2015**, *17*, 21356-21363.
- 169) Wen-Han, L., Rong-Hui, Y., Yuan-Jie, T. *Acta Physico-Chimica Sinica.* **2013**, *29*, 2599-2607.

- 170) Reipa, V., Gaigalas, A., Abramowitz, S. *J. Electroanal. Chem.* **1993**, 348, 413-428.
- 171) Sarroukh, R., Goormaghtigh, E., Ruyschaert, J. M., Raussens, V. *Biochim. Biophys. Acta.* **2013**, 1828, 2328-2338.
- 172) Haris, P. I. *Biochim. Biophys. Acta.* **2013**, 1828, 2265-2271.
- 173) PerkinElmer Life, *FT-IR Spectroscopy Attenuated Total Reflectance (ATR)*, Bridgeport, USA.
- 174) Dole, M. N., Patel, P. A., Sawant, S. D., Shedpure, P. S. *Int. J. Pharm. Sci. Rev. Res.*, **2011**, 7, 159-166.
- 175) Alvarez-Ordóñez, A. *Fourier Transform Infrared Spectroscopy in Food Microbiology*, Springer Science: Spain, **2012**, pg 7-9.
- 176) Tilstone, W. J., Savage, K. A., Clark, L. A. *Forensic Science: An Encyclopedia of History, Methods, and Techniques*, ABC-CLIO: New York, **2006**, pg 190-192.
- 177) Williams, D. B., Carter, C. B. *Transmission Electron Microscopy: A Textbook for Materials Science*, Springer Science: New York, **1996**, pg 5-8.
- 178) Buseck, P., Maxwell, C. J., LeRoy, E. *High-Resolution Transmission Electron Microscopy: and Associated Techniques*, Oxford University: New York, **1988**, pg 5-13.
- 179) Reimer, L. *Transmission Electron Microscopy: Physics of Image Formation and Microanalysis*, Springer-Verlag Berlin Heidelberg: Germany, **1993**, pg 6-9.
- 180) Egerton, R. F. *Physical Principles of Electron Microscopy: An Introduction to TEM, SEM, and AEM*, Springer Science: Canada, **2005**, chapter 3.
- 181) Wilson, S. M., Bacic, A. *Nature*, **2012**, 7, 1716-1727.
- 182) Goldstein, J., Newbury, D., Joy, D., Lyman, C., Echlin, P., Lifshin, E., Sawyer, L., Michael, J. *Scanning Electron Microscopy and X-ray Microanalysis*, Springer Science: New York, **2003**, pg 1-10.
- 183) Goldstein, J. I., Newbury, D. E., Echlin, P., Joy, D. C., Romig, A. D., Jr., Lyman, C. E., Fiori, C., Lifshin, E. *Scanning Electron Microscopy and X-ray Microanalysis: A Text for Biologists, Materials Scientists, and Geologists*, Plenum Press: New York, **1992**, pg. 1-10.
- 184) Reimer, L., *Transmission Electron Microscopy: Physics of Image Formation and Microanalysis*, Springer-Verlag Berlin Heidelberg: Germany, **1998**, pg 6-20.

- 185) Khursheed, A. *Scanning Electron Microscope Optics and Spectrometers*, World Scientific Publishing Ltd.: London, **2011**, pg. 2-15.
- 186) Egerton, R. F. *Physical Principles of Electron Microscopy: An Introduction to TEM, SEM, and AEM*, Springer Science: Canada, **2005**, chapter 2.
- 187) Rajakumar, G., Rahuman, A. A., Roopan, S. M., Khanna, V. G., Elango, G., Kamaraj, C., Zahir, A. A., Velayutham, K., *Spectrochimica Acta A.*, **2012**, *91*, 23-29.
- 188) Yoon, K., Lee, D., Kim, J. W., Kim, J., Weitz, D. A., *Chem. Commun.*, **2012**, *48*, 9056-9058.
- 189) Rechtes, M., Gazit, E., *Science*, **2003**, *300*, 625-627.
- 190) Ishfaq, S., Ali, N., Tauseef, I., Khattak, M. N. K., Shinwari, Z. K., Ali, M. I., *Pak. J. Bot.*, **2015**, *47*, 753-760.
- 191) Puga, A. P., Abreu, C. A., Melo, L. C. A., Beesley, L., *J. Environ. Manage.*, **2015**, *159*, 86-93.
- 192) Zhang, L., Ren, L. L., Luo, Y. Q., Zong, S. X., *Microsc. Res. Techniq.*, **2013**, *76*, 423-431.
- 193) Cheville, N. F., Stasko, J., *Vet. Pathol.*, **2013**, *10*, 1-14.
- 194) Zhao, X., Zhu, H., Zhang, B., Chen, J., Ao, Q., *J. Am. Oil Chem. Soc.*, **2015**, *92*, 975-983.
- 195) Brady-Estevez, A. S., Kang, S., Elimelech, M., *Small*, **2008**, *4*, 481-484.
- 196) Merchant, S., *Electrochemical Surface-Enhanced Raman Spectroscopy Used in the Characterization of Langmuir Blodgett / Langmuir Schaefer Biomimetic Membranes*. **2014**, Master's Thesis, Saint Mary's University
- 197) Wang, S. H., Dong, X. Y., Sun, Y. *Biochem. Eng. J.* **2012**, *63*, 38-49.
- 198) Nilsson, M. R., *Methods*, **2004**, *34*, 151-160.
- 199) Sarroukh, R., Goormaghtigh, E., Ruyschaert, J. M., Raussens, V. *Biochimica et biophysica Acta*. **2013**, *1828*, 2328-2338.
- 200) Liang, E. J., Engert, C., Kiefer, W. *Vib. Spec.*, **1995**, *8*, 435-444.
- 201) Matulaitienė, I., Kuodis, Z., Eicher-Lorka, O., Niaura, G. *J. Electroanal. Chem.* **2013**, *700*, 77-85.

- 202) Venkataramanan, M., Skanth, G., Banyopadhyay, K., Vijayamohanan, K., Pradeep, T. *J. Colloid Interface Sci.* **1999**, *212*, 553-561.
- 203) Jian, Z. Y., Chang, T. Y., Yang, Y. C., Dow, W. P., Yau, S. L., Lee, Y. L. *Langmuir*, **2009**, *25*, 179-184.
- 204) Techane, S. D., Gamble, L. J., Castner, D. G. *J. Phys. Chem.* **2011**, *115*, 9432-9441.
- 205) Ulman, A. *Chem. Rev.* **1996**, *96*, 1533-1554.
- 206) Ansar, S. M., Gadogbe, M., Siriwardana, K., Howe, J. Y., Dogel, S., Hosseinkhannazer, H., Collier, W. E., Rodriguez, J., Zou, S., Zhang, D. *J. Phys. Chem.* **2014**, *118*, 24925-24934.
- 207) Johnson, P. S., Goel, M., Abbott, N. L., Himpsel, F. J. *Langmuir*, **2014**, *30*, 10263-10269.
- 208) Goodall, B. L., Robinson, A. M., Brosseau, C. L. *Phys. Chem. Chem. Phys.* **2013**, *15*, 1382-1388.
- 209) Bensebaa, F., Zhou, Y., Brolo, A. G., Irish, D. E., Deslandes, Y., Kruus, E., Ellis, T. H.
- 210) Moskovits, M., Suh, J. S. *J. Phys. Chem.* **1984**, *88*, 5526-5530.
- 211) Petersen, F. N. R., Nielsen, C. H. *Spectroscopy*, **2009**, *24*, 1-8.
- 212) Zawisza, I., Burgess, I., Szymanski, G., Lipkowski, J., Majewski, J., Satija, S. *Electrochimica Acta*, **2004**, *49*, 3651-3664.
- 213) Foucault, R., Brike, R. L., Lombardi, J. R. *Langmuir*, **2003**, *19*, 8818-8827.
- 214) Socrates, G. *Infrared and Raman Characteristic Group Frequencies: Tables and Charts*, 3rd ed.; John Wiley & Sons, LTD.: Chichester, England, **2001**, pp 335-336.
- 215) Karp, G., "Cell and Molecular Biology, Concepts and Experiments", John Wiley & Sons Inc., England, (1996).
- 216) Léonard, A., Escrive, C., Laguerre, M., Pebay-Peyroula, E., Néri, W., Pott, T., Katsaras, J., Dufourc, E. J., *Langmuir*, *17* (2001) 2019.
- 217) Brosseau, C., L., Bin, X., Roscoe, S. G., Lipkowski, J., *J. Electroanal. Chem.*, **2008**, *621*, 222-228.
- 218) Marsan, M. P., Muller, I., Ramos, C., Rodriguez, F., Dufourc, E. J., Czaplicki, J., Milon, A., *Biophys. J.*, **1999**, *76*, 351.
- 219) Harroun, T.A., Katsaras, J., Wassall, S.R., *Biochemistry*, **2006**, *45*, 1227-1237.

- 220) Brosseau, C. L. *Electrochemical and PM-IRRAS Studies of Cholera Toxin Binding at a Model Biological Membrane*, Ph.D. thesis, **2007**, University of Guelph.
- 221) Kobayaski, T. *J-aggregates*, Volume 2. Danvers, USA: World Scientific, 2012, pg 352-355.
- 222) Krafft, C., Neudert, L., Simat, T., Salzer, R. *Spectrochimica Acta Part A*, **2005**, *61*, 1529-1535.
- 223) Baraga, J. J., Feld, M. S., Rava, R. P., *Proc. Natl. Acad. Sci.*, **1992**, *89*, 3473-3477.
- 224) Weinmann, P., Jouan, M., Dao, N. Q., Lacroix, B., Groiselle, C., Bonte, J.-P., Luc, G., *Atherosclerosis*, **1998**, *140*, 81-88.
- 225) Buschman, H. P., Deinum, G., Motz, J. T., Fitzmaurice, M., Kramer, J. R., Van der Laarse, A., Bruschke, A. V., Feld, M. S., *Cardiovascular Path.*, **2001**, *10*, 69-82.
- 226) Kneipp, J., Kneipp, H., Rajadurai, A., Redmond, R. W., Kneipp, K., *J. Raman Spec.*, **2009**, *40*, 1-5.
- 227) Bin, X., Lipkowski, J., *J. Phys. Chem. B.*, **2006**, *110*, 26430-26441.
- 228) Dzwolak, W., Ravindra, R., Lendermann, J., Winter, R. *Biochemistry*, **2003**, *42*, 11347-11355.
- 229) Choi, I., Huh, Y. S., Erickson, D., *Microfluid Nanofluid*, **2012**, *12*, 663-669.
- 230) Barth, A., *Biochim. Biophys. Acta*, **2007**, 1767, 1073-1101.
- 231) Wang, C., Neugebauer, U., Bürck, Myllykoski, M., Baumgärtel, P., Popp, J., Kursula, P. *PLoS ONE*, **2011**, *6*, 1-15.
- 232) Rehman, I. U., Movasaghi, Z., Rehman, S., *Vibrational Spectroscopy for Tissue Analysis*, Taylor and Francis, New York: USA, **2012**.
- 233) Movasaghi, Z., Rehman, S., Rehman, I. U., *Applied Spec. Rev.*, **2007**, *42*, 493-541.
- 234) Lokszejn, A., Dzwolak, W., Krysiński, P. *Bioelectrochem.* **2008**, *72*, 34-40.
- 235) Nielsen, C. H., Abdali, S., Lundbaek, J. A., Cornelius, F. *Spectroscopy*, **2007**, *22*, 52-63.
- 236) Nielsen, L., Frokjaer, S., Carpenter, J. F., Brange, *J. Pharm. Sci.* **2001**, *90*, 29-37.

- 237) Li, S., Leblanc, M. *J. Phys. Chem. B.* **2014**, *118*, 1181-1188.
- 238) Wang, S. H., Dong, X. Y., Sun, Y. *J. Biochem. Eng.* **2012**, *63*, 38-49.
- 239) Wójcik, S., Babenko, V., Dzwolak, W. *Langmuir*, **2010**, *26*, 18303-18307.
- 240) Reipa, V., Gaigalas, A., Abramowitz, S. *J. Electroanal. Chem.*, **1993**, *348*, 413-428.
- 241) Tah, B., Pal, P., Roy, S., Dutta, D., Mishra, S., Ghosh, M., Talapatra, G. B. *Spectrochimica Acta Part A*, **2014**, *129*, 345-351.
- 242) Kurouski, D., Sorci, M., Postiglione, T., Belfort, G., Lednev, I. I. *Biotechnol. Prog.* **2014**, *30*, 488-495.
- 243) Pepper, I. L., Gerba, C. P., Gentry, T. J. *Environmental Microbiology*, Waltham, USA: Elsevier Inc. **2009**, pp.219-220.
- 244) Kiskis, J., Fink, H., Nyberg, L., Thyr, J., Li, J. Y., Enejder, A. *Nature*, **2015**, *5*, 1-9.
- 245) Drachev, V. P., Thoreson, M. D., Khaliullin, E. N., Davisson, V. J., Shalaev, V. M. *J. Phys. Chem. B.* 2004, *108*, 18046-18052.
- 246) Connelly, L., Jang, H., Arce, F. T., Capone, R., Kotler, S. A., Ramachandran, S., Kagan, B. L., Nussinov, R., Lal, R. *J. Phys. Chem. B.* **2012**, *116*, 1728-1735.
- 247) Nilsson, M. R. *Methods*, **2004**, *34*, 151-160.
- 248) Bell, S. E. J.; Sirimuthu, N. M. S. *J. Am. Chem. Soc.* **2006**, *128*, 15580-15581.
- 249) Xu, M., Luo, X., Davis, J. J. *Biosens. Bioelectron.* **2013**, *39*, 21-25.
- 250) Arenas-Alatorre, J., Silva-Velazquez, Y., Medina, A. A., Rivera, M. *Appl. Phys. A.* **2010**, *98*, 617-624.
- 251) Hoyer, W., Cherny, D., Subramaniam, V., Jovin, T. M. *J. Mol. Biol.* **2004**, *340*, 127-139.
- 252) Seneci, P., *Molecular Targets in Proteins Misfolding and Neurodegenerative Disease*. San Diego, USA: Academic Press, **2015**, pp. 242-243.
- 253) Huang, Y., Huang, J., Chen, Y. *Protein Cell*, **2010**, *1*, 143-152.
- 254) Shai, Y., Oren, Z. *Peptides*, **2001**, *22*, 1629-1641.
- 255) Bucciantini, M., Giannoni, E., Chiti, F., Baroni, F., Formigli, L., Zurdo, J., Taddei, N., Ramponi, G., Dobson, C. M., Stefani, M. *Nature*, **2002**, *416*, 507-511.

- 256) Carlo, M. D. *Eur. Biophys. J.* **2010**, *39*, 877-888.
- 257) Meier, R. J., Csiszár, A., Klumpp, E. *J. Phys. Chem.*, **2006**, *110*, 5842-5844.
- 258) Maiti, N. C., Apetri, M. M., Zagorski, M. G., Carey, P. R., Anderson, V. E. *J. Am. Chem. Soc.*, **2004**, *126*, 2399-2408.
- 259) Wrzosek, B., Bukowska, J., Kudelski, A. *J. Raman Spectrosc.*, **2005**, *36*, 1040-1046.
- 260) Kurouski, D., Van Duyne, R. P., Lednev, I. K. *Analyst*, **2015**, *140*, 4967-4980.

Appendix

Table A-1: Peak assignment for DMPC powder.

Peak / (cm ⁻¹)	Assignment ^{220, 224}
719	(C-N ⁺ (CH ₃)). Symmetric choline group stretch vibration.
883	
1062	$\nu(\text{C-O-PO}_2^-)$, C-C. Phosphate ester stretch. Skeletal stretch vibration.
1090	$\nu_s(\text{CO-O-C})\text{PO}_2$. Ester C-O symmetric stretch. Stretch in the phosphate group.
1125	C-C. Skeletal transformation stretch of lipids.
1294	CH ₂ . Wagging and twisting methylene vibration.
1438	CH ₂ . Methylene deformation.
1734	$\nu(\text{C=O})$. Ester carbonyl stretch.
2724	C-H. Stretch vibration.
2848	$\nu_s(\text{CH}_2)$. Symmetric stretch
2880	$\nu_{as}(\text{CH}_2)$. Asymmetric stretch.
2930	$\nu_{as}(\text{CH}_2)$. Asymmetric stretch.
3035	$\nu_{as}(\text{CH}_3)_3 \text{N}^+$. CH ₃ asymmetric stretch in the choline group

Table A-2: Peak assignment for cholesterol powder.

Peak / (cm ⁻¹)	Assignment ^{220, 224}
426	Raman deformation
699	$\delta_r(-\text{CH}_2)$. Rocking vibration
1439	$\delta_d(-\text{CH}_2)$. Deformation
1671	$\nu(\text{C=C})$. Stretch vibration of the alkene
2716	Stretching vibrations of CH and OH
2867	$\nu_{\text{sym}}(-\text{CH}_3)$. Symmetric stretch vibration
2932	$\nu_{\text{as}}(-\text{CH}_2)$. Asymmetric stretch vibration
3037	

Table A-3: Peak assignment for the recombinant human insulin powder

Peak / (cm ⁻¹)	Assignment ^{220,224}
642	C-C twisting mode of phenylalanine
849	Single bond stretching vibrations for valine
892	C-C stretching
951	$\nu(\text{CH}_3)$ of protein (α -helix)
1002	phenylalanine
1029	phenylalanine
1125	(C-N), protein
1206	CH ₂ wagging vibrations from glycine backbone and proline side chains, tyrosine
1267	Amide III (of proteins α -helix conformation), tryptophan
1338	CH ₂ wagging vibrations from glycine backbone and proline side chains
1447	CH ₂ bending mode of proteins
1609	Tyrosine, phenylalanine ring vibration
1656	Amide I (α -helical conformation)
2438	
2930	Symmetric CH ₃ stretches due to protein, CH ₂ asymmetric stretch
3058	

Table A-4: Peak assignment for native human insulin on AgNP surface.

Peak / (cm^{-1})	Assignment ²²⁴
398	
490	ring deformation of phenylalanine
530	cysteine
609	phenylalanine ring twist
634	N(C-S) _G methionine, C-S stretching, C-C twisting of tyrosine
677	N(C-S) cysteine
774	tryptophan
822	Protein band
874	Hydroxyproline, tryptophan
1018	phenylalanine $\delta(\text{CH})$
1080	phenylalanine ring breathing, (C-N) stretch
1132	palmitic acid
1178	C-H bending of tyrosine
1202	CH ₂ wagging vibration from glycine backbone and proline side chain
1303	C-N asymmetric stretching, CH ₂ bending
1393	C-N stretching
1495	C=C stretching
1590	(C=O) stretching of glutamic acid / aspartic acid
2167	
2933	CH ₂ bending and stretching
3228	OH and NH stretching vibration

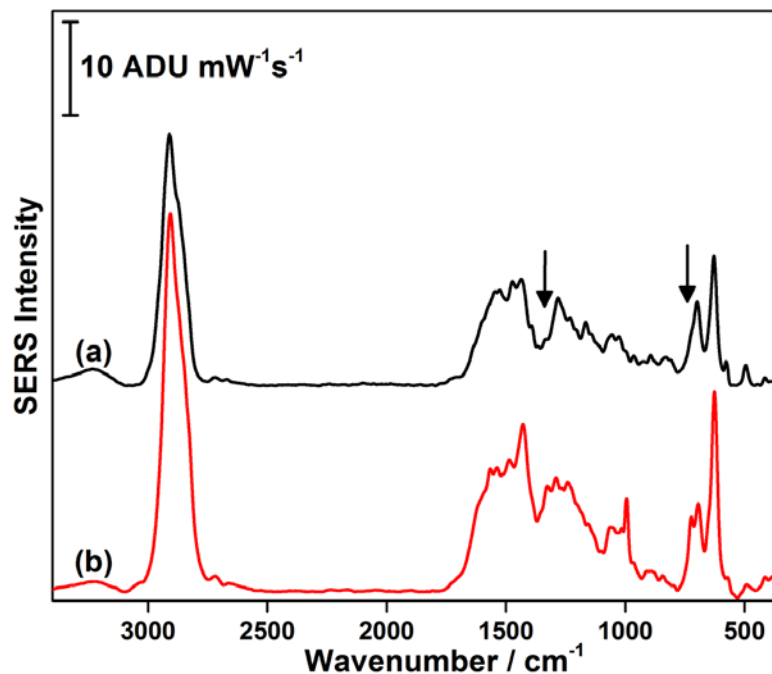


Figure A-1: EC-SERS comparison at -1.0 V between a) s-BLM without dAMP, b) s-BLM with dAMP. dAMP peaks indicated by arrows.

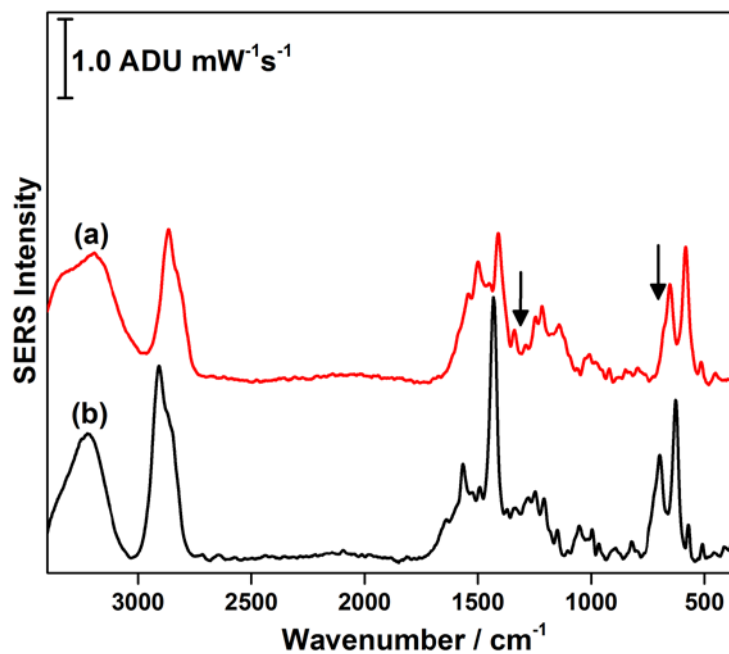


Figure A-2: EC-SERS comparison at -1.0 V between s-BLM + native insulin a) without dAMP, b) with dAMP. dAMP peaks indicated by arrows. No dAMP peaks were observed.

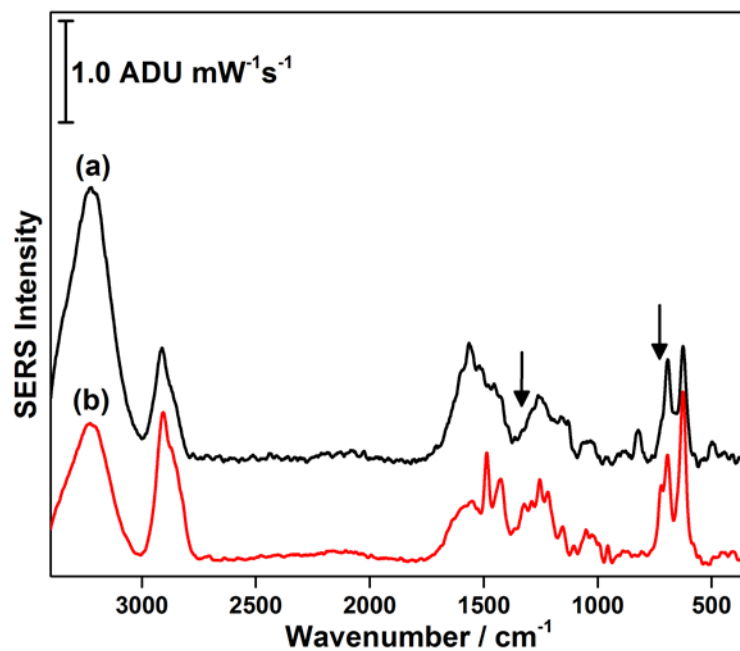


Figure A-3: EC-SERS comparison at -1.0 V between s-BLM + oligomers insulin a) without dAMP, b) with dAMP. dAMP peaks indicated by arrows.

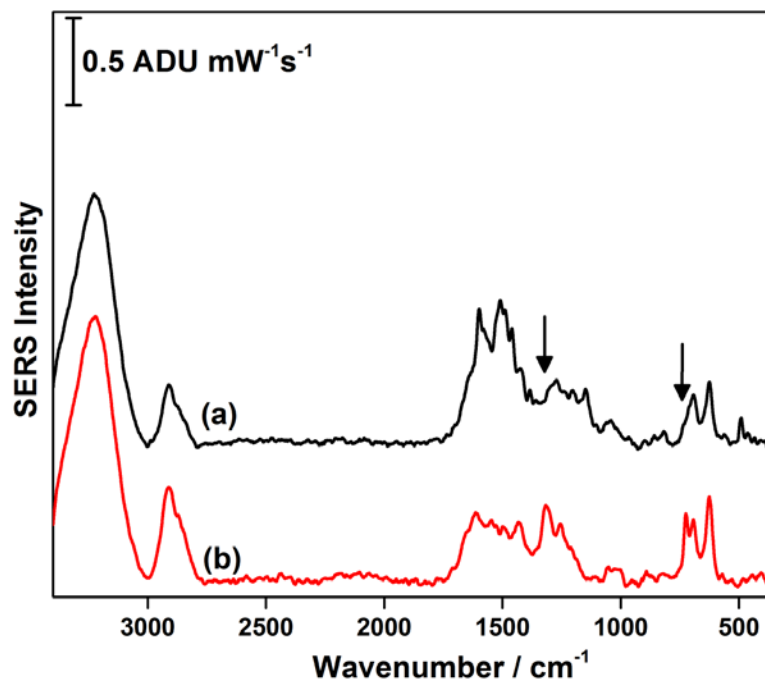


Figure A-4: EC-SERS comparison at -1.0 V between s-BLM + protofibrillar insulin a) without dAMP, b) with dAMP. dAMP peaks indicated by arrows.

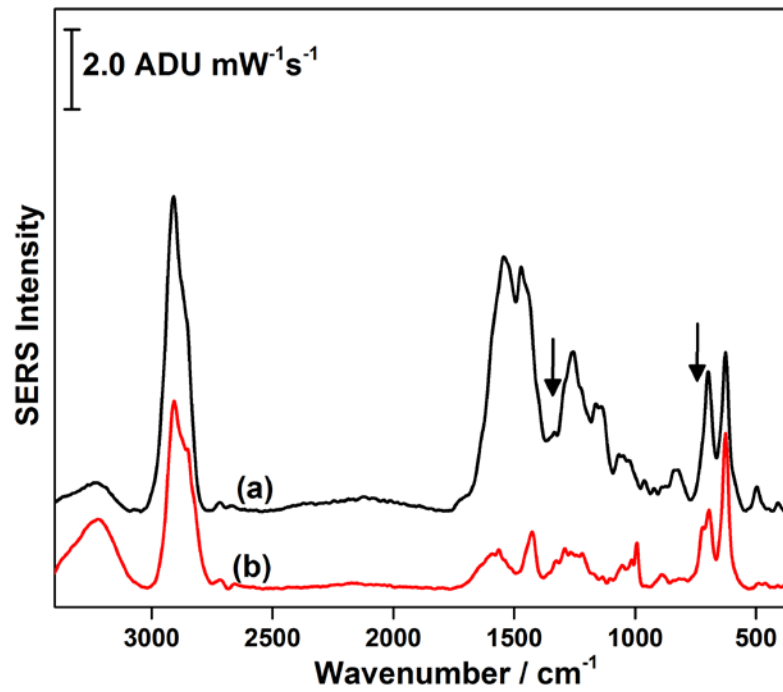


Figure A-5: EC-SERS comparison at -1.0 V between s-BLM + fibrillar insulin a) without dAMP, b) with dAMP. dAMP peaks indicated by arrows.